PhD Thesis

Mechanistic Studies of Zinc Electrodeposition from Deep Eutectic Solvents

Luciana Vieira

Institute for Chemistry and Technology of Materials
Graz University of Technology

CEST
Competence Center for Electrochemical Surface Technology

Supervisor: Assoc.Prof. Dipl.-Chem. Dr.rer.nat. Bernhard Gollas

Graz, April of 2014

to my grands Luiza and Jacob
who inspired my mother to dream beyond
and to my mother Nadir
who taught and inspired me to make it real

Statutory Declaration

I declare that I have authored this thesis independently, that I have not used other than the declared sources/resources, and that I have explicitly marked all material which has been quoted either literally or by content from the used sources.

Date Signature

Eidesstattliche Erklärung

Ich erkläre an Eides statt, dass ich die vorliegende Arbeit selbstständig verfasst, andere als die angegebenen Quellen/Hilfsmittel nicht benutzt, und die den benutzten Quellen wörtlich und inhaltlich entnommenen Stellen als solche kenntlich gemacht habe.

Datum Unterschrift

The work that originated this PhD thesis was carried out between January of 2010 and February of 2014 under supervision of Prof. Dr. Bernhard Gollas at the Institute for Chemistry and Technology of Materials, at the Graz University of Technology.

This work was financially supported by industrial projects from CEST (Competence Centre for Electrochemical Surface Technology GmbH). Most of the experiments that originated this thesis were carried out from January of 2010 to December of 2011 during the ARIoL project (Anodic Reactions from Ionic Liquids), which had as industrial partners the following companies: Atotech Deutchland GmbH (Germany), Akzo Nobel (Netherlands) and Andritz AG (Austria). Thereafter, the work was performed independently and concomitant with the Alumiol project (Electroplating of Aluminium from Ionic Liquids), in cooperation with the German companies: Atotech Deutchland GmbH, BASF and EADS.

Acknowledgment

Firstly I would like to thanks Prof. Dr Bernhard Gollas for his supervision, guidance, support and all the opportunities he has provided me since I arrived in Graz. His friendly, human and intelligent way of supervising helped me enormously to grow scientific, professional and personally.

Thanks to Prof. Dr Robert Schennach for the motivating and optimistic co-guidance in the PM-IRRAS experiments and for accepting being the co-referee of this thesis.

I am very thankful to my working colleges, specially to Christian Zelger, Stella Postlethwaith, Patrick Kosmus, Daniel Schloffer and Andreas Luegger for making it a nice working environment, for the friendship, support and also for the best Austrian dialect course I could ever have! Thanks a lot guys!

Thanks to IAESTE, which organized the first traineeship I made at the TU Graz. All the events, trips and friends I made through IAESTE are among my best memories of Austria. Special thanks to Teresa Flock, Natalie Proskurnia and Andrew Kelly.

A special thanks to the friends I made in Graz, you made my stay in Austria to feel like home. Asita Askari, Marjiana Racic, Faia Amoná, Fernando Campos, Caroline Mendon***c***a, Lígia Pasqualin, Gustavo Arruda, Luiza Soares, Marco García, Iris Lassnig and so many others. Thanks to the group of Capoeira Senzala Graz, my favourite sport after long working hours.

I could not forget Lennart and Gustavo, the treasure I found in Munich. Guys, you really made the end of this PhD and the whole final writing process incredibly happy. Through daily intensive laughing-sessions with you I did not have a chance to ever think negatively. I'm extremely grateful for all the care and motivation you gave me. Gustavo my dearest, I struggle to find words to describe how important you are to me. Thanks for your patience, love and friendship.

Furthermore I would like to thank Prof. Oswaldo Alves and the Solid State Chemistry Laboratory from UNICAMP, for the basis that led me here and for being always an inspiration of passion for chemistry. I'll carry the working philosophy I learned at the LQES for my life.

To my family all my gratitude. My mom Nadir, my dear cousin and best friend Ivan, my sister Vanessa with the kids, my brothers Thiago and Igor, thanks for everything.

Finally, I would like to emphasize that it would be much harder, if not impossible, to come to the end of this PhD without the support of my friends. Many of them so far away, but so present in my life. I am very grateful for being surrounded by such warm-hearted people. I am thankful for all the good moments we had together. Yet, I am even more thankful for the hard times we had because it allowed us to recognize each other more easily. There was always somebody there for me and I hope I can be there for you too. Thanks!

Abstract

Deep eutectic solvents (DES) have been suggested as alternatives to classical room temperature ionic liquids (RTILs) and been used for the electrodeposition of metals. We have investigated the electrodeposition of zinc from a Lewis-basic choline chloride (ChCl)/ethylene glycol (EG) DES containing $ZnCl_2$. Raman spectroscopy confirmed the presence of the $[ZnCl_4]^{2-}$ ion in the electrolyte. Infrared spectroscopy revealed strong hydrogen-bond interactions between the hydrogen-bond donor (EG) and the acceptor (ChCl).

The system was examined by cyclic voltammetry and potential step techniques at static and rotating disc electrodes. Glassy carbon (GC), platinum, gold, copper and stainless steel (SS) were used as working electrodes. The influence of the substrate material on Zn deposition and dissolution from this deep eutectic system is discussed.

On GC and SS an unusual voltammetric behavior was observed. On the forward cathodic sweep, very little current is observed. However, a cathodic peak attributed to the electrodeposition of zinc was observed on the anodic backward scan within -0.4 and $-0.2\,\mathrm{V}$ *vs.* $\mathrm{Zn/Zn^{2+}}$. Formation of a dissolved, reducible intermediate species Z on the cathodic sweep was proposed to account for the observed deposition behavior in the DES. Furthermore, the electrochemical behavior upon addition of sodium ethoxide to the deep eutectic mixture supports the suggestion that Z is a complex of Zn^{2+} and deprotonated components of the solvent with formula $[Zn(RO)_xCl_{4-x}]^{2-}$.

On gold, platinum and copper electrodes, which all can form extensive intermetallic phases with zinc, a distinctly different behavior was found. For these substrates, voltammetry showed a pronounced cathodic peak during the cathodic as well as the subsequent anodic sweep. The effect of scan rate on the peak currents together with the electrode material-dependent behavior can be explained by the different hydrogen overpotentials for each substrate and adsorption phenomena of components present in the DES. Besides the reflexes for the elemental metals, XRD of zinc deposits on Pt and Cu reveals the typical pattern for the Pt_7Zn_{12} and Cu_4Zn phases, respectively. SEM and FIB of both coatings show a nanostructured surface morphology with nanoplatelets.

The DES/electrode interface was investigated by polarization-modulation infrared reflection-absorption spectroscopy (PM-IRRAS). This technique allows distinguishing between chemical information from the solution and the species adsorbed on the electrode surface. The first *in situ* PM-IRRAS study of an electrode reaction in an RTIL shows the kinetically extremely slow formation of an adsorbed solvent layer at open circuit potential (OCP). *In situ* PM-IRRAS on an electrified GC electrode reveals that adsorbed hydrogen probably blocks the electrodeposition of zinc. A re-orientation of the interfacial species takes place when the electrode is polarized at potentials more positive or negative than the OCP. The species adsorbed on GC and their effect on zinc electrodeposition is discussed.

Kurzfassung

Stark eutektische Lösungsmittel (DES) wurden als Alternative zu klassischen ionischen Flüssigkeiten (room temperature ionic liquids, RTILs) vorgeschlagen und zur elektrochemischen Abscheidung von Metallen herangezogen. In dieser Arbeit wurde die elektrochemische Abscheidung von Zink aus einer Lewis-basischen Mischung von $ZnCl_2$ mit Cholinchlorid (ChCl)/Ethylenglykol (EG) als stark eutektisches Lösungsmittel untersucht. Mittels Raman Spektroskopie konnte das $[ZnCl_4]^{2-}$ Ion im Elektrolyt nachgewiesen werden. Infrarot Spektroskopie zeigte eine starke Wasserstoffbindungswechselwirkung zwischen dem Wasserstoffbindungs-Donor (EG) und –Akzeptor (ChCl).

Das System wurde mittels zyklischer Voltammetrie und Potentialsprungmethoden an statischen und rotierenden Scheibenelektroden untersucht. Die Arbeitselektrodenmaterialien waren Glaskohlenstoff (glassy carbon, GC), Platin, Gold, Kupfer und Edelstahl (stainless steel, SS). Die Abhängigkeit der Zinkabscheidung und -auflösung vom Substratmaterial im vorliegenden DES wurde diskutiert.

An GC- und SS-Elektroden wurde ein ungewöhnliches voltammetrisches Verhalten beobachtet. Im kathodischen Hinscan findet man nur sehr geringe Ströme. Ein kathodischer Peak, der der Zinkabscheidung zugeordnet wird, tritt im anodischen Rückscan zwischen -0.4 und $-0.2\,\mathrm{V}$ *vs.* Zn/Zn^{2+} auf. Es wird die Bildung einer löslichen, reduzierbaren intermediären Spezies Z im kathodischen Scan vorgeschlagen, welche verantwortlich ist für das gefundene Abscheidungsverhalten im DES. Die Hypothese, dass Z ein Komplex aus Zn^{2+} und deprotonierten Lösungsmittelbestandteilen der Form $[Zn(RO)_xCl_{4-x}]^{2-}$ sei, wird durch das gefundene elektrochemische Verhalten bei Zugabe von Natrium Ethanolat zum DES bekräftigt.

An Au-, Pt- und Cu-Elektroden, welche alle intermetallische Phasen mit Zink bilden, wurde ein anderes Verhalten beobachtet. Mit diesen Elektrodenmaterialien wurde in cyclischen Voltammogrammen sowohl im kathodischen Scan als auch im darauffolgenden anodischen Scan ein kathodischer Peak gefunden. Der Einfluss der Spannungsvorschubgeschwindigkeit auf den Peakstrom und das elektrodenmaterialabhängigen Verhalten kann man durch die unterschiedlichen Überspannungen der Substrate für die Wasserstoffentwicklung und Adsorptionsphänomene von Bestandteilen der DES erklären. Röntgendiffraktogramme der Zinkschichtten auf Pt und Cu zeigen neben den Reflexen der Elemente jeweils auch die charakteristischen Reflexe von Pt_7Zn_{12} and Cu_4Zn. Die REM- und FIB-Aufnahmen der Schichten zeigen eine nanostrukturierte Oberflächenmorphologie in Form von Nanoplättchen.

Die Grenzfläche GC-Elektrode/DES wurde mittels Polarisationsmodulations Infrarot-Reflexions-Absorptions-Spektroskopie (PM-IRRAS) untersucht. Diese Technik erlaubt es, chemische Informationen der Lösung von jenen adsorbierter Spezies zu unterscheiden. Die ersten *in situ* PM-IRRAS Untersuchungen einer Elektrodenreaktion in einer ionischen Flüssigkeit zeigten die kinetisch extrem langsame Bildung einer adsorbierten Schicht am Ruhepotential (open circuit potential, OCP). *In situ* PM-IRRAS Ergebnisse einer polarisierten GC-Elektrode lassen vermuten, dass adsorbierter Wasserstoff die elektrochemische Abscheidung von Zink blockiert. Eine Re-orientierung der Grenzflächenspezies findet statt, wenn ein höheres oder niedrigeres Potential als das OCP angelegt wird. Es werden die an der GC-Elektrode adsorbierten Spezies und deren Effekt auf die elektrochemische Abscheidung von Zn diskutiert.

Abbreviations

2D-N	two-dimensional nucleation
3D-N	three-dimensional nucleation
AFM	atomic force microscopy
ATR	attenuated total reflection
CE	counter electrode
CE	coulombic efficiency
CV	cyclic voltammetry
DES	deep eutectic solvent
DL	double layer
ECE	electron transfer, chemical and electron-transfer mechanism steps
EDL	electrical double layer
EDX	energy dispersive X-ray spectroscopy
EIS	electrochemical impedance spectroscopy
EXAFS	extended X-ray absorption fine structure
FIB	focused ion beam
FTIR	fourier transform infra-red
GC	glassy carbon
GIXD	grazing incidence X-ray diffraction
HBD	hydrogen bond donor
HREELS	high resolution electron energy loss spectroscopy
IN	instantaneous nucleation
IR	infra-red
OM	optical microscopy
PM-IRRAS	polarization modulation infrared reflection-absorption spectroscopy
PN	progressive nucleation
RDE	rotating disk electrode
RE	reference electrode

RTIL	room temperature ionic liquid
SCE	saturated calomel electrode
SEC	spectroelectrochemistry
SECC	spectroelectrochemical cell
SEIRAS	surface-enhanced infrared absorption spectroscopy
SEM	scanning electron microscopy
SFG	sum frequency generation spectroscopy
SH	Sharifker and Hills
STM	scanning tunneling microscopy
SS	stainless steel
XRF	X-ray fluorescence
XRD	X-ray diffraction
WE	working electrode

Chemicals and Ionic Liquids

12CE	1:2 molar ratio choline chloride : ethylene glycol
12CU	1:2 molar ratio choline chloride : urea
AC	acetate
BMIMC	1-n-butyl-3-methylimidazolium chloride
[BMIM][TFSA]	1-butyl-3-methylimidazolium bis(trifluoromethanesulfonyl)-amide
[BMIM][BF_4]	1-butyl-3-methylimidazolium tetrafluoroborate
BMP	1-butyl-1-methylpyrrolidinium
[BMP][DCA]	1-butyl-1-methylpyrrolidinium dicyanamide
[BMP][Tf_2N]	1-butyl-1-methylpyrrolidinium bis(trifluoromethylsulfonyl)imide
[C_8MIM]Cl	1-octyl-3-methylimidazolium chloride
ChCl	choline chloride
DCA	dicyanamide
DMPC	1,2-dimyristoyl-*sn*-glycero-3-phosphocholine
EG	ethylene glycol
EMIM	1-ethyl-3-methylimidazolium
EMIB	1-ethyl-3-methylimidazolium bromide
EMIMCl	1-ethyl-3-methylimidazolium chloride
[EMIM][BF_4]	1-ethyl-3-methylimidazolium tetrafluoroborate
[EMIM][FAP]	1-ethyl-3-methylimidazolium tris(pentafluoroethyl)trifluorophosphate

[EMIM][Tf_2N]	1-ethyl-3-methylimidazolium [bis(trifluoromethyl)sulfonyl]amide
[EMIM][TfO]	1-ethyl-3-methylimidazolium trifluoromethylsulfonate
FAP	tris(pentafluoroethyl)trifluorophosphate
Fc	ferrocene
FcMeOH	ferrocene methanol
MBIC	1-methyl-3-butylimidazolium chloride
MEIC	1-methyl-3-ethylimidazolium chloride
OEt^-	ethoxide ($C_2H_6O^-$)
[$Py_{1,4}$][FAP]	1-butyl-1-methyl-pyrrolidinium tris(pentafluoroethyl)trifluorophosphate
[$Py_{1,4}$]TfO	1-butyl-1-methylpyrrolidinium trifluoromethylsulfonate

Symbols

A	area (cm^2)
C	concentration ($\mathrm{mol{\cdot}L^{-1}}$)
D	diffusion coefficient ($\mathrm{cm^2\ s^{-1}}$)
δ	diffusion layer thickness
E	potential (V)
E_a	activation energy ($\mathrm{kJ{\cdot}mol^{-1}}$)
E_η	activation energy for the viscosity ($\mathrm{kJ{\cdot}mol^{-1}}$)
E_Λ	activation energy for conduction ($\mathrm{kJ{\cdot}mol^{-1}}$)
ΔE_p	$E_\mathrm{p}^\mathrm{ox} - E_\mathrm{p}^\mathrm{red}$ in CV (V)
E_p^ox	oxidation peak potential (V)
$E_\mathrm{p}^\mathrm{red}$	reduction peak potential (V)
F	the Faraday constant (96485.3 $\mathrm{C\ mol^{-1}}$)
i	current (A)
I	current density ($\mathrm{mA{\cdot}cm^{-2}}$)
i_dl	double layer current (A)
I_p^ox	oxidation peak current density ($\mathrm{mA{\cdot}cm^{-2}}$)
$I_\mathrm{p}^\mathrm{red}$	reduction peak current density ($\mathrm{mA{\cdot}cm^{-2}}$)
$I_\mathrm{p}(\nu)$	*p*-polarized IR spectrum
$I_\mathrm{s}(\nu)$	*s*-polarized IR spectrum
n	total number of electrons passed per molecule
η	viscosity (mPa·s)
η	overpotential (V or mV)

ν	scan rate ($\mathrm{mV\cdot s^{-1}}$)
σ	conductivity ($\mathrm{mS\cdot cm^{-1}}$)
$S(\nu)$	PM-IRRAS surface spectrum
$\Delta S(\nu)$	subtractively normalized PM-IRRAS surface spectrum
r_o	electrode radius (cm)
R	the gas constant (8.31447 J $\mathrm{K^{-1}}$ $\mathrm{mol^{-1}}$)
t	time
T	temperature

Table of Contents

1 Introduction

1.1 Electrodeposition of zinc from ionic liquids

Zinc electrodeposition is one of the most common industrial electrochemical processes, e.g. for the anti corrosion coating of steel. Due to its lower equilibrium potential, a zinc coating can provide cathodic protection by sacrificially corroding before the steel does [1]. However, electroplating of zinc from aqueous solution involves massive hydrogen evolution at the cathode, hence decreasing the current efficiency and causing hydrogen embrittlement, which can be a significant problem for some substrates, especially for high strength steels [2]. Alternative hydrogen-free techniques include hot dip galvanizing, thermal spraying and mechanical plating. These techniques have several drawbacks. Mechanical plating requires impact resistant samples, while hot dip and thermal-spraying techniques, which are carried out at the melting point of zinc (450 °C), are only suitable for thermally insensitive substrates [3]. It is therefore desirable to investigate a low temperature and hydrogen-free electrochemical process for the electrodeposition of zinc.

Room temperature ionic liquids (RTILs) are ionic substances that are liquid under ambient conditions. These compounds have many attractive applications, including electroplating [4–8]. Among their features, RTILs have a negligible vapor pressure, good ionic conductivity, show good solvation of many metal salts and good thermal stability. One of the most attractive characteristics of RTILs is their wide potential window (even higher than 4 volts), which allows the electrodeposition of metals that cannot be electroplated from aqueous solutions due to the cathodic decomposition of water generating hydrogen [9]. Furthermore, with the exclusion of water, hydrogen embrittlement could be avoided.

Deep eutectic solvents (DES) are an alternative class of RTILs which are easy to prepare and low in cost. One type of DES that has been successfully used as electrolyte to deposit metals is a combination of choline chloride (2-hydroxy-N, N, N-trimethylethanaminium chloride, ChCl) with hydrogen bond donor compounds, such as urea or ethylene glycol (EG) in a molar ratio of 1:2 [10, 11]. The molecular structure of ethylene glycol and choline chloride are shown in Figure 1.1. These types of mixtures are liquid at room temperature, relatively insensitive to water, its constituents have a low toxicity and cost, and are also biodegradable [12–17]. Besides, they have many of the same properties of RTILs, including a wide electrochemical window, low vapor pressure and high solubility of many metal salts [18, 19]. Moreover, DES are considered less expensive than true ionic liquids, which makes them attractive for use in green deposition processes on industrial scale [20, 21].

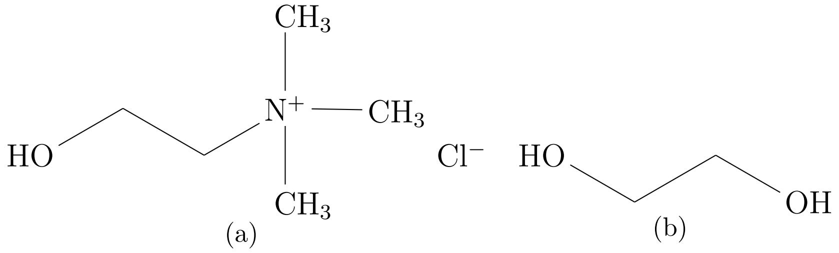

(a) (b)

Figure 1.1. The molecular structure of a) choline chloride and b) ethylene glycol.

Electrodeposition of zinc has been reported in a range of ionic liquids [22–33] and choline chloride based deep eutectic solvents [34–44]. With the exclusion of water, hydrogen evolution would not be anticipated. Yet, the nature of the ionic liquid [33, 45, 46] and the speciation of zinc [24, 30, 44, 47–49] play a significant role in the electrochemical behavior of Zn^{2+} ions. The organization of the double layer and strongly adhering solvation layers of ionic liquids on the metal surface also seem to affect drastically the zinc nucleation and consequently the morphology of the deposit as reported for zinc deposition from DES [45] and pyrrolidinium-based RTILs [33].

Abbott et al. [45] investigated the electrodeposition of zinc from two different deep eutectic solvents comprising 1:2 molar ChCl:EG and 1:2 molar ChCl:Urea. EXAFS measurements showed that the main zinc species in both DES is $[ZnCl_4]^{2-}$. Nevertheless, significant differences were found in the chronoamperometric and gravimetric data, as well as in the morphology of the zinc deposit for both deep eutectics. The differing electrodeposition rates are attributed to the different chloride activity in the solvents, changing the zinc concentration in the electrochemical double layer and consequently the mechanism of zinc electrodeposition. Thus, the different morphology of the zinc deposits from these two deep eutectics were attributed to specific chloride adsorption.

The effect of additives on the electrodeposition of zinc from 1:2 molar ratio of choline chloride:ethylene glycol (12CE) DESs has also been investigated. Abbott's group [37] has shown that additives such as ammonia and ethylene diamine had a pronounced effect on the cyclic voltammetric and gravimetric behavior of zinc chloride in 12CE, as well as on the resultant morphology of the deposit, acting as effective brighteners, whereas acetonitrile does not significantly change the behavior of this electrolyte on a platinum substrate. EXAFS measurements of the electrolyte containing additives showed that all solutions contained the same zinc species $[ZnCl_4]^{2-}$, excluding the possibility of complexation of the additives with zinc. Rather, changes in the electrochemical behavior of the zinc electrolyte in the presence of additives were explained in terms of differing hydrogen bond strengths of the additives and adsorption of chloride.

Pereira et al. [39] investigated the effect of chelating agents such as ethylenedinitrilotetraacetic acid (EDTA), N-(2-hydroxyethyl)ethylenediamine-N,N',N'-triacetic acid (HEDTA) and N-(2-hydroxyethyl)ethylenediamine-N,N',N' triacetic acid trisodium salt (EDTA-Na_3) have on zinc deposition from 12CE on a platinum electrode. Compared to the other compounds, HEDTA had the most remarkable effect by decreasing the current density of zinc deposition and also changing the morphology of the deposit. Another study with tartrate ions (potassium hydrogen tartrate and tartaric acid) in the same deep eutectic system [40], showed that, like the deep eutectic without additive, the deposition of zinc on a steel electrode in the presence of potassium hydrogen tartrate proceeds via a 3D progressive nucleation and growth mechanism. With tartaric acid, 2D progressive nucleation has been observed, which changes to 3D progressive growth during the electrodeposition process.

Whitehead et al. [41, 42] have previously investigated the zinc electrodeposition from a deep eutectic solvent comprising a 1:2 molar ratio of choline chloride:ethylene glycol on a glassy carbon (GC) substrate and discussed the role of choline chloride on the voltammetric response of zinc compared with a choline-free electrolyte. Unusual cyclic voltammetric zinc electrodeposition was observed, in which a cathodic peak appeared in the anodic sweep after the cathodic potential switch. It was suggested that choline ions block the surface of the electrode during the forward cathodic potential sweep and that zinc is deposited during the backward scan from intermediate zinc species formed at potentials more negative than $-0.6\,\mathrm{V}$ *vs.* $\mathrm{Zn/Zn^{2+}}$. More recently, the same unusual voltammetric behavior for zinc deposition has been reported for 12CE electrolyte on steel substrates [40] and for imidazolium-based ionic liquids on GC [30]. We have investigated this interesting voltammetric behavior in more detail [43, 44] and the range of substrates to include gold, platinum, copper and steel. The system was examined by classical electrochemical methods such as cyclic voltammetry and potential step techniques at static and rotating disc electrodes [50–55]. The mechanistic aspects of the reaction and the influence of the substrate material on Zn deposition and dissolution from this deep eutectic system have been studied thoroughly.

Spectroscopic methods such as Raman [56] and Infrared (IR) [57, 58] were used to characterize the electrolyte and the speciation of zincate ions in the deep eutectic electrolyte. *In situ* electrochemical polarization modulation infrared reflection absorption spectroscopy (PM-IRRAS) [59–62] was used to investigate the properties of the interface between 12CE electrolyte and a glassy carbon electrode. Therefore, a spectroelectrochemical cell was constructed. The effect of the electrode potential on the structure of the 12CE/GC interface has been explored. This is the first spectroelectrochemical study of ionic liquids using the PM-IRRAS technique.

1.2 The ionic liquid/electrode interface

The mechanism of zinc electrodeposition from deep eutectic solvents is closely related to the processes and reactions that take place at the interface electrolyte/electrode [44, 45]. However, very little is known about the structure and dynamics of RTILs at the interface. The Gouy-Chapman-Stern model of the electric double layer (EDL) for aqueous electrolyte solutions/metal interfaces [52] can not be directly transferred to ionic liquids, because the former has been formulated to explain diluted electrolytes, in which the ions are treated as point charges, whereas ionic liquids are highly concentrated ionic fluids [63, 64].

The fact that IL are composed of only cations and anions implies that the solvation of an ionic solute might be entirely different [65, 66] as well as the electrostatic interactions near charged surfaces. Consequently, mass transfer and kinetics of electrode reactions can be significantly affected leading to unexpected electrochemical outcomes [67], as it is presented for zinc electrodeposition from 12CE [44].

X-ray reflectometry [68] and atomic force microscopy [69] have been used to investigate the near-surface structure of metal/ionic liquids. Multi-layers of alternating ions with well ordered nanostructures of IL have been proposed to explain such interfaces [70]. Such multi-layered ionic liquid structures have also been modeled by molecular dynamic simulations [71–75].

Surface sensitive *in situ* spectroscopic techniques, such as sum frequency generation (SFG) [76–79], surface-enhanced Raman spectroscopy (SERS) [80, 81] and surface-enhanced infrared absorption spectroscopy (SEIRAS) [82, 83] have been successfully used to study the structures of IL/metal interfaces.

Infrared reflection absorption spectroscopy (IRRAS or RAIRS) is a powerful technique to interrogate metal-liquid interfaces at a molecular level [59, 84]. However, difficulties may arise from the strong IR absorption of the background, which usually suppresses the IR signals of the surface species. Due to the difficulty of acquiring a background spectrum of the solution (for a solid-liquid interface) under exactly the same conditions, the background correction can be made by either potential or polarization modulation [60].

In potential modulation, the background is an IRRAS spectrum recorded at a given reference potential. The difference between the reference and a second spectrum at a sample potential, divided by the sum of the two, yields a surface spectrum, in which the creation or destruction of surface species generates positive or negative bands, respectively. This technique is called subtractively normalized interfacial Fourier transform infrared spectroscopy (SNIFTIRS) [60].

Polarization modulation is carried out based on the surface selection rules [85], which state that the *p*-polarized radiation is absorbed by surface and liquid phase species, while the *s*-polarized is only absorbed by the species in the liquid phase. By using a photoelastic modulator and simultaneously measuring the two IR radiations, the *s*-spectrum can be used as a background, hence the liquid phase contribution can be subtracted from the IR spectrum [86]. The difference between the *p*- and *s*- polarized spectra divided by the sum of the two yields an IR spectrum of the surface species. Therefore, this technique is called polarization modulation infrared reflection absorption spectroscopy (PM-IRRAS).

IRRAS has already been used to study ionic liquids/metal interfaces, namely [EMIM] [Tf_2N] (1-ethyl-3-methylimidazolium bis-(trifluoromethylsulfonyl)imide) on Ag. The temperature effect was investigated and the thin-film IRRAS spectra were compared to spectra of the bulk liquids [87]. Some differences of the IR bands for bulk and thin film spectra arising from the substrate-IL interactions at open circuit potential were reported [88]. Apparently, preferential adsorption would affect the crystalline growth of the thin IL film by changing the temperature.

A spectroelectrochemical investigation of [EMIM][BF_4] (1-ethyl-3-methylimidazolium tetrafluoroborate) ionic liquid at charged gold electrodes by SNIFTIRS has been reported [89]. Varying the electrode potential changed the intensity of the bands from anions and cations in the IR spectra, which indicated an overall change of the charged species at the interface. Changes in orientation of the $EMIM^+$ cations to a more vertical position were suggested to explain the variation of IR absorption within -1.3 and $+0.6\,V$ *vs.* Ag/Ag^+.

PM-IRRAS has been successfully employed to study the molecular structure of self-assembled monolayers, biomimetic membranes and Langmuir Blodgett films at charged electrodes by Lipkowski's group [60, 90–99]. Yet, to the best of our knowledge, no PM-IRRAS study of ionic liquids/electrode interfaces have been reported. We have extensively investigated the electrochemistry of zinc in 12CE electrolytes, mainly at glassy carbon electrodes [41–44]. Herein, we present the first *in situ* PM-IRRA spectro-electrochemical study on the interface of this deep eutectic solvent with a glassy carbon electrode. The results obtained in this thesis not only help understanding the zincate reduction mechanism but it also provides an insight of the structure and dynamics of the electrolyte/electrode interface for ionic liquids.

1.3 Objectives

The aim of this thesis is to investigate the mechanism of zinc electrodeposition from deep eutectic solvents. Therefore, electrochemical and spectroscopic methods have been used. The two methods are complementary, as the spectroscopy provides chemical information about the species involved in the electrochemical reactions.

In order to perform *in situ* PM-IRRAS, a spectroelectrochemical cell for analysing the DES/electrode interface was developed.

1.4 Scope of the thesis

This thesis is organized in three parts: Part I presents the investigation on zinc electrodeposition on glassy carbon electrodes and focuses on the speciation of zinc and the electrochemical aspects of the reaction. Part II shows the deposition of zinc on different substrates materials. This part is divided into two chapters: platinum and gold; copper and stainless steel. The characterization of the morphology and phases of the deposited zinc is explored in more detail. Finally, Part III presents the spectroscopic investigation of deep eutectic solvents in two chapters. Firstly, the spectroscopic characterization of the electrolyte is presented. Thereafter, the *in situ* electrochemical PM-IRRAS experiments on a glassy carbon electrode are presented and discussed.

2 Experimental

2.1 Electrolyte

2.1.1 Preparation of the electrolyte

Solutions of 1:2 molar ratio choline chloride: ethylene glycol (12CE) were prepared by firstly drying the choline chloride (99 % Fluka) at 100 °C under reduced pressure $8 \cdot 10^{-3}$ mbar) in a schlenk flask for $\geq$ 48 h. When the flask had cooled down close to room temperature the flask was isolated from the vacuum pump and transferred to an argon filled glove box, where anhydrous ethylene glycol (99.8 %, Aldrich) was added as supplied, without further drying. The mixture was stirred using a PTFE-coated magnetic stir bar until a single, colorless liquid phase resulted.

Electrolytes containing $ZnCl_2$ were prepared similarly by adding pre-dried powdered $ZnCl_2$ (99.999 %, Aldrich, dried at room temperature at $8 \cdot 10^{-3}$ mbar for $\geq$ 48 h) to the 12CE electrolyte. The solution was stirred until all of the salt was dissolved. Higher temperatures were avoided to limit reactions between the $ZnCl_2$ and the hydroxyl group of the choline.

$ZnCl_2$ solutions of 12CE containing sodium ethoxide ($NaOC_2H_5$, Sigma-Aldrich, 95 %) were prepared by adding a pre-weighed amount of $NaOC_2H_5$ to the 0.3 $mol \cdot L^{-1}$ $ZnCl_2$ 12CE and stirred for ca. 30 min. The $NaOC_2H_5$ was used as supplied and not heated with the $ZnCl_2$ to avoid reaction with water, which would produce ethanol and NaOH, and cause a large uncertainty in the concentration.

2.1.2 Physical chemical characterization

Karl-Fischer Titration

Karl-Fischer analysis was performed to determine the initial water content of the electrolytes using an automatic titrator (CA-100/VA-100, Mitsubishi Chemicals Corp.). Ethylene glycol contained 40 ppm water and the freshly prepared and dried 12CE electrolyte had about 92 ppm water content.

Conductivity measurements

Conductivity measurement of the deep eutectic electrolyte was performed in the temperature range of 0 to 100 °C. A 4 electrode platinum sensor with a glass body (Knick-4-pol-cell ZU6985) was assembled with the DES in the glove box. The measurement was run by dipping the cell containing 12CE into a thermostated bath (Huber, CC156w, Polystat CC2) and measuring the conductivity of the electrolyte at a certain stabilized temperature using an AC conductivity meter (Konduktometer 703, Knick Konduktometer, Germany).

Viscosity measurements

Viscosities were measured with a Anton Paar Stabinger Viscosimeter SVM 3000/G2. The reported values are averages of at least 5 measurements, respectively, having standard deviations within ±0.5 mPa·s.

Raman

Raman spectra were recorded using a Horiba Jobin Yvon LabRAM ARAMIS Raman spectrometer with a 532 nm focused laser beam. Quartz cuvettes with a path length of 5 mm were filled with 1 mL of electrolyte in the glove box, closed with a Teflon cap and sealed with parafilm. Three 60 s scans were recorded for each sample.

Infrared

Infrared spectra of the bulk electrolyte were measured using a Bruker Alpha FTIR spectrometer equipped with ALPHA's Platinum ATR single reflection diamond. The spectra were recorded in an ATR module with a spectral range between 4000 and 400 cm^{-1} and a resolution of 2 cm^{-1}.

2.2 Electrochemical apparatus

The electrochemical measurements were carried out in a three-electrode electrochemical cell set up in a dry, argon-filled glove box. The cell body, including a thermostated jacket, was made of glass to enable visual inspection of the electrodes for positioning and during the experiments. All experiments, unless specified, were carried out at 30 °C. The temperature was kept constant by a circulating thermostated oil bath (Huber, CC156w, Polystat CC2). A sketch of the electrochemical cell is shown in Figure 2.1.

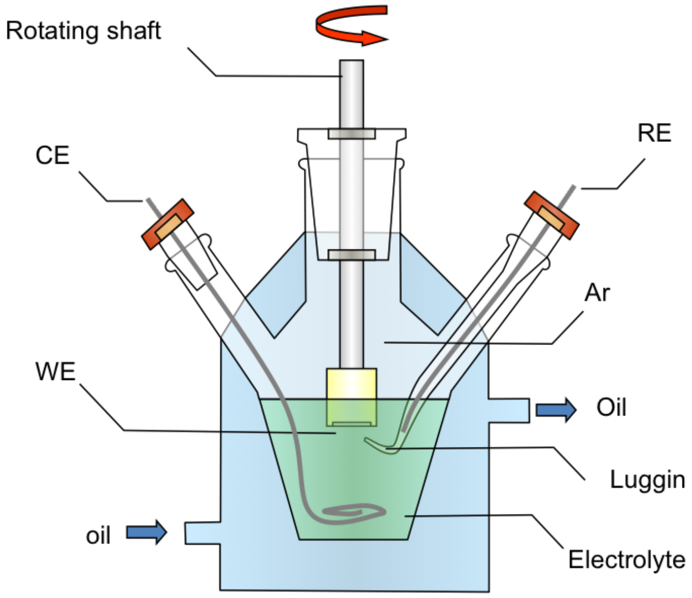

Figure 2.1. Sketch of the electrochemical cell. The cell was kept in the glove box under Argon atmosphere (Ar). WE, CE, RE indicate working, counter and reference electrode, respectively.

A round zinc wire (99.99 % purity, Advent Research Materials, 1 mm diameter and 150 mm long counter electrode (CE) was used directly in the bulk electrolyte in order to try and maintain a constant zinc concentration in the electrolyte during deposition and dissolution.

Zinc wire was reported to be suitable as reference electrode (RE) in the DES 12CE [42]. The zinc wire RE was placed in a compartment with an open Luggin capillary placed approximately 3 mm from the working electrode, as indicated in Figure 2.1 [41]. For experiments with Zn-containing electrolytes the reference compartment contained electrolyte with the same composition as the bulk solution. For examination of Zn-free electrolytes the reference solution was saturated with $ZnCl_2$ (solubility limit of $ZnCl_2$ in 12CE: $0.52\,mol{\cdot}L^{-1}$ at 23 °C) and separated from the bulk electrolyte by a microporous glass frit in addition to the Luggin capillary. All potentials are quoted with respect to the respective Zn/Zn^{2+} couple.

The working electrodes (WE) were made of nonporous glassy carbon, platinum, copper, gold and stainless steel (1.4404) set up as stationary or a rotating disc assembly. The area of all electrodes used are summarized in Table 2.1.

The working electrodes of glassy carbon, platinum and gold were polished to a mirror finish with alumina powder. They were rinsed with deionised water and acetone and dried in air prior to use. Stainless steel and copper disks were degreased in Uniclean 155 (Atotech Deutschland GmbH) for 10 min at 60 °C, rinsed, pickled in 10 % H_2SO_4 (technical grade, Carl Roth GmbH & Co.) for 1 min, rinsed again, dried and quickly transferred to the glove box to avoid passivation.

Table 2.1. Working electrodes used and their respective area. RDE indicates Rotating Disk Electrode and PM-IRRAS is Polarization Modulation Infrared Reflection Absorption Spectroscopy.

Electrode Material		**Electrode area (cm^2)**		
Name	Abreviation/Symbol	Stationary WE	RDE	PMIRRAS-WE
Glassy Carbon	GC	0.071	0.126	1.54
Platinum	Pt	0.071	0.126	
Gold	Au	0.071		
Copper	Cu	0.950	0.950	
Stainless Steel	SS	0.950	0.950	

A Metrohm Echo Chemie Autolab PGSTAT100 potentiostat/galvanostat controlled by NOVA 1.6 software and hooked up to a glove box (MBraun, MB G-120) was used to perform cyclic voltammetry and potential step techniques under computer control.

2.3 Spectroelectrochemical measurements

2.3.1 Spectroelectrochemical cell

For *in situ* experiments, a special spectroelectrochemical cell was designed and constructed in house. An illustration of the spectroelectrochemical cell is shown in Figure 2.2 and a picture of it in Figure 2.3. The cell was custom-made of steel and can be sealed with o-rings. Ports with Teflon tubes connected to 3-port valves, permit gas purging, filling with electrolyte or total sealing of the cell. The working electrode consists of a 14 mm diameter glassy carbon disk inserted into an insulating threaded holder, which is used to control the distance between the electrode and the optical window by a micrometre screw. The electrode is carefully pressed against the ZnSe window until it is separated by only a few micrometers thick electrolyte layer. A piece of copper wire attached to the glassy carbon disk by conductive silver epoxy is used as connection between the working electrode and the electric cable that is wired to the potentiostat. Zinc wires are used as reference and counter electrodes connected to insulated wires and an external pin connector wired to the potentiostat. The temperature of the cell can be controlled internally by a ceramic heating element (Figure 2.2 b).

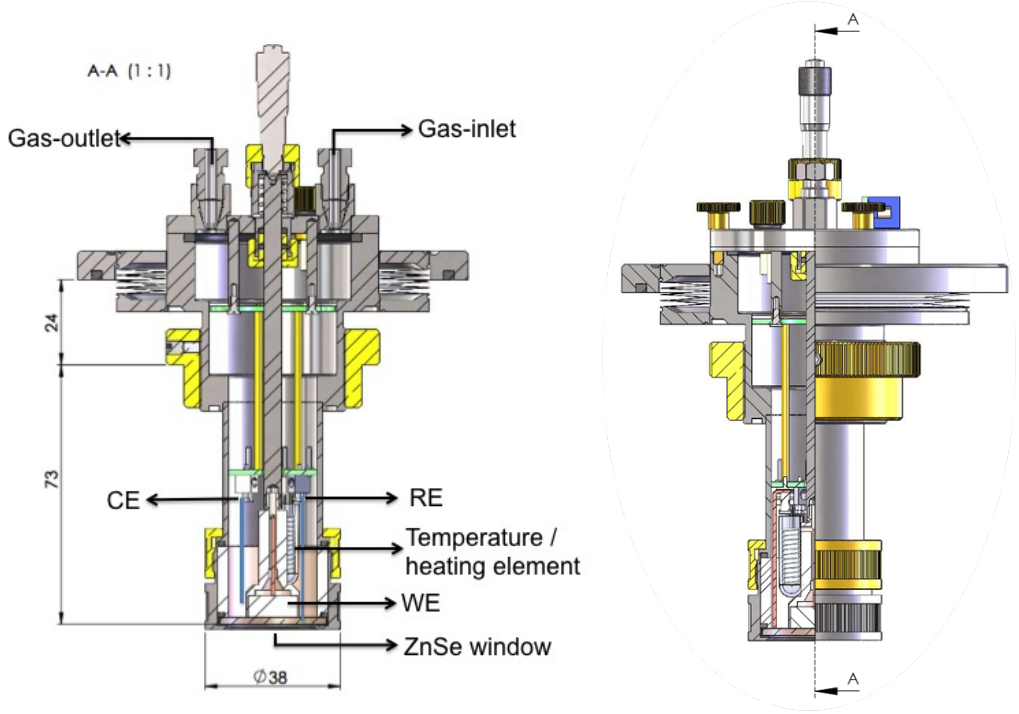

(a) (b)

Figure 2.2. Drawings of the spectroelectrochemical cell designed for PM-IRRAS experiments. WE - working electrode, RE - reference electrode, CE - counter electrode.

Figure 2.3. Picture of the lower end of the spectroelectrochemical cell showing the in- and out-let tubes, the glassy carbon working electrode and zinc wires as counter (around the WE) and reference electrodes.

2.3.2 *In-situ* PM-IRRAS measurements

The electrolyte 1:2 molar ratio of choline chloride to ethylene glycol (12CE) was dried and prepared as described in Section 2.1. Ethylene glycol (99.8 %, anhydrous, Sigma Aldrich) was used as received. All the electrolytes were added to the cell via syringes through T-3-port inlet and outlet Hamilton valves.

PM-IRRAS measurements were carried out using a Bruker IFS66 vacuum Fourier transform infrared spectrometer. The reflection unit is mounted with a variable angle and a polarizer from Brucker Optics. The light beam was incident at 70° with respect to the surface normal onto the sample (grazing angle) and the light was detected using a liquid nitrogen-cooled mercury cadmium telluride detector. Two wire-grid polarizers were placed in the incident beam light path, one mounted onto a rotatable mount and the other on a motor mount controlled by the spectrometer software. A script was written to rotate the polarizer through 65° and to collect the spectrum sequentially with *s*- and *p*-polarized radiation. Final adjustments were made by manually aligning the fixed mirrors to produce the best background. These alignments were carried out with the cell mounted, so the best angle of incidence from the incoming radiation could be achieved and the same setup can be reproduced after addition of the electrolyte. All spectra were collected at $4\,\mathrm{cm}^{-1}$ spectral resolution using 200 scans and are presented without smoothing correction. A more detailed description of this quasi PM-IRRAS method was described by Schennach et al. [86].

Electrochemical *in-situ* experiments were carried out by hooking up the spectroelectrochemical cell to the potentiostat (Figure 2.4). The cell was fitted with a glassy carbon disc electrode aligned against the ZnSe window leaving a small volume of electrolyte in the optical path and Zn wires as reference and counter electrodes.

Electrochemical measurements were performed with a Metrohm Echo Chemie Autolab PGSTAT100 potentiostat/galvanostat controlled by NOVA 1.6 software.

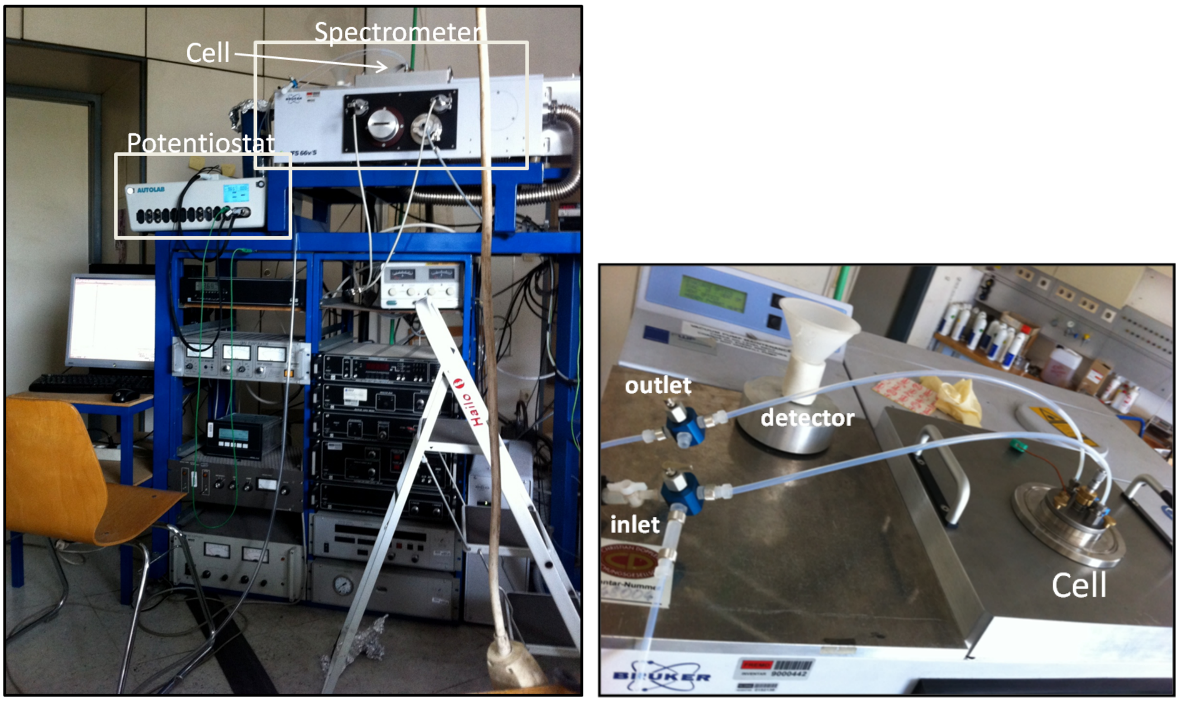

(a) (b)

Figure 2.4. Experimental setup for spectroelectrochemistry experiments. a) Overview of the potentiostat and IR spectrometer and b) top view of the IR spectrometer showing the mounted spectroelectrochemical cell and the valves to add and remove the electrolyte.

Part I

Zinc Electrodeposition on Glassy Carbon Electrodes

3 Zinc electrodeposition on glassy carbon

3.1 Voltammetric studies

Figure 3.1 shows the cyclic voltammogram of 12CE without and with $ZnCl_2$ at 30 °C. The scan in the Zn-free electrolyte was started at 0 V *vs.* Zn/Zn^{2+}, swept to -0.8 V and back to $+2.4$ V at 10 $mV \cdot s^{-1}$ scan rate (Figure 3.1a). The cathodic reaction at -0.8 V may be assigned to the reduction of ethylene glycol (EG), choline (Ch) or trace water with formation of hydrogen gas, observed as small bubbles on the electrode surface. The anodic reaction at ca. $+2.4$ V is likely due to the oxidation of Cl^- and the formation of Cl_3^- according to Equation 3.1 [13], followed by a cathodic peak after reversal of the sweep direction, which might be due to the reduction of Cl_3^- to chloride. Although there is a significant increase of the current at $+2.4$ V *vs.* Zn/Zn^{2+}, no evolution of chlorine gas was observed at this potential.

$$3\,Cl^- \rightleftharpoons Cl_3^- + 2\,e^- \tag{3.1}$$

When 0.3 $mol \cdot L^{-1}$ zinc chloride is dissolved in the eutectic mixture, two additional peaks are observed in Figure 3.1b. The CV started at 0 V *vs.* Zn/Zn^{2+} going cathodically and until -0.6 V there was little cathodic current. From -0.6 to -0.8 V there is an increase of current due to cathodic decomposition of the electrolyte along with the deposition of zinc. During the subsequent anodic sweep, the cathodic current decreased initially and then increased again to a cathodic peak at ca. -0.2 V. The anodic charge from 0 to $+2.4$ V was 63 % of that passed cathodically, which indicates that a significant fraction of the current was used for side-reactions.

It is important to note that the reduction peak appears on the anodic scan after the sweep direction has been reversed. This is a very unusual electrochemical behavior and it has been observed for the electrodeposition of zinc from 12CE on glassy carbon [41–44] and steel substrates [40] and from ionic liquids on glassy carbon electrodes [30, 31]. Two complementary explanations for this unusual electrochemical behavior of zinc

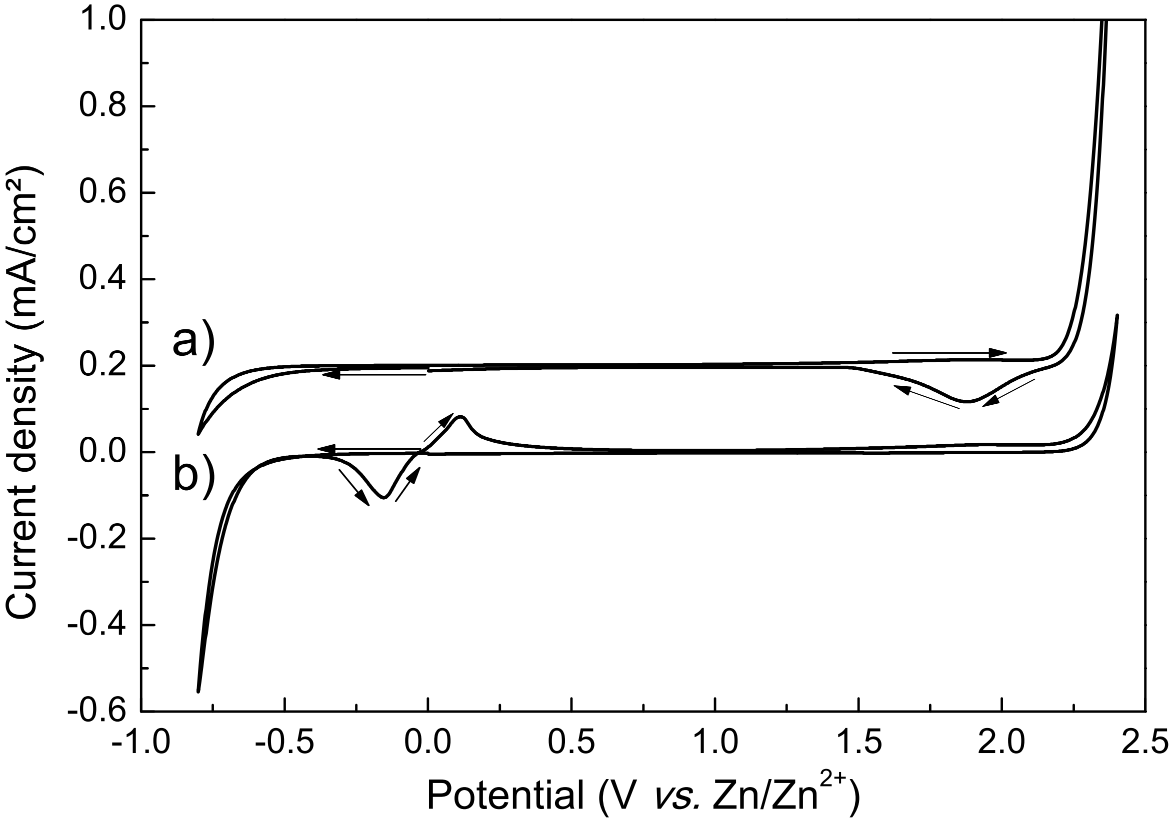

Figure 3.1. Cyclic voltammogram (CV) of 12CE electrolyte without a) and with b) $0.3\,\mathrm{mol{\cdot}L^{-1}}$ $ZnCl_2$; The CVs were recorded at a glassy carbon disk electrode ($A = 0.07\,\mathrm{cm^2}$, $\nu = 10\,\mathrm{mV{\cdot}s^{-1}}$, $T = 30\,°\mathrm{C}$) starting from 0 V *vs.* Zn/Zn^{2+} with a negative sweep direction. The CV a) is displaced on the current axis by $+0.2\,\mathrm{mA{\cdot}cm^{-2}}$.

compounds in ionic liquids, have been proposed by Whitehead [42] and Simons [30], which involve adsorption and blocking of the electrode surface by multilayers of ionic liquids on the forward scan and complexation of zinc by the ionic liquid. However, the mechanism including the speciation of zinc and the reduction on the reverse anodic scan is not understood.

The deep eutectic 12CE is a strong Lewis basic solution with a large excess of Cl^- ions. Raman studies on the speciation of chlorozincate(II) in ionic liquids showed the presence of $[ZnCl_4]^{2-}$ in Lewis basic media [49, 100], which is similar to the coordination chemistry of chlorozincate(II) species in aqueous [101] and in high temperature chloride melts [102, 103]. Based on that, Whitehead [42] suggested that the main Zn-containing species in 12CE electrolytes was $[ZnCl_4]^{2-}$. Later on, EXAFS measurements of zinc solutions in 12CE have confirmed that the dominant Zn-species in 12CE electrolyte are tetrachlorozincate ions stabilized by choline cations [37].

Figure 3.2 shows Raman spectra of the deep eutectic solvent without and with zinc chloride. In the spectral region corresponding to Zn−Cl stretching (170 to $400\,\mathrm{cm^{-1}}$)

a Raman signal at 275 cm^{-1} is observed for the DES containing zinc, which can be attributed to the $\nu_1(a_1)$ vibration of tetrahedral $[ZnCl_4]^{2-}$ [49, 100, 103–105].

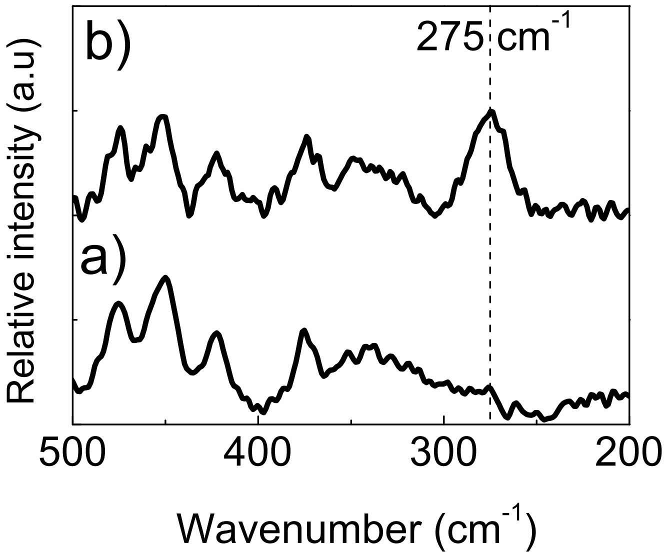

Figure 3.2. Raman spectra of 12CE electrolyte a) without and b) with 0.3 mol·L^{-1} $ZnCl_2$.

Estager et al. [49] has studied the speciation of zinc(II) chloride at several molar ratios in 1-octyl-3-methylimidazolium chloride $[C_8MIM]Cl$ by Raman spectroscopy and differential scanning calorimetry. In Lewis basic solutions, the main species characterized was $[ZnCl_4]^{2-}$ with a peak at 275 cm^{-1}. Similar Raman signals also attributed to $[ZnCl_4]^{2-}$ have been observed by Alves et al. [100] in Lewis basic solutions of zinc chloride in 1-n-butyl-3-methylimidazolium chloride (BMIMCl). Raman spectra of tetrachlorozincates in aqueous solutions [104, 105] and $ZnCl_2$−Li,K/Cl melts [103] also show the same feature for the T_d structure of $[ZnCl_4]^{2-}$.

Thus, based on our Raman measurements and supported by literature data [37, 49, 100, 103–105] we can conclude that the main zinc species in the deep eutectic 12CE is $[ZnCl_4]^{2-}$.

In chloroaluminate ionic liquid systems based on 1-ethyl-3-methylimidazolium chloride (EMIMCl), Al can not be plated from Lewis neutral or basic melts due to prior reduction of the $EMIM^+$ cation in favour of $AlCl_4^-$, although it can be plated in Lewis acidic solutions from $Al_2Cl_7^-$ [106, 107]. Similarly, it is suggested that in Lewis basic chlorozincate EMIMCl ionic liquids, the $[ZnCl_4]^{2-}$ anions can not be reduced to the metal form within the cathodic limit of the EMIMCl [23, 24, 47, 108].

By analogy with Lewis basic imidazolium systems [23, 24, 27, 108, 109] it is unlikely that the reverse cathodic peak presented in Figure 3.1b would originate from the reduction of $[ZnCl_4]^{2-}$ to Zn, due to its very negative reduction potential. The tetrachlorozincate would be reduced only very slowly on glassy carbon in the potential region of 0.0 to −0.8 V. In order to explain this, we suggest that an intermediate species Z is formed during the cathodic polarization of the electrode and that zinc is deposited from this species on the reverse scan at a much higher rate than from $[ZnCl_4]^{2-}$ [42–44]. However, it is still unclear why Z is not reduced at more negative potentials but gives rise to a cathodic peak during the positive sweep. Whitehead et al. [42] have proposed that the electrode surface is blocked at potentials more negative than −0.4 V *vs.* Zn/Zn^{2+} by adsorbed choline (Ch^+), hydrogen (H_{ads}) or ethylene glycol. Therefore, the electrodeposition of zinc from Z does not take place in this potential region but only on the reverse anodic scan at potentials more positive than −0.4 V with a peak potential, E_p^{red}, of −0.2 V.

Deng et al. [108] reported the electrodeposition of zinc from 1-ethyl-3-methylimidazolium dicyanamide [EMIm][DCA], which is a Lewis basic liquid. On a later study they investigated the electrodeposition of zinc from 1-butyl-1-methylpyrrolidinium dicyanamide [BMP][DCA] on GC and Mg alloy electrodes [27]. From amperometric titration experiments they suggested that the electrodeposition of zinc from Lewis basic media was possible due to the formation of a reducible intermediate complex $Zn(DCA)_3{}^-$ with an electrochemical reduction potential more positive than that of $[ZnCl_4]^{2-}$.

Simons et al. [30] investigated the effect of different Zn^{2+} salts in the ionic liquid [EMIm][DCA]. Cyclic voltammograms of $ZnCl_2$, $Zn(dca)_2$, $Zn(SO_4)_2$ and $Zn(ac)_2$ (ac = acetate) in [EMIM][DCA] showed in all cases a similar cathodic peak during the anodic reverse sweep. The authors have attributed these unusual cathodic peaks on the anodic scan to the formation of a potential-dependent compact layer of the ionic liquid ions at the electrode surface, described by Endres [110] and Atkin [111], which may block the surface at certain potentials. This would affect the mass transport rates of the electroactive species and their access to the electrode surface [112]. When the ionic liquid layer relaxes during the anodic return sweep, deposition of zinc takes place and a cathodic peak is observed. In a more recent study [31], spectroscopic investigation of [EMIM][DCA] containing $ZnCl_2$ and $Zn(dca)_2$, pointed to the formation of Zn/dca complex anions in the IL solution, which may be related to the appearance of the cathodic deposition peak on the anodic scan. The explanation proposed by Simons differs from that of Whitehead, however, as the first considers that the complexation of zinc takes place in the bulk of the electrolyte whereas the latter proposes the formation of a reducible intermediate zinc species Z only in the diffusion layer and at certain potentials. Nevertheless, this study opens the question of whether this unusual electrochemical behavior can be generalized to different ionic liquid systems containing zinc ions.

Pereira et al. [40] have recently shown the same electrochemical behavior for Zn electrodeposition from 12CE on a stainless steel substrate. The reduction peak after reversing the scan direction was explained in terms of the overpotential for nucleation and growth of the deposit, however, they also consider the possibility suggested by Whitehead [42] of electrode passivation by adsorption of choline or ethylene glycol during the forward scan.

Figure 3.3 shows a set of experiments in which the cathodic limit of the cyclic voltammograms was gradually increased from −0.8 to −0.3 V.

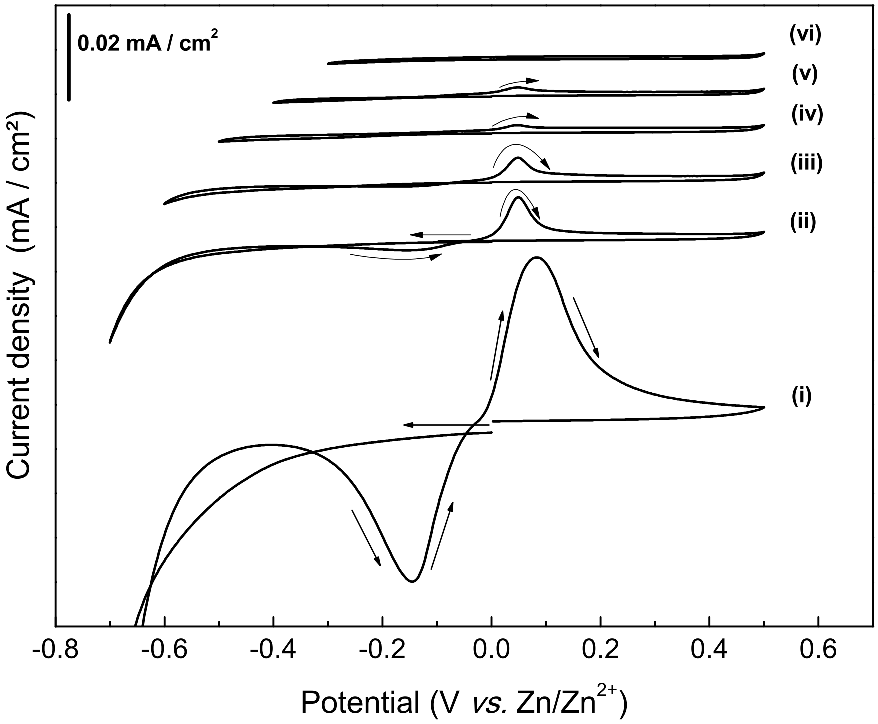

Figure 3.3. Cyclic voltammograms of 0.3 mol·L^{-1} $ZnCl_2$ in 12CE electrolyte ($\nu = 10\,mV{\cdot}s^{-1}$, $T = 30\,°C$) at a stationary glassy carbon disk electrode starting from 0 V *vs.* Zn/Zn^{2+} with a negative sweep direction. The cathodic potential limits of each scan were: (i) −0.8 V, (ii) −0.7 V, (iii) −0.6 V, (iv) −0.5 V, (v) −0.4 V and (vi) −0.3 V with an anodic potential limit fixed at +0.5 V. The part of the curve below −0.65 V in (i) is omitted to better scale the CVs. The CVs are offset on the current density scale for clarity.

From the stripping peak, it can be seen that the amount of deposited zinc decreases significantly as the cathodic switching potential becomes less negative, showing that a negative overpotential of at least −0.5 V is required to form the species Z. Additionally, the coulombic efficiency (the ratio between the total anodic charge from 0 to 0.5 V and the cathodic charge from the respective switching potential until 0 V) of the cycles (i) to (vi) were 10, 23, 41, 53, 57 and 81 %, respectively, which indicates that the cathodic charge is related not only to the deposition of zinc, but also to reduction of other species on the electrode surface.

Rotating disc electrode voltammetry (RDE) at glassy carbon shows that the current density of the reverse cathodic and anodic peak also decreases with increasing rotation rate (Figure 3.4). This implies that the intermediate species Z forms in the diffusion layer, consequently they are transported away from the electrode into the bulk of the electrolyte, when hydrodynamic force is applied. One can also observe that on the static electrode, the current density increases from the first to the third cycle, indicating a gradual increase of the concentration of Z in the diffusion layer during the anodic redissolution of Zn.

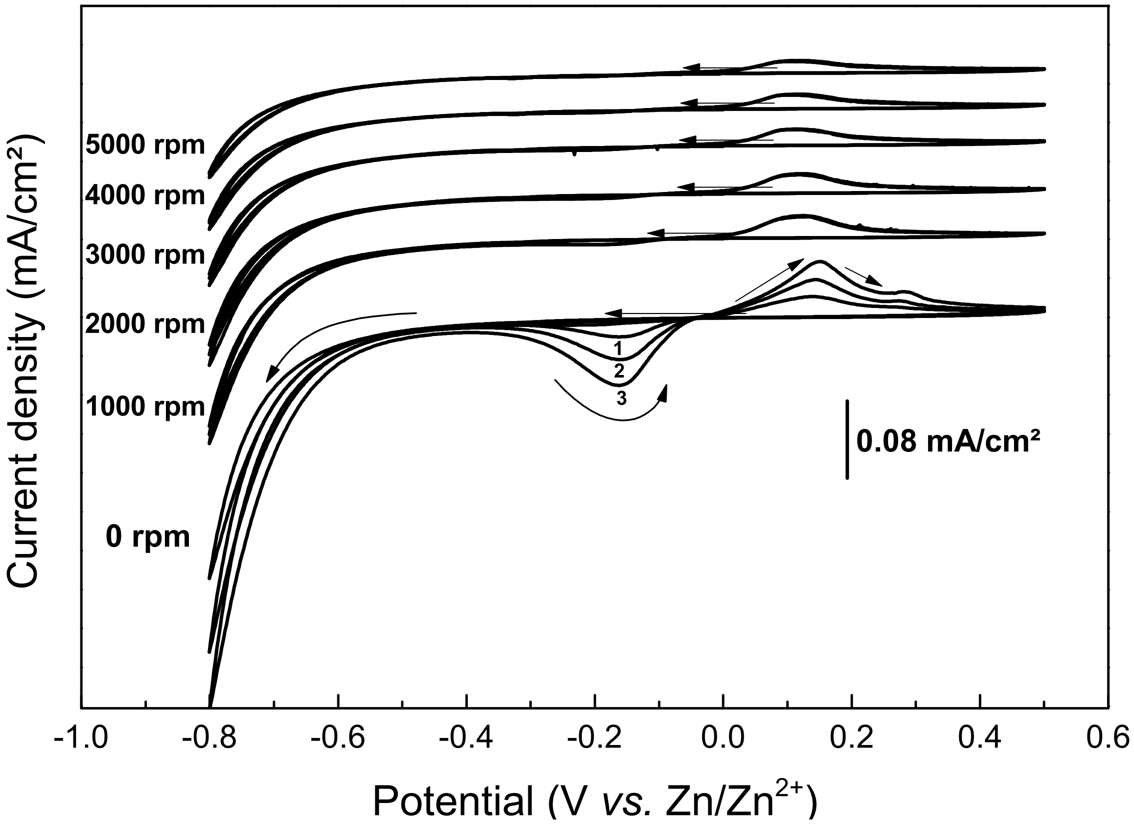

Figure 3.4. The first three voltammetric cycles of 0.3 mol·L^{-1} of $ZnCl_2$ in 12CE electrolyte at a rotating glassy carbon disk electrode (ν = 10 mV·s^{-1}, T = 30 °C, rotation rate indicated) starting from 0 V *vs.* Zn/Zn^{2+} with a negative sweep direction. The numbers 1, 2 and 3 indicate cycle number. Arrows indicate sweep direction. The voltammograms are offset on the current density axis for clarity.

Figure 3.5 shows the effect of the scan rate on the electrodeposition of zinc from 12CE. By increasing the scan rate from 10 to 50 mV·s^{-1} the deposition time decreases, therefore the peak current density decreases, indicating that the formation of Z in the diffusion layer proceeds at a very low rate. Decreasing the sweep rate to 5 and 1 mV·s^{-1} results in an increase of the the peak current (Figure 3.6) and a second anodic peak, at ca. +0.3 V *vs.* Zn/Zn^{2+} becomes more pronounced at scan rates as low as 2 and 1 mV·s^{-1}. This second peak might be due to local saturation of the DES with Zn^{2+}, caused by low solubility of the zinc ions.

Adsorption and desorption of quaternary ammonium ions are usually slow and may interfere with the voltammetric response of the electrolyte by blocking of the electrode surface. Abbott et al. [113–115] investigated the adsorption and desorption of tetraalkylammonium ions in cyclohexane on a platinum microelectrode. It was reported that quaternary ammonium cations adsorb strongly on the electrode surface and that the desorption is very slow. Consequently, the voltammetric response will be dependent upon the scan rate, i.e. the experimental time scale. Additionally, artefacts can be observed when measuring at faster sweep rates, because the cations will remain strongly adsorbed on the substrate and only for scan rates less than ca. $10\,\mathrm{mV{\cdot}s^{-1}}$ the potential at the outer Helmholtz plane will be in phase with the applied electrode potential. This explanation is consistent with our results, indicating that besides the slow formation of Z, the decrease in peak currents by increasing scan rate can also be a consequence of the slow desorption of choline ions.

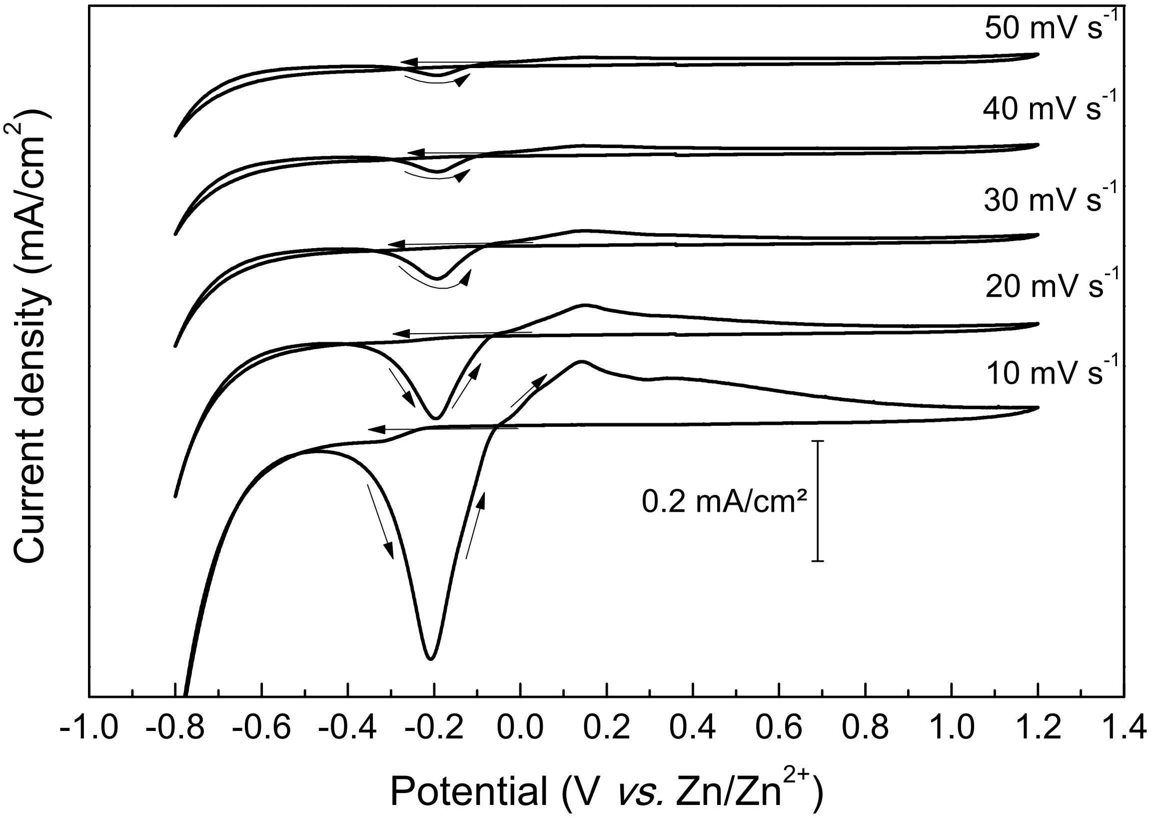

Figure 3.5. Cyclic voltammograms at different scan rates of $0.3\,\mathrm{mol{\cdot}L^{-1}}$ of $ZnCl_2$ in 12CE electrolyte ($T = 30\,°C$) at a stationary glassy carbon disk electrode starting from 0 V *vs.* Zn/Zn^{2+} with a negative sweep direction. The part of the CV at $10\,\mathrm{mV{\cdot}s^{-1}}$ below -0.75 V is not shown to better scale the CVs. The voltammograms are offset for clarity.

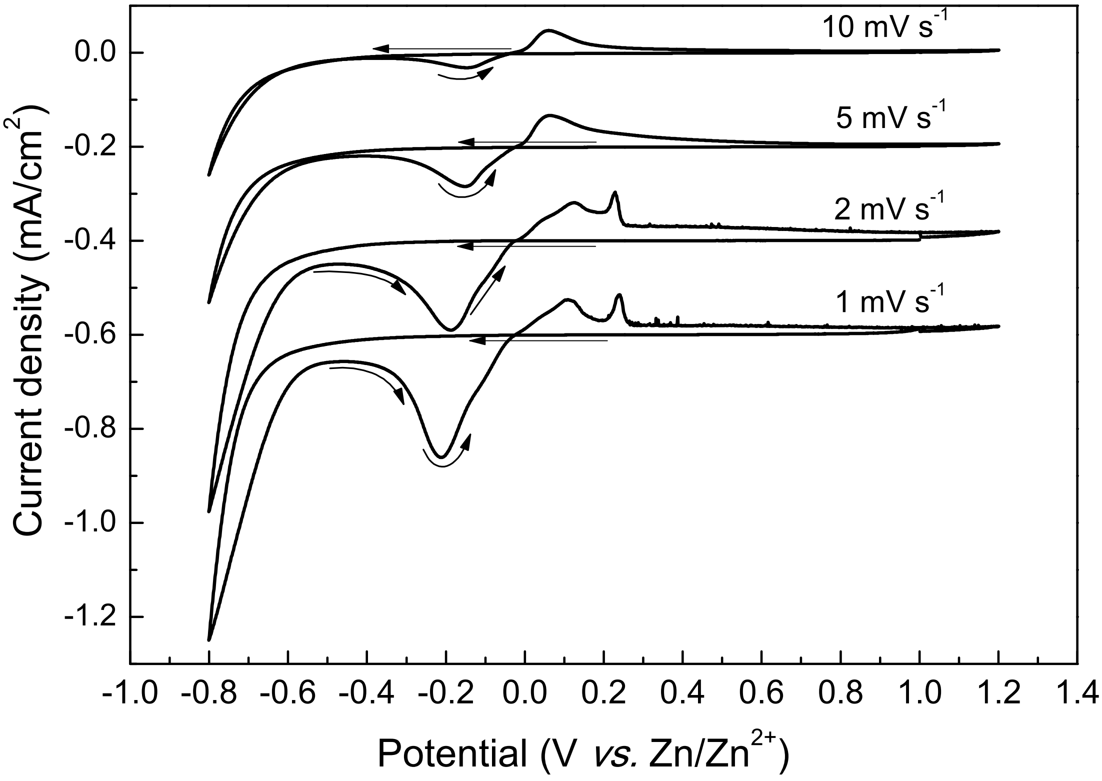

Figure 3.6. Cyclic voltammograms at different scan rates of 0.3 mol·L^{-1} of $ZnCl_2$ in 12CE electrolyte (T = 30 °C) at a stationary glassy carbon disk electrode starting from +1.0 V *vs.* Zn/Zn^{2+} with a negative sweep direction. The voltammograms are displaced on the current density axis by −0.2 mA·cm^{-2} for clarity.

The coulombic efficiency of the cyclic voltammograms as a function of scan rate is presented in Figure 3.7. The current efficiencies of the CVs were 17, 23, 25, 43, 50, 59, 69 and 75 % for scan rates of 1, 2, 5, 10, 20, 30, 40 and 50 mV·s^{-1}, respectively. The current efficiencies at slow scan rates are remarkably lower than those at faster sweep rates, which indicates that at slow scan rates, more current is used for side-reactions and the formation of intermediate species. Furthermore, at low scan rates, Z may diffuse into the bulk of the electrolyte, which lowers the current efficiency, whereas at faster scan rates, the species formed at the surface of the electrode are quickly reduced to zinc before they can escape into the bulk electrolyte. For cyclic voltammetry carried out at scan rates as low as 1 mV·s^{-1}, no current *plateau* was observed at potentials ≤ -0.6 V, where the reducible species Z could be reduced. Additionally, the peak potential of the backward cathodic peak and its charge varied little when the CV was performed over a range of scan rates from 1 to 5 mV·s^{-1}, which implies that potential is more significant than time in determining the local concentration of Z.

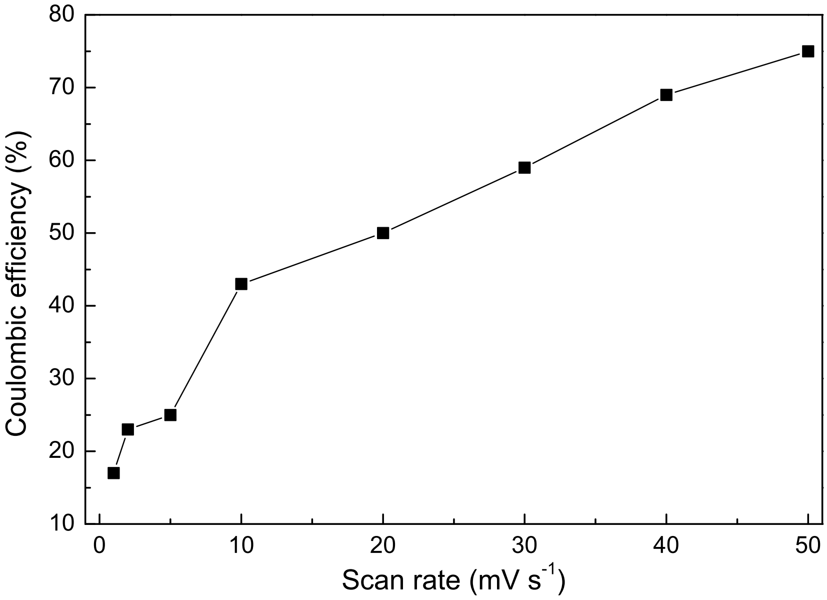

Figure 3.7. Coulombic efficiencies of zinc electrodeposition from 0.3 mol·L^{-1} $ZnCl_2$ 12CE on glassy carbon as a function of scan rate.

3.1.1 The effect of temperature

The effect of the temperature on the cyclic voltammetric behavior of the Zn ions at a glassy carbon electrode was investigated between 30 and 60 °C and is illustrated in Figure 3.8.

The peak current considerably increases with increasing temperature. This behavior can be correlated to the decreasing viscosity of the deep eutectic solvent with increasing temperature (Figure 3.9), also observed in other ionic liquids [33, 116]. It is reflected in the increase of conductivity of the 12CE deep eutectic solvent with temperature (Figure 3.8). From 30 to 60 °C the conductivity of the electrolyte increases from 9 to 21 mS·cm^{-1}. Although the conductivity measurement shown in Figure 3.10 is of the pure deep eutectic 12CE without $ZnCl_2$, the conductivity of the 12CE deep eutectic does not change significantly with the addition of $ZnCl_2$ even at high concentrations of the zinc salt [37]. Similarly to the conductivity, the viscosity is also not significantly affected by the addition of zinc salt (Figure 3.9). It is noteworthy that for temperatures up to 60 °C, the blocking layer is not desorbed from the electrode surface and that the overpotential for the nucleation of zinc does not change significantly with increasing temperature. The coulombic efficiencies in the cyclic voltammograms (calculated from the ratio between the total anodic over the cathodic charge) were 28, 40, 48 and 58 % for temperatures of 30, 40, 50 and 60 °C, respectively. The increase in coulombic efficiency with increasing temperature can be related to two factors: firstly, the kinetics of the chemical formation of Z is faster at higher temperatures, hence increasing the deposition rate of zinc. Secondly, the kinetics of the adsorption/desorption equilibrium of the blocking layer can also be affected, thus resulting in a faster deblocking of the active sites on the glassy carbon surface at temperatures of 60 °C. Furthermore, the current density at −0.8 V, related to the formation of RO^-, does not increase as much as the corresponding peak current densities for zinc deposition at −0.15 V and dissolution at +0.05 V *vs.* Zn/Zn^{2+}, which indicates that by raising the temperature the chemical kinetics of the formation of Z becomes faster, resulting in an increasing peak current density for zinc deposition from Z.

Table 3.1 shows all the voltammetric data from the CVs presented in Figure 3.8. In this table all the cathodic data is reported with respect to the cathodic peak at the backward scan (not considering that at −0.8 V), including the calculation of current efficiency, therefore the values are different from those mentioned before.

It is observed that increasing the temperature from 30 to 50 °C causes no significant shift of the peak potential for the reversal cathodic peak (ΔE_p^c). However, at 60 °C unblocking of the surface takes place at more negative potentials. The peak current I_p^c and the charge consumed Q^c show a more than 2-fold increase. The total anodic charge related to that consumed cathodically in the backward peak of zinc deposition for 50 and 60 °C was 85 and 70 %, respectively. This low current efficiency can be related to incomplete dissolution of zinc, as no side-reactions are expected in this potential range (between −0.4 and 0 V). At lower temperatures, a CE of over 100 % indicates that some of the zinc was deposited at more negative potentials, not only at the reversal cathodic peak.

Table 3.1. Voltammetric data for zinc deposition from 12CE at different temperatures presented in Figure 3.8. CE = Coulombic efficiency.

Temperature °C	E_p^c	ΔE_p^c (mV)	I_p^c (mA·cm^{-2})	Q^c (mC)	E_p^a	ΔE_p^a (mV)	I_p^a (mA·cm^{-2})	Q^a (mC)	CE[1]	CE[2] (%)
30	−168	–	−0.184	0.174	112	–	0.117	0.233	126	28
40	−161	+7.33	−0.231	0.234	83	−29.3	0.154	0.264	113	40
50	−164	+4.89	−0.812	0.881	59	−53.7	0.488	0.745	85	48
60	−186	−17.09	−2.328	2.600	59	−53.7	1.405	1.820	70	58

---

[1] CE calculated from the ratio of the anodic charge over the charge consumed on the reversal cathodic peak.

[2] CE based on the ratio of the anodic charge over the total cathodic charge.

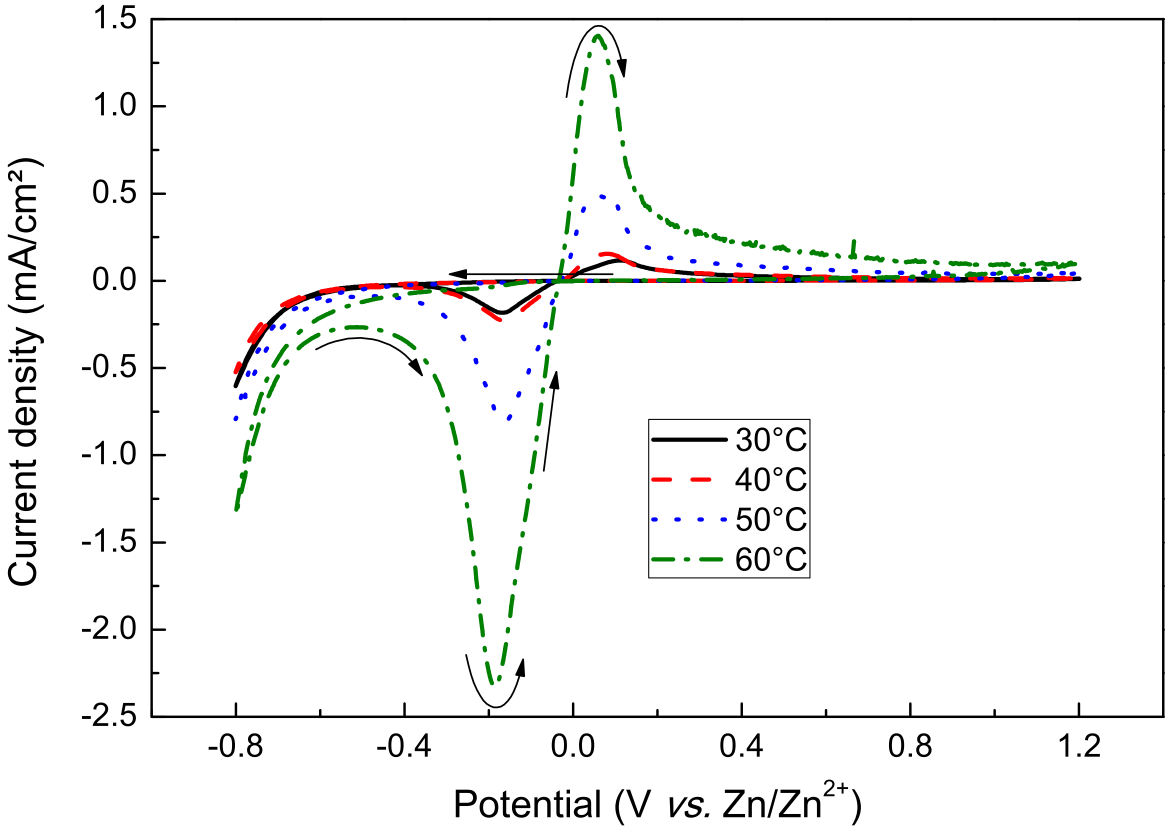

Figure 3.8. Cyclic voltammograms at different temperature of 0.3 mol·L^{-1} of ZnCl$_2$ in 12CE electrolyte at a static glassy carbon disk electrode ($\nu = 10$ mV·s^{-1}) starting from 0 V *vs.* Zn/Zn^{2+} with a negative sweep. Arrows indicate sweep direction.

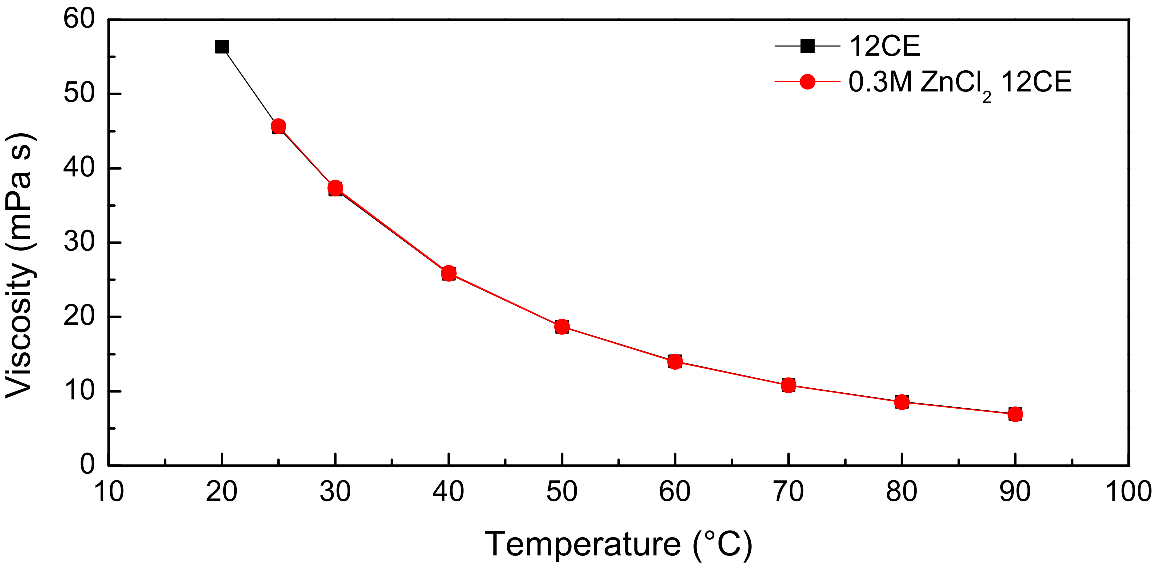

Figure 3.9. Viscosity of 12CE electrolyte with and without 0.3 mol·L^{-1} ZnCl$_2$ as function of temperature.

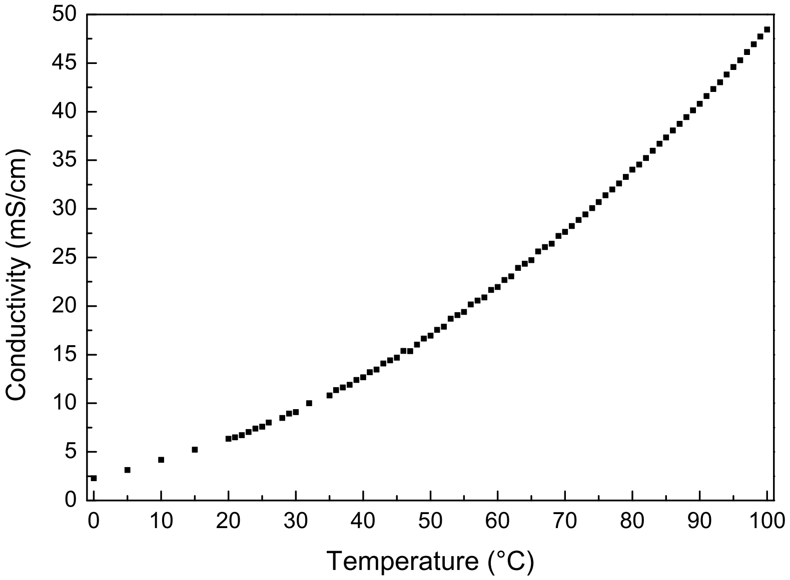

Figure 3.10. Conductivity of 12CE electrolyte as function of temperature.

Most of the reaction rates (k) vary with the Arrhenius exponential function of the temperature T (Equation 3.2):

$$k = Ae^{-E_a/RT} \tag{3.2}$$

where A is a constant, E_a is the activation energy (kJ·mol^{-1}) and R the gas constant ($8.31 J \cdot K \cdot mol^{-1}$) [52]. The dynamic viscosities and conductivities of the deep eutectic 12CE at different temperatures have been depicted as Arrhenius plots in Figure 3.11. Both conductivity and viscosity have a high degree of linearity (least square, correlation coefficient ≥ 0.995).

The calculation of the activation energy for the viscosity (E_η) and conductivity (E_Λ) can be obtained from the slope of the Arrhenius plot from Figure 3.11, according to the following equation for the viscosity (η):

$$ln\eta = ln\eta_0 - \frac{E_\eta}{RT} \tag{3.3}$$

and for the conductivity:

$$ln\sigma = ln\sigma_0 - \frac{E_\Lambda}{RT} \tag{3.4}$$

where η_0 and σ_0 would be the hypothetical viscosity and conductivity at infinite temperature.

The values of E_η and E_Λ obtained from the Arrhenius equation for viscosity and conductivity were respectively 26.6 and -22.9 kJ·mol^{-1}. Whereas η_0 and σ_0 were $9.5 \cdot 10^{-4}$ mPa·s and $8.2 \cdot 10^4\,\mathrm{mS{\cdot}cm^{-1}}$. These values for E_η and E_Λ, as well as the η_0 and σ_0, are in agreement with the literature for other DES [11, 117–119] and ionic liquids [120]. E_η calculated from the dynamic viscosity of 12CE have been reported to be $25.4\,\mathrm{kJ{\cdot}mol^{-1}}$ [121], $26.3\,\mathrm{kJ{\cdot}mol^{-1}}$ [122] and $28.4\,\mathrm{kJ{\cdot}mol^{-1}}$ [123], which is in good accordance with our result. As for E_Λ, no values have been reported in the literature for 12CE.

The E_η and E_Λ are inversely proportional and therefore have opposite signs and similar magnitude. This indicates that the Walden rule (Equation 3.5) is also valid for the 12CE system. The Walden rule states that the logarithmic viscosity and conductivity are proportional over a range of temperatures [124] and has been used to explain the rheological behavior of ionic liquids [124–126].

$$ln\eta \sim -ln\sigma \tag{3.5}$$

The linear behavior of the viscosity and conductivity with temperature is in good agreement the Stokes-Einstein and Nerst-Einstein equations, which connects the viscosity and conductivity with the diffusion of the ionic species (i) [124, 127], as well as the hole theory interpretation for the charge mobility in ionic liquids [128–130].

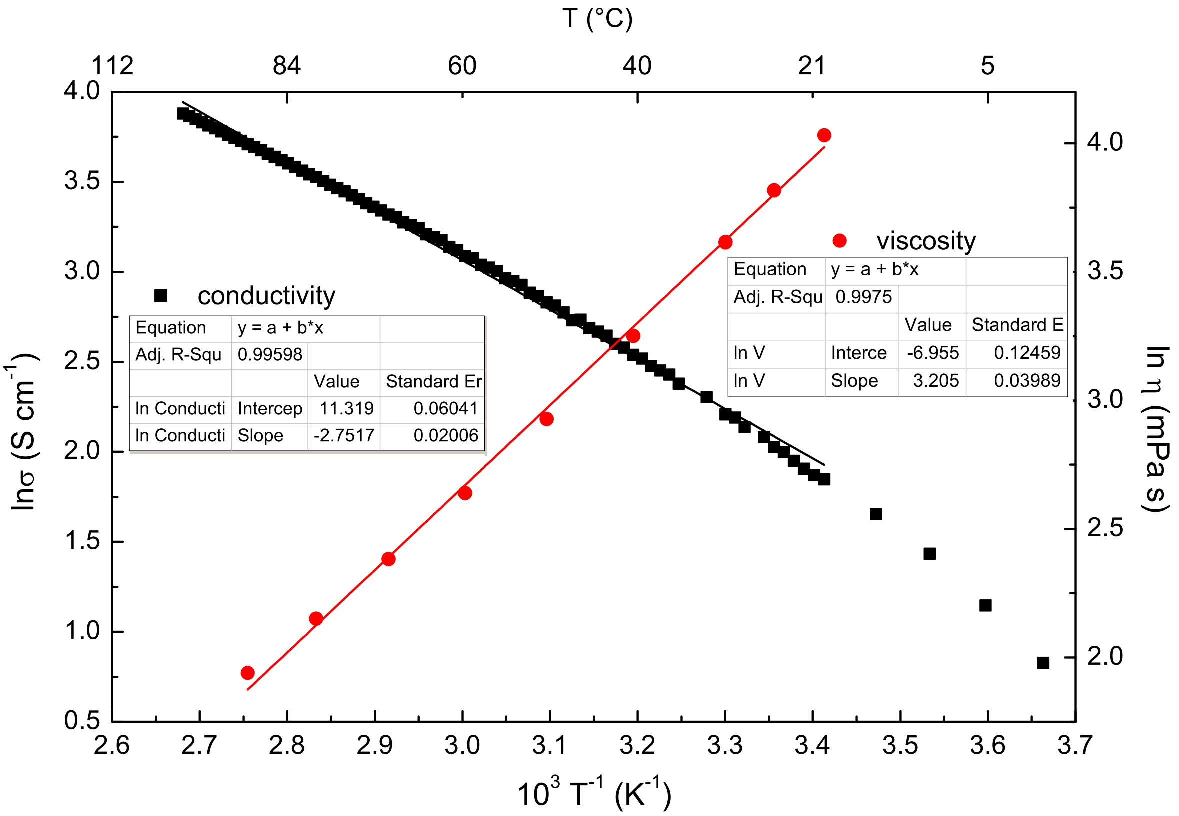

Equation	y = a + b*x		
Adj. R-Squ	0.99598		
		Value	Standard Er
ln Conducti	Intercep	11.319	0.06041
ln Conducti	Slope	-2.7517	0.02006

Equation	y = a + b*x		
Adj. R-Squ	0.9975		
		Value	Standard E
ln V	Interce	-6.955	0.12459
ln V	Slope	3.205	0.03989

Figure 3.11. Arrhenius plot of conductivity and dynamic viscosity of 12CE electrolyte as a function of temperature.

3.1.2 Proposed mechanism

The deposition of zinc on the reverse scan is clearly dependent on the overpotential applied and is not affected by increasing the temperature. As it has been proposed [42–44], zinc deposition occurs from an intermediate species Z. The formation of Z is potential-dependent and it proceeds with very slow kinetics. This kind of mechanism involving coupled chemical reactions has also been observed in the electrodeposition of zinc from other ionic liquids [27, 30, 31, 46] and can be classified as a multiple electron transfer with intervening chemical reaction or ECE mechanism (E and C are electron transfer and chemical steps, respectively) [131]. In such a mechanism, a chemical step is interposed between electron transfer steps. The generalized ECE mechanism is represented as follows:

$$\mathrm{A + n_1e^- \longrightarrow B} \tag{3.6}$$

$$\mathrm{B + C \rightleftharpoons Z} \tag{3.7}$$

$$\mathrm{Z + n_2e^- \longrightarrow D} \tag{3.8}$$

Z is only formed at potentials below $-0.4\,\mathrm{V}$, however, it is still intriguing why a cathodic peak arises on the reverse scan. It would rather be expected that the Z species get reduced as soon they are formed between -0.6 and $-0.8\,\mathrm{V}$. Instead, the current quickly decreases initially on the anodic return sweep and then increases again, giving rise to a cathodic peak at $-0.2\,\mathrm{V}$, before the deposited zinc layer is stripped again at positive potentials. In order to explain this, it is assumed that during the cathodic polarization of the electrode the surface is blocked by adsorbed choline ions ($\mathrm{Ch^+}$) or ethylene glycol (EG) or by adsorbed hydrogen ($\mathrm{H_{ads}}$), which is formed during the reduction of residual water or ROH (EG, $\mathrm{Ch^+}$) at potentials below $-0.5\,\mathrm{V}$ producing deprotonated species ($\mathrm{RO^- \equiv OH^-}$, $\mathrm{HOCH_2CH_2O^-}$ or $\mathrm{(CH_3)_3N^+CH_2CH_2O^-}$), according to Equation 3.9, 3.10 and 3.11. These deprotonated $\mathrm{RO^-}$ species from the electrolyte could replace one or more $\mathrm{Cl^-}$ ligands in $\mathrm{[ZnCl_4]^{2-}}$ to form an intermediate complex Z, according to Equation 3.12. Z would be formed in the diffusion layer and could be reduced to zinc as shown in Equation 3.13. If the applied overpotential is not high enough to form Z ($E > -0.4\,\mathrm{V}$), very little intermediate is formed, thus little deposition of zinc occurs and the stripping peak gradually decreases until it becomes negligible above a cathodic switching potential of $-0.3\,\mathrm{V}$ (Figure 3.3). Blocking of the surface hindering zinc deposition is also effective at elevated temperature. The mechanism assumed for ECE reduction of $\mathrm{[ZnCl_4]^{2-}}$ is represented as follows:

$$\mathrm{ROH} + \mathrm{e^-} \longrightarrow \mathrm{RO^-} + \mathrm{H_{ads}} \tag{3.9}$$

$$\mathrm{H_{ads}} + \mathrm{H_{ads}} \longrightarrow \mathrm{H_2} \tag{3.10}$$

$$\mathrm{ROH} + \mathrm{H_{ads}} + \mathrm{e^-} \longrightarrow \mathrm{H_2} + \mathrm{RO^-} \tag{3.11}$$

$$\mathrm{xRO^-} + [\mathrm{ZnCl_4}]^{2-} \rightleftharpoons [\mathrm{ZnCl_{(4-x)}(RO)_x}]^{2-} + \mathrm{xCl^-} \tag{3.12}$$

$$[\mathrm{ZnCl_{(4-x)}(RO)_x}]^{2-} + 2\,\mathrm{e^-} \longrightarrow \mathrm{Zn} + \mathrm{x(RO)^-} + (4-\mathrm{x})\mathrm{Cl^-} \tag{3.13}$$

Very little is known about the interface of an electrode with ionic liquids. Endres's and Atkin's groups [69, 110–112, 132, 133] have studied how the nature of the ionic liquid affects the interfacial structure on metal electrodes by *in situ* scanning tunneling microscopy (STM) and atomic force microscopy (AFM). They have described a potential-dependent multilayer architecture, which may affect electrochemical reactions in ionic liquids. Such a layer architecture might be present also in the 12CE system, hindering the deposition of zinc during the forward and the backward scan below −0.4 V. This topic will be discussed in further detail in Chapter 8.

3.2 Chronoamperometric studies

3.2.1 Investigations of the formation of Z

In order to systematically investigate the kinetics of potential-dependent effects taking place on the electrode surface, such as adsorption processes, blocking effects and the electrodeposition of zinc, multi-step potential experiments were carried out on a glassy carbon electrode in 0.3 mol·L^{-1} $ZnCl_2$ 12CE electrolyte. Under such conditions it is possible to analyse the electrode reactions under constant overpotential.

The electrode was stepped from open circuit potential at +0.5 V *vs.* Zn/Zn^{2+} ($E1$) to a potential sufficiently negative so the intermediate species Z could be formed ($E2$). This second step was varied between −0.2 and −0.8 V *vs.* Zn/Zn^{2+} for the purpose of examining the correlation of the formation of Z species with different overpotentials. Subsequently, a third step was applied at −0.2 V ($E3$) to simulate the reversal cathodic peak, related to the electrodeposition of zinc and finally, a last step at a potential where redissolution of the deposited metal occurs was applied at +1.0 V *vs.* Zn/Zn^{2+} ($E4$). A scheme of the 4-step chronoamperometric experiment is shown in Figure 3.12.

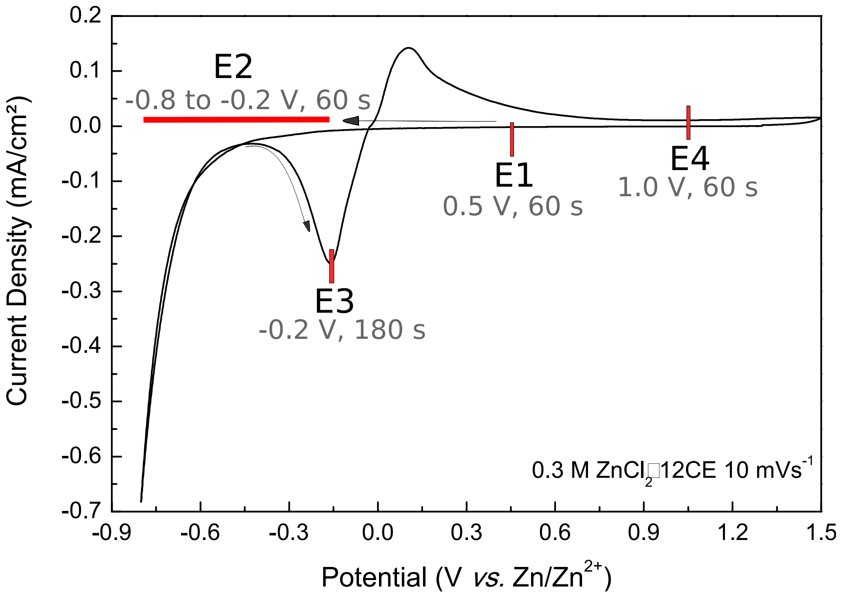

Figure 3.12. Schematic representation of the 4 step chronoamperometric experiments in 0.3 mol·L^{-1} $ZnCl_2$ 12CE on GC.

Representative current *vs.* time responses at constant potentials are shown in Figure 3.13 for $E1$, $E2$ and $E3$. The step at $E4$ is not shown.

The initial potential $E1$, was chosen to be the same as at open circuit potential, where no faradaic processes occur. The step from rest-potential $E1$ (+0.5 V) to a more negative

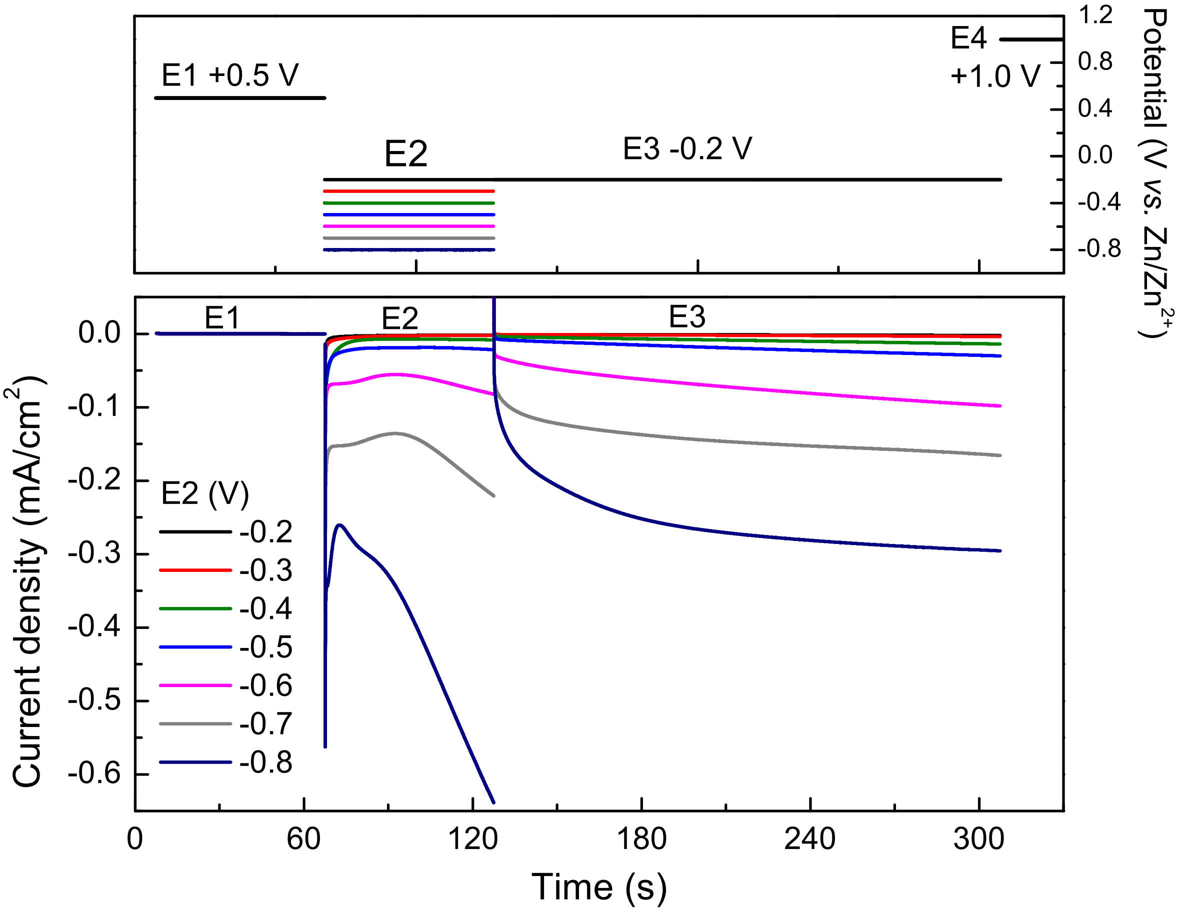

Figure 3.13. Current response for $0.3\,\mathrm{mol{\cdot}L^{-1}}$ $ZnCl_2$ 12CE on GC for different potential steps. Applied potentials at $E2$ are indicated.

potential ($E2$) caused a sharp spike in current density, due to the capacitive charging, followed by a current decay. An expanded graphic of the current and charge profile for the step $E2$ is shown in Figure 3.14.

The magnitude of the current density is remarkably high for potentials below -0.6 V. For these potentials (-0.6, -0.7 and -0.8 V *vs.* Zn/Zn^{2+}) there is a slow decay in current up to 5 s. At the potential -0.8 V there is a peak at ca. 1 s and a second one at 10 s. At potentials of -0.7 and -0.6 V, there is a broader peak with maximum at 8 s and 6 s, respectively, followed by a continuous increase in current density. Apparently, two processes are taking place at the electrode surface. Firstly, adsorption of species, probably Ch^{+}, onto the electrode surface, followed by reduction of the electrolyte, after the current decay, that takes place with a continuous current rising within the time of measurement, 60 s. This continuous increase in current is in agreement with cyclic voltammetric results showed previously for this system. From cyclic voltammetry, we have proposed that below -0.6 V there is reduction of the electrolyte with formation of hydrogen gas. Therefore, the current density does not decrease to a limiting current *plateau* but it continuously increases, as there is no significant change in local concentration of the species, but a continuous process, represented by Equation 3.9 followed by Equation 3.12.

At $E2$ for the potentials -0.5, -0.4, -0.3 and -0.2 V *vs.* Zn/Zn^{2+}, the current decayed faster and stayed almost constant at -0.03, -0.015, -0.004 and -0.002 mA·cm^{-2}, respectively. Following the initial capacitive decay for all of the 4 curves, there was no peak within the 60 s measuring period at each respective potential that would typically be associated with the nucleation in an electrocrystallization process.

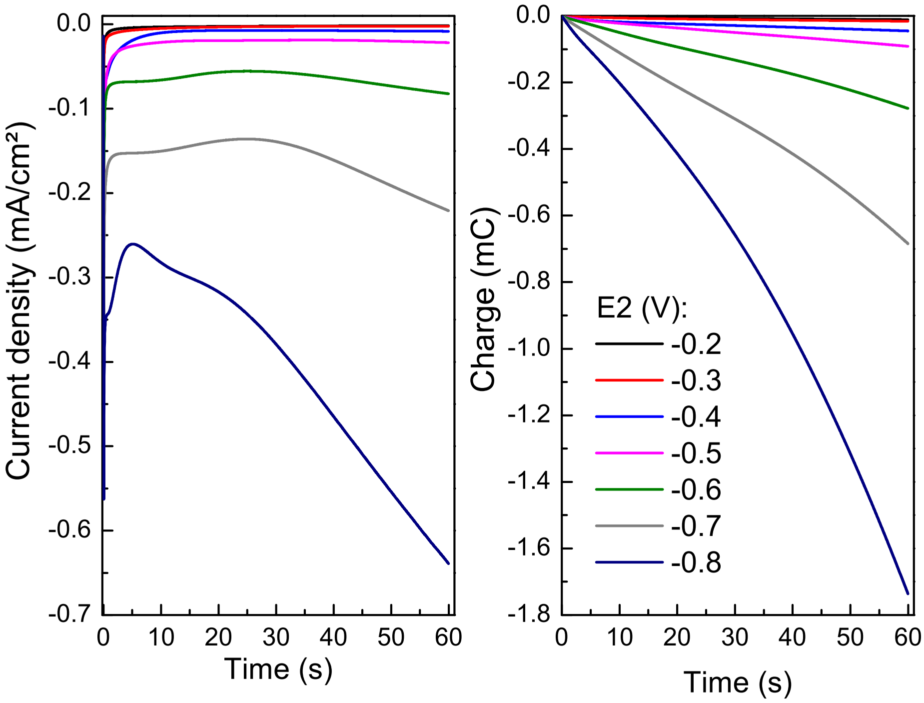

Figure 3.14. Current and charge *versus* time of 0.3 mol·L^{-1} ZnCl$_2$ 12CE on GC at the step $E2$ for the indicated potential.

Figure 3.15 shows the current and charge profile *versus* time for the step potential $E3$. At this third step, the potential was kept constant at -0.2 V *vs.* Zn/Zn^{2+} to simulate the cathodic peak of zinc deposition and to check its dependency on the overpotential necessary for the formation of Z. It is observed that the current density at this step is clearly dependent on the potential of the previous one, confirming our suggestion that reducible species are formed at potentials ≤ -0.6 V. When the previous potential $E2$ is kept at -0.2 or -0.3 V, the charge consumed at $E3$ is negligible, because there is no formation of Z but only very slow deposition of zinc from [ZnCl$_4$]$^{2-}$. However, it is noteworthy that in none of the current transients a nucleation peak is present, hence the reaction occurring at this potential can be associated with a continuous process taking place at the electrode surface, albeit at a lower rate than during the firsts 60 s at $E2$.

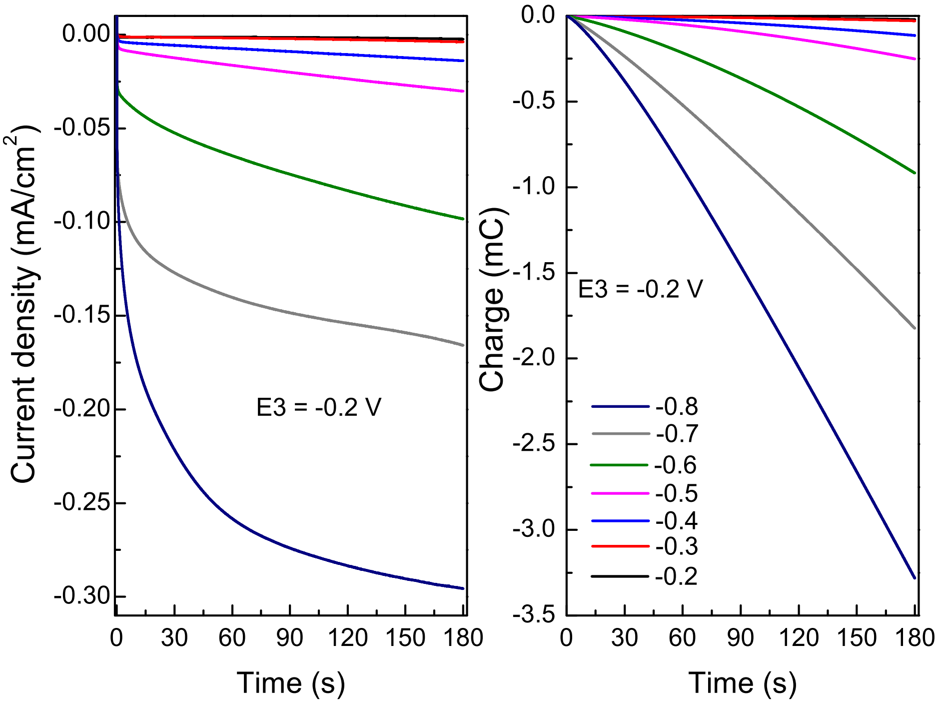

Figure 3.15. Current and charge *versus* time of $0.3\,\mathrm{mol{\cdot}L^{-1}}$ $ZnCl_2$ 12CE on GC at the step $E3 = -0.2\,\mathrm{V}$.

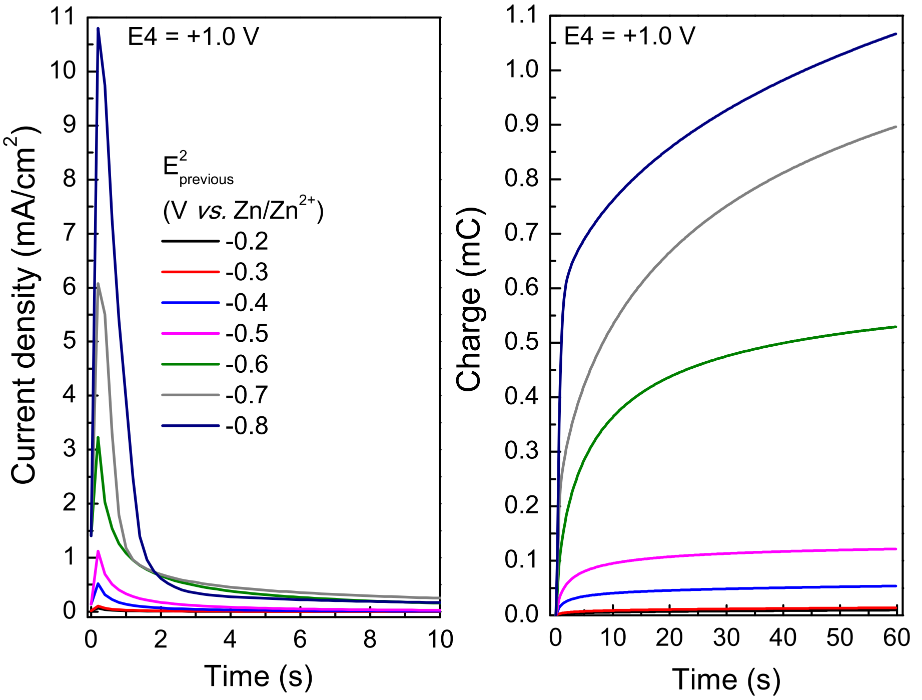

Figure 3.16. Current and charge *versus* time of $0.3\,\mathrm{mol{\cdot}L^{-1}}$ $ZnCl_2$ 12CE on GC at the step $E4 = +1.0\,\mathrm{V}$.

The current transients for $E4$, at the oxidation potential $+1.0\,\mathrm{V}$ *vs.* $\mathrm{Zn/Zn^{2+}}$ are presented in Figure 3.16. The charge consumed at this potential is also dependent on the second step $E2$, indicating the potential-dependent formation of an intermediate species. However, the dissolution charge is significantly lower than the deposition charge at $-0.2\,\mathrm{V}$, indicating incomplete dissolution during the period of measurement (60 s).

From this series of charge transients it was possible to construct sampled charge voltammograms for a constant sampling time. A typical sampled charge voltammogram is shown in Figure 3.17. The shape of this curve is consistent with the series of cyclic voltammograms shown in Figure 3.3, where the cathodic limit was decreased and there was an equivalent decay of the charge consumed at the reverse cathodic peak. Moreover, the electrochemical behavior of the zincate ions is still reproducible even for longer time, as the cumulative charge sample was collected at 60 s. The reproducibility found in the present system indicates very slow kinetics for this reaction.

A sampled voltammogram constructed from a series of transients acquired at different potentials from the deep eutectic 12CE with and without zinc chloride is shown in Figure 3.18. The voltammetric behavior of the two solutions shows that for the solution without zinc chloride the cumulative charge at potentials lower than $-0.5\,\mathrm{V}$ *vs.* $\mathrm{Zn/Zn^{2+}}$ is much higher compared to the electrolyte containing $0.3\,\mathrm{mol{\cdot}L^{-1}}$ of $\mathrm{ZnCl_2}$. This can be explained in terms of the overpotential required for hydrogen evolution at different electrode materials. To a small extent, there is already electrodeposition of zinc from $[\mathrm{ZnCl_4}]^{2-}$ in the electrolyte containing $\mathrm{ZnCl_2}$, changing the electrode surface. Consequently, compared to the electrolyte without zinc chloride, there is less charge consumed, because the overpotential for hydrogen evolution is higher on zinc than on glassy carbon. This result is in agreement with the cyclic voltammograms presented in Figure 3.1, where the current density shows the same behavior, for electrolytes with and without zinc, nevertheless, the difference is much smaller because of the shorter time scale of this measurement ($\nu = 10\,\mathrm{mV{\cdot}s^{-1}}$, which is equivalent to 1 s at each potential).

The current efficiencies (CEs) of the chronoamperograms are presented in Figure 3.19. The CEs were calculated from the ratio of the anodic charge at $E4$ over the cathodic charge at $E2$, at $E3$ or over the sum of the total cathodic charge $E2 + E3$.

From the CE related to the step $E2$ (i), which was varied between -0.2 and $-0.8\,\mathrm{V}$, the CE is over 100 % for -0.4, -0.5, -0.6 and $-0.7\,\mathrm{V}$, which shows that zinc is not deposited at these potential steps but at the next step at $-0.2\,\mathrm{V}$, therefore the magnitude of the charge is much larger at the oxidation potential $E4$ compared with $E2$. At $-0.8\,\mathrm{V}$ there is massive reduction of the electrolyte, so the CE decreases to 61 %. At $-0.6\,\mathrm{V}$ the CE related to $E2$ is 190 %, which clearly shows that some reaction takes place at this

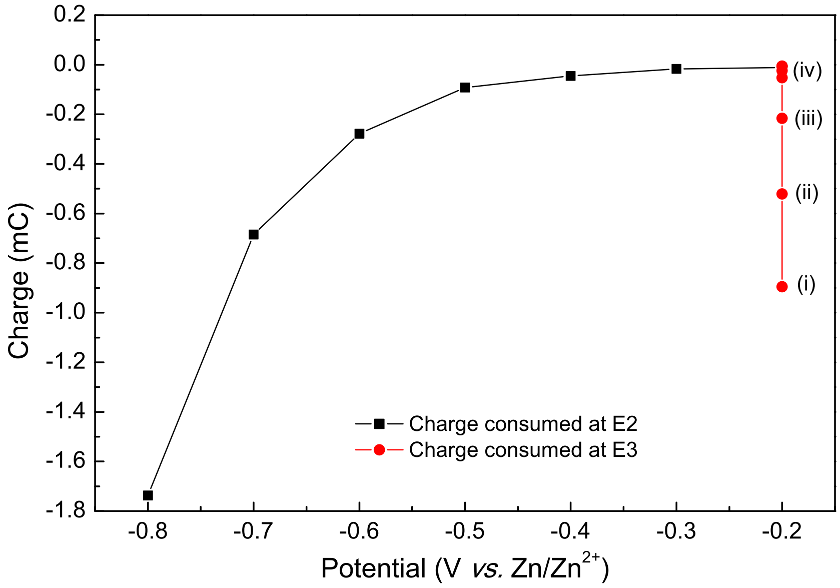

Figure 3.17. Sampled voltammogram constructed from charge-time transients for $E2$ and $E3$ at 60 s shown in Figure 3.14 and Figure 3.15. Corresponding previous potentials were (i) −0.8 V, (ii) −0.7 V, (iii) −0.6 V and (iv) −0.5 to −0.2 V.

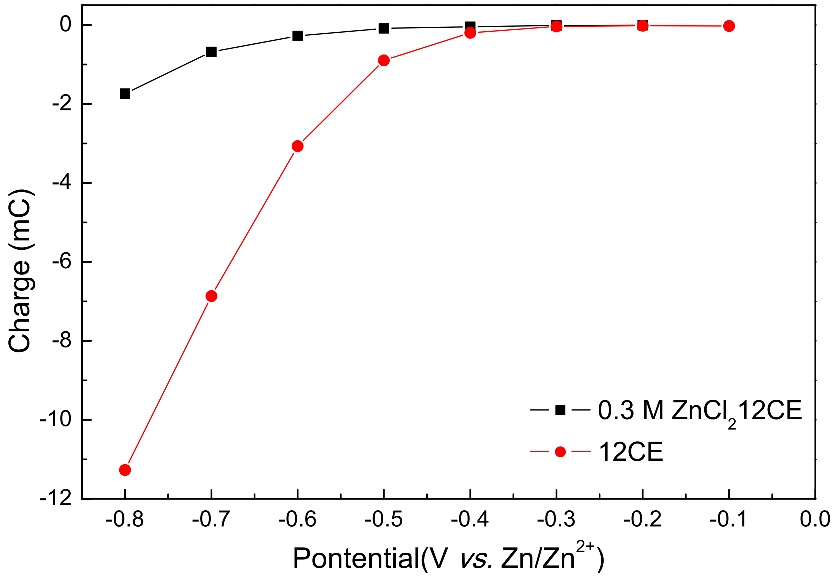

Figure 3.18. Sampled voltammogram constructed from cumulative charge *vs.* time transients from 12CE electrolyte with and without 0.3 mol·L^{-1} ZnCl$_2$. Samples collected at 60 s.

potential, but zinc deposition can not occur, due to blocking of the surface.

The CEs calculated from the charge at $E3$, constant at −0.2 V, are between 32 and 58 %, indicating incomplete dissolution of zinc within the time scale of the measurement. At −0.6 V there is a maximum in CE of 58 %, which might be due to formation of Z without blocking the surface with hydrogen at −0.7 and −0.8 V, decreasing the CE to

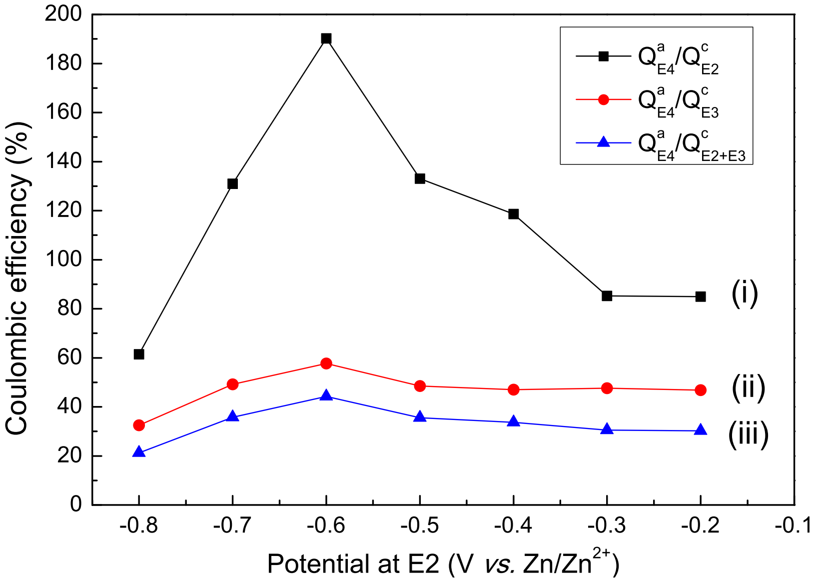

Figure 3.19. Coulombic efficiency of 4-step chronoamperometric experiments for 0.3 mol·L^{-1} ZnCl$_2$ 12CE on GC.

49 and 32 %, respectively.

The ratio of the oxidation charge over the total cathodic charge ($E2 + E3$) shows the same tendency as the previous calculation. There are clearly two tendencies. Decreasing $E2$ from -0.6 to -0.8 V increases hydrogen evolution, i.e. the total charge consumed, therefore CE drops off. Increasing $E2$ from -0.6 to -0.2 V diminishes the formation of Z, thus the total CE decreases. Hence, we can conclude that the optimal potential for the formation of Z without blocking the surface with hydrogen is -0.6 V.

Diffusion controlled current transients recorded by potential step chronoamperometry in unstirred solutions under semi-infinite diffusion conditions to a planar macro-electrode are described by the Cottrell equation (Equation 3.14), where the current i is inversely proportional to the square root of time t [52].

$$i = nFAC(D/\pi)^{1/2}t^{-1/2} \tag{3.14}$$

In this equation, F is the Faraday constant ($96485\, C\, mol^{-1}$), n is the number of electrons transferred, A is the electrode area (0.71 cm^2), C is the bulk concentration of the parent species (0.3 mol·L^{-1}) and D is the diffusion coefficient in $cm^2 s^{-1}$.

Deviation from linearity in a Cottrell plot ($i\, vs.\, t^{-1/2}$) usually indicates that the current is not diffusion-limited but other processes may limit the electrode reaction.

Cottrell plots of the current-time transients at potential $E2$ are presented in Figure 3.20.

Only for potentials within -0.2 and -0.3 V there is a linear correlation between current density and $t^{-1/2}$. At these potentials there is only reduction of zinc from $[ZnCl_4]^{2-}$, at

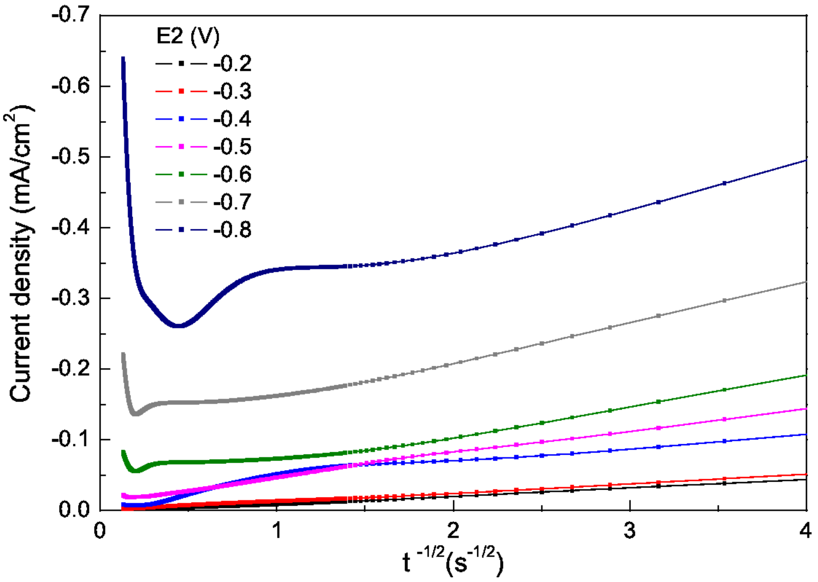

Figure 3.20. Cottrell plots of current-time transients for 0.3 mol·L^{-1} ZnCl$_2$/12CE at $E2$ at different potential steps on GC.

a very slow rate and a diffusion coefficient of $5.17 \cdot 10^{-14}$, $2.85 \cdot 10^{-13}$, $3.94 \cdot 10^{-12}$, and $1.11 \cdot 10^{-12}$ cm^{2}s^{-1} for −0.2, −0.3, −0.4, and −0.5 V, respectively. Below −0.5 V adsorption processes occur, and the transients are no longer linear. The non-linear behavior is accentuated below −0.6 V, due to an increase on the rate of reduction of the electrolyte, which are not diffusion controlled processes.

Studies of adsorption from quaternary ammonium ions gave similar results for chronoamperograms of ferrocene solutions in acetone, acetonitrile and dichloroethane containing tetrabutylammonium tetrafluoroborate (TBABF$_4$) [115]. The ammonium cations strongly adsorb on the surface of the electrode and desorb very slowly (between 2 and 20 s), hence a plot of I *vs* $t^{-1/2}$ was not linear. Moreover, it has also been shown that chronoamperometric measurements in ionic liquids behave differently when compared to other non-aqueous electrolytes, as for example acetonitrile [134]. Although most electrocrystallization processes take place very quickly, the time scale in ionic liquids is apparently much longer due to the slow kinetics of the assembly of the ionic liquid molecules at the interface. Hence adsorption, self-diffusion and potential-dependent blocking might influence significantly the voltammetric behavior of redox species observed in these measurements [110, 135, 136].

3.2.2 Investigations on the electrodeposition of zinc from Z

In the chronoamperometric studies described in the previous Subsection 3.2.1, the maximum current density at the step potential $E2$, for the formation of Z species, was obtained at $-0.8\,\mathrm{V}$. Although this potential is very negative leading to hydrogen evolution, and a decrease of the current efficiency of the reaction, it is also negative enough to form Z species. Therefore, similar 4-step chronoamperometric investigations were carried out by jumping from the rest-potential $E1$ to a constant step potential $E2$ at $-0.8\,\mathrm{V}$ *vs.* $\mathrm{Zn/Zn^{2+}}$ and varying the third step $E3$ between -0.1 and $-0.5\,\mathrm{V}$ and then back to the oxidation potential $E4$ at $+1.0\,\mathrm{V}$. This experiment was performed for investigating the potential-dependence of zinc electrodeposition from the intermediate Z, or to mimic the reverse scan, as it was done in previous sections. A schematic representation of the 4-step potential experiment is shown in Figure 3.21.

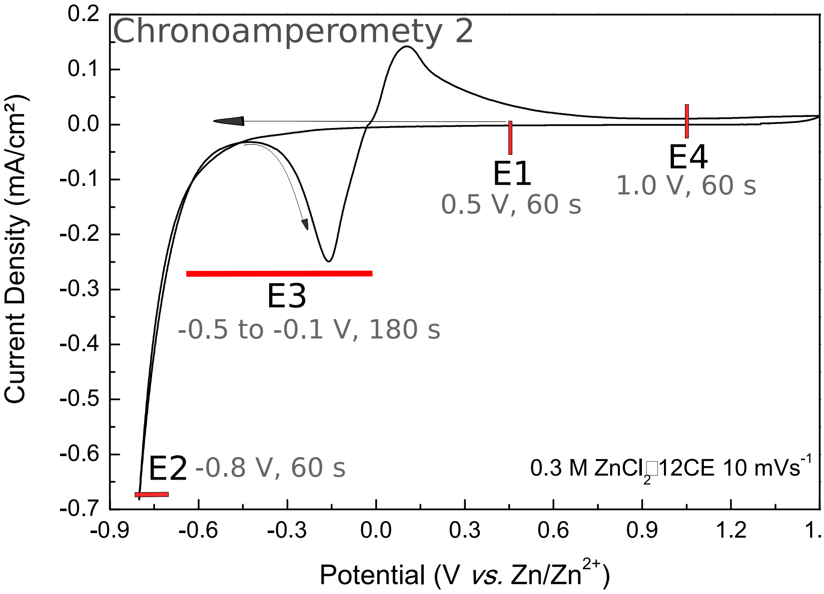

Figure 3.21. Schematic representation of 4 step chronoamperometric experiments with $0.3\,\mathrm{mol{\cdot}L^{-1}}$ $\mathrm{ZnCl_2}$ 12CE on GC.

Representative current *vs.* time transients at constant potentials are shown in Figure 3.22 for $E1$, $E2$ and $E3$. The step to $E4$ is not shown.

The current-time profile at the step $E2$ is not always constant as it involves reduction of the electrolyte, adsorption of hydrogen and/or gas evolution, which can block the surface and cause a breakdown in current. This step was kept at such a negative potential in order to ensure the formation of Z. The current profile at $E3$ (Figure 3.22) is clearly dependent on the potential applied and not on the total charge consumed in the previous step $E2$.

Chronamperometric and chronocoulometric plots of zinc deposition at different po-

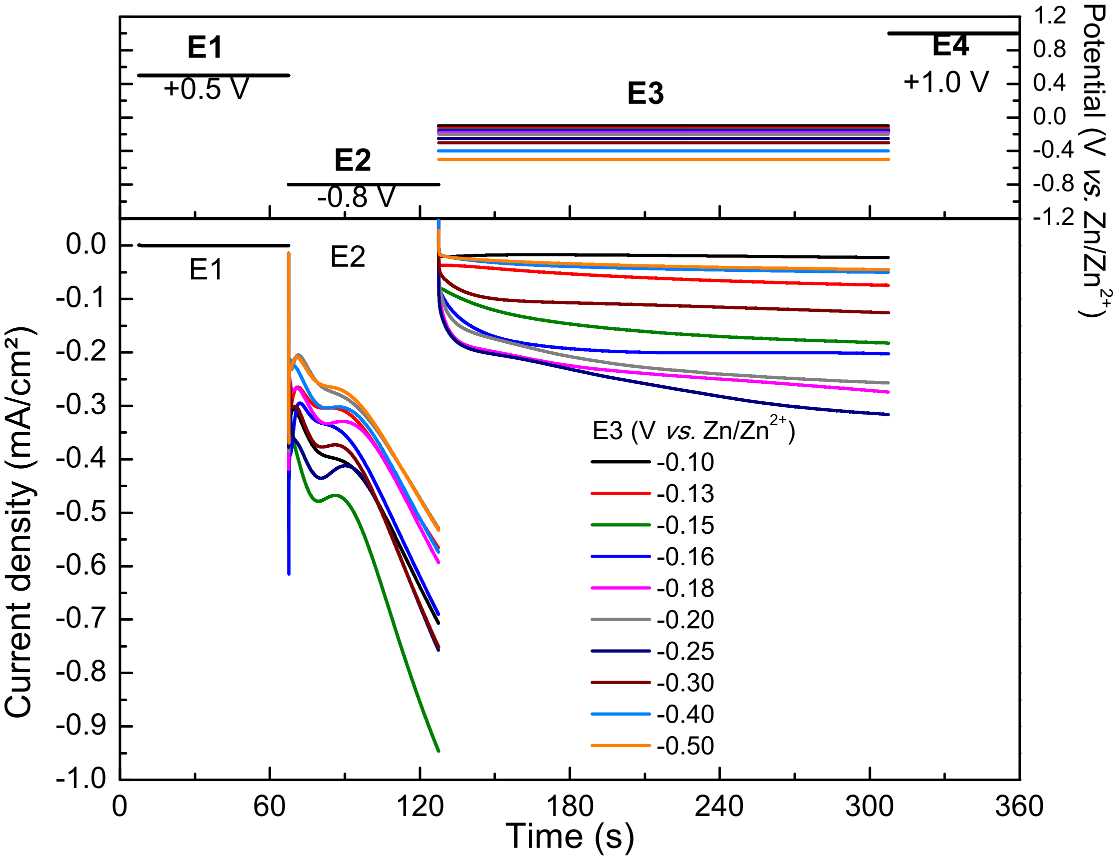

Figure 3.22. Current response of 0.3 mol·L^{-1} $ZnCl_2$ 12CE on GC for different potential steps. Applied potentials at E2 are indicated.

tentials *E*3 are shown in Figure 3.23. The magnitude of the current density and the cumulative charge are evidently dependent on the potential applied. At small overpotentials of −0.1 and −0.13 V zinc electrodeposition occurs at a very low rate, evident from the low current density up to 180 s. Decreasing the potential to −0.15 V and further down to −0.25 V *vs.* Zn/Zn^{2+} leads to an increase of the current density, due to a higher rate of zinc electrodeposition. Interestingly, although there are Z species in the diffusion layer, decreasing the potential further to −0.3 and −0.5 V causes a decay in current density, in agreement with our hypothesis of blocking of the electrode surface at these potentials. Therefore the consumed charge is also very low at these potentials.

The anodic charge consumed during step *E*4 correlates with that consumed at *E*3, as presented in Figure 3.24, and confirms that most of zinc electrodeposition occurs between −0.15 and −0.25 V.

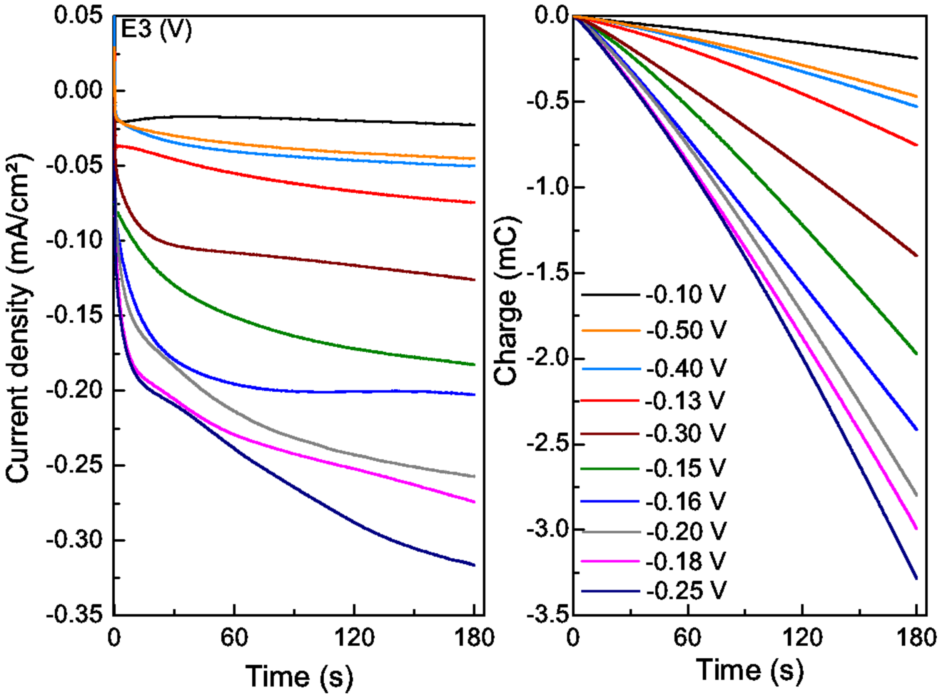

Figure 3.23. Current and charge *versus* time of 0.3 mol·L^{-1} $ZnCl_2$ 12CE on GC at the step $E3$.

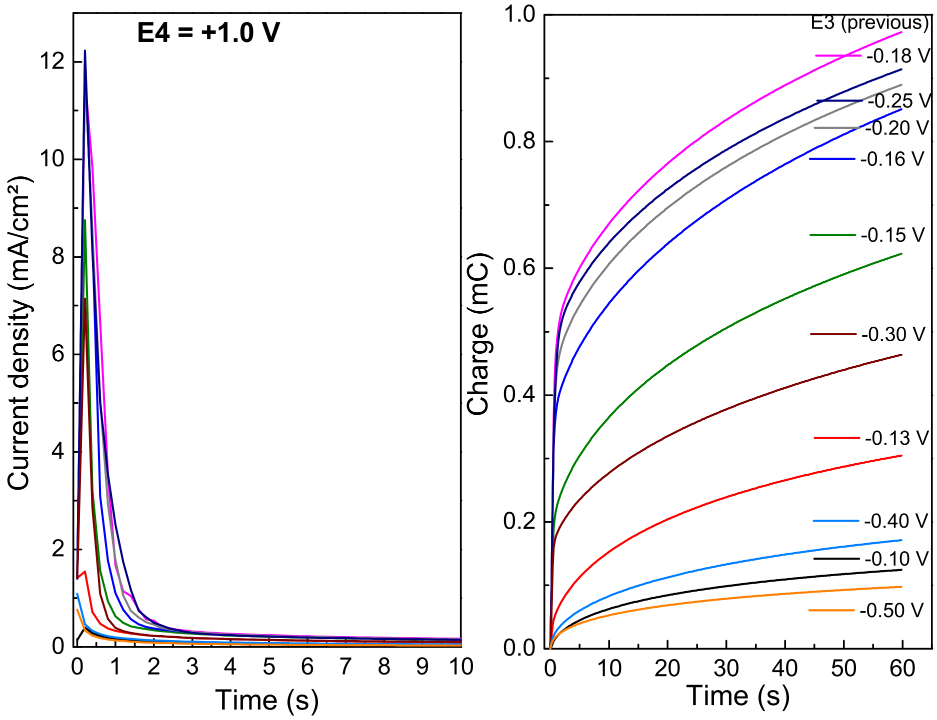

Figure 3.24. Current and charge *versus* time of 0.3 mol·L^{-1} $ZnCl_2$ 12CE on GC at the step $E4 = +1.0\,V$.

The analysis of coulombic efficiencies derived from the ratio of the anodic charge from Figure 3.24 over the cathodic charge either at the potential $E2$ at -0.8 V or $E3$ from Figure 3.23, or over the sum of them (total cathodic charge) is presented in Figure 3.25.

The CE related to the step $E3$ shows that the ratio of $Q^{\mathrm{a}}_{\mathrm{E4}}/Q^{\mathrm{c}}_{\mathrm{E3}}$ does not vary significantly, as the zinc deposited on $E3$ is proportional to that reoxidized at $E4$, with a very low efficiency, which might be due to the slow re-dissolution of zinc. Nevertheless, the ratio related to the second potential step $Q^{\mathrm{a}}_{\mathrm{E4}}/Q^{\mathrm{c}}_{\mathrm{E2}}$ shows a tendency, indicating the reduction of Z to Zn. Starting from -0.1 to -0.13 V, the efficiency is low, with maximum of 15 % due to the low overpotential for the electrodeposition of zinc. From -0.15 to -0.25 V, CE increases to 60 %, which indicates that a significant part of Z is reduced to zinc. Reducing the potential to -0.3 V results in a decrease of the CE to ca. 20 %, which decays further as the potential is decreased to -0.4 V. At -0.5 V the CE reaches a minimum of 7 %, which is in agreement with the explanation of electrode blocking at such potentials. This blocking could be caused by multilayers of the ionic liquid hindering Z to reach the electrode surface. Interestingly, this blocking is effective for long periods of time, as the potential $E3$ was held for 180 s.

The coulombic efficiency calculated from the sum of $E2$ and $E3$ followed the same pattern as of $Q^{\mathrm{a}}_{\mathrm{E4}}/Q^{\mathrm{c}}_{\mathrm{E2}}$, because the magnitude of the current density is much higher in the latter, so the contribution to CE is bigger.

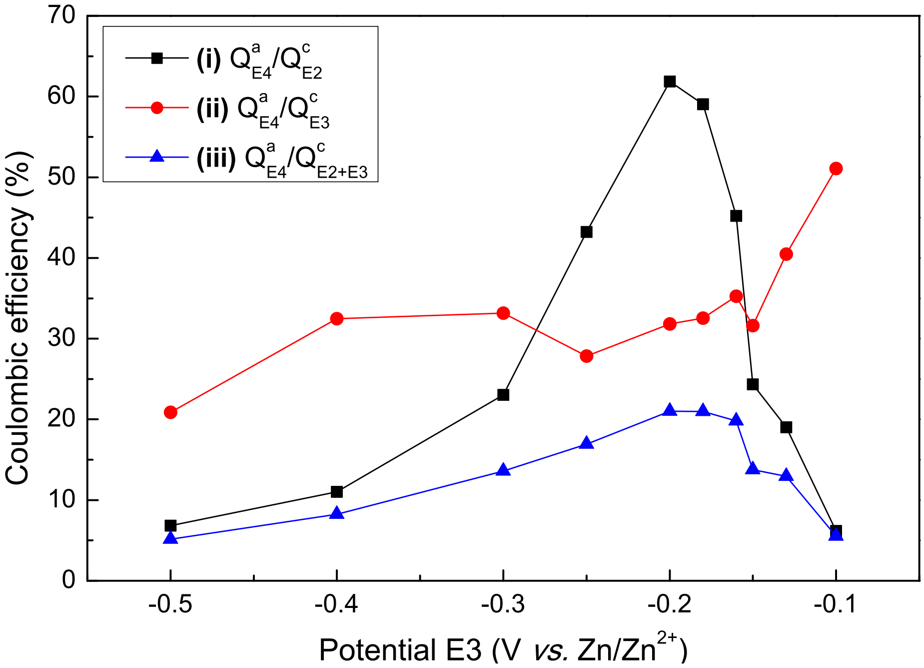

Figure 3.25. Coulombic efficiency of 4-step chronoamperometric experiments for 0.3 mol·L^{-1} ZnCl$_2$ 12CE on GC.

Figure 3.26 shows a sampled voltammogram constructed from the cumulative charge at 60 s plotted together with that of previous experiments of varying $E2$ (Figure 3.17). The sampled voltammograms reveal a very reproducible behavior for zinc electrodeposition on glassy carbon. The plot is totally consistent with cyclic voltammograms already shown for this system (Figure 3.1) and corroborates the suggested theory of potential-dependent blocking/unblocking of the electrode surface.

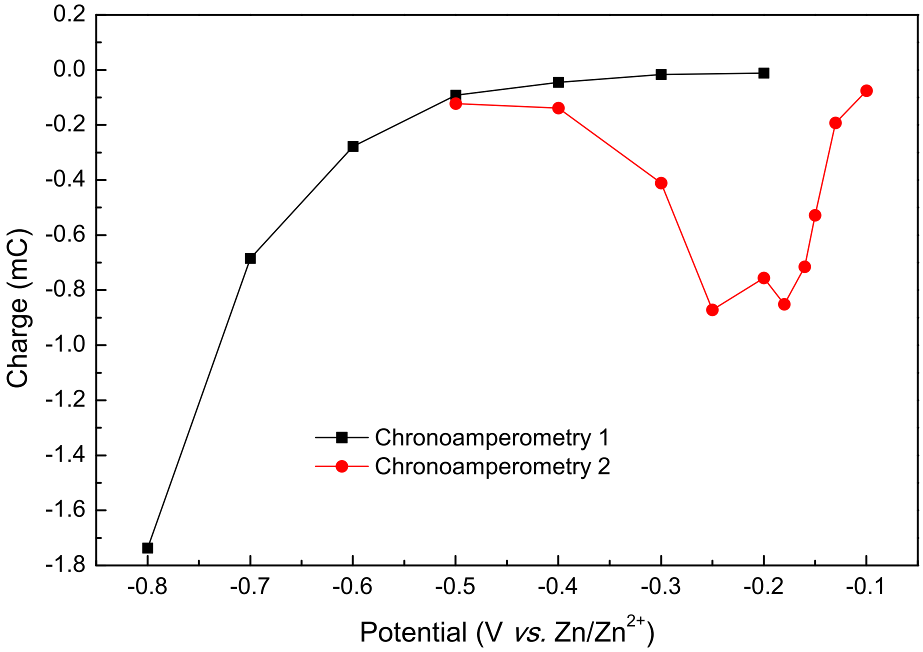

Figure 3.26. Sampled voltammogram constructed from 60 s charge-time transients for chronoamperometric experiments varying $E2$ (Chronoamperometry 1) and $E3$ (Chronoamperometry 2).

3.3 The effect of sodium ethoxide

In order to investigate the hypothesis that RO^- species are involved in the formation of the intermediate Z, an alkoxide was added to the solution at high concentration ($0.9\,mol{\cdot}L^{-1}$ $NaOC_2H_5$). Thereby, dissociation of $NaOC_2H_5$ and/or proton exchange with the other hydroxyl-containing species, would lead to the formation of RO^- anions in the bulk electrolyte, according to Equation 3.12.

The pKa values of ethanol, ethylene glycol and choline in dilute aqueous solution are 15.5, 15.1 and 13.9, respectively [137]. If this order of acidity holds also for ethoxide in the DES, mainly deprotonated choline would be produced according to the following equilibrium:

$$RO^- + R'OH \rightleftarrows ROH + R'O^- \tag{3.15}$$

where $R = -CH_2CH_3$ and $R' = -CH_2CH_2N(CH_3)_3{}^+$. This zwitterion would certainly be a stronger ligand than the undissociated choline cation. Since ethanol is the least acidic, ethoxide would be protonated and ethanol would be formed, which should result in a viscosity decrease of the mixture. Experimentally, however, we find the opposite (Figure 3.27). While the addition of $0.3\,mol{\cdot}L^{-1}$ $ZnCl_2$ in agreement with previous reports [45, 123] results in a negligible change in the viscosity of 12CE, the addition of sodium ethoxide substantially increases the viscosity of 12CE without and even more drastically of 12CE with $0.3\,mol{\cdot}L^{-1}$ $ZnCl_2$. If the order of pKa values and the resulting proton exchange equilibria are correct, the formation of ethanol and the expected decrease in viscosity is obviously overcompensated for by another effect. An appreciable amount of sodium ions is generated by the dissociation of sodium ethoxide. Ethylene glycol is known to be a relatively weak hydrogen bond donor [45] and the partial replacement of protons with sodium ions in the 12CE obviously leads to a much stronger interaction between its two components choline chloride and ethylene glycol thereby increasing the viscosity. Chloride ions released upon replacement of one or more chloride ligands with choline in the tetrachlorozincate complex increase the concentration of anionic hydrogen bond donor complexes, while the zwitterionic choline ligands in the resulting zinc complexes have an alkylammonium group that bears a positive charge. This might lead to a much stronger interaction of the zinc complex with the DES and could explain the substantial viscosity increase of the $ZnCl_2$ containing 12CE with increasing amounts of sodium ethoxide.

The cyclic voltammetric behavior in this electrolyte was significantly different from that observed without $NaOC_2H_5$ (Figure 3.28). In contrast to the voltammograms

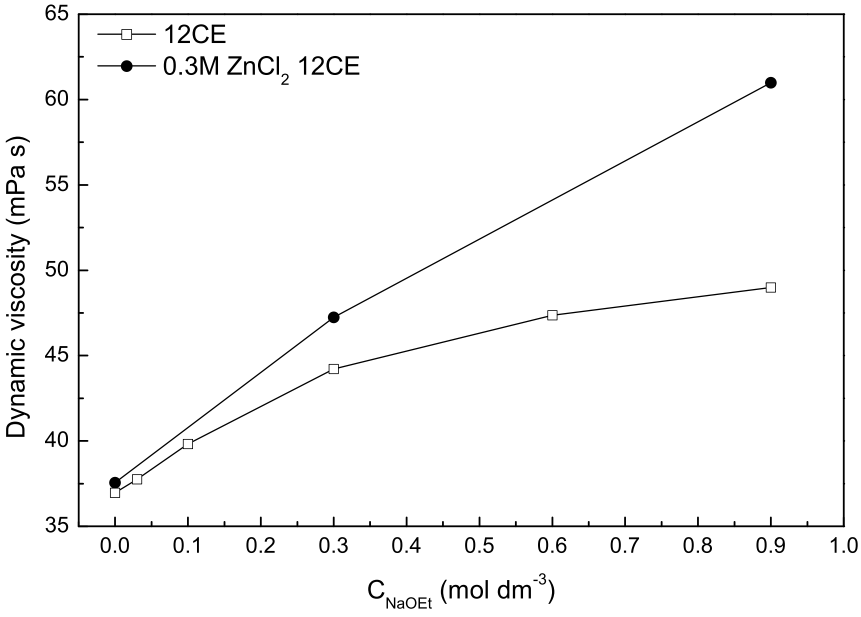

Figure 3.27. Viscosity at 30 °C of 12CE and 0.3 mol·L^{-1} of $ZnCl_2$/12CE electrolytes containing various amounts of sodium ethoxide.

without the ethoxide (Figure 3.1), a cathodic peak was observed on the initial forward scan at ca. −0.2 V, and a second one with almost the same peak current density and at the same potential on the reverse anodic sweep. The peak potentials are similar to those observed previously for the solution without the additive, which were assigned to the reduction of Z to zinc. We therefore conclude that the presence of the strong base $NaOC_2H_5$ caused the formation of reducible species in the bulk electrolyte with a reduction potential similar to that observed in electrolytes without the ethoxide, which had been assigned to Z. The ratio of the anodic charge (from 0 to 1.0 V) over the cathodic (from 0 to −0.6 V) was 32 %, showing that there is still a significant contribution of side-reactions, such as decomposition of the electrolyte, although the cathodic switching potential was increased to −0.6 V. Additionally, low solubility and incomplete dissolution of zinc in the electrolyte can account for the low coulombic efficiency.

Rotating the electrode in the solution containing $NaOC_2H_5$ resulted in an increase of the peak currents at −0.2 V as presented in Figure 3.29. The ratio of the anodic charge passed from 0 to 1.0 V over the cathodic charge from 0 to −0.6 V were around 25–30 % for the static and rotating electrodes, which can be the result of side reactions such as the reduction of EG or Ch^+ or possibly dendritic zinc deposition with detachment of the dendrites. The increase in current density with rotation rate is in marked contrast to the behavior found for the electrolyte without NaOEt and indicates that species present in the bulk of the electrolyte are reduced rather than intermediates formed in the diffusion

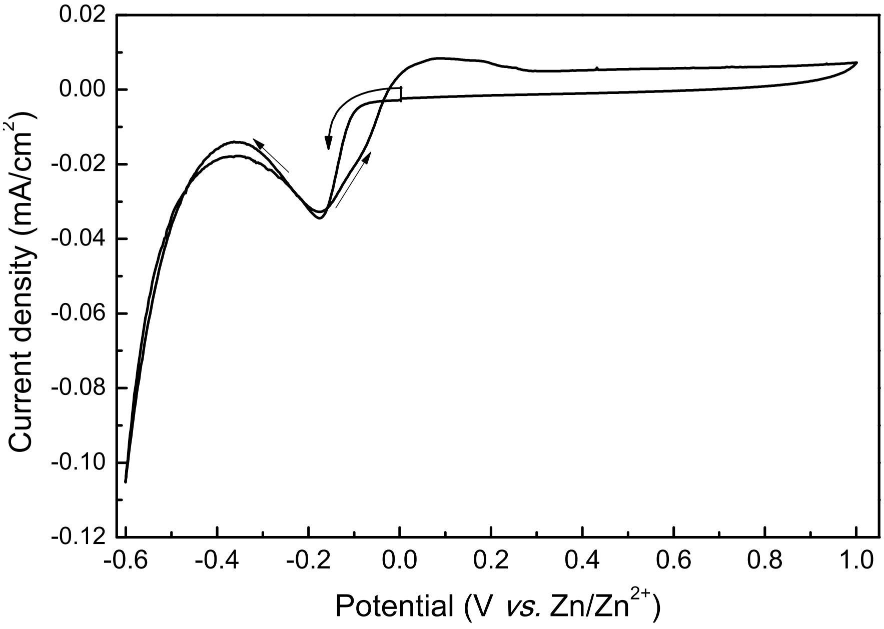

Figure 3.28. Cyclic voltammogram of 0.3 mol·L^{-1} of $ZnCl_2$ and 0.9 mol·L^{-1} of $NaOC_2H_5$ in 12CE on a glassy carbon disk electrode ($\nu = 10$ mV·s^{-1}, $T = 30$ °C) starting from 0 V *vs.* Zn/Zn^{2+} with a negative sweep direction. Arrows indicate sweep direction.

layer as would be expected if NaOEt was not involved in the formation of Z. It is also interesting to note that no *plateau* for a diffusion limited reduction current was observed even at rotation rates as high as 5000 rpm. Again this can be explained by potential dependent blocking of the electrode.

Rotating disc voltammograms of $ZnCl_2$ in 12CE containing an excess of $NaOC_2H_5$ are presented in Figure 3.30 as a function of scan rate. Decreasing the potential scan rate increases the magnitude of the cathodic peak at −0.2 V and decreases the anodic stripping current, consequently decreasing the coulombic efficiency. The ratio of the anodic over the cathodic charge passed are: 26 % at 10 mV·s^{-1}, 20 % at 5 mV·s^{-1}, 14 % at 2 mV·s^{-1} and 8 % at 1 mV·s^{-1}. Inefficiency could be related to parasitic reactions and a low re-dissolution rate of zinc. The peak current density increasing with lower scan rates can be explained by slow adsorption/desorption kinetics of the blocking layer.

At sufficiently high overpotentials, RDE voltammograms are usually characterized by a mass-transport-limited current *plateau* rather than a peak [52]. However, in our RDE voltammograms even at scan rates as low as 1 mV·s^{-1}, no limiting current is observed. This again shows that a slow step with kinetics on the timescale of several seconds is likely to limit the rate of the electrode reaction below −0.2 V. Moreover, it is alleged that not merely speciation of zinc plays a role in this reaction, but that also the structure of the electrode/electrolyte interface in the DES affects the unusual reduction behavior of

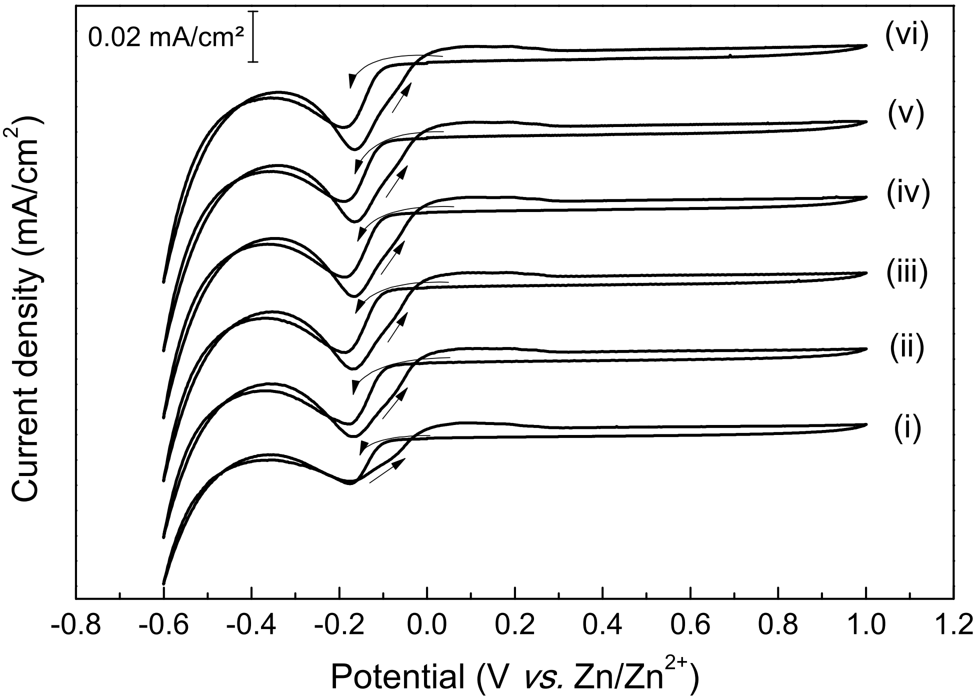

Figure 3.29. Cyclic voltammogram of 0.3 mol·L^{-1} of $ZnCl_2$ and 0.9 mol·L^{-1} of $NaOC_2H_5$ in 12CE on a glassy carbon disk electrode ($\nu = 10\,\text{mV·s}^{-1}$, $T = 30\,°\text{C}$) starting from 0 V *vs.* Zn/Zn^{2+} with a negative sweep direction. The rotation rate of each scan was: (i) 0, (ii) 1000, (iii) 2000, (iv) 3000, (v) 4000 and (vi) 5000 rpm. Arrows indicate sweep direction. The voltammograms are offset for clarity.

the zinc species.

Peak-shaped responses instead of a steady-state limiting current have been observed for RTILs, even in cyclic voltammetry using microdisk electrodes and RDEs under high rates of rotation, which is commonly not the case [136, 138]. This difference arises from the high viscosity of the ionic liquids and consequently the much smaller diffusion coefficients of the electroactive species. On the voltammetric timescale this gives rise to peaks similar to planar diffusion conditions. Consequently, the classical Levich description for hydrodynamic voltammetry [52] breaks down, because the contribution of convection is minimized and no limiting current is observed in the range of rotation speed employed. Furthermore, a near steady-state response could in principle be achieved by increasing the rotating rate until the Levich limiting current value is achieved. However, at rotation rates as high as the maximum used for 12CE (5000 rpm), air bubbles become trapped in the ionic liquid-electrode interface, giving rise to a noisy current response. Moreover, due to the potential-dependent blocking of the electrode, the current density decreases after the forward peak, thus no steady state can be achieved.

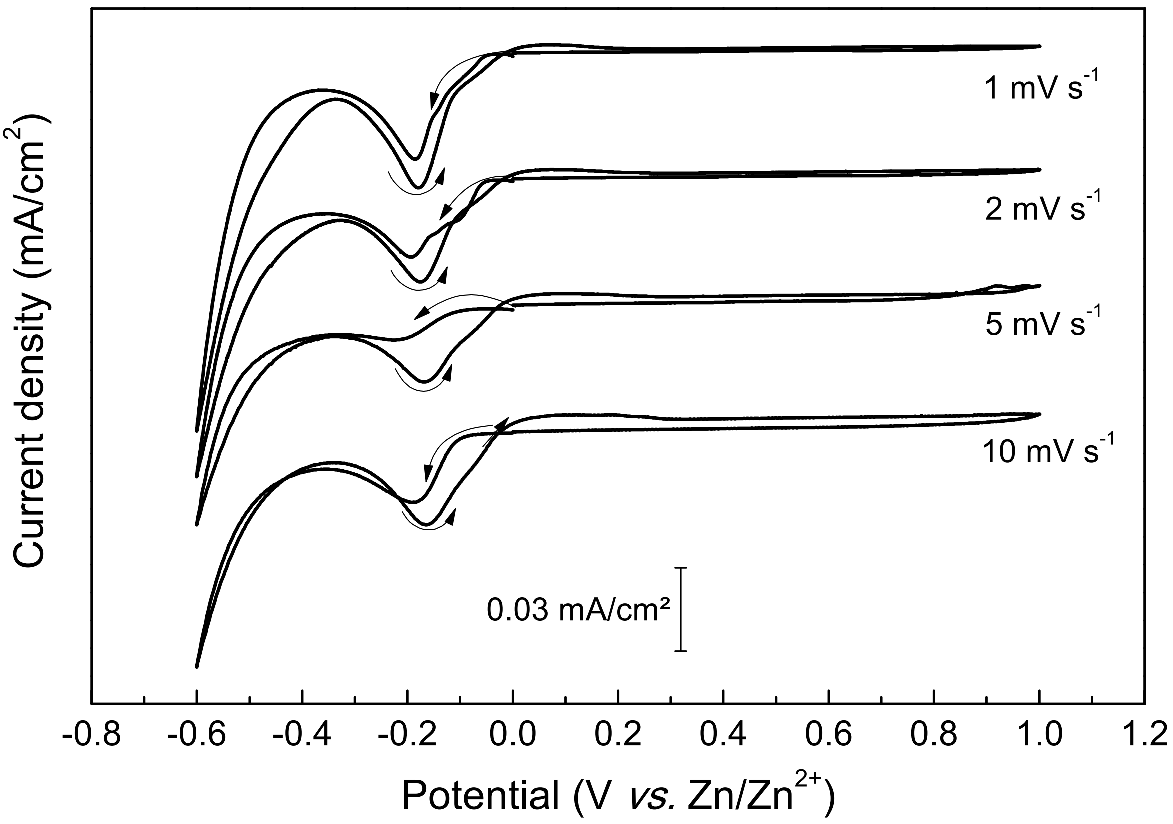

Figure 3.30. Cyclic voltammogram of 0.3 mol·L^{-1} of $ZnCl_2$ and 0.9 mol·L^{-1} of $NaOC_2H_5$ in 12CE on a rotating glassy carbon disk electrode at a rotation speed of 4000 rpm and the indicated scan rates, $T = 30\,°C$; starting from 0 V *vs.* Zn/Zn^{2+} with a negative sweep direction. The voltammograms are offset for clarity.

3.4 Electrodeposition of zinc from ethylene glycol

Since the electrodeposition of zinc from 12CE electrolyte has a mechanism involving not only the formation of intermediate species but also blocking of the electrode surface, probably by choline ions, cyclic voltammetry in a solution of 0.3 mol·L^{-1} $ZnCl_2$ in ethylene glycol (EG) without choline chloride was carried out in order to make a direct voltammetric comparison to a more conventional system. The cyclic voltammetric response of zinc ions in ethylene glycol should provide some hints on the mechanism and on the adsorption effects taking place in the deep eutectic solvent.

A typical cyclic voltammogram of a 0.3 mol·L^{-1} solution of $ZnCl_2$ in ethylene glycol is shown in Figure 3.31. A cathodic wave started at roughly −0.2 V and it was attributed to the electrodeposition of zinc with an associated anodic peak at ca. +0.5 V assigned to the stripping of the zinc deposit. The current density of the anodic peak decreased from the first to the second cycle. The coulombic efficiency was 86 % in the first cycle and 71 % in the second and third cycle, which is much higher than in the solution of 12CE (usually between 20 and 60 %).

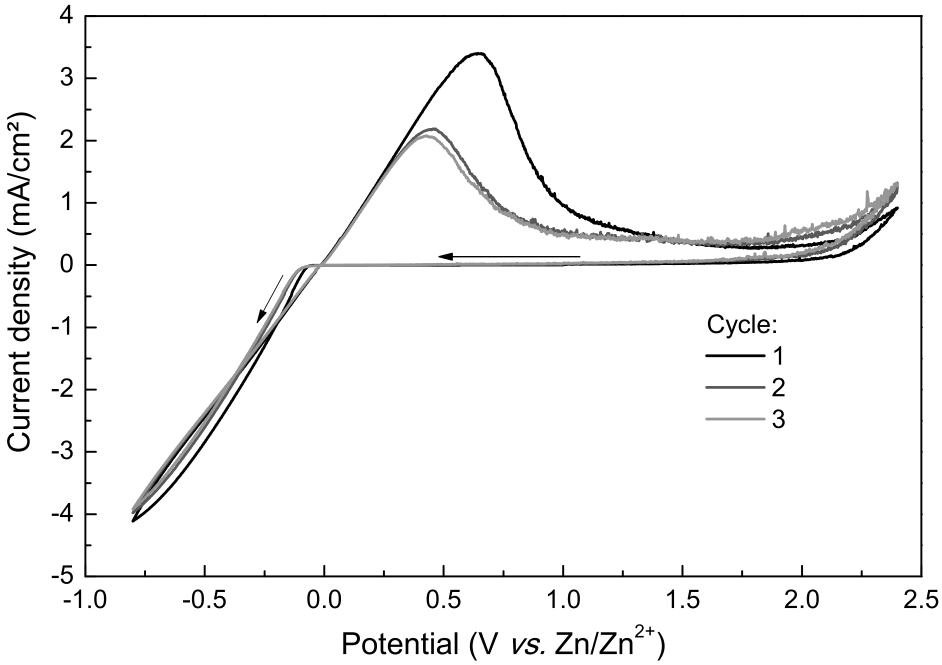

Figure 3.31. Cyclic voltammograms of 0.3 mol·L^{-1} of $ZnCl_2$ in ethylene glycol at a static glassy carbon disk electrode (ν = 10 mV·s^{-1}) starting from 1.0 V *vs.* Zn/Zn^{2+} with a negative sweep direction. Arrows indicate sweep direction.

A characteristic nucleation loop, often found for metal electrodeposition on dissimilar substrates, was also observed. Such current loops occur because metal deposition on some foreign substrates require a considerable overpotential to initiate nucleation, but less for the growth of the nuclei from a certain critical size on. Nucleation loops have often been observed for zinc plating on glassy carbon, for example, in 1-ethyl 3-methylimidazolium chloride (EMIC) [22, 23] aqueous KCl [139], or NH_4Cl [140] solutions, and apparently on Pt from 12CE with 0.5 mol·L^{-1} $ZnCl_2$ [34].

Decreasing the cathodic limit from −0.8 V to −1.0, −1.2 and −1.5 V *vs.* Zn/Zn^{2+} results in an increase of the anodic peak currents, as shown in Figure 3.32. It is also noteworthy that the magnitude of the current density is slightly higher for the zinc electrodeposition in ethylene glycol compared to that seen for the deep eutectic. The coulombic efficiency of the CVs were 85, 81 and 87 % for cathodic limits of −1.0, −1.2 and −1.5 V *vs.* Zn/Zn^{2+}, respectively, indicating that there is not a significant contribution of side reactions with an increase of the cathodic potential limit, although it would be expected that there would be a higher contribution from the reduction of EG.

Figure 3.33 shows a set of CVs at different potential scan rates. Varying the scan rate of the CV results in a slight increase in current density, which could be due to a small

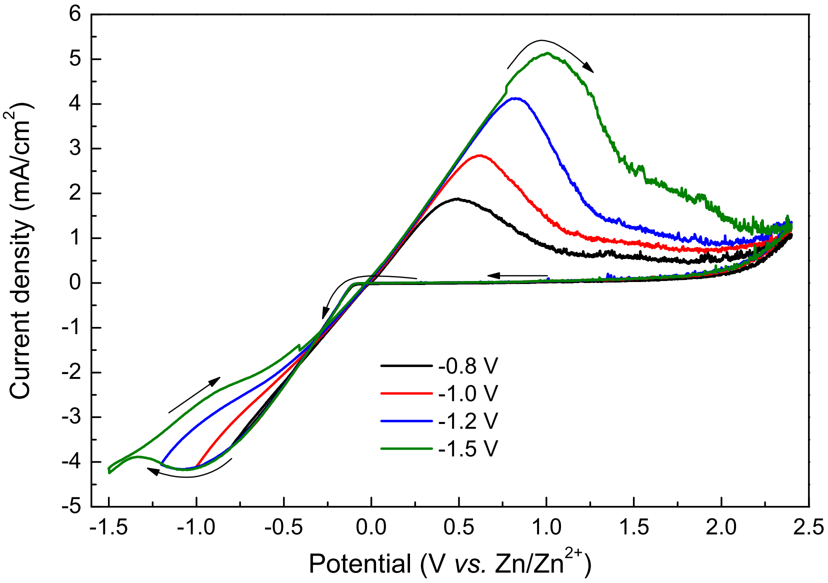

Figure 3.32. Cyclic voltammograms of 0.3 mol·L^{-1} of $ZnCl_2$ in ethylene glycol with different cathodic limits at a static glassy carbon disk electrode (ν = 10 mV·s^{-1}) starting from 1.0 V *vs.* Zn/Zn^{2+} with a negative sweep direction. Arrows indicate sweep direction.

increase of the capacitive charge. Additionally, for faster scan rates the cathodic current is peak shaped whereas at slower rates there is a continuous increase in current density.

The coulombic efficiency of the CVs performed at different scan rates is presented in Figure 3.34. The faster the potential is swept, the lower the efficiency of the reaction, which might be due to the temporary exceedance of the solubility limit of zinc ions in the diffusion layer.

The cyclic voltammetric behavior of zinc in ethylene glycol is significantly different from that observed in 12CE electrolyte, since a cathodic peak is observed already in the forward scan, which is consistent with the suggestion that the choline ions block the surface of the glassy carbon electrode in the cathodic range of the cyclic voltammogram. However, it is important to note that the conditions are different due to the lower viscosity of ethylene glycol compared to 12CE and the different Lewis character of the solution, which may result in a different speciation of zinc. Moreover, the conductivity of ethylene glycol alone is low, thus the Ohmic drop in the solution is higher.

In order to overcome this divergence and make the Zn:Cl ratio equal in both electrolytes, KCl was added to the solution. The addition of an ionic salt would also have the advantage of enhancing the ionic conductivity of the electrolyte. A cyclic voltammogram of the solution containing 1 mol·L^{-1} of KCl is shown in Figure 3.35.

Electrodeposition of zinc from $ZnCl_2$:KCl:EG system is remarkably different from that in the absence of KCl. The cathodic current density increases sharply when the nucleation

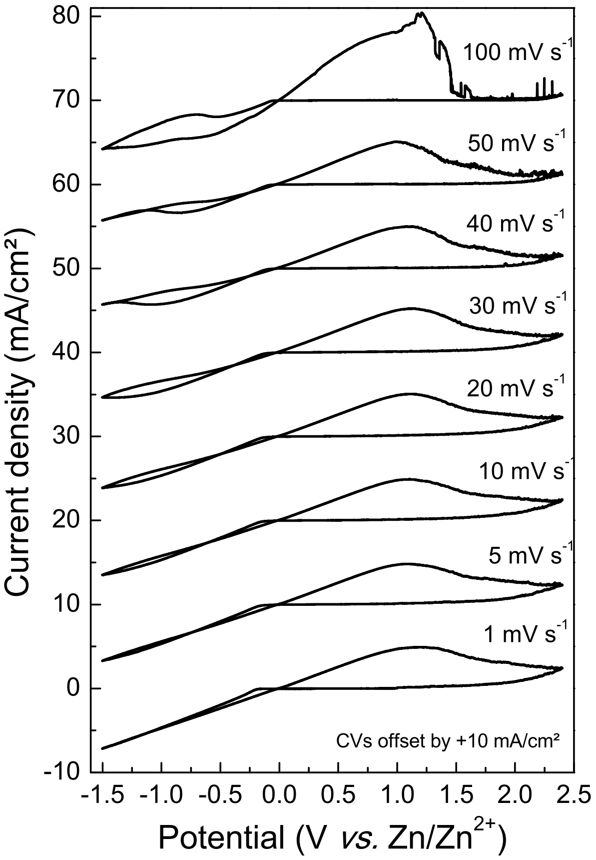

Figure 3.33. Cyclic voltammograms at different scan rates of 0.3 mol·L^{-1} of $ZnCl_2$ in ethylene glycol at 30 °C and at a stationary glassy carbon disk electrode starting from +1.0 V *vs.* Zn/Zn^{2+} with a negative sweep direction. The voltammograms are displaced on the current density axis by +10 mA·cm^{-2} for clarity.

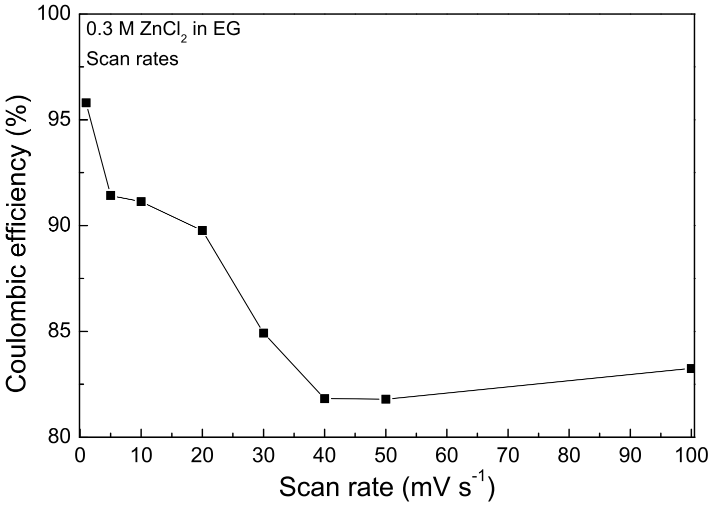

Figure 3.34. Coulombic efficiencies as a function of scan rate for the cyclic voltammograms of 0.3 mol·L^{-1} of $ZnCl_2$ in ethylene glycol at 30 °C shown in Figure 3.33.

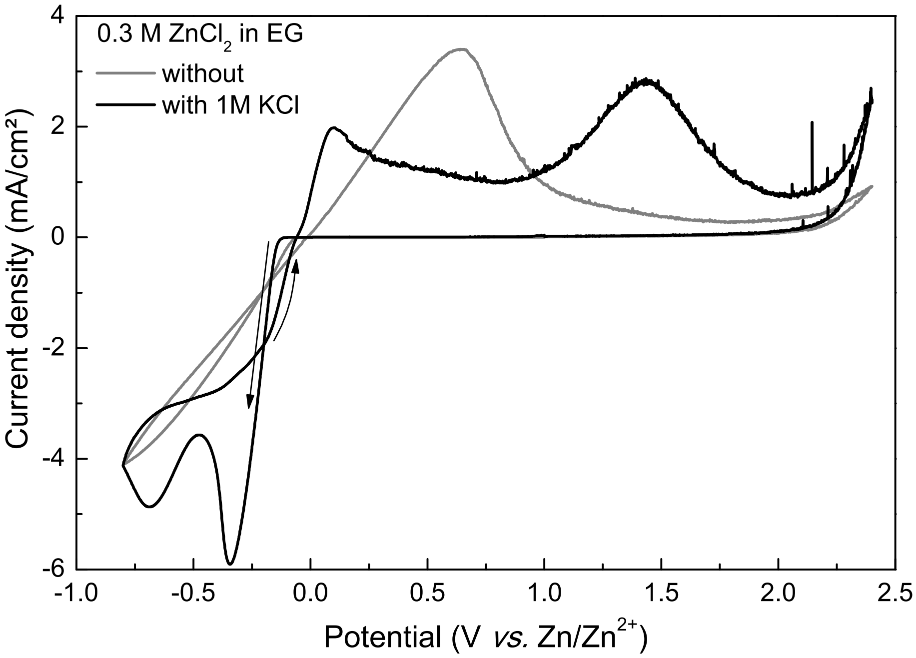

Figure 3.35. Cyclic voltammograms of $0.3\,\mathrm{mol{\cdot}L^{-1}}$ of $ZnCl_2$ in ethylene glycol with and without $1\,\mathrm{mol{\cdot}L^{-1}}$ of KCl at a static glassy carbon disk electrode ($\nu = 10\,\mathrm{mV{\cdot}s^{-1}}$) starting from 1.0 V *vs.* Zn/Zn^{2+} with a negative sweep direction. Arrows indicate sweep direction.

has begun, giving rise to a peak shaped deposition with maximum current desity at ca. −0.3 V, differently from the CV recorded previously. A second cathodic peak is also observed at ca. −0.7 V. Multiple cathodic peaks indicate that zinc is deposited from more than one zinc species, probably $ZnCl_3^-$ at −0.3 V and $ZnCl_4^{2-}$ at more negative potentials (−0.7 V). A nucleation loop with an overpotential of ca. 150 mV is observed.

During the reverse sweep, two anodic waves are observed at +0.1 and +1.6 V, which can be associated with the two cathodic peaks, or firstly to zinc dissolution and at −1.5 V to the oxidation of Cl^- to Cl_3^-. The coulombic efficiency was 87 %, which is higher compared to 63 % in the 12CE electrolyte over the same potential range (cathodic range: 0 to −0.8 V and anodic 0 to −2.4 V). In both cases, inefficiency could arise through parasitic reactions such as hydrogen evolution and disconnection of dendritic zinc deposits, although the formation of dendrites was not seen during both experiments. The obvious difference in the potential region from −0.8 to 0 V between the two electrolytes may be due to the lack of choline to block the surface or the different mole fractions of zinc chloride species, especially as choline would be expected to stabilize $[ZnCl_4]^{2-}$ [42]. Nevertheless, stabilization of zinc ions by coordination with ether chains has already been suggested for quarternary alkoxy alkyl ammonium ionic liquids with various oligo-ether side chains [46].

A series of voltammetric measurements was carried out varying the cathodic switching potential. Figure 3.36 shows the cyclic voltammograms with different cathodic limits. Changing the cathodic limit from −0.8 V to −1.2 V increases the magnitude of the peak current of the first anodic peak at +0.1 V and also shows that the reduction of ethylene glycol occurs at ca. −1.1 V. The coulombic efficiency was 86, 76 and 52 % for cathodic limits of −0.8, −1.0 and −1.2 V, indicating that as the reverse potential goes negative, more charge is consumed for the reduction of ethylene glycol to form hydrogen as shown in Equation 3.16.

$$\mathrm{HOCH_2CH_2OH + e^- \longrightarrow HOCH_2CH_2O^- + \tfrac{1}{2}\,H_2} \qquad (3.16)$$

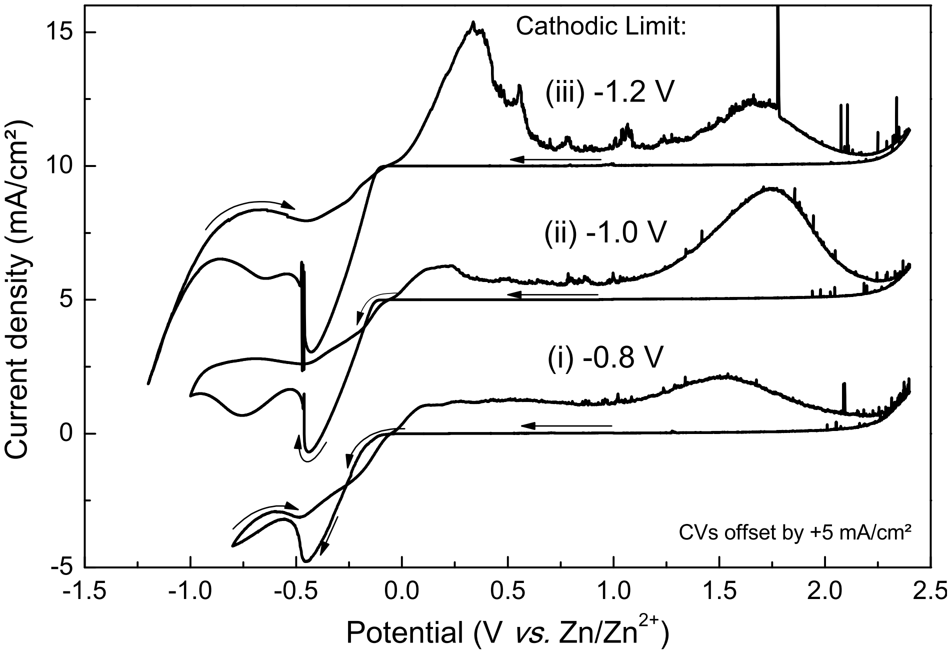

Figure 3.36. Cyclic voltammograms of 0.3 mol·L^{-1} of $ZnCl_2$ in 1 mol·L^{-1} KCl ethylene glycol with different cathodic limits at a static glassy carbon disk electrode (ν = 10 mV·s^{-1}) starting from 1.0 V *vs.* Zn/Zn^{2+} with a negative sweep direction. Arrows indicate sweep direction.

Ethylene glycol has a number of advantages in comparison with aqueous baths, for example a larger electrochemical window, higher boiling temperature (197 °C) and lower vapor pressure (8 Pa), which allows the deposition of metals that can not be reduced in aqueous solution. Solutions of EG are also known to form stable complexes with some metals as divalent metal halides with general formula $M(EG)_nX_2$, where M = Mn, Co, Ni, Cu, Mg, Ca, Sr; n = 1 – 4 and X = Cl, Br [141]. Nevertheless, many electrolytes based on organic solvents have insufficient solution conductivity and higher viscosity than aqueous solutions, although still fairly low compared to ionic liquids.

EG has been used as solvent for the electrodeposition of zinc and thermoelectric semiconductor films of Zn−Sb alloys, from a zinc chloride and antimony potassium tartrate solution at 120 °C [142]. Other compounds such as CdS_xSe_{1-x} for solar cell applications [143], AuSn [144], Bi_2Te_3 [145] and Co−Sb alloys [146] have also been successfully deposited from this electrolyte. Moreover it has also been used as additive for 1-ethyl-3-methylimidazolium bromide (EMIB) ionic liquids and has shown to improve the quality of zinc deposits obtained from $ZnBr_2$ in EMIB. By adding EG to the ionic liquid the authors reported that the dissociation of EMIB to EMI^+ and Br^- is promoted. Consequently, Br^- ions are coordinated with $ZnBr_2$, increasing the activity of the effective species for zinc deposition, such as ${ZnBr_4}^{2-}$ [147–149].

The solution without KCl, is Lewis neutral, so it is likely that the zinc ions are stabilized by coordination with EG. The EG mixture turns Lewis basic by adding 1 mol·L^{-1} of KCl due to the excess of Cl^-, and the equilibrium is shifted as shown in Equation 3.17 and 3.18.

$$ZnCl_2 + Cl^- \rightleftarrows {ZnCl_3}^- \tag{3.17}$$

$${ZnCl_3}^- + Cl^- \rightleftarrows {ZnCl_4}^{2-} \tag{3.18}$$

Due to the large excess of Cl^- ions in the solution of 0.3 mol·L^{-1} $ZnCl_2$ 1 mol·L^{-1} KCl in EG, it is likely that the main active species is $[ZnCl_4]^{2-}$. However, as already discussed previously for the 12CE system, it is unlikely that zinc would be deposited from $[ZnCl_4]^{2-}$, although deposition of zinc from $[ZnBr_4]^{2-}$ solutions of EMIB containing EG [147–149] and from $ZnCl_2$ in ethylene glycol [142] has been described in the literature. Nevertheless, the formation of complexes such as $[Zn(EG)_xCl_{(4-x)}]^{(2-x)-}$ is possible and it is likely that the electrodeposition of zinc occurs through the formation of such compounds. Furthermore, the lower viscosity of EG compared with 12CE allows a faster mass transport of the electroactive species, therefore a higher current density in the $ZnCl_2$:EG system is observed. Additionally, no blocking effects are observed, in contrast to the 12CE system containing choline [42, 43]. Obviously, the physical effects at the interface of glassy carbon and EG are conspicuously different from those of glassy carbon and 12CE, as the ionic liquid plays a dual role of solvent and electrolyte, which and it may interfere with the voltammetric response of the system [120, 134].

3.5 Partial conclusions

Cyclic voltammetry on glassy carbon electrodes of $ZnCl_2$ in a strongly Lewis-basic deep eutectic solvent comprising choline chloride and ethylene glycol has revealed an unusual cathodic peak on sweeping the potential positive from $-0.8\,\mathrm{V}$ *vs.* Zn/Zn^{2+}. A possible explanation for the cause of this feature has been given, namely, that active sites on the glassy carbon are blocked by adsorbed species such as choline or hydrogen at low potentials, which gradually desorb at potentials $> -0.5\,\mathrm{V}$. This hypothesis was supported by cyclic voltammetry in an ethylene glycol solution without choline chloride, which shows conventional zinc electrodeposition. This indicates that choline ions are blocking the surface during the negative sweep in the deep eutectic solvent. Zinc is deposited from a reducible Zn species Z formed as intermediate during the cathodic sweep. Z is formed in the diffusion layer by replacement of one or more chloride ligands in the $[ZnCl_4]^{2-}$ ion, which Raman spectroscopy confirmed to be the dominating zinc species in the Lewis-basic DES. Furthermore, Z can be transported into the bulk of the electrolyte by rotating the electrode. The formation of Z has slow chemical kinetics and increasing the potential scan rate decreases the zinc deposition rate. The formation of an intermediate and the blocking of the surface is not affected by increasing the temperature.

The addition of sodium ethoxide to the solution facilitated the deposition of zinc. A cathodic peak for Zn deposition was observed at the same potential as without the ethoxide, on the forward cathodic, as well as on the backward anodic sweep. RDE experiments with the ethoxide containing electrolyte caused the current to increase with rotation rate, which supports the hypothesis that the intermediate Z contains RO^- anions and that in presence of an alkoxy base they are already formed in the bulk of the electrolyte. This observation is consistent with the hypothesis that Z is a complex having the formula $[ZnCl_{(4\text{-}x)}(RO)_x]^{2-}$.

The unusual electrochemical behavior of zinc in choline-based deep eutectic electrolytes opens many questions not only on the mechanism of zinc reduction from ionic liquids but also on the structure of the electrode/electrolyte interface in such deep eutectic solvents and how this affects electrochemical reactions. Further investigations are required on the complexation of the Zn^{2+} ions and on the potential dependent blocking of the electrode to corroborate this hypothesis. Therefore, PM-IRRAS spectroelectrochemistry was carried out and will be discussed in Chapter 8.

Part II

Zinc Electrodeposition on Metal Electrodes

4 Zinc electrodeposition on platinum and gold

The electrodeposition of zinc from 12CE on glassy carbon shows a very interesting mechanism involving formation of intermediate species and blocking of the substrate by adsorbed species. Since glassy carbon is a non-metallic electrode and electrodeposition as well as adsorption processes are often strongly affected by the electrode material, it is of interest whether the phenomena observed on glassy carbon would occur also on metal substrates. Therefore, in order to better understand the mechanism of zinc electrodeposition from 12CE electrolytes, investigations on platinum, copper, gold and stainless steel electrodes were carried out and are presented in this and the next chapter.

4.1 Zinc deposition on platinum

4.1.1 Voltammetric studies

The 12CE electrolyte without $ZnCl_2$ was examined by cyclic voltammetry within -0.3 and $+2.4\,V$ using a platinum working electrode (Figure 4.1). The CV started from open circuit potential at $+0.9\,V$ *vs.* Zn/Zn^{2+} with a negative sweep direction. From $+0.2\,V$ there is an increase of current, which can be attributed to reduction of ethylene glycol, choline or traces of water. From $-0.2\,V$, massive gas bubbling was observed at the electrode surface due to formation of hydrogen, because the overpotential for hydrogen evolution is much lower on platinum compared to glassy carbon.

In the anodic range, there is a remarkable increase of current at $E \geq +2.3\,V$ *vs.* Zn/Zn^{2+}, followed by a cathodic peak on the return sweep at $+2.2\,V$. This is attributed to the oxidation of chloride ions to chlorine and its respective reduction to chloride, according to Equation 3.1 [13]. No evolution of chlorine gas was visually observed at $E = +2.4\,V$.

Figure 4.2 shows a cyclic voltammogram for $0.3\,mol{\cdot}L^{-1}$ $ZnCl_2$ 12CE on a stationary platinum electrode at $10\,mV{\cdot}s^{-1}$ scan rate. The voltammogram started cathodically from $+0.4\,V$ *vs.* Zn/Zn^{2+} swept to $-0.8\,V$ and then cycled to $+1.2\,V$ and back to zero. In the

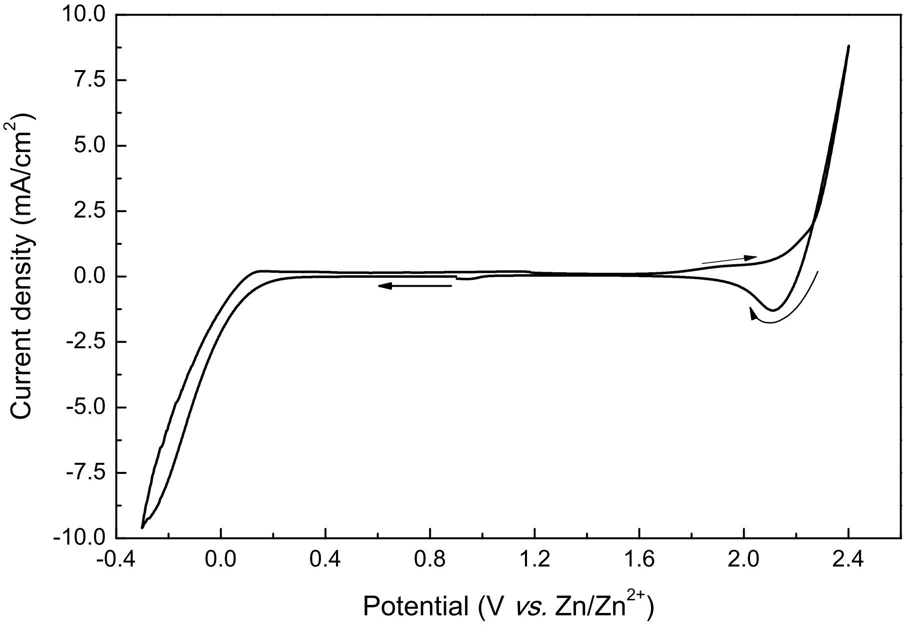

Figure 4.1. Background cyclic voltammogram of 12CE at 10 mV·s^{-1} using a platinum working electrode at 30 °C.

CV containing $ZnCl_2$, two cathodic peaks and two anodic waves are observed in the region of -0.6 to $+1.2$ V, which were not present in the CV of the DES without zinc. The two extra cathodic peaks are observed at -0.3 V on the forward scan and on the backward sweep at ca. -0.35 V.

Hydrogen evolution takes place on the electrode surface whose kinetics strongly depend on the electrode material. Platinum is regarded as excellent electrocatalyst for hydrogen evolution, as the formation of adsorbed hydrogen lowers the energy of activation at such materials [53, 131, 150–153]. Consequently, platinum metals favours the reaction to occur more readily, hence the proton-transfer step (Volmer Reaction, shown in Equation 4.1) takes place close to the equilibrium potential, whereas for glassy carbon hydrogen evolution occurs at more negative potentials, changing the voltammetric response for these two electrode materials in 12CE electrolytes.

$$H^+ + M + e^- \rightarrow M{-}H \tag{4.1}$$

According to the mechanism proposed for zinc electrodeposition from 12CE on glassy carbon electrodes, the electrodeposition of zinc takes place from an intermediate species formed on the cathodic sweep by a ligand exchange reaction of $[ZnCl_4]^{2-}$ with RO^-, which is generated by electrolyte reduction (Equations 3.9 to 3.12). Because the formation and adsorption of hydrogen takes place on transition metals at a more positive potential than on sp metals, the reduction of the deep eutectic solvent (ROH) to form adsorbed hydrogen and RO^- species occurs at $E \leq +0.2\,V$ on platinum electrodes. Consequently, the zinc deposition from Z occurs during the forward cathodic scan, simultaneously with hydrogen evolution, differently from glassy carbon. Since the reduction of the electrolyte is continuous and the electrodeposition of zinc is not only mass-transport controlled but also depends on the formation of Z, the current would rather be expected to continuously increase till the switching potential is reached at −0.6 V. Instead, the cathodic wave with its maximum at −0.3 V is peak-shaped on the forward and on the backward sweep at −0.35 V. Thus, it is likely that on platinum substrates there is also blocking of the surface by choline ions, although to a smaller extent compared to glassy carbon, for this reason the current decreases between −0.35 and −0.4 V on the forward scan.

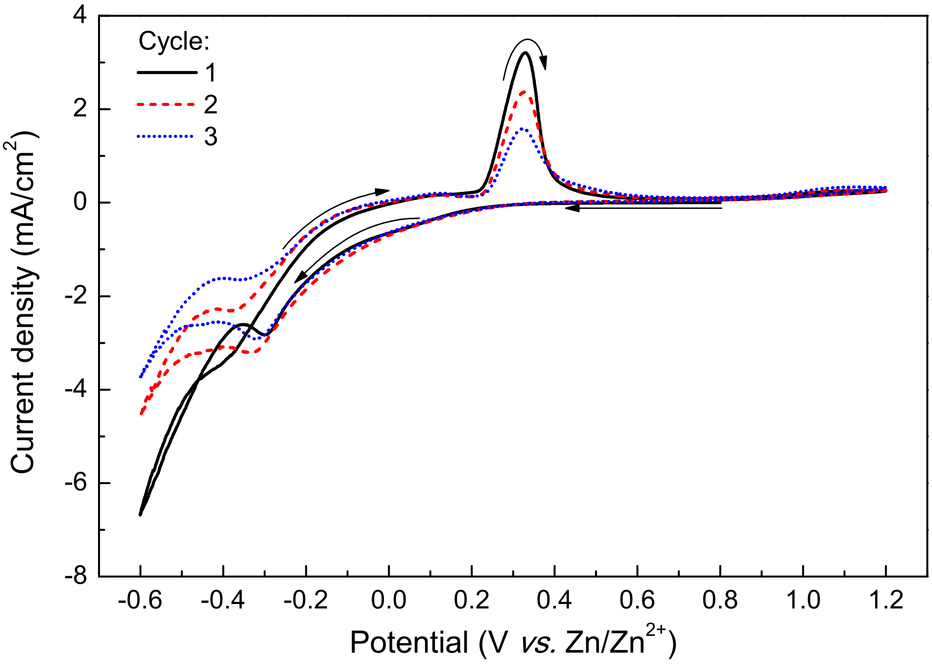

Figure 4.2. Cyclic voltammograms of 0.3 mol·L^{-1} $ZnCl_2$ in 12CE electrolyte on a stationary platinum disc electrode (10 mV·s^{-1}, 30 °C) starting from +0.8 V *vs.* Zn/Zn^{2+} with a negative sweep direction. Arrows indicate sweep direction.

The voltammetric response for 0.3 mol·L^{-1} $ZnCl_2$ in 12CE on platinum and glassy carbon electrodes are plot together and presented in Figure 4.3. The current density for zincate reduction on platinum is significantly higher compared to that on GC. Moreover, the CV recorded on platinum differs essentially from that on GC by the presence of a cathodic peak on the forward scan, which can be explained in terms of the overpotential for hydrogen evolution.

In the anodic range of the CV on Pt two distinct stripping peaks were recorded. A small anodic peak at +0.12 V *vs.* Zn/Zn^{2+} (A1), which is barely seen in Figure 4.2, and

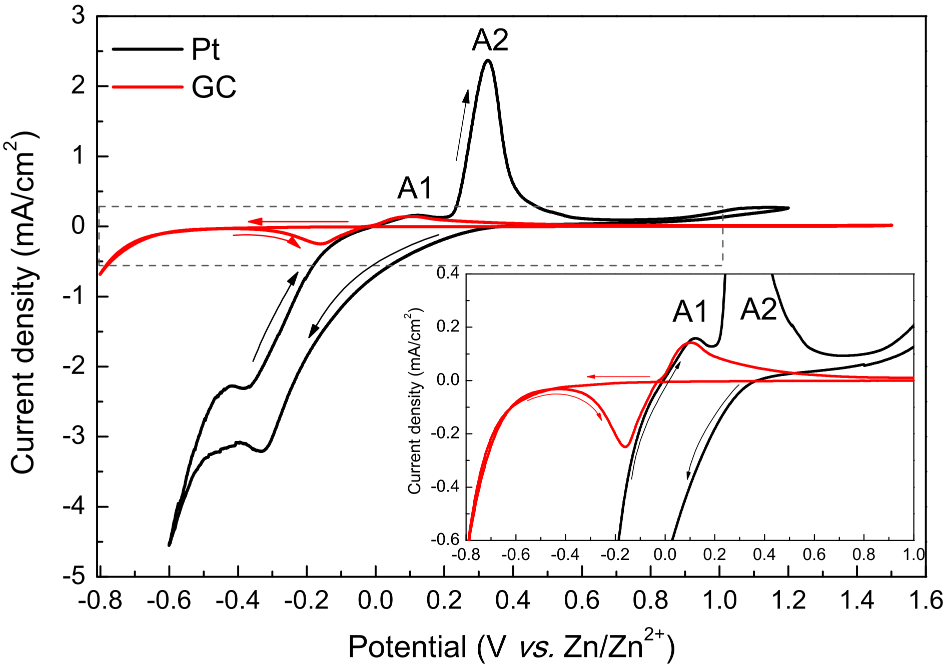

Figure 4.3. Cyclic voltammogram of stationary glassy carbon and platinum electrodes (as for cycle 2 from Figure 4.2) in 12CE electrolyte with 0.3 mol·L^{-1} ZnCl$_2$ at 10 mV·s^{-1}, 30 °C) starting from +0.8 V *vs.* Zn/Zn^{2+} with a negative sweep direction. Arrows indicate sweep direction.

a dominating wave at +0.37 V *vs.* Zn/Zn^{2+} (A2). Apparently, zinc deposited on the platinum electrode consists of two different energy states. The first anodic peak (A1) coincides with the peak attributed to dissolution of zinc on glassy carbon, as better visualised in the expanded graphic from Figure 4.3, and it is likely to be on the same energy state (elemental zinc), whereas the second dominating wave might be related to zinc, which is alloyed with the platinum substrate.

The total anodic charge was between 19 and 21 % of the cathodic charge for the three cycles shown in Figure 4.2. Low coulombic efficiency can be attributed to parasitic reactions from −0.4 to −0.6 V *vs.* Zn/Zn^{2+}, where formation of bubbles on the electrode surface — hydrogen gas due to reduction of ethylene glycol, choline or trace water in the electrolyte — was observed, and/or to incomplete dissolution of zinc. Furthermore, from the CVs of Figure 4.2 it can be seen that the current response decreased considerably from the first to the third cycle. Apparently, as the platinum electrode is subjected to zinc deposition/stripping cycles, this leads to a change in surface structure, due to incomplete dissolution of zinc. Since the overpotential for hydrogen evolution on zinc-platinum intermetallics is probably higher than on pure platinum, the reduction of the electrolyte is slower and a lower current density is recorded in the second and third cycle.

Abbott et al. [36] investigated the deposition of zinc on a platinum substrate from 12CE electrolytes. Two different anodic peaks for zinc dissolution were observed and attributed to the dissolution of nano- and bulk phase zinc. The authors discarded the possibility of Pt−Zn alloy formation by comparing with the behavior of zinc deposition on a glassy carbon substrates, where they also observed two anodic peaks. However, based on the phase diagram of platinum and zinc (Figure 4.4) and comparing with our results of zinc deposition on a glassy carbon substrate, in which only one main anodic peak is observed and no alloy formation takes place, as GC is an inert non-metal electrode, we suggest that the multiple dissolution peaks are not due to the formation of nano and bulk crystalline phases but due to the formation of intermetallic compounds between the platinum substrate and zinc plus the dissolution of unreacted zinc. Thus the first peak A1 on $+0.12\,\mathrm{V}$ *vs.* $\mathrm{Zn/Zn^{2+}}$ (Figure 4.3) is assigned to oxidation of Zn, whereas the second more positive peak on $+0.37\,\mathrm{V}$ *vs.* $\mathrm{Zn/Zn^{2+}}$ (A2) is assigned to the dissolution of zinc from Pt−Zn intermetallics.

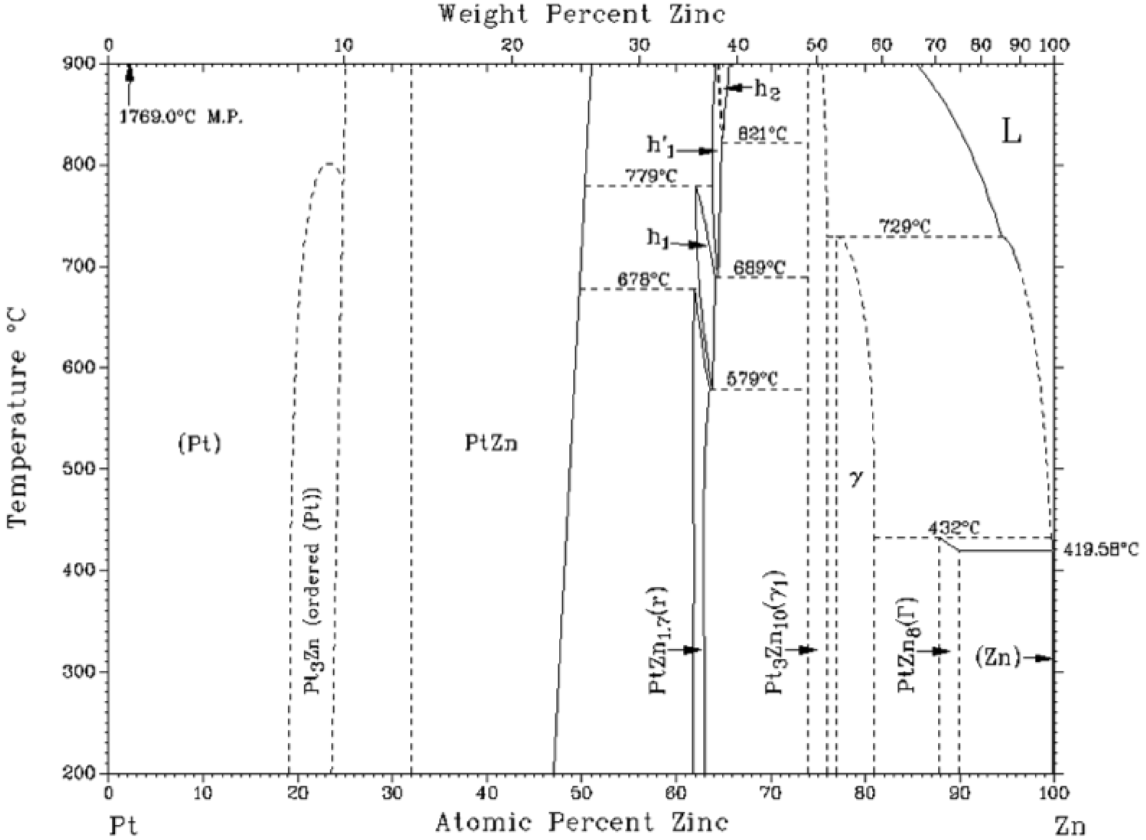

Figure 4.4. Pt−Zn binary phase diagram [154].

The formation of Pt−Zn alloys from ionic liquids has been reported in the literature, either from co-deposition of Zn and Pt onto GC and W electrodes from Lewis acidic ionic liquids based on $ZnCl_2$-EMIMCl (1-ethyl-3-methylimidazolium chloride) containing Pt [155], or similarly to the procedure presented above, from electrodeposition of zinc on Pt electrodes in pure $ZnCl_2$-EMIMCl melts [155–157].

Electrodeposition of zinc on platinum electrodes with formation of Pt−Zn alloys has also been described from $ZnCl_2-NaCl$ melts at 450 °C [158] and from alkaline aqueous [159–161] as well as acidic sulphate solutions [162–164].

Further CV was performed by fixing the anodic switching potential at +1.2 V and decreasing the cathodic limit from −0.8 to −0.7, −0.6, −0.5 and −0.4 V (Figure 4.5). It can be seen that for platinum electrodes the cathodic limit does not play such a significant role as for glassy carbon electrodes, because the Z species can be formed at less negative potentials. For the CV with a cathodic switching potential of −0.8 V, apart from the first anodic peak at +0.14 V related to oxidation of bulk Zn and the second anodic wave at +0.4 V, another anodic peak is observed at +0.5 V, indicating that for such a cathodic polarization of the platinum substrate, multiple Pt−Zn phases may be formed. Increasing the cathodic limit from −0.7 to −0.5 V does not affect significantly the cathodic peaks and the alloying, as the anodic peak current A2 does not decrease in magnitude.

The total anodic charge related to the total cathodic one are: 12, 19, 32, 43 and 19 % for switching potentials of −0.8, −0.7, −0.6, −0.5 and −0.4 V, respectively, indicating that from −0.6 to −0.8 V, most of the cathodic current is consumed for hydrogen evolution. The low efficiency for the cathodic limit at −0.4 V indicates that besides hydrogen evolution, no significant amount of zinc was deposited within this potential limit. Nevertheless, the decreasing wave at A2 (+0.4 V) by increasing the cathodic limit from −0.5 to −0.4 V clearly indicates that the electrodeposited zinc reacts with the Pt substrate to form Pt−Zn alloy in this potential range ($E \leq -0.4$) and it is also consistent with the fact that the peak current at +0.14 V becomes smaller as the switching potential goes more negative, as by decreasing the cathodic limit, the driving force for Pt−Zn alloying increases, therefore more of the electrodeposited zinc is alloyed with the platinum substrate.

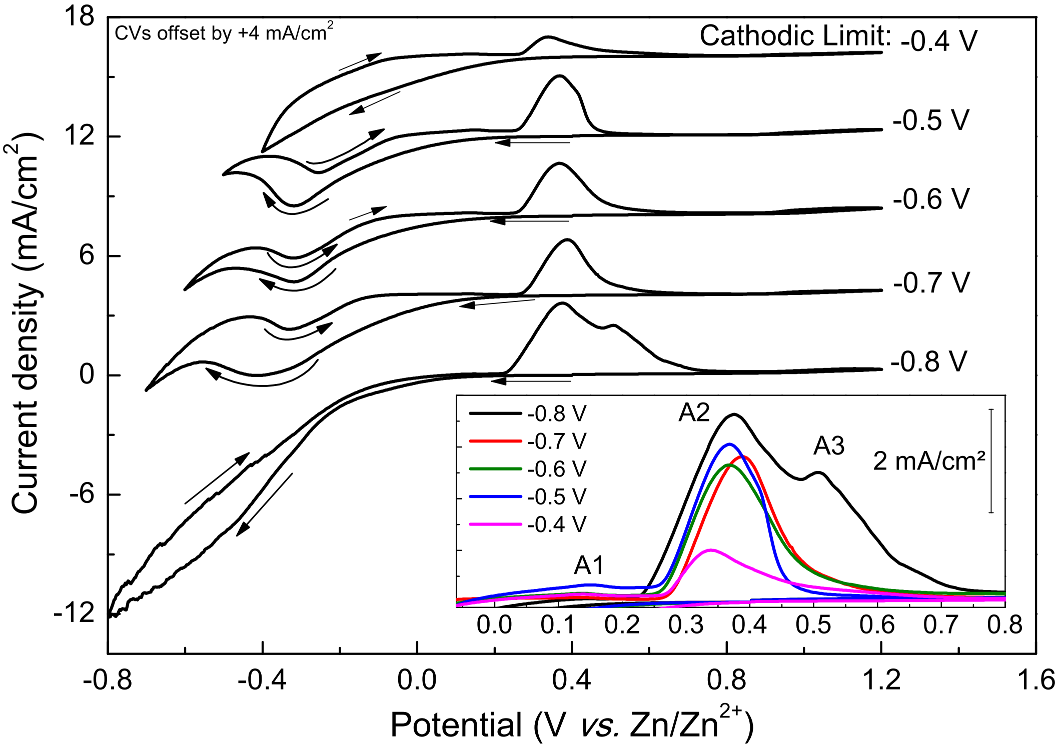

Figure 4.5. Cyclic voltammograms of 0.3 mol·L^{-1} $ZnCl_2$ in 12CE electrolyte on a stationary platinum disc electrode (10 mV·s^{-1}, 30 °C) starting from 0.4 V *vs.* Zn/Zn^{2+} with a negative sweep direction. Arrows indicate sweep direction.

Figure 4.6 shows a set of experiments with potential limits between −0.7 and +1.2 V and varying scan rate. Increasing the scan rate shifts the forward reduction peak to more negative potentials indicating slow kinetics. Additionally, three anodic peaks are observed (signed as A1, A2 and A3 in Figure 4.7). The first peak (A1) is hardly visible and can be assigned to the oxidation of Zn. The stripping charge from A1, corresponds to 3.5 monolayer of zinc at 5 mV·s^{-1}, 2.5 at 10 mV·s^{-1} and 0.2, 0.4, 0.3 and 0.3 monolayers of zinc at 20, 30, 40 and 50 mV·s^{-1}, respectively (calculated from the atomic volume of zinc onto the geometric area of the platinum electrode).

The second stripping peak assigned to dissolution of alloyed zinc (A2) shifts positively and decreases in magnitude by increasing the scan rate. This behavior supports our suggestion of alloy formation between zinc and platinum with slow kinetics. A third peak is also observed at around +1.1 V (labelled as A3), suggesting that the deposit may contain multiple Pt−Zn phases. The peak A3 is more pronounced for higher sweep rates, which is consistent with the slow kinetics of the system also for stripping of the Pt−Zn alloy, shifting the oxidation potential to more positive values by scanning faster.

The ratio of the total anodic charge from 0 to +1.2 V related to that consumed from 0 to −0.7 V *vs.* Zn/Zn^{2+} was 33, 19, 10, 13, 10 and 7.5 % for the scan rates of 5, 10, 20, 30, 40 and 50 mV·s^{-1}, respectively, which confirms that the zinc-platinum alloying has very slow kinetics. Moreover, the very low coulombic efficiency for scan rates of 50 mV·s^{-1}, indicates that for such a high scan rate, only fast reactions take place in the cathodic range, e.g. adsorption of hydrogen and hydrogen evolution, which may happen remarkably fast on platinum electrodes in protic ionic liquids [151–153].

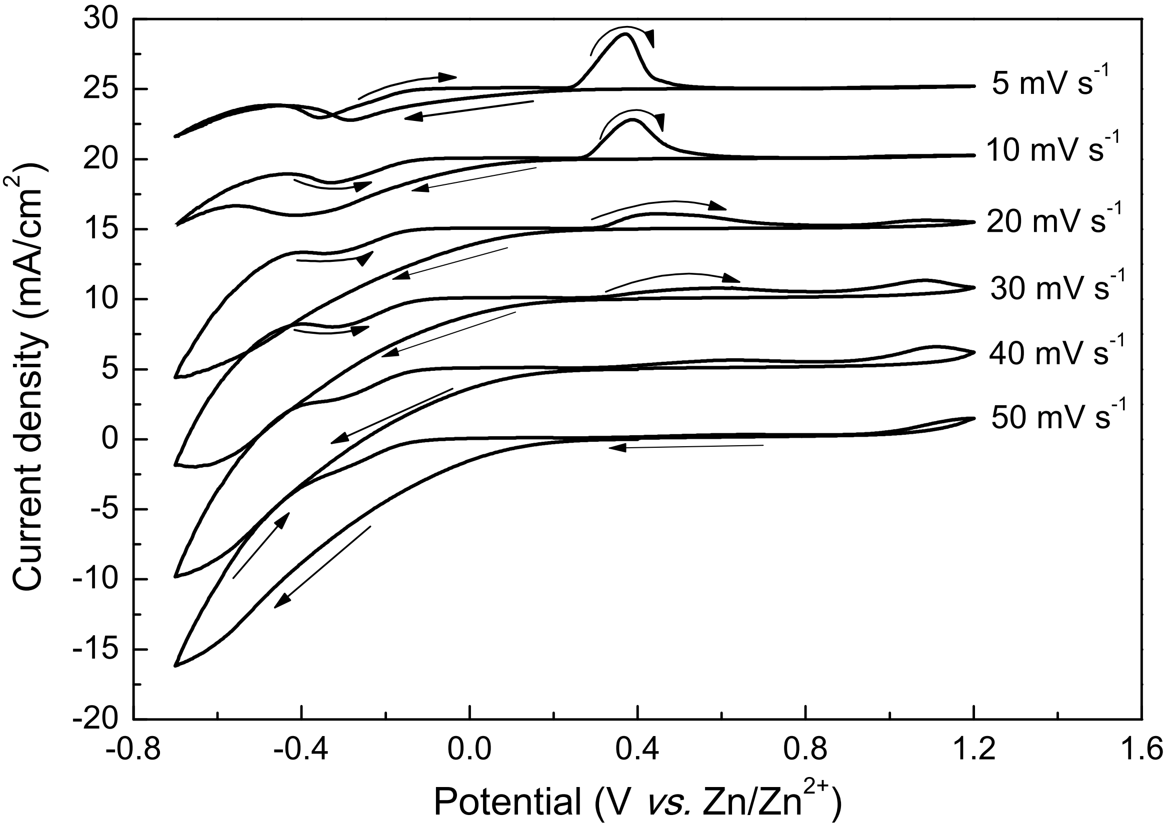

Figure 4.6. Cyclic voltammograms of 0.3 mol·L^{-1} $ZnCl_2$ in 12CE electrolyte on a stationary platinum disc electrode 30 °C starting from 0.4 V *vs.* Zn/Zn^{2+} with a negative sweep direction. Arrows indicate sweep direction.

Zinc deposition from 12CE on a platinum rotating disc electrode (RDE) has been performed at 30 °C and rotation rates ranging from 100 to 3000 rpm (Figure 4.8). The sweep was started at +0.4 V with a negative direction and 10 mV·s^{-1} scan rate. Upon rotation of 100 rpm, the peak currents on the cathodic forward and backward scan, as well as the anodic stripping peak, increase significantly, whereas the current attributed to hydrogen evolution does not change to the same extent. This indicates that the convection increases the transport of electroactive species to the electrode surface.

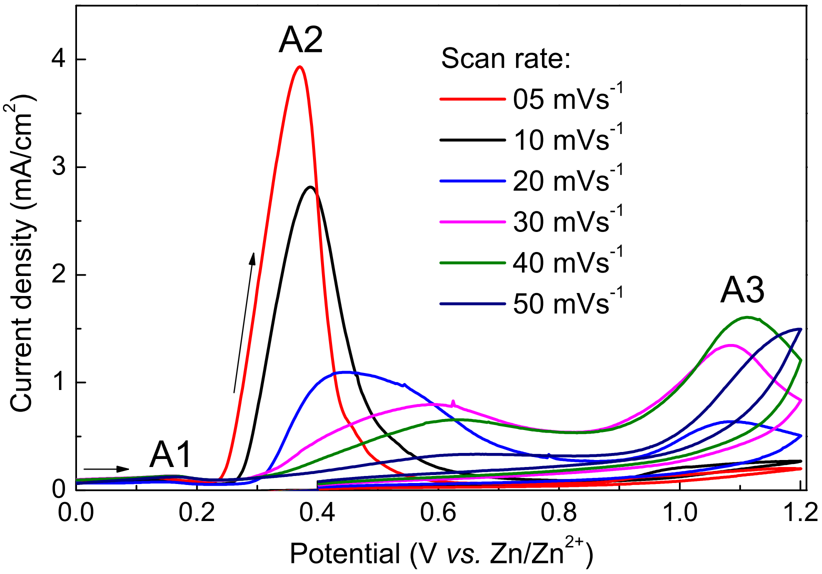

Figure 4.7. Anodic range of the CV from Figure 4.6 on an expanded scale.

Increasing the rotation rate further causes a decrease of the cathodic peak current compared to the CV recorded at 100 rpm, although still with higher peak currents than at the static electrode. The potentials for the forward cathodic peak shift negatively, whereas in the backward scan peak potentials shift positively, as better visualised in Figure 4.9. At $-0.7\,\mathrm{V}$, the current is not significantly affected by the rotation rate. Moreover, the cathodic peak on the backward scan approaches a constant peak current and peak potential (at ca. $-0.1\,\mathrm{V}$) at rotation rates higher than 600 rpm and it does not change significantly with an increase of the hydrodynamic force. It is noteworthy that the current density of the forward peak is much higher than that of the peak on the reverse scan. This is probably due to the increased transport rate of the reducible species into the bulk of the electrolyte by rotating the electrode.

In the anodic range, the increase in rotation rates higher than 300 rpm causes a decrease in current density and a shift on the stripping peak potentials, initially at $+0.4$ to $+0.26\,\mathrm{V}$ *vs.* $\mathrm{Zn/Zn^{2+}}$, pointing out that by rotating the electrode, the reducible species Z are transported into the electrolyte, causing a decrease of the zinc deposition rate.

The coulombic efficiency of the CVs as a function of rotation rate is presented in Figure 4.10. The ratio of the anodic over the cathodic charge substantially decreases from 29 % on the static electrode to 17 % with a rotation rate of 100 rpm and to 11 % for 300 rpm. Increasing the rotation rate further does not affect much the current efficiency. This implies that much of the cathodic current is consumed in side reactions e.g. decomposition of the electrolyte with formation of hydrogen. With convection, more of the hydrogen gas formed can be transported away from the electrode surface avoiding a decrease in current, simultaneously with a higher transport rate of electrolyte species to the electrode surface, favouring their reduction and consequently decreasing the current efficiency.

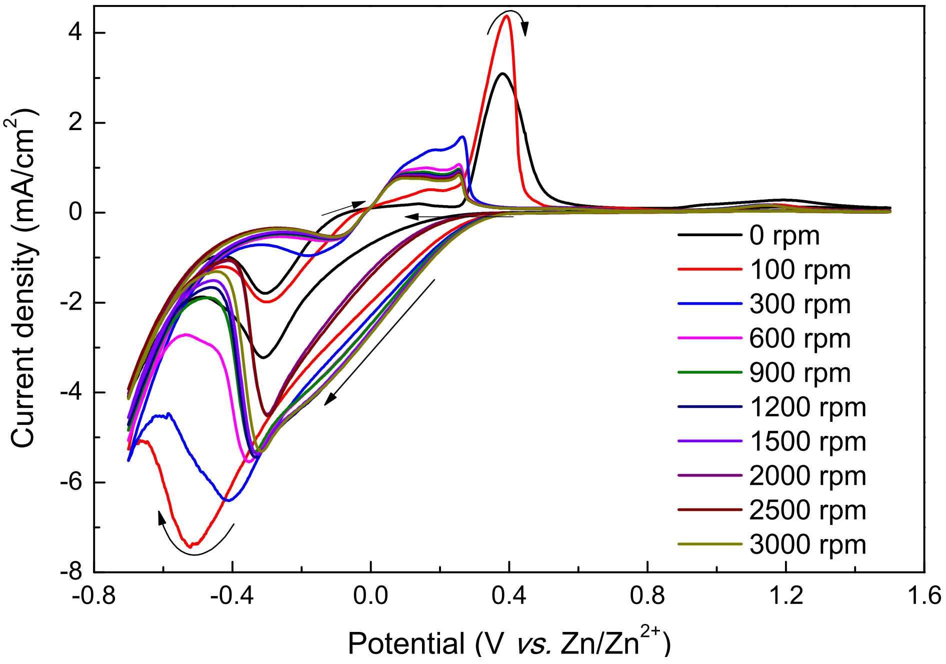

Figure 4.8. RDE cyclic voltammogram of a platinum electrode at different rotation speeds in 0.3 mol·L^{-1} of $ZnCl_2$ in 12CE, 10 mV·s^{-1}, 30 °C, starting from +0.4 V *vs.* Zn/Zn^{2+} with a negative sweep direction. Arrows indicate sweep direction.

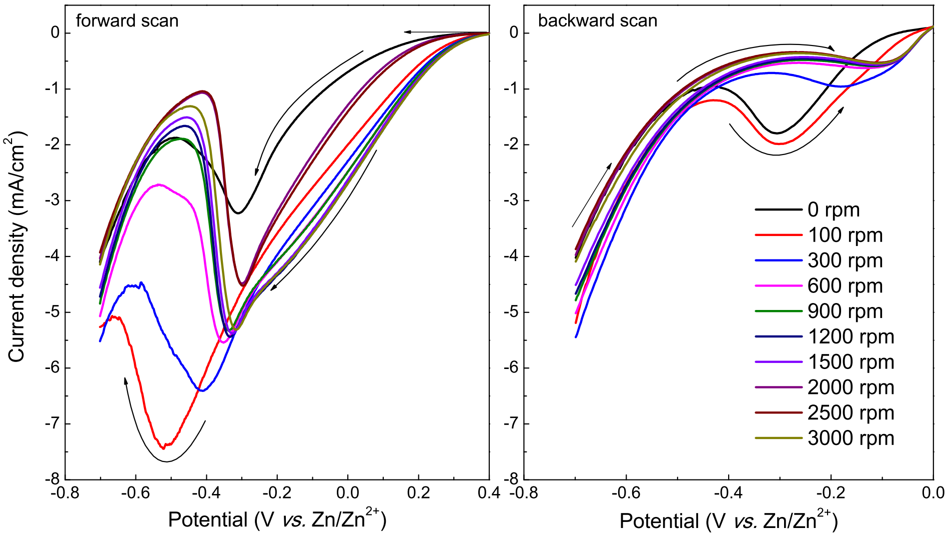

Figure 4.9. Forward and backward peaks assigned for deposition of Zn from the CVs shown in Figure 4.8 (0.3 mol·L^{-1} of $ZnCl_2$ in 12CE, 10 mV·s^{-1}, 30 °C on a Pt-RDE with different rotation rates). Arrows indicate sweep direction.

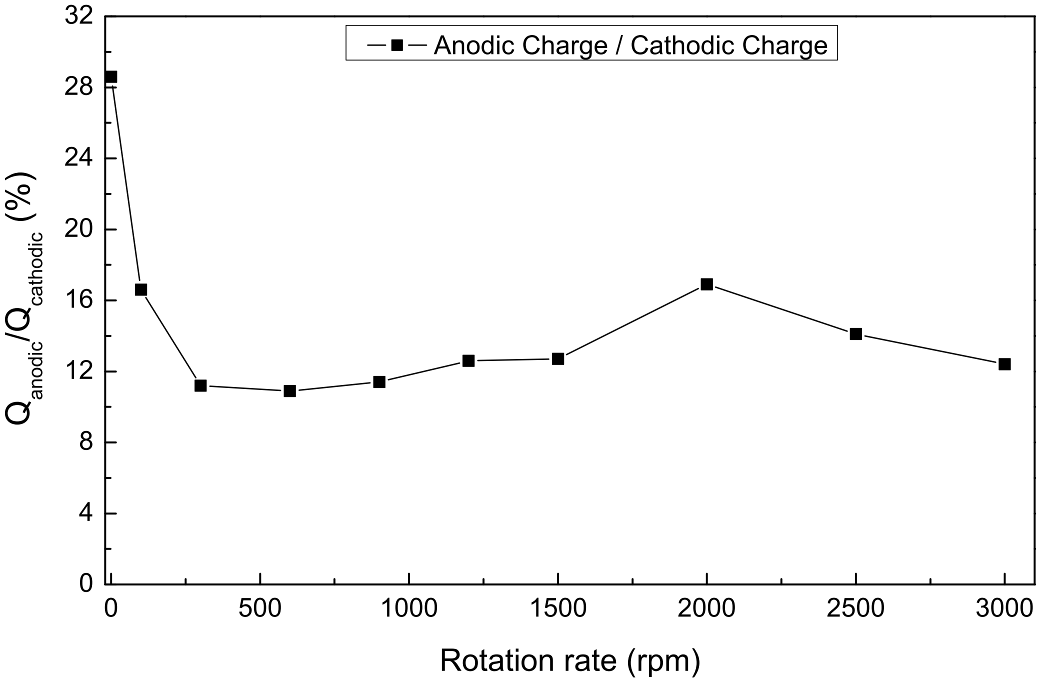

Figure 4.10. Coulombic efficiency versus rotation rate for RDE experiments of 0.3 mol·L^{-1} of $ZnCl_2$ in 12CE on a Pt substrate shown in Figure 4.8.

The voltammetric studies varying the scan rate and the cathodic potential limit revealed that multiple Pt−Zn phases might form during cathodic polarization. For the purpose of investigating the alloying kinetics and the subsequent anodic stripping of Pt−Zn phases, a series of experiments was carried out, in which the potential was held constant at −0.3 V *vs.* Zn/Zn^{2+} for a certain period of time followed by a linear voltammetric scan from −0.3 to +1.8 V. The time at −0.3 V *vs.* Zn/Zn^{2+} was varied from 0 to 200 s, as indicated in Figure 4.11.

A dwell time of 10 to 20 s causes no significant increase in anodic current. Increasing the time to 50 s two anodic peaks appear, indicating alloy formation. For 100 and 200 s, several stripping peaks are observed, which is consistent with the formation of multiple Pt−Zn phases.

Similar experiments for zinc electrodeposition on platinum microelectrodes from 12CE was carried out by Abbott et al. [36], in which it was suggested that the multiple stripping peaks observed were due to bulk and nano-scale growth. However, our results are similar to those obtained by Huang et al. [155], in which linear scan stripping voltammograms from zinc deposited with similar holding times from $ZnCl_2$-EMIMCl on platinum disks also presented multiple anodic waves, which were attributed to bulk-Zn and Zn-alloy stripping. Multiple Pt−Zn phases formation was also observed by Okano and Katagiri [158] for zinc electrodeposition on platinum electrodes from 60 − 40 mol % $ZnCl_2$−NaCl melts at 450 °C. In this study, different alloy phases were obtained depending on the overpotential applied: $\gamma-$PtZn, γ_1-PtZn and γ_2-PtZn, from the less to the more negative potential applied.

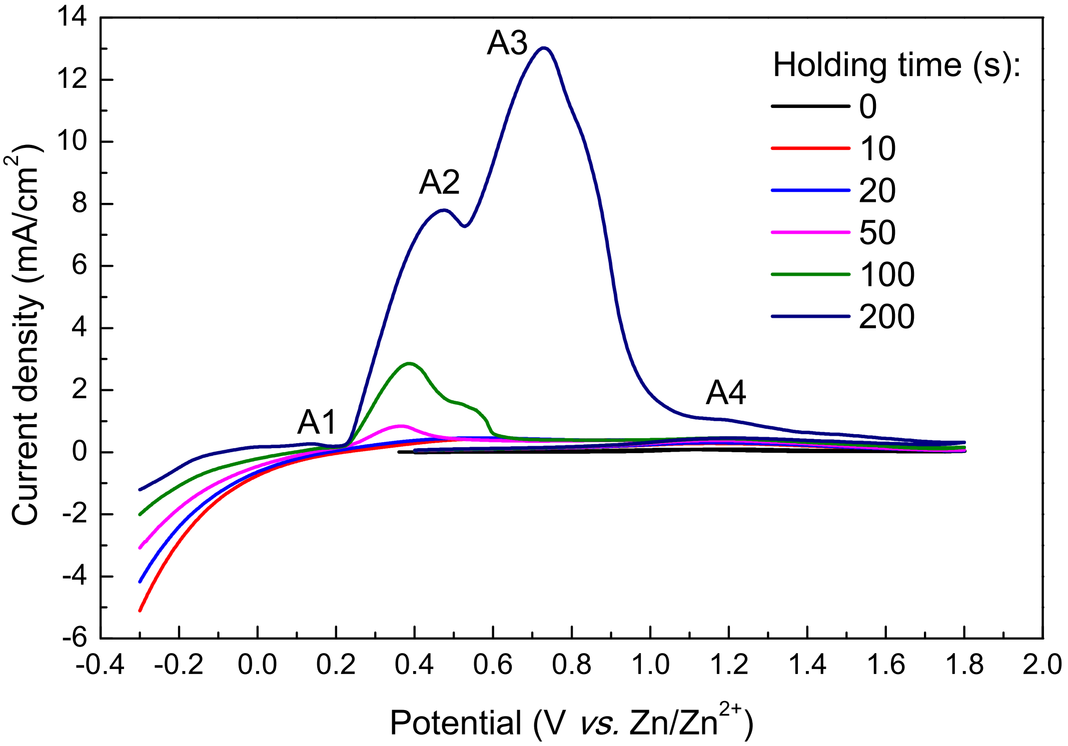

Figure 4.11. Linear sweep voltammetry of 0.3 mol·L^{-1} of ZnCl$_2$ in 12CE on a Pt substrate at 10 mV·s^{-1} starting from -0.3 V *vs.* Zn/Zn^{2+} with a positive sweep direction. The LSV were recorded after several deposition times for a constant-potential step. A1 to A4 indicate anodic peaks.

Raising the temperature from 30 to 60 °C results in an increase in the overall current density of the CV, as shown in Figure 4.12. Such an increase is consistent with the rise in conductivity, as also observed in the previous section for glassy carbon electrodes. Nevertheless, it is remarkable that the forward cathodic peak (marked as C1) increases considerably by increasing the temperature, although the backward peak does not expand so significantly. Moreover, for 50 and 60 °C a third anodic peak (A3) becomes more pronounced. In total, four oxidation peaks are observed. The first anodic peak A1, is attributed to the oxidation of Zn(II) whereas the anodic waves A2, A3 and A4 are ascribed to the oxidation of zinc in different Pt−Zn phases.

The coulombic efficiencies for the CVs recorded at 30, 40, 50 and 60 °C were 33, 62, 75 and 76 %, indicating zinc electrodeposition is favoured by raising the temperature. This result is consistent with the literature, as it has been reported that zinc electrodeposition and effective formation of M−Zn alloys from EMIMCl based ionic liquids are favoured by higher deposition temperatures. This also increases the thickness of the alloy layer, since higher temperatures enhance the surface and bulk diffusion of the metals [6, 155, 156, 165, 166]. Furthermore, studies of anodic dissolution of platinum in a Lewis basic 25:75 mol % $ZnCl_2$/EMIC IL at different temperatures suggested that new anodic reactions can be induced by an increase in temperature when dealloying Pt−Zn compounds [157].

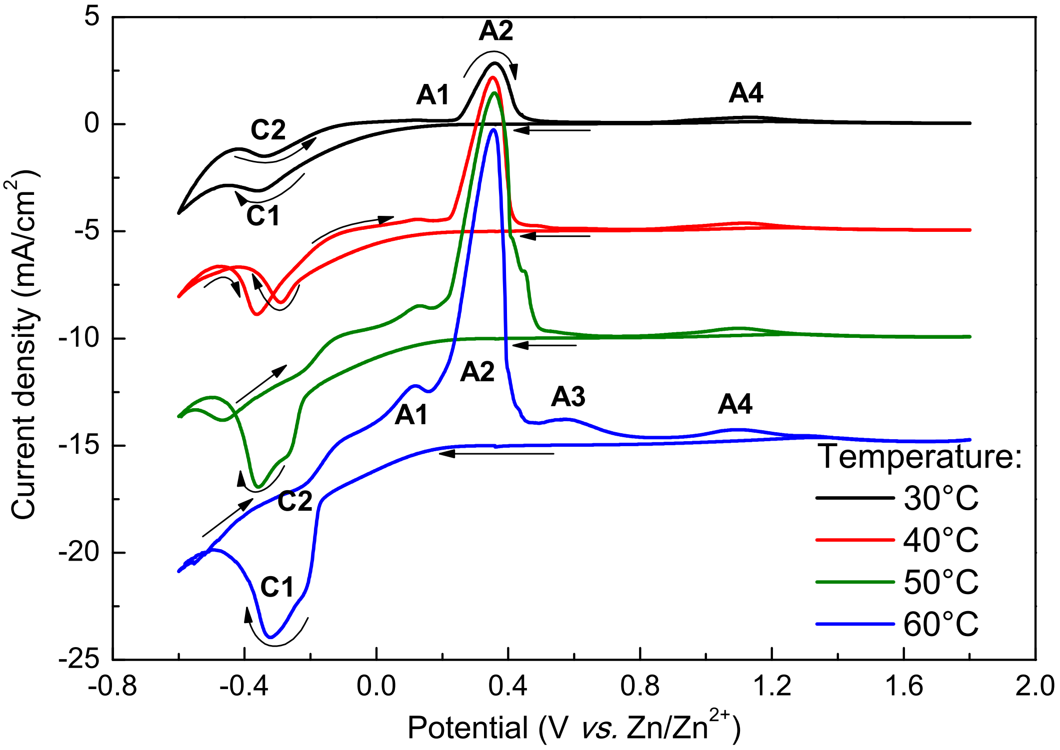

Figure 4.12. Cyclic voltammograms at different temperatures of 0.3 mol·L^{-1} $ZnCl_2$ in 12CE electrolyte at a static platinum electrode at 10 mV·s^{-1} starting from +0.5 V vs. Zn/Zn^{2+} with a negative sweep direction. C and A indicate cathodic and anodic peaks. Arrows indicate sweep directions.

4.1.2 Chronoamperometric studies

Chronoamperometry experiments were performed for the purpose of investigating the nucleation and growth processes of zinc on a platinum substrate in more detail. These experiments were carried out by stepping the potential of the working electrode from an initial value ($E1$) , where no faradaic reaction takes place ($E2 = +0.5\,\text{V}$ *vs.* Zn/Zn^{2+}), to potentials sufficiently negative to initiate zinc nucleation/growth process ($E2$). After each set of data was collected the resulting electrodeposit was anodically stripped from the electrode surface by holding the potential at a value positive enough for the zinc electrodissolution ($E3 = +0.3\,\text{V}$ *vs.* Zn/Zn^{2+}). The complete sequence was then repeated at another deposition potential ($E2$). Typical current-time transients resulting from such experiments on platinum electrodes are shown in Figure 4.13.

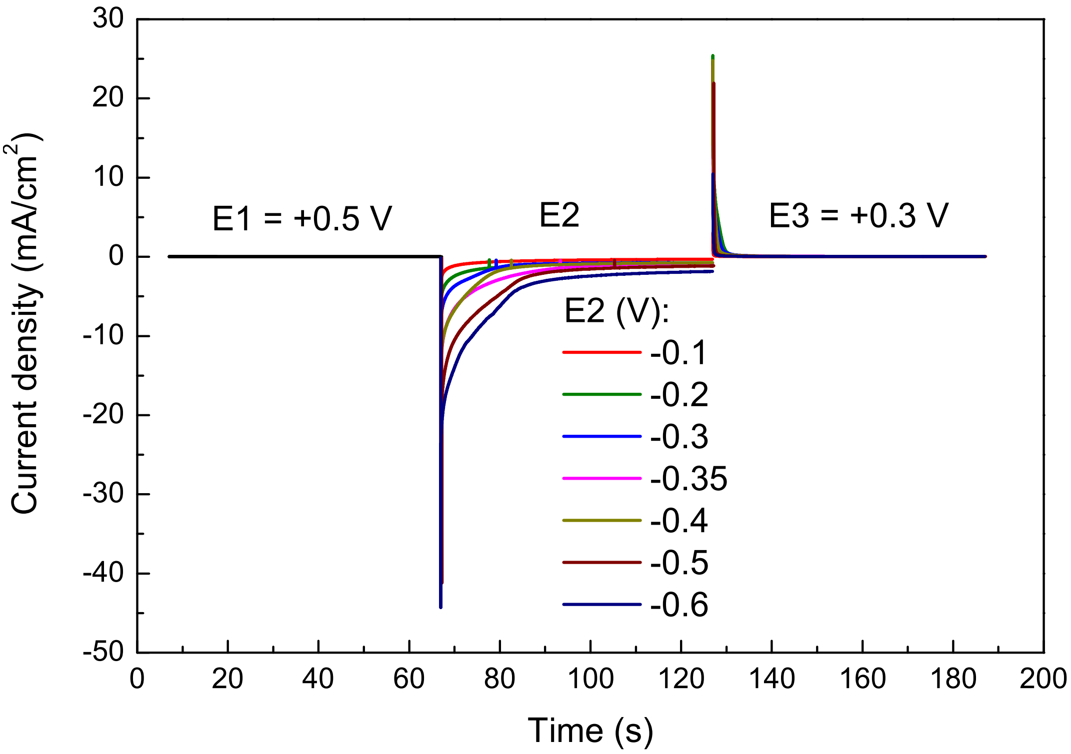

Figure 4.13. Chronoamperometric experiments for $0.3\,\text{mol}\cdot\text{L}^{-1}$ ZnCl_2 12CE on Pt at different potential steps. Applied potentials at $E2$ are indicated.

Stepping from the equilibrium potential $E1$ to a more negative potential $E2$ causes a spike in current due to the capacitive charge, followed by a relatively slow decay in current (from 2 to 15 s). All current transients exhibit limiting currents after about 20 s, as better visualized in Figure 4.14, indicating that at this point the diffusion of species from the bulk of the electrolyte to the electrode surface followed by formation of Z and electrodeposition of zinc from Z occurs at a constant rate. Moreover, the more negative the applied potential, the more the total charge consumed, with exception of the step at $-0.4\,\mathrm{V}$ *vs.* $\mathrm{Zn/Zn^{2+}}$, which had a lower cumulative charge after 60 s than that at $E2 = -0.35\,\mathrm{V}$. It is also noticeable that the limiting current *plateau* does not correspond linearly to the applied potential, as the current *plateau* for the steps at $E2 = -0.35$ and $-0.4\,\mathrm{V}$ *vs.* $\mathrm{Zn/Zn^{2+}}$ are higher than the *plateau* reached for $E2 = -0.5\,\mathrm{V}$. Either the nucleation and growth of zinc is fast at $-0.5\,\mathrm{V}$ and the current decays rapidly, or at $-0.4\,\mathrm{V}$ there might be blocking of the surface by the electrolyte molecules and therefore the electrodeposition of zinc is slower.

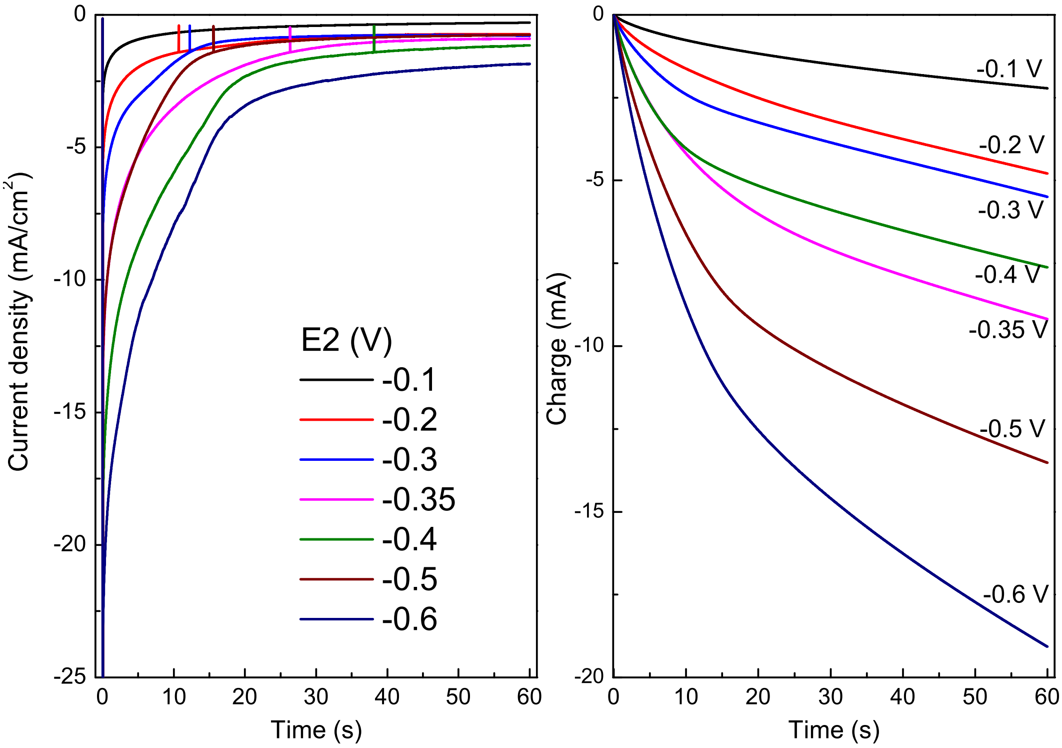

Figure 4.14. Current and charge *versus* time for $0.3\,\mathrm{mol\cdot L^{-1}}$ $\mathrm{ZnCl_2}$ 12CE on Pt at the step $E2$ with the indicated applied potential.

It is noteworthy that in the current-time transients for zinc deposition on platinum at $E2$, no peak which could be correlated to electrocrystallization was observed. The transients do not display Cottrell behavior, due to the intermediate step involved in this reaction, making it not diffusion-controlled only, but dependent on a chemical step before the electron transfer (ECE mechanism). The Cottrell plots for the step $E2$ are presented in Figure 4.15.

The Cottrell plot for the zinc electrodeposition on platinum shows no linearity. The curve shape is significantly different from Cottrell plots obtained from glassy carbon electrodes. This suggests that on this kind of substrate the mechanism is somewhat different, because hydrogen evolution occurs at less negative potentials (near the equilibrium potential) on platinum electrodes.

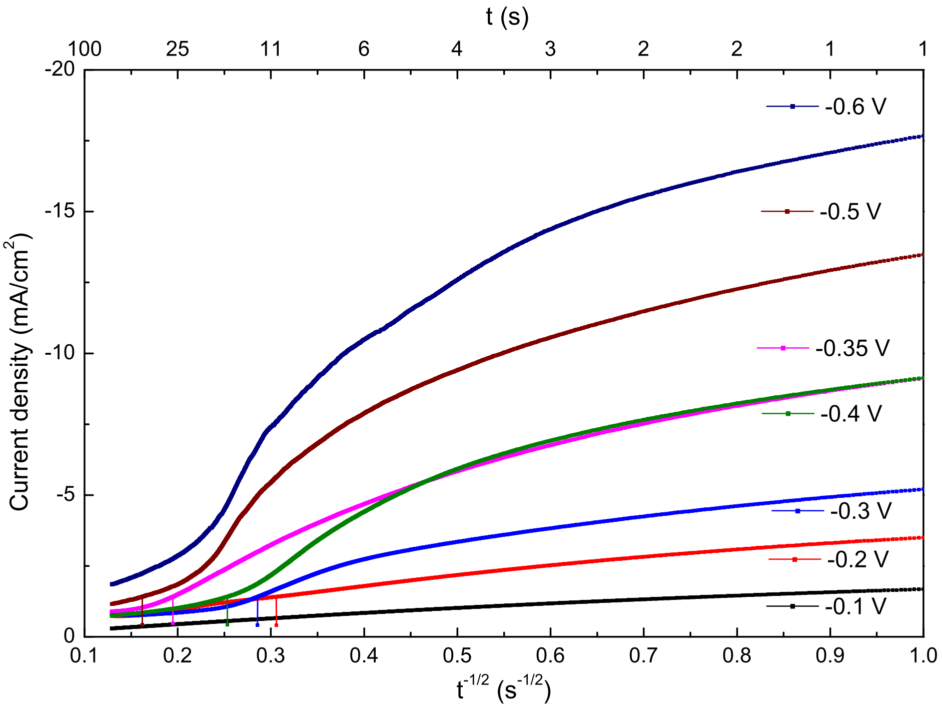

Figure 4.15. Cottrell plot from current-time transients from Figure 4.14 obtained at $E2$ at different potentials on a Pt electrode.

The anodic charge consumed during the oxidation step at $E3 = +0.3\,\mathrm{V}$ (Figure 4.16) does not correlate directly to the charge consumed at $E2$, with exception of the step $E2 = -0.1\,\mathrm{V}$. This had a low cathodic charge and a low anodic charge at $E3$, indicating that this potential was too low to promote the deposition of zinc from the reducible zinc species. On the other hand, by a applying potentials of $E2 = -0.5$ and $-0.6\,\mathrm{V}$, from the anodic charge it is possible to deduce that most of the charge was consumed in side-reactions, i.e. hydrogen evolution. It is also important to mention that the potential applied at $E3$ is positive enough to oxidise the zinc species, however, it might not be enough to oxidise all alloyed zinc. There is a possibility that the PtZn phases formed at $E2 = -0.5$ and $-0.6\,\mathrm{V}$ are not oxidized at $E3 = +0.3\,\mathrm{V}$, but would require a higher anodic polarization. For $E2 = -0.2\,\mathrm{V}$ the highest anodic charge was recorded. It is likely that for this potential, mostly zinc is deposited, which can easily be redissolved in the deep eutectic. The ratio of anodic over cathodic charge can be better visualized in the plot of coulombic efficiency *versus* $E2$ presented in Figure 4.17. It can be seen that there is a slow decay in coulombic efficiency when decreasing the potential from -0.2 to $-0.3\,\mathrm{V}$. Nevertheless, the step at $-0.35\,\mathrm{V}$ *vs.* $\mathrm{Zn/Zn^{2+}}$ was associated with a CE of 7 %, which increased to 11 % for $E2 = -0.4\,\mathrm{V}$.

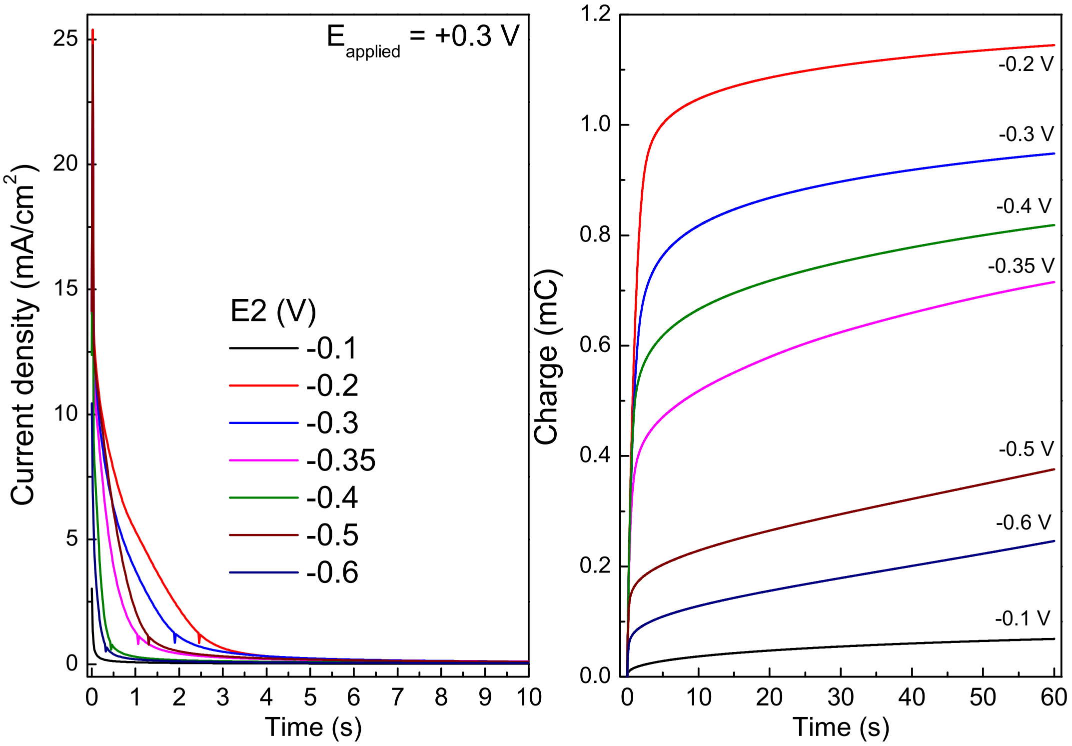

Figure 4.16. Current and charge *versus* time from $0.3\,\mathrm{mol{\cdot}L^{-1}}$ $ZnCl_2$ 12CE on Pt at the step $E3 = +0.3\,\mathrm{V}$. The anodic current and charge are related to the indicated previous step $E2$.

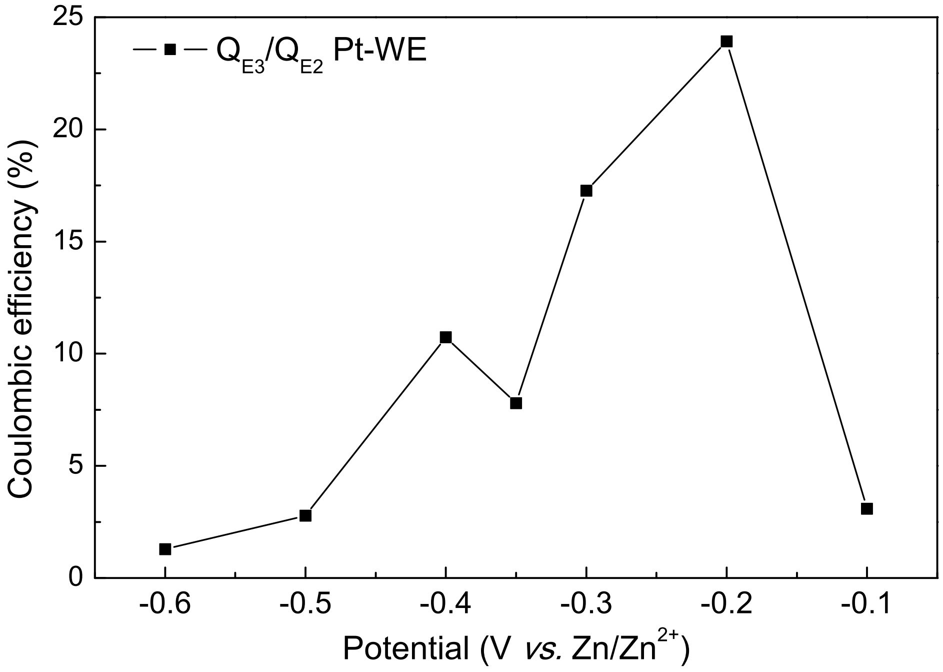

Figure 4.17. Coulombic efficiency of 3-step chronoamperometric experiments with $0.3\,\mathrm{mol{\cdot}L^{-1}}$ $ZnCl_2$ in 12CE on a platinum disk working electrode at 30 °C.

Figure 4.18 displays a sampled voltammogram constructed from a series of transients acquired at different potentials from the deep eutectic electrolyte 12CE with and without zinc chloride. The resulting sampled voltammograms exhibit an increase of the charge by decreasing the applied potential for both electrolytes. Nevertheless, for potentials $\leq -0.2\,\mathrm{V}$ *vs.* $\mathrm{Zn/Zn^{2+}}$ the cumulative charge is substantially higher for the solution without zinc compared to that containing $0.3\,\mathrm{mol{\cdot}L^{-1}}$ of $ZnCl_2$, due to the lower overpotential for hydrogen evolution on platinum compared to that on the zinc-plated substrate. Since zinc is electrodeposited on platinum in the electrolyte containing $ZnCl_2$, the overpotential for hydrogen evolution increases at the same time decreasing the charge consumed for that reaction.

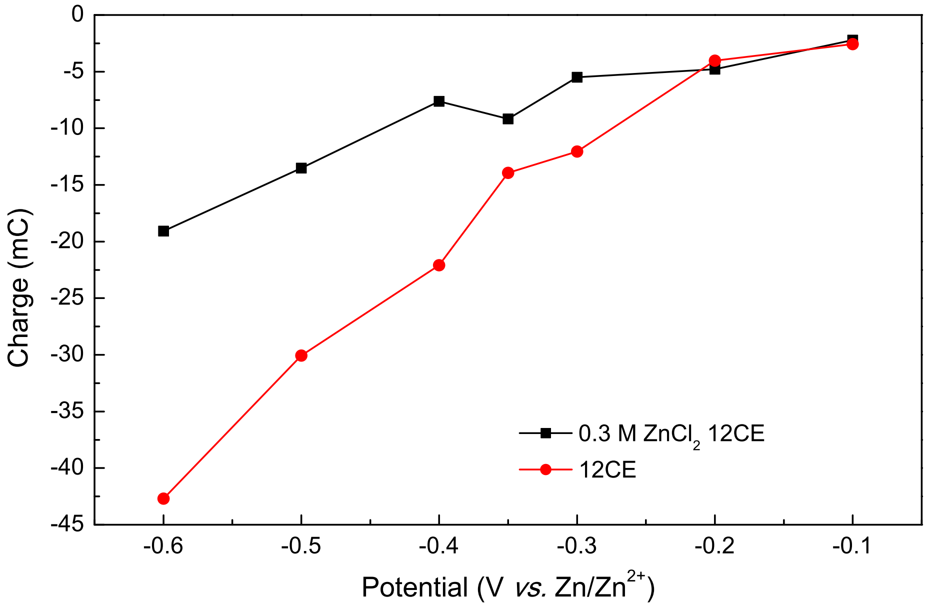

Figure 4.18. Sampled voltammogram contructed from cumulative charge *vs.* time transients from 12CE electrolytes with and without $0.3\,\mathrm{mol{\cdot}L^{-1}}$ of $ZnCl_2$ on a platinum electrode at 30 °C.

4.1.3 Characterization of zinc deposits on platinum

Bulk electrodeposits of zinc were prepared on (1 cm × 1 cm) platinum foils by potentiostatic electrolysis at $-0.3\,\mathrm{V}$ *vs.* $\mathrm{Zn/Zn^{2+}}$ for 2800 s, which would lead to a zinc deposit of 2 μm thick (each side), based on Faraday's law and assuming 100 % coulombic efficiency [167]. In the chronoamperometric experiments, the current first increased to a peak and after 400 s it reached a steady-state with a constant current of 3.10 mA. The electrodeposited samples were taken off the glovebox, washed with water and acetone, dried in air and examined by optical microscopy (OM), scanning electron microscopy (SEM), focused ion beam (FIB) and X-ray diffraction (XRD).

Morphology and composition characterization

The deposited zinc had a dark gray colour and poor adhesion on the platinum substrate, as it could be easily removed by scratching. A picture of a coated together with a non-coated platinum foil and optical microscopy of the deposit is presented in Figure 4.19. Optical microscopy shown in Figure 4.19, reveals the presence of surface defects, in the form of white pores, probably caused by the concurrent hydrogen evolution during zinc electrodeposition.

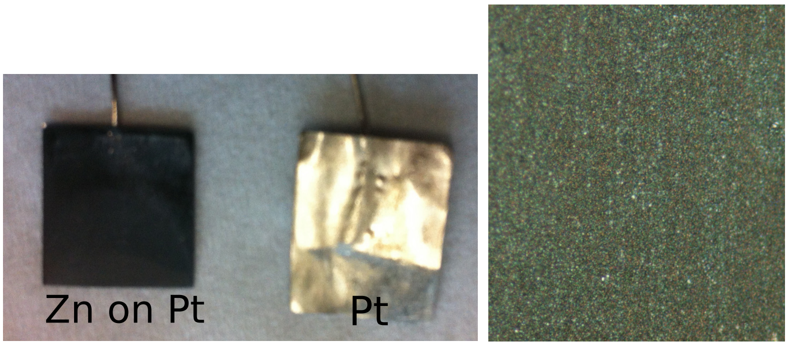

(a) Zinc coated and non-coated Pt foils (b) 50× magnification OM

Figure 4.19. a) Photography and b) optical microscopy (OM) with a magnification of 50× of a zinc-coated Pt foil.

SEM micrographs of the zinc deposit presented in Figure 4.20 reveal a nanostructured surface, which is consistent with the dark color of the deposit [156]. The surface morphology in Figure 4.20 a shows that the zinc deposited on platinum has a nano-platelet morphology, which is remarkably homogeneous throughout the analysed region (100 × 120 $\mu\mathrm{m}^2$). Scanning electron microscopy of other regions of this sample and of a second sample (not shown) showed precisely the same surface morphology. Increasing the magnification as shown in Figure 4.20 b and c reveals that the platelets have ca. 10 nm thickness. EDX composition analysis of the Figure 4.20 d reveal the presence of both Pt and Zn in the sample, besides oxygen, which is probably due to the formation of zinc oxide or to residual electrolyte in the pores.

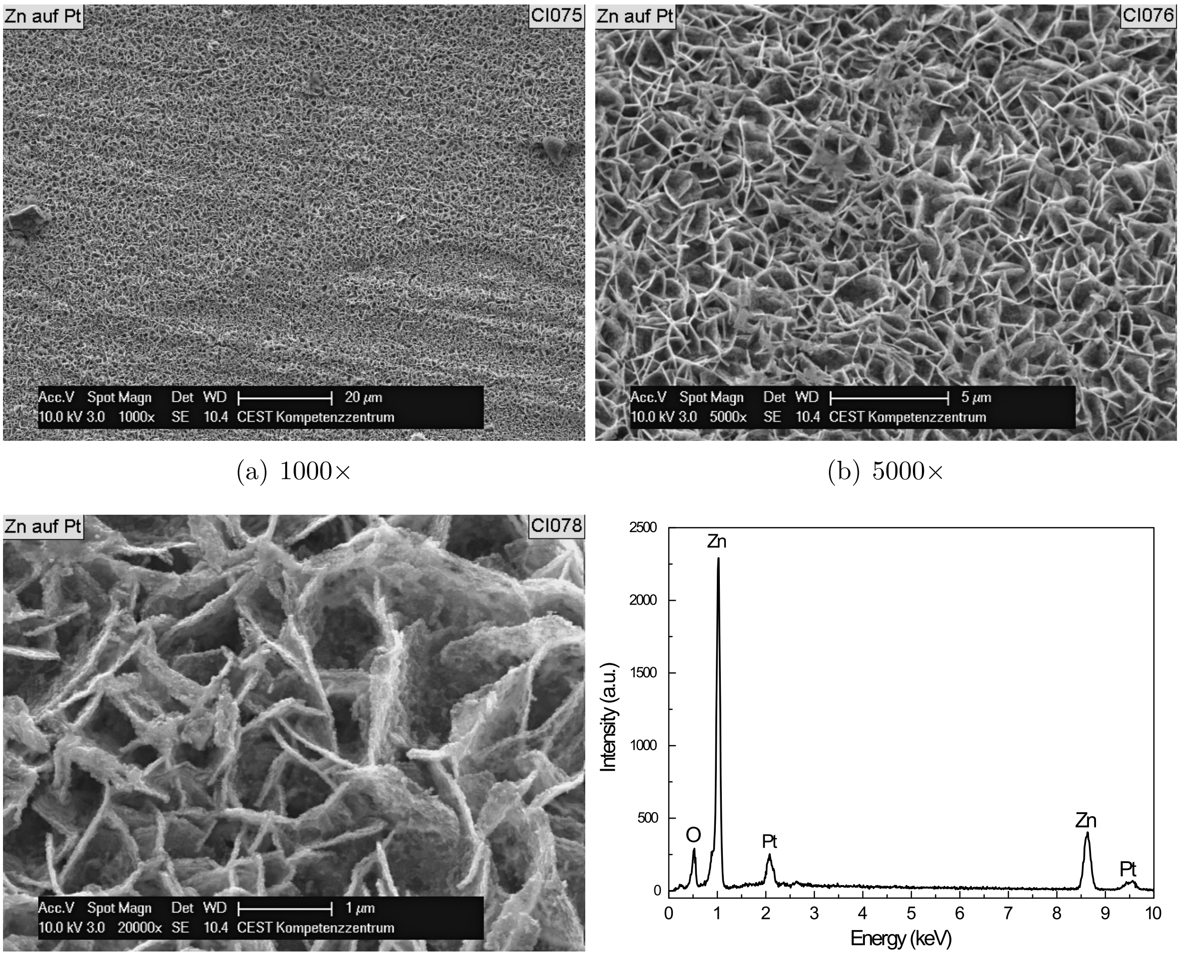

(a) 1000×

(b) 5000×

(c) 20000×

(d) EDX

Figure 4.20. a)–c) SEM micrographs of zinc deposits on platinum foil substrates with different magnifications and d) EDX plots for surface composition analysis. The deposits were produced in $0.3\,\mathrm{mol{\cdot}L^{-1}}$ $ZnCl_2$ 12CE at 30 °C at $-0.3\,\mathrm{V}$ *vs.* Zn/Zn^{2+}.

Micrographs of a cross section of the deposit milled by a gallium ion source in a focused ion beam (FIB) microscope is presented in Figure 4.21. Differently from the secondary electrons (SE) imaging in SEM, the contrast in ion imaging in FIB reveals chemical differences of the sample [168]. FIB-cuts shown in Figure 4.21 a and b reveal the presence of two different phases, from the bottom to the top of the foil there is firstly pure platinum, followed by a brighter layer, which is likely to consist of Pt−Zn intermetallics. The third and slightly darker phase on the top corresponds to a sputtered Pt film for FIB machining. The middle Pt−Zn layer has a thickness of ca. 1.3 μm.

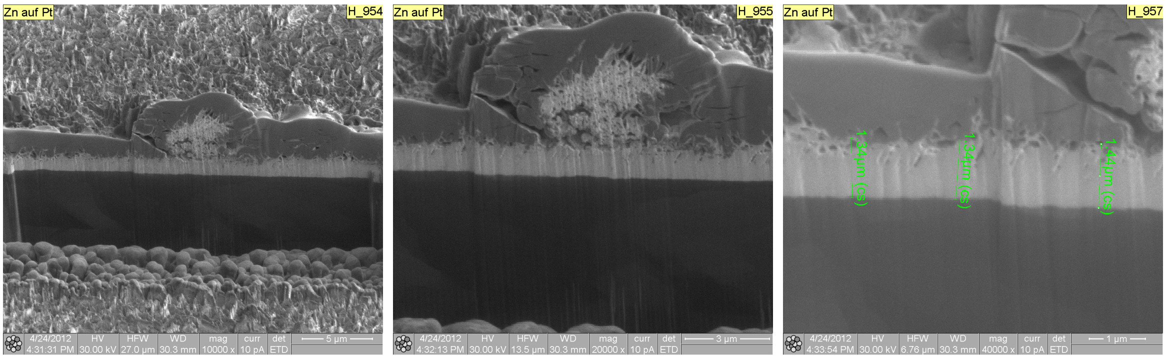

(a) (b) (c)

Figure 4.21. FIB micrographs of a cross-section of a zinc deposit on platinum foil with different magnifications. The deposits were produced in 0.3 mol·L^{-1} $ZnCl_2$ 12CE at 30 °C at −0.3 V *vs.* Zn/Zn^{2+}.

EDX composition analysis of the three different phases in the cross section of the sample (Figure 4.22) reveal the composition of the phases. The upper layer is composed of 72 wt % Zn and 19 wt % Pt (wt = weight %), confirming that also the surface of the coating is composed mainly of Pt−Zn alloy and not pure metallic zinc, although it is present in a higher proportion. The composition of the intermediate layer (indicated as spot Y901 in Figure 4.22a) calculated from EDX measurements indicated 32 % of zinc and 67 % of platinum. The EDX analysis in spot Y902 on the foil confirmed 100 % of Pt composition. Besides, it is also possible to observe the grain boundary contrast of the platinum foil in the backscattered electrons image of Figure 4.22 a. It is noteworthy that the intermediate alloy layer is more compact, whereas the upper layer is quite porous.

The EDX composition analysis of the zinc coating on a platinum substrate is in agreement with the results obtained by cyclic voltammetry, which indicated the formation of multiple Pt−Zn phases. Moreover, it is also in agreement with the literature description for zinc deposition on platinum from ionic liquids [155, 156].

Porous platinum and its alloys are of interest due to their potential application in catalysis [156, 169–171], fuel cells [172] and chemical sensors [157, 173, 174]. Nanoporous platinum electrodes fabricated in by electrochemical dealloying of PtZn in ionic liquids have already been tested for electro-oxidation of methanol and showed a much higher current density than on polished platinum electrodes [156, 172].

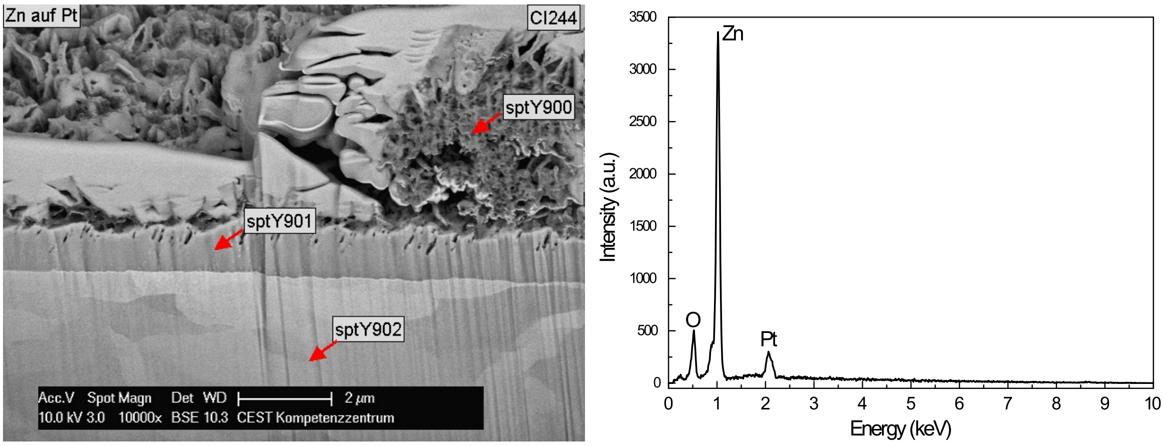

(a) SEM image (b) spot Y900

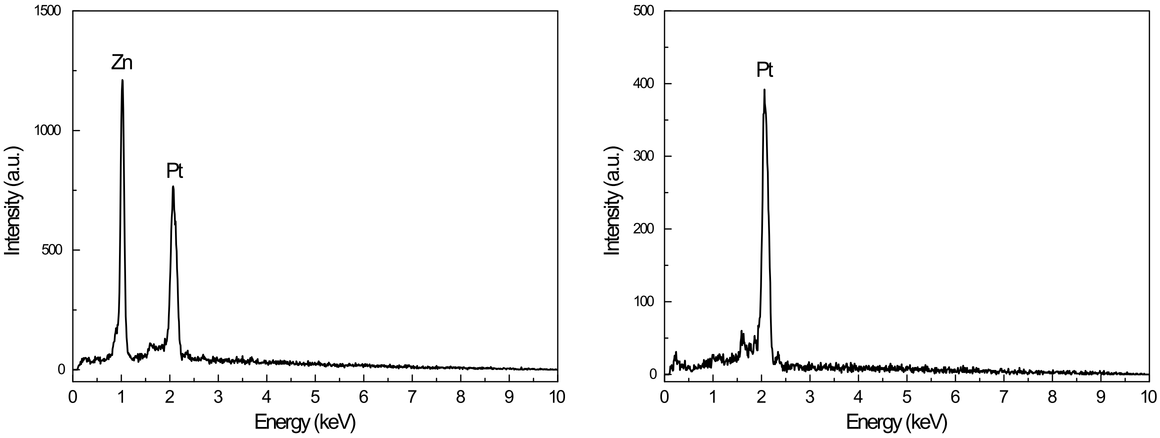

(c) spot Y901 (d) spot Y902

Figure 4.22. a) Scanning electron micrograph of a zinc deposit cross section on platinum foil. b), c) and d) EDX plots obtained from the spots indicated in image a).

Phase characterization

The X-ray diffractogram of the electrodeposited zinc on platinum foil measured in GIXD geometry with an incidence angle of 2° is presented in Figure 4.23. Qualitative XRD analysis revealed the presence of three crystalline phases: Pt, Zn and Pt_7Zn_{12}. These results are consistent with the cyclic voltammetric and EDX measurements, which indicated that the deposit consists of a mixture Pt−Zn intermetallics and zinc.

The Pt reflexes are slightly shifted to lower angles in comparison with the theoretical positions obtained from platinum powder samples. This could indicate a distortion of the Pt crystal lattice due to the incorporation of the Zn atoms to form a solid solution.

Quantitative Rietveld refinement analysis revealed that the Pt_7Zn_{12} phase had a relative weight fraction of 29 ± 1 *wt* % and a crystallite size of 9 ± 1 nm. Pure platinum and zinc phases presented a weight fraction of 4 ± 1 *wt* % and 67 ± 1 *wt* % with a crystallite size of 7 ± 1 nm and 8 ± 1 nm, respectively.

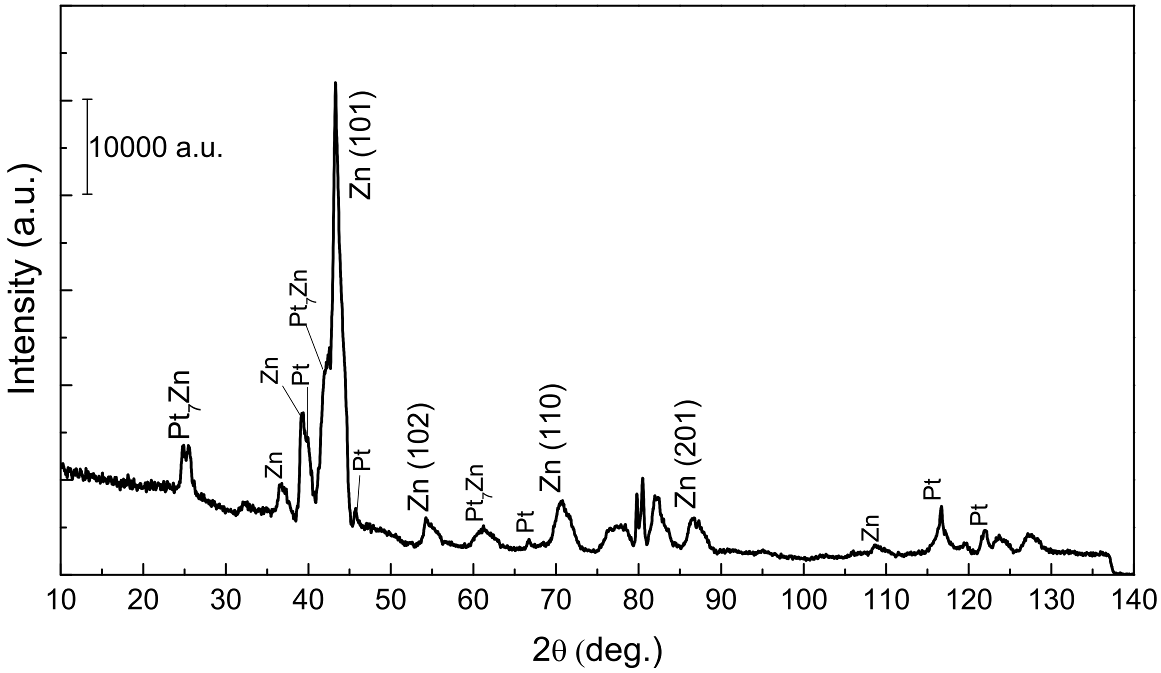

Figure 4.23. X-ray diffraction patterns of electrodeposited zinc at platinum substrates from 0.3 mol·L^{-1} $ZnCl_2$ 12CE at 30 °C.

4.1.4 Partial conclusions

The electrodeposition of Zn on Pt electrodes from a choline-based deep eutectic solvent led to the formation of PtZn alloys. The mechanism of zinc electrodeposition on platinum is similar to that on glassy carbon, as zinc is reduced from intermediate species Z with the formula $[ZnCl_{(4\text{-}x)}(RO)_x]^{2-}$. However, as hydrogen evolution takes place at exceptionally low overpotentials on Pt, Z is formed already during the forward scan and deposition of zinc occurs at potentials of ca. −0.2 V *vs.* Zn/Zn^{2+} on the forward and backward sweep. Zinc is incorporated into the platinum surface on the time-scale of a cyclic voltammetric scan at 10 mV·s^{-1} sweep rate.

Multiple stripping peaks observed by cyclic voltammetry indicated the formation of multiphasic Pt−Zn compounds. EDX of a cross-section of the coating on a platinum foil confirmed the formation of two different phases, Pt−Zn alloy. XRD of the deposit revealed the typical pattern for the Pt_7Zn_{12} phase. SEM and FIB micrographs showed that the zinc deposits have a nanostructured surface morphology with the shape of nanoplatelets.

The results presented in this section indicate that Pt electrodes can be modified by direct electrochemical surface alloying with zinc using a deep eutectic electrolyte. Such materials may have several applications in electrocatalysis and for sensors. Therefore, the results of this study may provide a simple way to prepare a Pt−Zn catalyst.

4.2 Zinc deposition on gold

4.2.1 Voltammetric studies

The voltammetric behavior of the deep eutectic solvent 12CE containing $ZnCl_2$ on gold electrodes was investigated. A representative cyclic voltammogram at a scan rate of $10\,mV{\cdot}s^{-1}$ is shown in Figure 4.24. The cyclic voltammogram started from open circuit potential at $+0.9\,V$ *vs.* Zn/Zn^{2+} with a negative direction.

Compared to platinum electrodes, gold ones have higher overpotential for hydrogen evolution. Nevertheless, the reduction of ROH (ROH = EG and ChCl, Equation 3.9) to form hydrogen starts at a quite low overpotential ($-0.3\,V$) also with formation of bubbles at the electrode surface, similarly to platinum. It can be seen that the 12CE electrolyte exhibits an electrochemical stability window ranging from $-0.4\,V$ to at least $+1.2\,V$ *vs.* Zn/Zn^{2+} at a gold substrate. Since gold electrodes can easily be dissolved in highly concentrated chloride solutions [175], the potential range was not extended further into the anodic region.

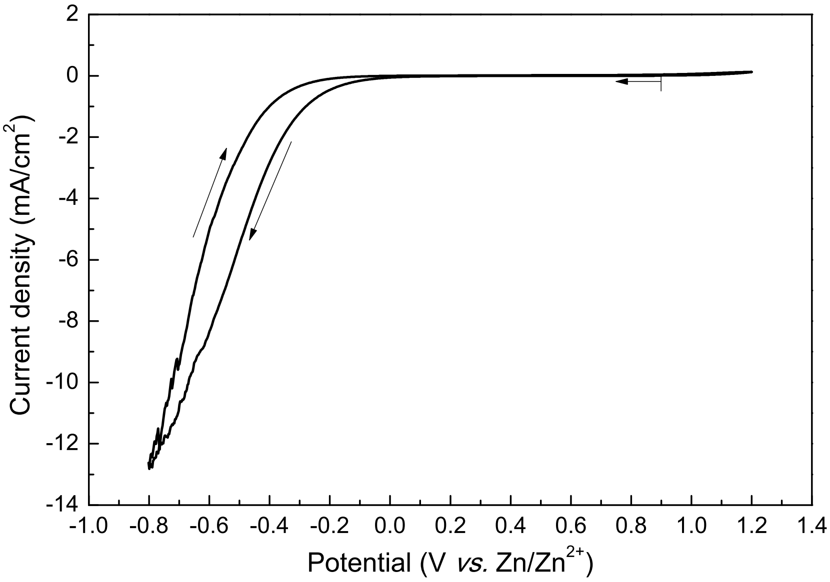

Figure 4.24. Background cyclic voltammogram of 12CE at $10\,mV{\cdot}s^{-1}$ using a gold working electrode at 30 °C.

Figure 4.25 shows the cyclic voltammogram of 12CE containing $0.3\,mol{\cdot}L^{-1}$ $ZnCl_2$ at a gold substrate. Differently from glassy carbon and similarly to platinum, a clear cathodic peak is observed at $-0.25\,V$ *vs.* Zn/Zn^{2+} (C1) already on the forward cathodic scan. During the subsequent anodic return sweep, another cathodic peak is observed at $-0.24\,V$ *vs.* Zn/Zn^{2+} (C2) with a larger peak current. At positive potentials of the anodic scan, three different anodic peaks were observed at $+0.15$, $+0.40$ and $+0.72\,V$ *vs.* Zn/Zn^{2+}

(A1, A2 and A3). From the phase diagram of gold and zinc, presented in Figure 4.26, it can be seen that zinc forms many intermetallic phases with gold, which is likely to be the reason for the presence of multiple anodic peaks in the CV.

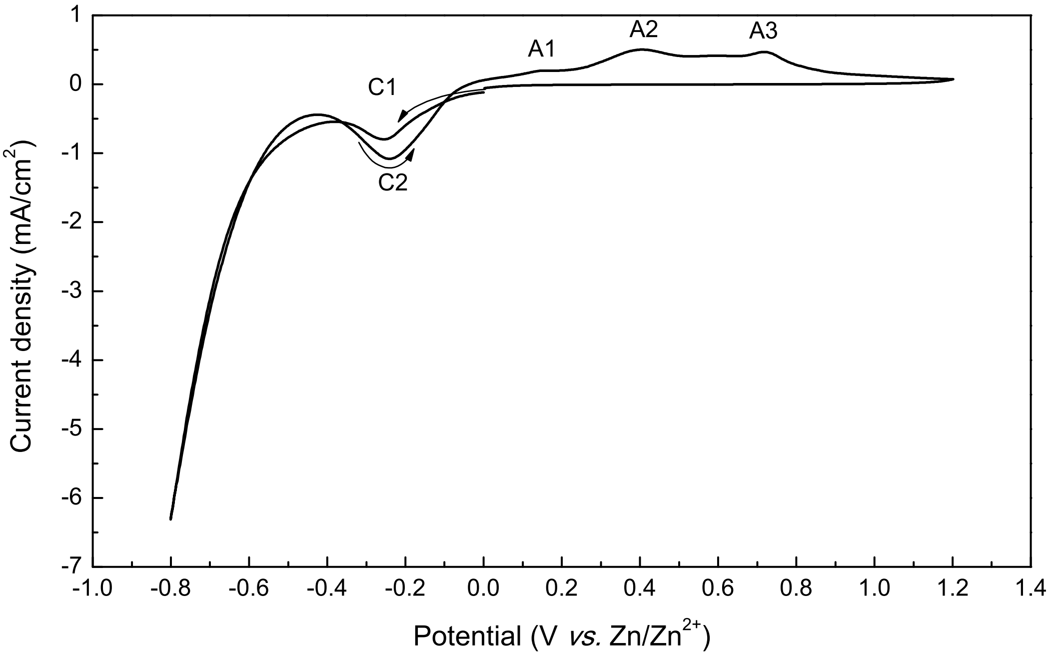

Figure 4.25. Cyclic voltammograms of 0.3 mol·L^{-1} $ZnCl_2$ in 12CE electrolyte on a stationary gold disc electrode (10 mV·s^{-1}, 30 °C) starting from +0.9 V *vs.* Zn/Zn^{2+} with a negative sweep direction. Arrows indicate sweep direction.

Comparing the CVs for 0.3 mol·L^{-1} $ZnCl_2$ 12CE on gold with that on glassy carbon (Chapter 3), which exhibits only one main stripping peak at the anodic side (no alloy formation), it is suggested that the first anodic peak at +0.15 V (A1) is due to the oxidation of zinc, whereas the second and third peaks on +0.40 (A2) and +0.72 V *vs.* Zn/Zn^{2+} (A3) are related to the dissolution of zinc from Au–Zn intermetallics.

Multiple anodic peaks due to the formation of Au–Zn alloys by the incorporation of zinc atoms onto gold electrodes during cyclic voltammetry has been described for $ZnCl_2$ in $AlCl_3$-EMIC ionic liquids [22, 25, 177], lewis acidic $ZnCl_2$-EMIMCl [165] and $ZnCl_2$-BIMIC [26]; zinc triftalate ($Zn(TfO)_2$) in 1-butyl-1-methylpyrrolidinium trifluoromethylsulfonate ($[Py_{1,4}]$TfO) and [EMIM]TfO [33], as well as from organic solutions of $ZnCl_2$ in benzyl alcohol [178]. Additionally, Au–Zn alloy formation has been reported for aqueous zinc sulphate [162] and alkaline zincate solutions [179]. Nevertheless, in none of the studies a cathodic peak on the anodic scan has been reported.

Borisenko et al. [112] have carried out *in situ* STM studies of gold interfaces with the RTIL 1-butyl-1-methylpyrrolidinium bis(trifluoromethylsulfonyl)imide ($[BMP]Tf_2N$) containing 0.1 mol·L^{-1} of $SiCl_4$. In the presence of the chloride silicon salt a cathodic

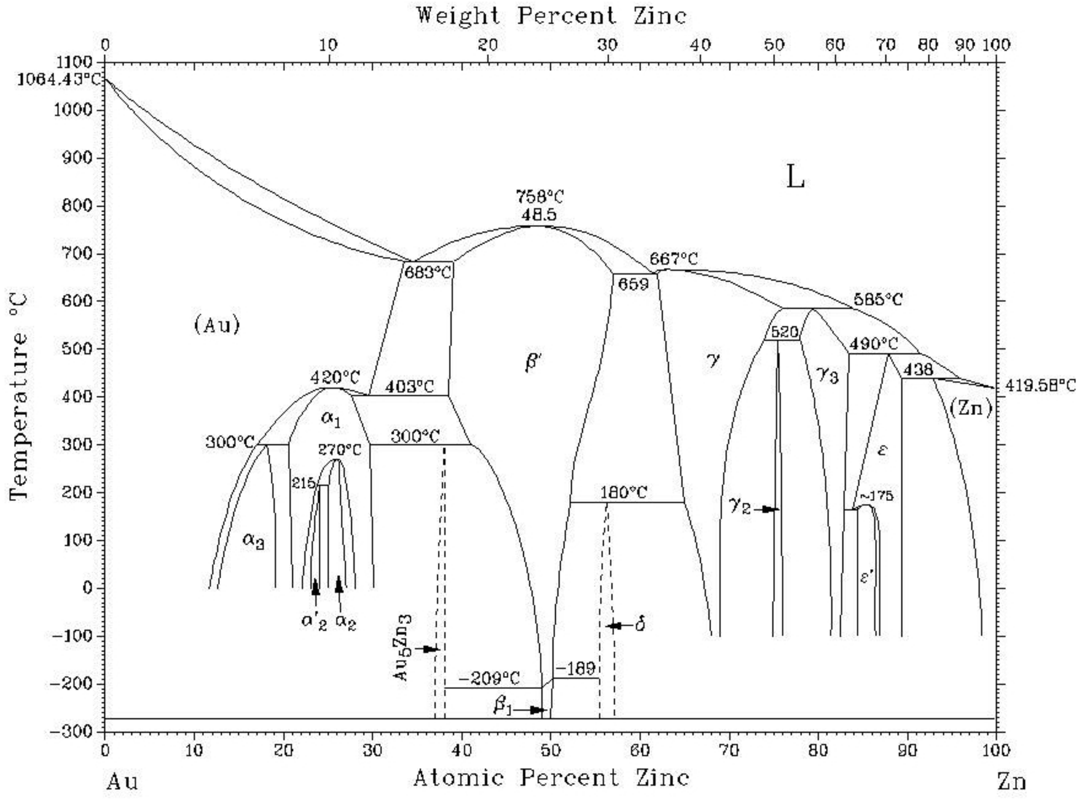

Figure 4.26. Au−Zn binary phase diagram [176].

peak was observed during the reverse scan, indicating passivation of the Au surface. However, no correspondent oxidation peak was attributed to the backward cathodic peak. Infrared spectroscopy investigations indicates that apparently, different silicon complexes are formed [180]. STM, AFM and EIS also reveals that the assembly of the ionic liquid at the interface may interfere with the electrochemical behavior of the species in solution [70, 110].

The mechanism of zinc deposition from 12CE on glassy carbon electrodes involves the formation of intermediate species Z by replacement of chloride ions in $[ZnCl_4]^{2-}$ by RO^-. On such non-metallic electrodes, this reaction only happens at potentials $\leq -0.6\,V$ *vs.* Zn/Zn^{2+}. However, the electrode surface is blocked by strongly adsorbed Ch^+ ions and electrodeposition of zinc occurs on the backward sweep at $-0.15\,V$, when the adsorbate layer desorbs. At platinum electrodes, the reduction of the electrolyte is observed at relatively low overpotentials ($\leq -0.2\,V$ *vs.* Zn/Zn^{2+}), giving rise to a cathodic peak on the forward scan at $-0.3\,V$. On gold electrodes, two effects play a role: firstly, the reduction of the electrolyte at a relatively low overpotential leads to the formation of Z and a cathodic peak on the forward scan, similarly to platinum.

Secondly, quaternary ammonium electrolytes may adsorb strongly at gold substrates, forming a close-packed monolayer [113]. Thus, due to the adsorption of Ch^+ ions on gold, the current density decreases at $E \leq -0.3\,V$, followed by a reduction of ROH at $E \leq -0.6\,V$ *vs.* Zn/Zn^{2+}. At this point, the concentration of the Z on the diffusion layer increases, but the electrodeposition is hindered by the blocking layer. When depletion of choline cations occurs, at the backward scan, another cathodic peak with a higher peak current arises at $E = -0.24\,V$.

The current efficiency calculated from the total anodic charge over the total cathodic charge of the CV in Figure 4.25 is 15 %, which is rather low, indicating parasitic reactions in the cathodic range. Nonetheless, the current efficiency calculated from the ratio of the total anodic charge over the integration of the peaks C1 plus C2 is 78 %, confirming that most of the zinc was deposited between 0 and −0.4 V and that in this region there is also reduction of the electrolyte, decreasing the efficiency.

The effect of the cathodic switching potential on the forward and backward reduction peaks was investigated. The cathodic potential limit was increased from −0.8 V to −0.7, −0.6 and −0.4 V *vs.* Zn/Zn^{2+} (Figure 4.27). The forward peak C1 did not change significantly, whereas the peak current of the backward peak C2 decreased remarkably with less negative cathodic switching potentials. A similar decay in current density is observed for the anodic peaks. This voltammetric behavior is consistent with the suggestion that C2 originates from the reduction of Z and the concentration of Z in the diffusion layer increases when sweeping to more negative potentials.

The current efficiency for the three scans calculated from the total anodic charge over the sum of the area from C1 and C2 were 78, 89 and 93 % for −0.4, −0.6 and −0.7 V *vs.* Zn/Zn^{2+}, respectively.

The scan rate effect on the Zn deposition at a gold substrate is shown in Figure 4.28. Differently from platinum electrodes, in which the kinetics of surface alloying is relatively slow, Zn deposition on gold shows a considerably faster kinetics, as the peak currents increase with increasing scan rate. Even for scan rates as fast as $100\,mV{\cdot}s^{-1}$, Au−Zn surface alloying can be detected by the presence of multiple anodic peaks. Moreover, when scanning at faster sweep rates, the forward peak C1 is shifted to more negative potentials, whereas the C2 peak potential is not much affected by the scan rate.

The current efficiency calculated from the total anodic charge over the charge of C1+C2 for the CVs with 10, 50 and $100\,mV{\cdot}s^{-1}$ scans rates were 75, 87 and 82 %, respectively. Efficiencies below 100 % indicate parasitic reactions in these cathodic potential regions, e.g. reduction of the electrolyte to form hydrogen.

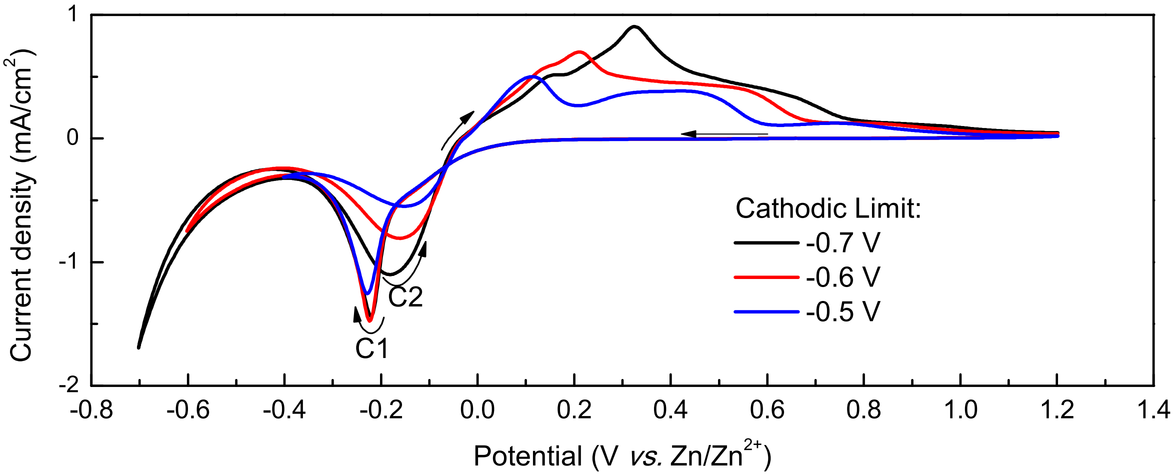

Figure 4.27. Cyclic voltammograms of 0.3 mol·L^{-1} $ZnCl_2$ in 12CE electrolyte on a stationary gold disc electrode (10 mV·s^{-1}, 30 °C) starting from 0.9 V *vs.* Zn/Zn^{2+} with a negative sweep direction, with different cathodic limits. Arrows indicate sweep direction.

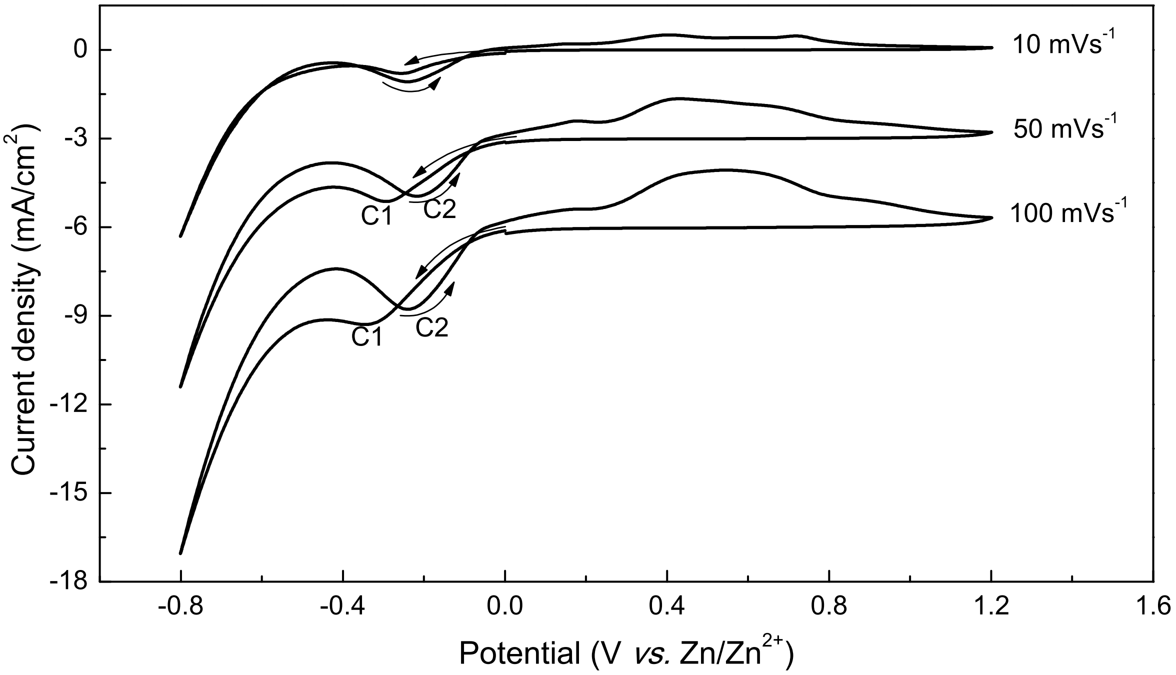

Figure 4.28. Cyclic voltammograms of 0.3 mol·L^{-1} $ZnCl_2$ in 12CE electrolyte at a stationary gold disc electrode at 30 °C starting from 0 V *vs.* Zn/Zn^{2+} with a negative sweep direction and different scan rates. Arrows indicate sweep direction.

Borissov et al. [26] investigated the electrodeposition of Zn on a gold substrate from a $ZnCl_2$-1-butyl-3-methylimidazolium chloride (BMIC) ionic liquid by *in situ* X-ray diffraction. The authors observed the formation of several Au−Zn intermetallics, namely AuZn, $AuZn_3$ and $Au_{1.2}Zn_{8.8}$ along with the Zn phase. The cyclic voltammetric behavior of zinc deposition on gold compared to a glassy carbon electrode also confirmed the alloy formation in the former.

Zn deposition on Au (111) from 1-methyl-3-butylimidazolium chloride (MBIC) was also investigated by *in situ* electrochemical scanning tunneling microscopy (STM) by Dogel et al. [25, 177]. The authors reported multiple stripping waves by cyclic voltammetry and evidence for Au−Zn surface alloying has been found by STM after the dissolution of Zn bulk deposits.

More recently, zinc electrodeposition from zinc triftalate ($Zn(TfO)_2$) solutions in 1-butyl-1-methylpyrrolidinium trifluoromethylsulfonate ($[Py_{1,4}]TfO$) and 1-ethyl-3-methylimidazolium trifluoromethylsulfonate ([EMIM]TfO) has been reported to form both Zn and $AuZn_3$ phases [33]. SEM of the zinc coatings showed that the morphology of the deposit changes by changing the ionic liquid cation. The authors suggested that strongly adsorbed solvation layers, which depend on the applied potential, might influence the reaction mechanism and thus the morphology of the final deposit.

4.2.2 Chronoamperometric studies

Four-step chronoamperometric measurements in 0.3 mol·L^{-1} $ZnCl_2$ 12CE on Au were carried out (Figure 4.29). The potential was stepped from open circuit potential at +0.9 V ($E1$) to more negative potentials ($-0.6 \leq E2 \leq 0$ V *vs.* Zn/Zn^{2+}) to investigate the formation of Z. A third step at $E3 = -0.2$ V *vs.* Zn/Zn^{2+} was carried out in order to investigate the deposition of zinc from Z. Finally, a last step potential for the re-oxidation of the deposited zinc was recorded at $E4 = +1.0$ V *vs.* Zn/Zn^{2+}.

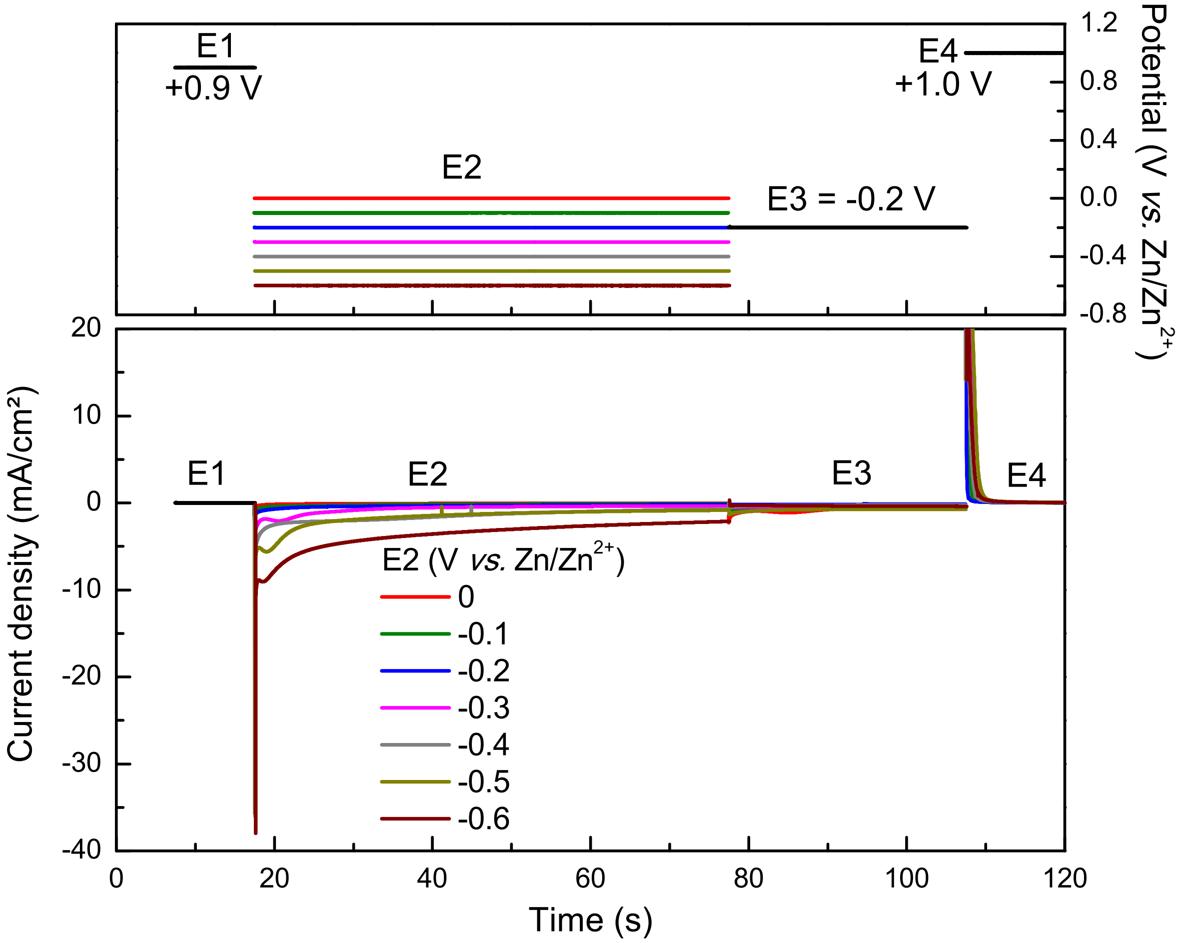

Figure 4.29. Chronoamperometric experiments for 0.3 mol·L^{-1} $ZnCl_2$ 12CE on Au at different potential steps. Applied potentials at $E2$ are indicated.

Figure 4.30 shows the current and charge profile of the potential step $E2$. Stepping from open circuit to more negative potentials ranging from 0 to −0.6 V *vs.* Zn/Zn^{2+} initially resulted in a current spike, attributable to double layer charging. For potential steps to between −0.3 and −0.6 V a typical electrocrystallization peak was observed during the first 20 s of the amperometric experiment. This nucleation peak has not been observed for glassy carbon or platinum electrodes, indicating that the mechanism of zinc deposition on gold is different from previously observed. The charge increases as the applied potential becomes more negative.

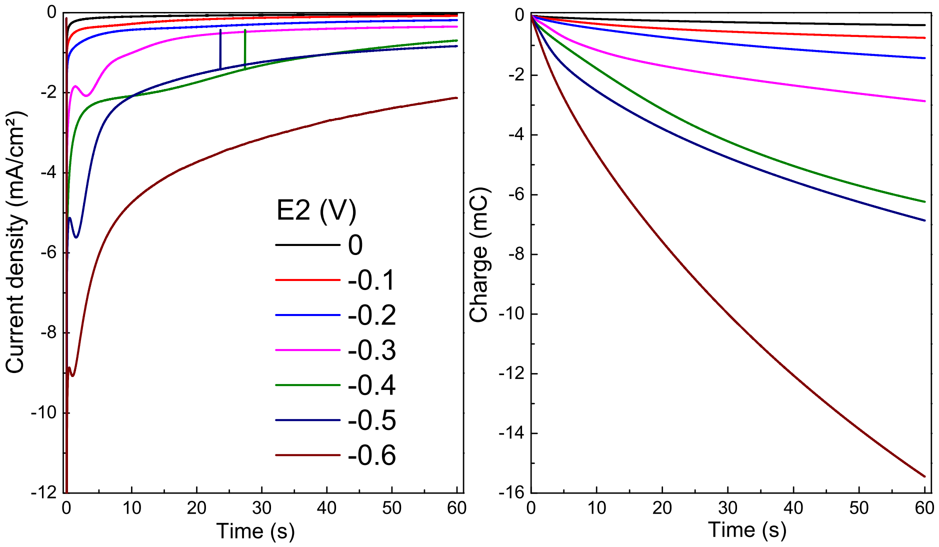

Figure 4.30. Current and charge *versus* time for $0.3\,\text{mol}\cdot\text{L}^{-1}$ $ZnCl_2$ 12CE on Au at the step $E2$ with the indicated applied potential.

A third step at $E3 = -0.2\,\text{V}$ *vs.* Zn/Zn^{2+} for 30 s was performed in order to study the origin of the backward cathodic peak in the CV (Figure 4.31). It is noticeable that only when the previous step $E2$ was more positive than $E3$ ($E2 = 0$ and $-0.1\,\text{V}$ *vs.* Zn/Zn^{2+}) a nucleation peak arises within 10 s in $E3$. When $E2$ was more negative than $E3$, nucleation took place in $E2$. Therefore, the current density and the charge consumed is considerably smaller in $E3$ compared to the previous step $E2$. For $E3 \leq -0.2\,\text{V}$ the current density can be attributed to the growth of the nuclei.

Previous chronoamperometric experiments of zinc on gold (not shown), stepping from $-0.6\,\text{V}$ to $-0.3\,\text{V}$ caused a peak with a maximum of 7 s after the change in potential. It has been alleged in the literature that nucleation studies by potentiostatic polarization are not always reproducible in ionic liquids [33, 134]. Apparently, nucleation can be influenced by strongly adsorbed ionic liquid solvation layers, which themselves might be influenced by nucleation [181].

Stepping the potential positively from -0.2 to $+1.0\,\text{V}$ causes the anodic oxidation of the deposited zinc (Figure 4.32). Nonetheless, the anodic charge is not directly corresponding to the potential applied in $E2$. The coulombic efficiency calculated from the anodic charge in $E4$ over $E2$, $E3$ and $E2$+$E3$ is presented in Figure 4.33. It can be observed that when $E2 = 0, -0.1$ and $-0.2\,\text{V}$, most of the zinc is deposited in step $E3$. The potential step at $E2 = -0.3\,\text{V}$ had the highest current efficiency. When $E2$ becomes more negative ($\leq -0.4\,\text{V}$) most of the current is consumed by parasitic reactions, therefore the overall efficiency decays. Moreover it is noteworthy that for $E2 \leq -0.3\,\mathrm{V}$ 30 to 50 % of the zinc is deposited in this step and not at $E3$.

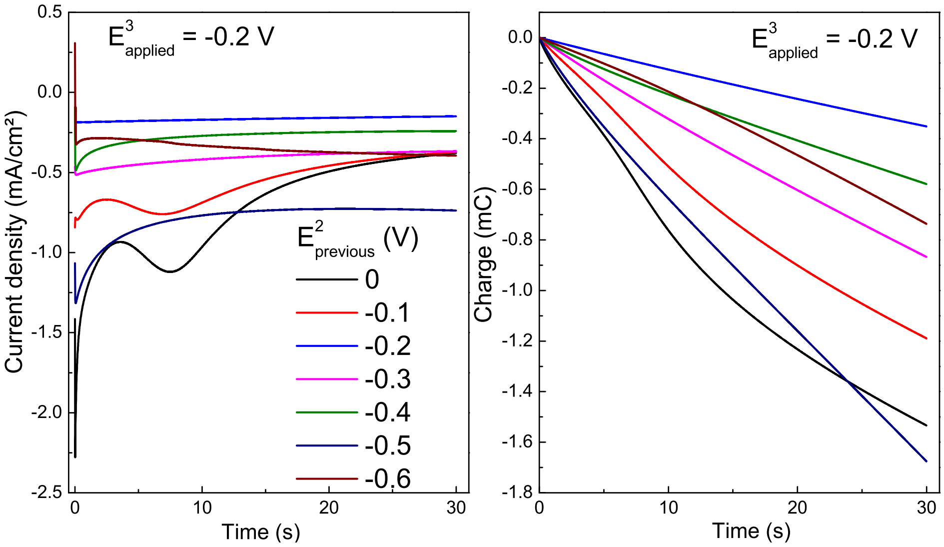

Figure 4.31. Current and charge *versus* time from $0.3\,\mathrm{mol{\cdot}L^{-1}}$ $ZnCl_2$ 12CE on Au at the step $E3 = -0.2\,\mathrm{V}$. The anodic current and charge are related to the indicated previous step $E2$.

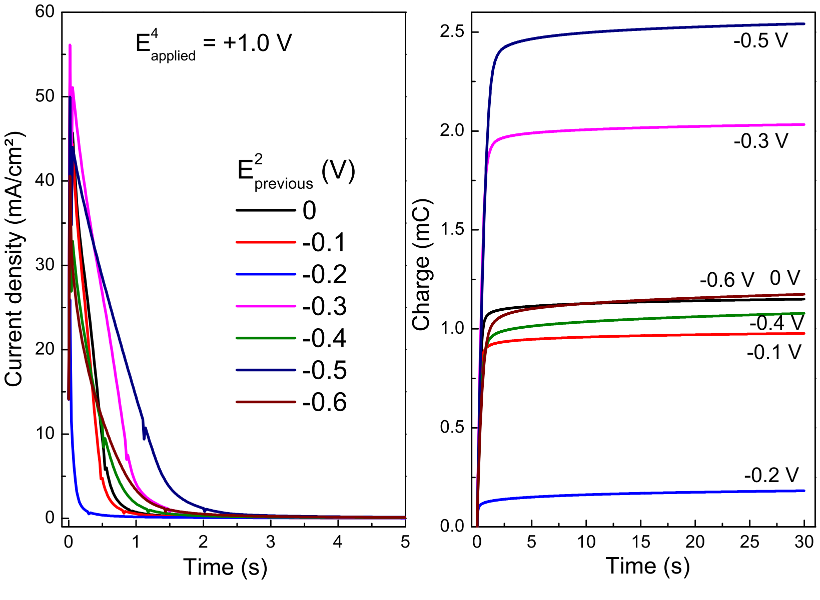

Figure 4.32. Current and charge *versus* time from $0.3\,\mathrm{mol{\cdot}L^{-1}}$ $ZnCl_2$ 12CE on Pt at the step $E3 = +1.0\,\mathrm{V}$. The anodic current and charge are related to the indicated previous step $E2$.

Similarly to platinum and glassy carbon electrodes, the charge consumed at step potentials $\leq -0.4\,\mathrm{V}$ are significantly higher for the 12CE electrolyte without zinc compared to that containing $0.3\,\mathrm{mol{\cdot}L^{-1}}$ of $ZnCl_2$ (Figure 4.34), which is due to the overpotential needed for hydrogen evolution being higher on zinc than on gold.

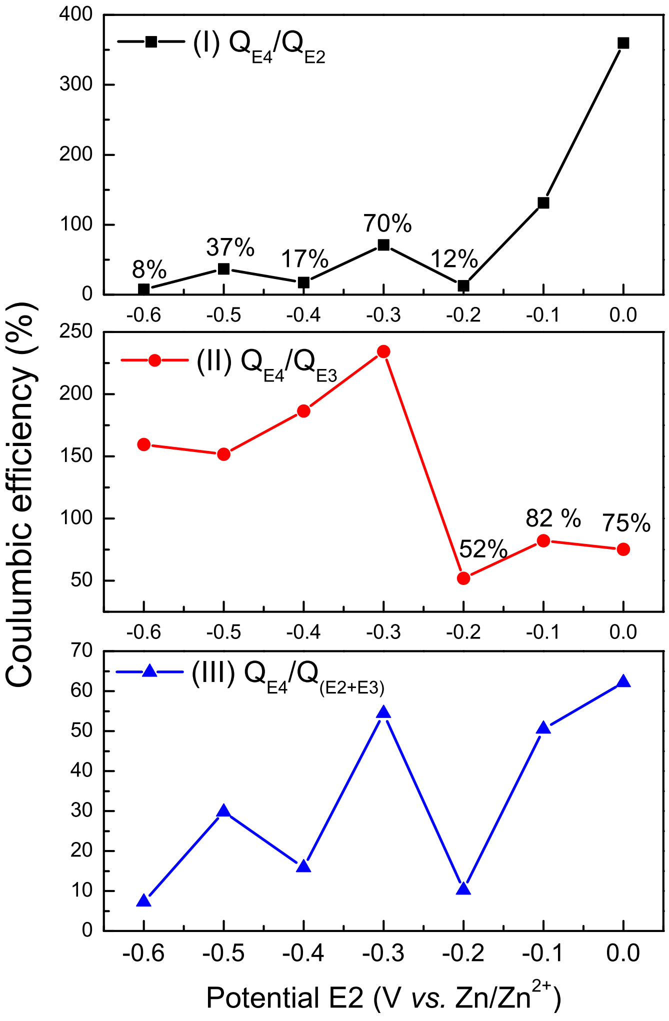

Figure 4.33. Coulombic efficiencies of 4-step chronoamperometric experiments for 0.3 mol·L^{-1} ZnCl$_2$ 12CE on a gold working disk electrode at 30 °C.

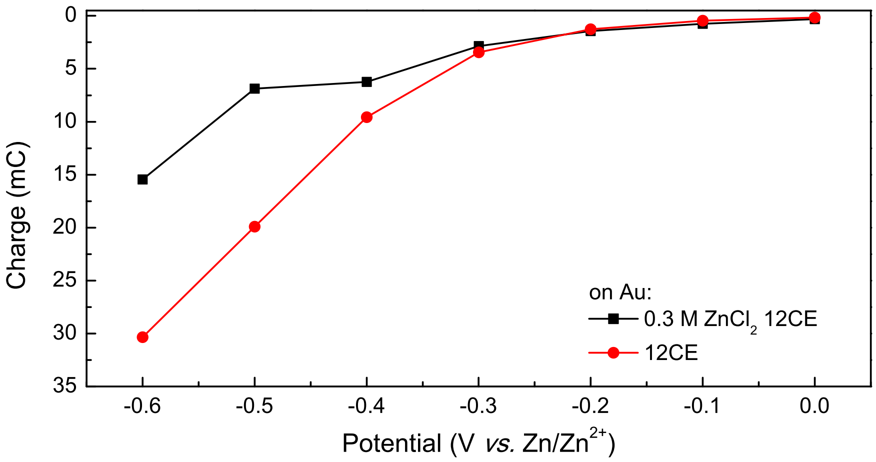

Figure 4.34. Sampled voltammogram constructed from cumulative charge *vs.* time transients from 12CE electrolytes with and without 0.3 mol·L^{-1} of ZnCl$_2$ on a gold electrode at 30 °C.

Studies of the interface of glassy carbon, platinum and gold electrodes with a deep eutectic electrolyte based on choline chloride and glycerol have shown that the double layer differential capacitance is slightly dependent on the potential, however it is significantly sensitive to the electrode material. Furthermore, the double layer differential capacitance effect is larger for Au than for Pt or glassy carbon [182]. Further investigations of DESs based on choline chloride mixtures with 1,2-ethanediol, 1,2-propanediol, 1,3-propanediol, urea and thiourea on Hg electrodes [183], showed adsorption of choline cations at large negative polarization while at less negative or positive polarization the adsorbed species were predominantly chloride anions.

In our chronoamperometric experiments of zinc in 12CE on GC and Pt electrodes, no peak that could be attributed to an electrocrystallization process was observed (Sections 3.1 and 4.1). Nonetheless, on a gold electrode, nucleation peaks are detected in most of the potential steps at negative polarizations. This change may be due to adsorption of chloride on the gold surface changing the mechanism from outer to inner-sphere electron transfer reactions. In an outer-sphere electrode reaction, the reactant and product do not interact strongly with the electrode surface, they are generally at a distance of at least a solvent layer from the electrode. In an inner-sphere electrode reaction, there is a strong interaction of the reactant, intermediates, or products with the electrode, that is, such processes involve specific adsorption of species involved in the electrode reaction [52]. Thus, it may be that at gold substrates, chloride ions from the reducible species adsorb onto the gold surface and an inner-sphere reaction takes place, causing a peak to rise on the first 10 s of negative polarization. Nevertheless, *in situ* spectroscopic measurements on gold would be necessary to study in further details the interface of the deep eutectic solvent with Au.

Recently, *in situ* SEIRAS (surface-enhanced infrared absorption spectroscopy) studies on gold electrodes in contact with [BMIM][TFSA] (1-butyl-3-methylimidazolium bis(trifluoromethane-sulfonyl)amide) showed potential-dependent restructuring of cations and anions on Au surfaces [83] and reinforced the proposed structure for the interface of ionic liquids with metal electrodes to be assembled multilayers of the liquid salt [63, 184]. The hypothesis of multilayers was also confirmed by STM, AFM and EIS experiments on the interface of Au (111) with two different ionic liquids: [Py][FAP] and [EMIM][FAP] (FAP = tris(pentafluoroethyl)trifluoro- phosphate) [70]. Assembled and ordered ionic liquid nanostructures at the electrode interface was account for influence electrochemical reactions. Moreover, experiments of *in situ* electrochemical surface plasmon resonance (SPR) with 12CE have been carried out in order to study the interface of the deep eutectic with a gold substrate. We expected to be able to study the potential-dependent organization of the ionic liquid, as it has been shown in the literature for trioctylmethylammonium bis(ninafluorobutanesulfonyl)amide ([TOMA$^+$][$C_4C_4N^-$]) [185]. However, the angle of maximum absorption for 12CE was out of the detectable range.

4.2.3 Partial conclusions

Zinc was deposited on a gold substrate from $0.3\,\mathrm{mol{\cdot}L^{-1}}$ of $ZnCl_2$ in 12CE. Formation of interfacial Au−Zn alloys was indicated by multiple stripping peaks in cyclic voltammetry and supported by the literature of zinc deposition on gold from other ionic liquids. A forward and backward cathodic peak was observed by cyclic voltammetry. Potential-dependent blocking effects and formation of zinc intermediate species appear to play a role in this mechanism. Chronoamperometric measurements showed a typical nucleation peak within 10 s of electrode polarization. An inner and outer-sphere electron transfer reaction was suggested to explain the distinct amperometric response.

5 Zinc electrodeposition on copper and steel

5.1 Zinc deposition on copper

5.1.1 Voltammetric studies

Typical cyclic voltammograms of 12CE on a copper electrode without and with 0.3 mol·L^{-1} of $ZnCl_2$ are shown in Figure 5.1. Both scans started cathodically from +0.6 V *vs.* Zn/Zn^{2+} with a negative sweep direction.

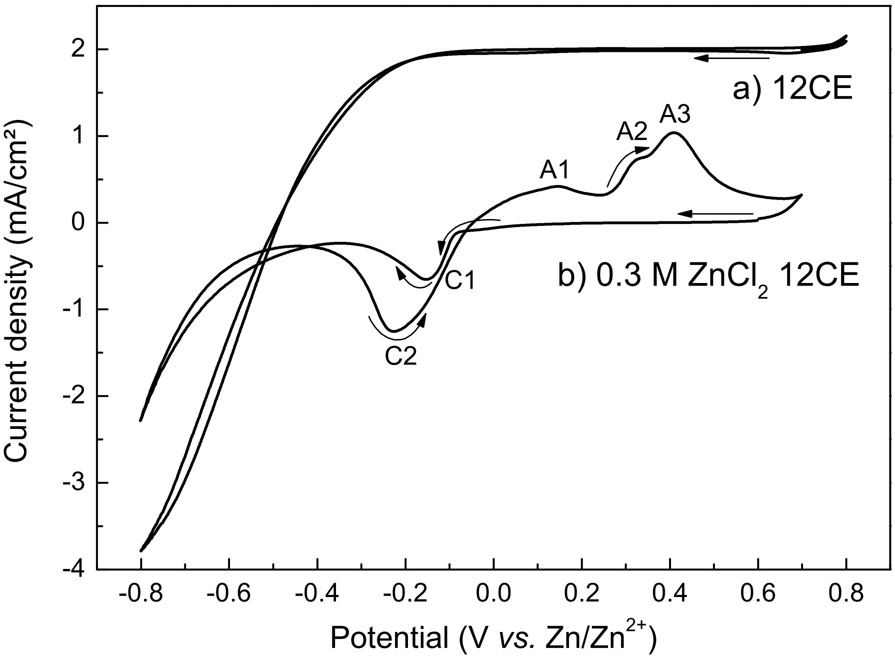

Figure 5.1. Cyclic voltammograms of 0.3 mol·L^{-1} $ZnCl_2$ in 12CE electrolyte on a stationary copper disk electrode (10 mV·s^{-1}, 30 °C) starting from +0.6 V *vs.* Zn/Zn^{2+} with a negative sweep direction. Arrows indicate sweep direction. The CV a) is offset in +2 mA·cm^{-2} for better visualization.

On the background scan, similarly to platinum and gold, reduction of the electrolyte starts at relatively low overpotentials ($E \leq -0.2$ V *vs.* Zn/Zn^{2+}). In the presence of zinc chloride, a cathodic peak is clearly observed at −0.15 V in the forward scan. After the cathodic switching potential, another cathodic peak is observed at −0.23 V in the anodic backward scan. At positive potentials three anodic waves are observed, at +0.15, +0.32 and +0.41 V *vs.* Zn/Zn^{2+}. The total anodic charge (from 0 to +0.7 V) was 34 % of the total cathodic charge (from 0 to −0.8 V). However, when the anodic charge was calculated over the cathodic charge of C1+C2 (sum of the integration area of both peaks), the current efficiency was 94 %, indicating that most of the zinc was deposited in C1 and C2.

Zinc deposition on copper looks similar to that on gold (Section 4.2). Moreover, from the binary phase diagram of the Cu−Zn system (Figure 5.2), it can be seen that zinc can also form several alloy phases with copper. Hence, the dissolution peaks can be assigned to dissolution of bulk zinc at +0.15 V (which coincides with the peak potential on glassy carbon) followed by oxidation of different phases of zinc-copper alloys at +0.32 and +0.41 V. It was avoided to scan further positive in order to not dissolve the copper substrate in the solution.

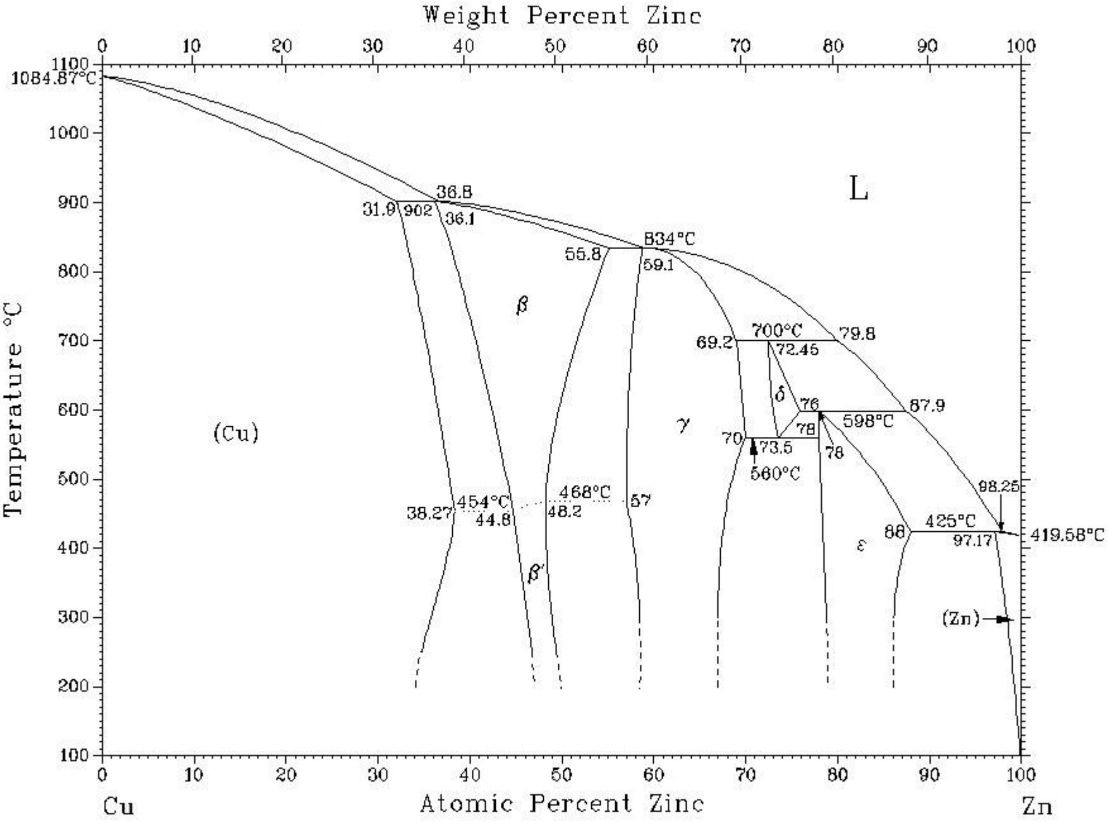

Figure 5.2. Cu−Zn binary phase diagram [186].

Figure 5.3 shows a set of cyclic voltammograms data recorded with the same scan rate at 10 mV·s^{-1} and progressively decreasing the cathodic limit of the scan, while the anodic limit was fixed at +0.7 V. For all CVs a forward cathodic peak is observed at about −0.15 V *vs.* Zn/Zn^{2+}. However, decreasing the cathodic switching potential, the backward peak on the anodic scan proportionally decreases in magnitude, as can be seen in better detail in Figure 5.4.

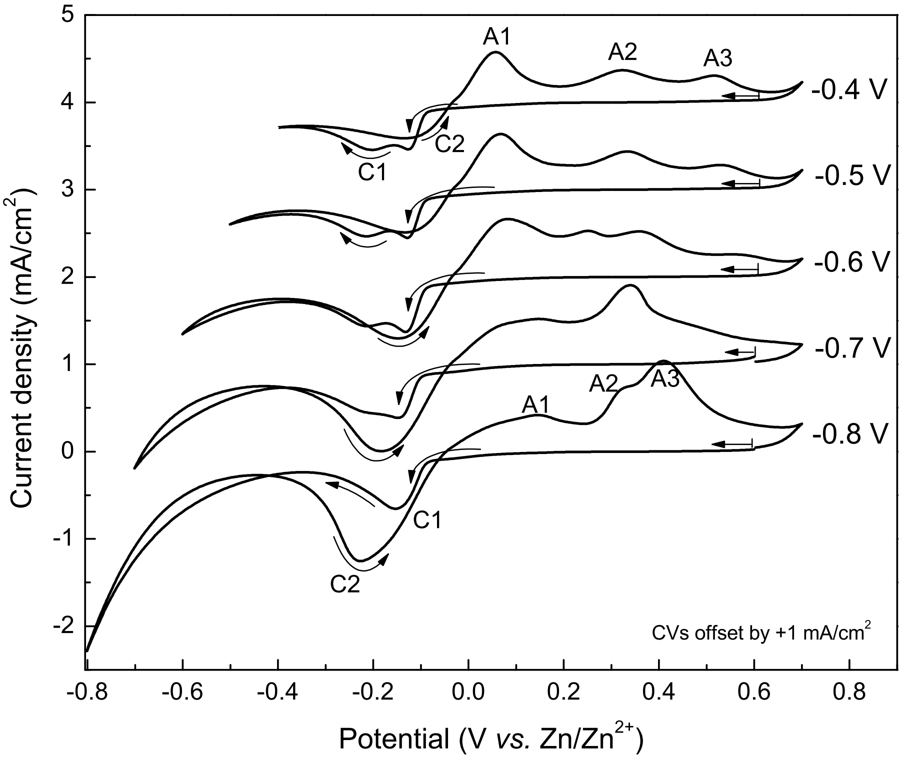

Figure 5.3. Cyclic voltammograms of a stationary copper electrode in 0.3 mol·L^{-1} ZnCl$_2$ 12CE electrolyte at a scan rate of 10 mV·s^{-1}, 30 °C, starting from +0.6 V *vs.* Zn/Zn^{2+} with a negative sweep direction. Arrows indicate sweep direction.

Similarly to gold electrodes, chloride ions may also adsorb at copper substrates, leading to an inner-sphere electron transfer on the forward sweep, while the backward peak is dependent on the formation of Z, which might lead to a deposition involving an outer-sphere electron transfer mechanism. In the anodic range the first anodic peak (A1, at −0.15 V) related to the oxidation of bulk zinc has a higher peak current for cathodic limits $E \geq -0.6$ V *vs.* Zn/Zn^{2+}. Decreasing the switching potential to more negative values, causes A1 to decrease, while A2 and A3 (at +0.32 and +0.41 V *vs.* Zn/Zn^{2+}) increase in magnitude. Because A2 and A3 are related to the oxidation of alloyed zinc, this may indicate that for cathodic limits more negative than −0.6 V *vs.* Zn/Zn^{2+} the formation of alloys is favoured. Interestingly, the same voltammetric behavior is not observed for the electrodeposition of zinc on copper electrodes from 1:2 ChCl:urea DES

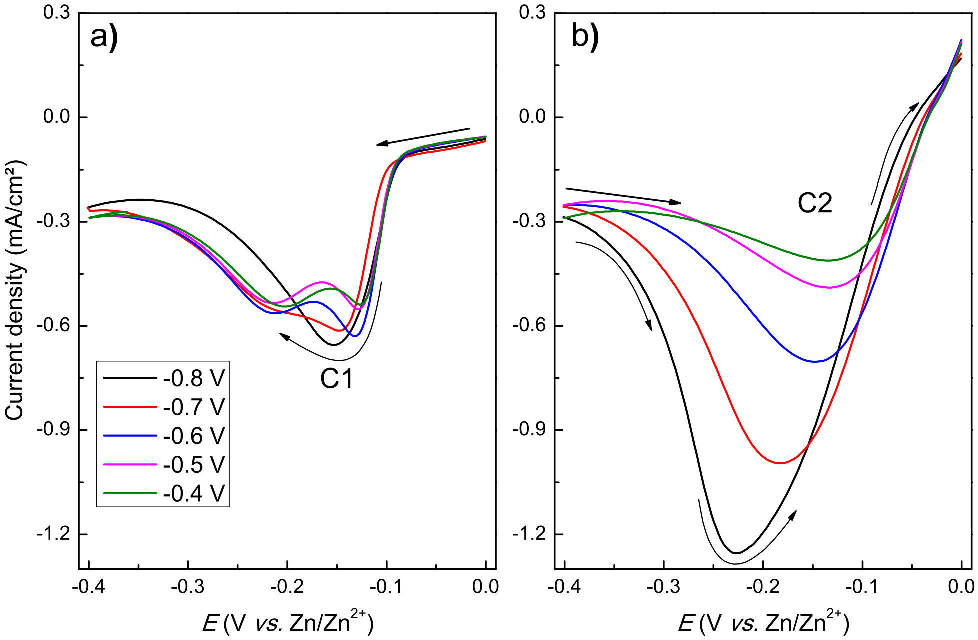

Figure 5.4. a) forward and b) backward peaks assigned to the deposition of Zn in the CVs shown in Figure 5.3 (10 mV·s^{-1}, 30 °C on Cu substrate). Arrows indicate sweep direction.

at 70 °C [38], which is likely to be due to the fact that urea is much less acidic than ethylene glycol, changing the mechanism of the zinc deposition reaction, as well as the speciation of zinc.

The coulombic efficiencies for the CVs with cathodic limits of −0.4, −0.5, −0.6, −0.7 and −0.8 V *vs.* Zn/Zn^{2+} were: 96, 99, 100, 96 and 94 %, respectively, calculated from the total anodic charge (A1+A2+A3) over the cathodic charge of the forward and backward cathodic peaks (C1+C2).

Increasing the scan rate of the cyclic voltammograms caused a potential shift of the forward reduction peak C1 to more negative values (Figures 5.5, 5.6 and 5.7) indicating relatively slow kinetics for the electron-transfer [136, 187]. The current density for both C1 and C2, increase linearly with the scan rate (forward i_p $R^2 = 0.996$, backward i_p $R^2 = 0.981$, from Figure 5.7 c-d). This dependence of peak current with the scan rate is indicative of electrode reaction controlled by mass transport of Z [52, 131], which itself is limited by a slow chemical step. In the anodic range, the peak currents also increase, although in a somewhat irregular fashion.

The integration of the anodic peaks from Figure 5.5 are 95, 103, 115 and 109 % of the area from the sum of C1+C2 for scan rates of 10, 20, 50 and 100 mV·s^{-1}, respectively. Coulombic efficiencies above 100 % indicate that for faster scan rates, zinc is also deposited at potentials below −0.4 V *vs.* Zn/Zn^{2+}, which is outside of the integration range.

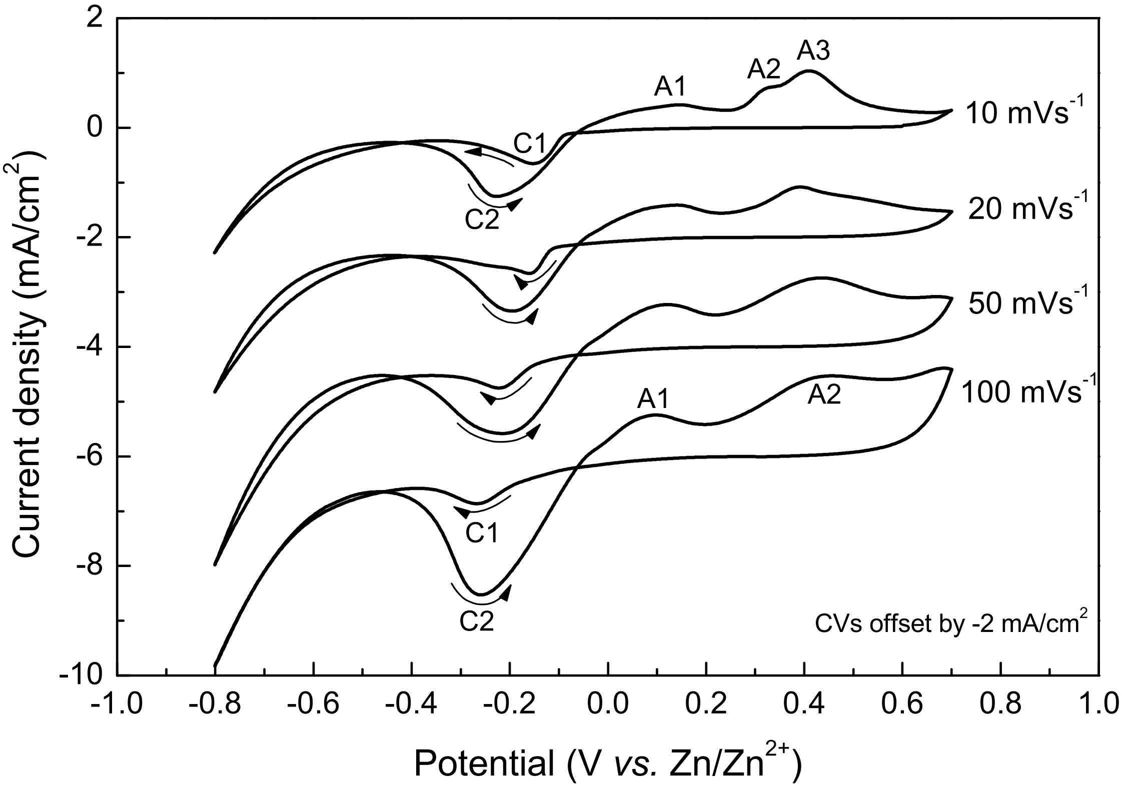

Figure 5.5. Cyclic voltammograms of 0.3 mol·L^{-1} ZnCl$_2$ in 12CE electrolyte on a stationary copper disc electrode at 30 °C, starting from 0.6 V *vs.* Zn/Zn^{2+} with a negative sweep direction. Arrows indicate sweep direction.

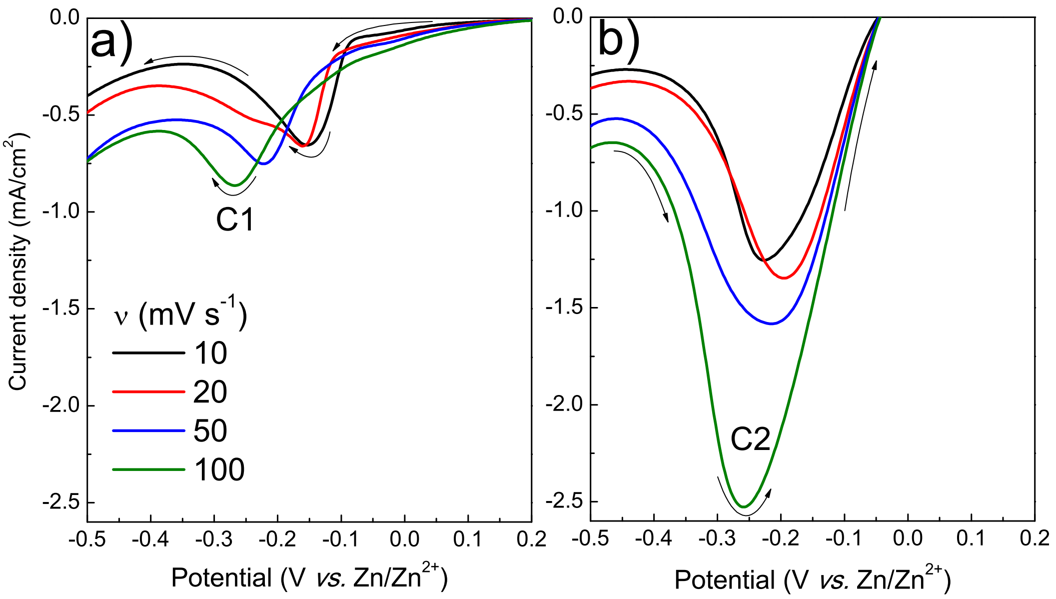

Figure 5.6. a) forward and b) backward peaks assigned to the deposition of Zn in the CVs at different scan rates shown in Figure 5.5. Arrows indicate sweep direction.

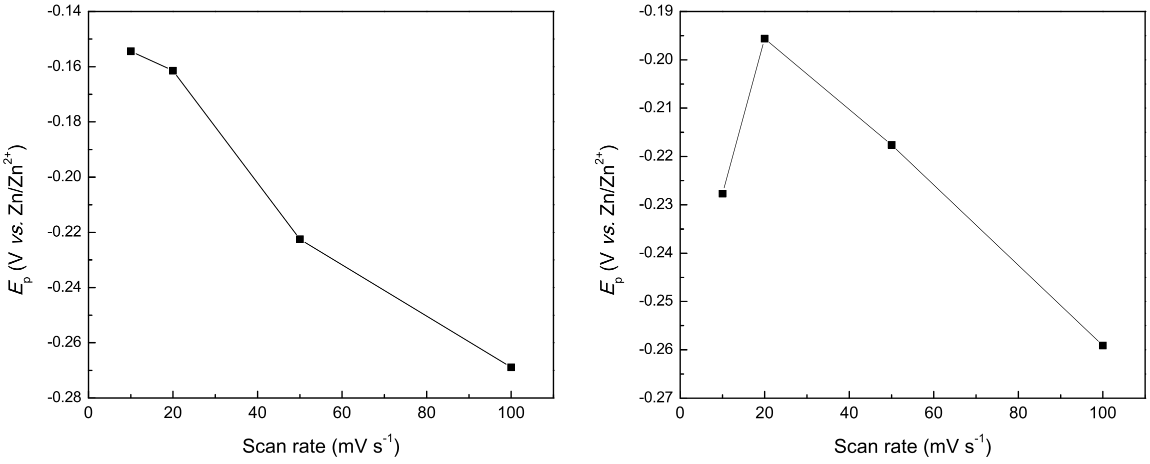

(a) forward E_p (b) backward E_p

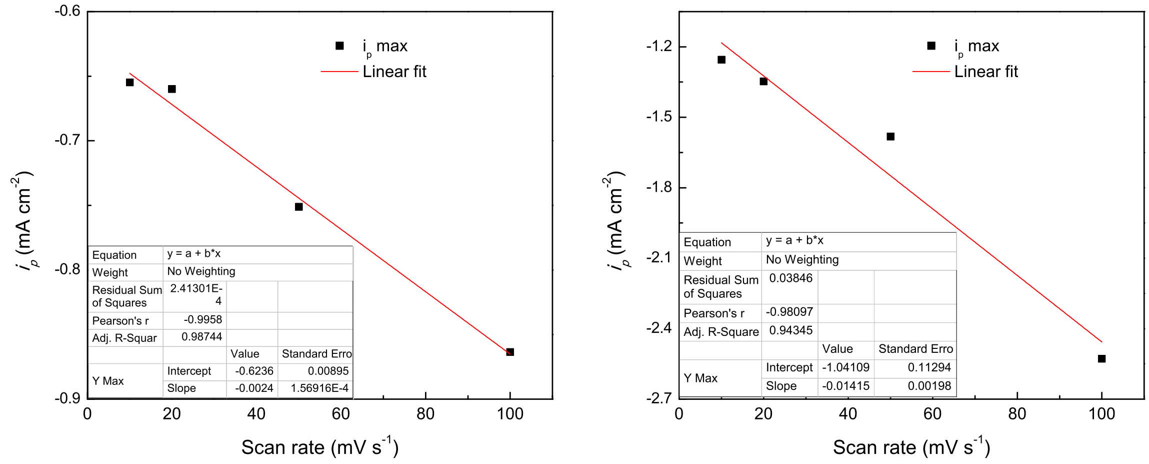

Equation	y = a + b*x		
Weight	No Weighting		
Residual Sum of Squares	2.41301E-4		
Pearson's r	-0.9958		
Adj. R-Squar	0.98744		
		Value	Standard Erro
Y Max	Intercept	-0.6236	0.00895
	Slope	-0.0024	1.56916E-4

Equation	y = a + b*x		
Weight	No Weighting		
Residual Sum of Squares	0.03846		
Pearson's r	-0.98097		
Adj. R-Square	0.94345		
		Value	Standard Erro
Y Max	Intercept	-1.04109	0.11294
	Slope	-0.01415	0.00198

(c) forward i_p (d) backward i_p

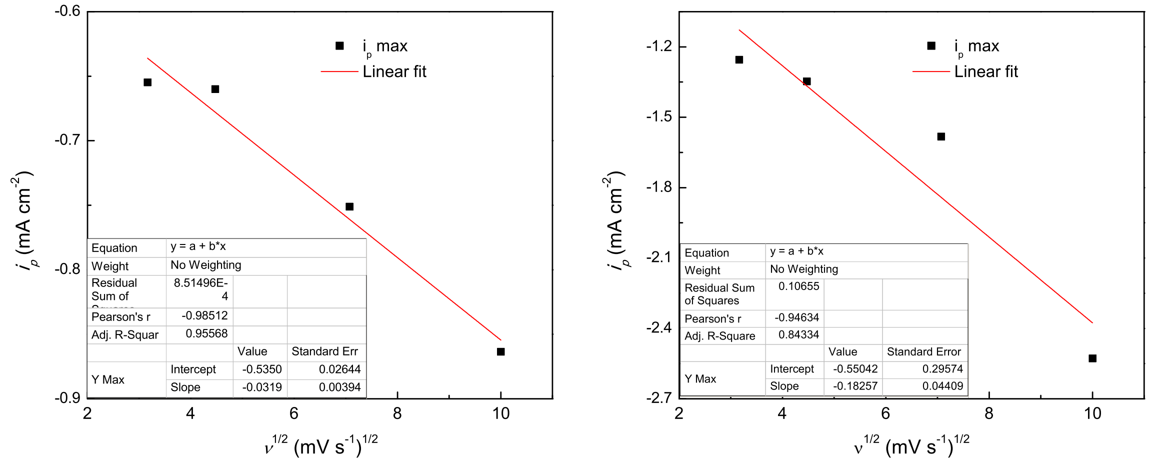

Equation	y = a + b*x		
Weight	No Weighting		
Residual Sum of	8.51496E-4		
Pearson's r	-0.98512		
Adj. R-Squar	0.95568		
		Value	Standard Err
Y Max	Intercept	-0.5350	0.02644
	Slope	-0.0319	0.00394

Equation	y = a + b*x		
Weight	No Weighting		
Residual Sum of Squares	0.10655		
Pearson's r	-0.94634		
Adj. R-Square	0.84334		
		Value	Standard Error
Y Max	Intercept	-0.55042	0.29574
	Slope	-0.18257	0.04409

(e) forward i_p (f) backward i_p

Figure 5.7. Forward and backward peak potentials (E_p) *versus* scan rate (a and b), peak current (i_p) *versus* scan rate (c and d) and *versus* square root of the scan rate (e and f). E_p and i_p are assigned to the deposition of Zn in the CVs at different scan rates shown in Figure 5.6.

Studies of the deposition of zinc on a copper substrate from 12CE using a rotating disc electrode (RDE) have been performed at rotation rates ranging from 500 to 5000 rpm (Figure 5.8). The cyclic voltammograms reveal that both forward and backward peaks for Zn deposition decrease in magnitude with increasing rotation rate, as it can be better seen in Figure 5.9. The forward peak at $-0.15\,\mathrm{V}$ on the static electrode is also slightly shifted positively to $-0.13\,\mathrm{V}$ when the copper electrode is rotated. This decrease in current density by rotation of the electrode indicates that the reducible species are transported into the bulk of the electrolyte when hydrodynamic force is applied. Moreover, the forward peak splits in two, which to date has not yet a plausible explanation. Nonetheless, the peak current of the backward peak C2 decreases drastically compared with the forward peak C1, which is consistent with the interpretation of C1 to be an inner and C2 an outer-sphere electron transfer. The magnitude of the current density in C2 is dependent on the formation of Z species, and convection affects the outer sphere mechanism to a higher extent compared to the inner-sphere, as it leads to the transport of Z into the bulk of the electrolyte.

In the positive potential range of the CV, the three stripping peaks show different behavior with rotation rate. The dissolution peak A1 slightly shifts from +0.15 to $+0.08\,\mathrm{V}$ *vs.* $\mathrm{Zn/Zn^{2+}}$ and increases in magnitude when the copper disk is rotated. The second and third anodic peaks A2 and A3 shift positively to +0.34 and $+0.41\,\mathrm{V}$ and decrease in magnitude. This indicates that the deposition of bulk zinc, instead of Cu−Zn alloys, is favoured in hydrodynamic experiments.

The current efficiencies of the CVs calculated from the total anodic charge over the charge corresponding to C1+C2 increases from 95 % at the static electrode to 194, 184, 186 and 184 % for rotation rates of 500, 1000, 2000 and 5000 rpm, respectively. This indicates that the deposition of zinc is shifted to more negative potentials when the electrode is rotated. The ratio of the total anodic charge over the total cathodic charge (from 0 to $-0.8\,\mathrm{V}$ *vs.* $\mathrm{Zn/Zn^{2+}}$) is 34, 33, 29, 26 and 23 % for rotation speeds of 0, 500, 1000, 2000 and 5000 rpm, respectively, indicating that Z is transported into the bulk of the electrolyte and thus not reduced to zinc. Consequently, a decrease in the coulombic efficiency is observed, although the value for the static electrode is also rather low.

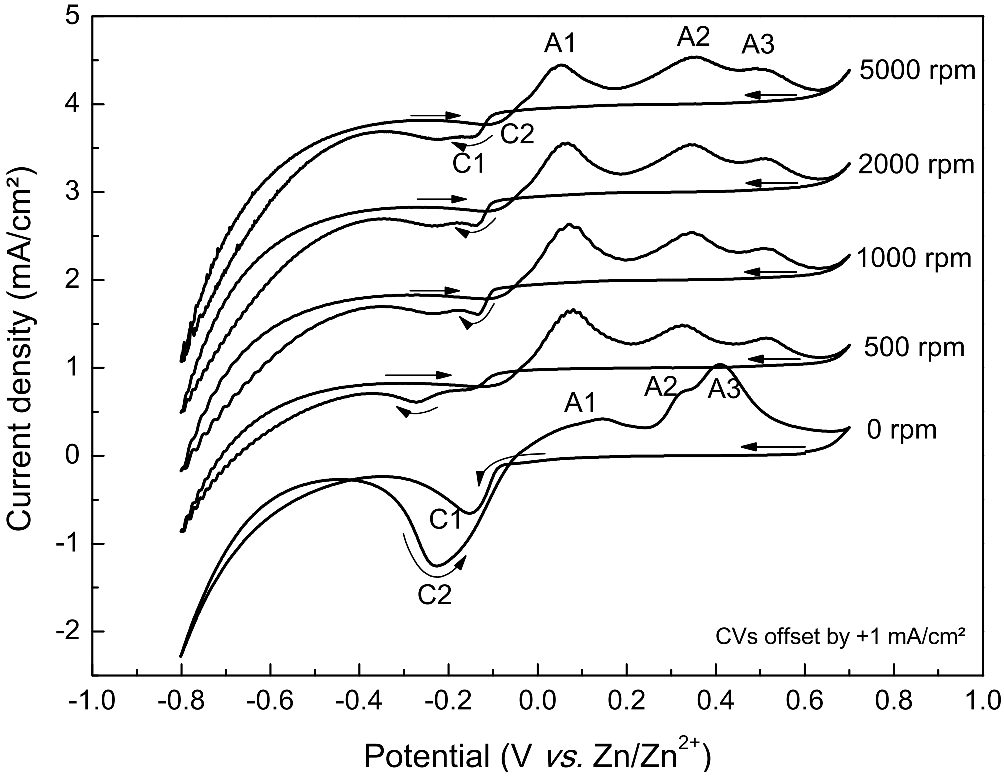

Figure 5.8. RDE cyclic voltammogram of a copper electrode at different rotation rates in 12CE containing 0.3 mol·L^{-1} of ZnCl$_2$ at a scan rate of 10 mV·s^{-1}, 30 °C, starting from +0.6 V *vs.* Zn/Zn^{2+} with a negative sweep direction. A1, A2 and A3 indicate different anodic peaks. Arrows indicate sweep direction.

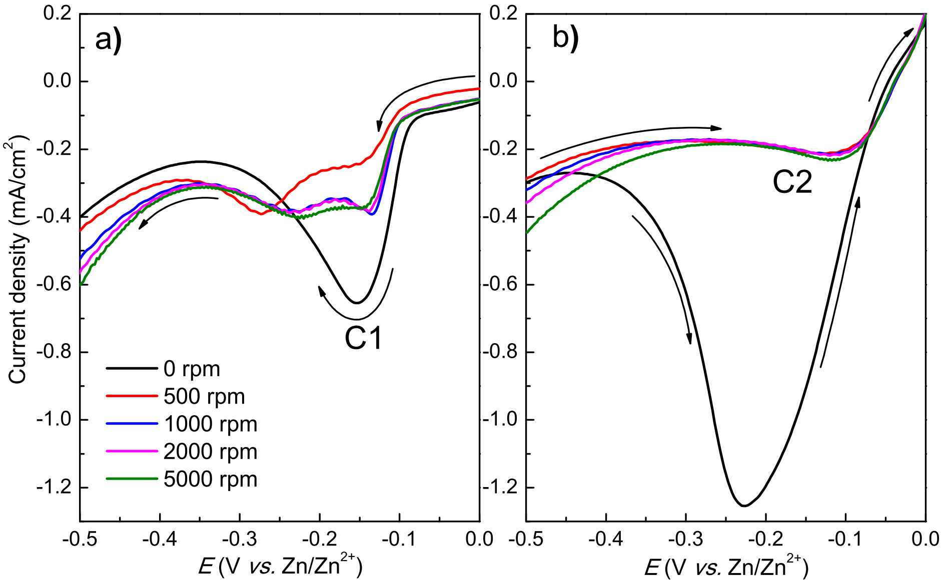

Figure 5.9. a) Forward and b) backward peaks from the CVs of Figure 5.8 (0.3 mol·L^{-1} ZnCl$_2$ 12CE, 10 mV·s^{-1}, 30 °C on Cu substrate with different rotation rates). Arrows indicate sweep direction.

5.1.2 Chronoamperometic studies

Multi-step potential experiments were performed on a copper disk electrode. The electrode potential was varied from open circuit potential at +0.5 V ($E1$) to more negative potentials ranging from −0.1 to −0.8 V *vs.* Zn/Zn^{2+}. The current and charge-time transients for this second step potential ($E2$) are presented in Figure 5.10.

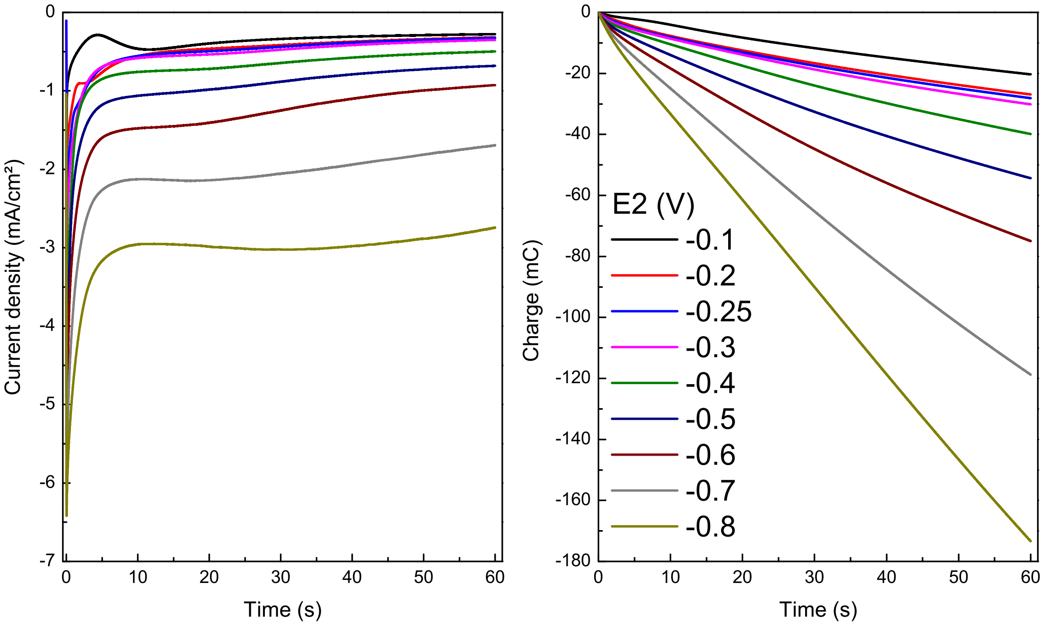

Figure 5.10. Current and charge *versus* time for 0.3 mol·L^{-1} ZnCl$_2$ 12CE on Cu at the step $E2$ with the indicated applied potential.

From the current-time profile it can be seen that for $E2 = -0.2$ V *vs.* Zn/Zn^{2+} a nucleation peak was observed after 5 s. The peak shape is typical for nucleation-growth processes. At more negative potentials, very broad peaks were observed. Moreover, the current density and its respective cumulative charge, increased proportionally as the applied potential becomes more negative, indicating no blocking effects on copper electrodes.

For potentials of $E2 = -0.4$ to -0.8 V *vs.* Zn/Zn^{2+}, a third potential step at $E3 = -0.2$ V was applied for the purpose of investigating the influence of the previous cathodic potential limit on the backward cathodic peak. The current response to this step $E3$ is presented in Figure 5.11. Higher peak currents were recorded when the previous step $E2$ was −0.5 and −0.6 V *vs.* Zn/Zn^{2+}, while for higher overpotentials ($E \leq -0.7$ V *vs.* Zn/Zn^{2+}) the peak current decreased, which can be due convection caused by vast formation of hydrogen.

From the charge-time profile at $E3$, it can be seen that the cumulative charge is dependent on the formation of Z in the previous step $E2$. Obviously, the amount of

Z produced at $E2$ decreases in the following order: $-0.5 > -0.6 > -0.8 > -0.7 > -0.4\,\mathrm{V}$ *vs.* Zn/Zn^{2+}, resulting in the respective current maximum and cumulative charge at $E3$. It is also noteworthy that after the potential $E2$ is applied there is a typical spike due to the double layer (DL) charging, however, from this point the current does not decay exponentially to a minimum, as it would be expected after the capacitive charging. Instead, after the maximum i_{dl}, the current decays continuously from this point. It is likely that, as nucleation of zinc has already taken place at $E2$, the current observed at $E3$ is related to the growth of the nuclei, with a cottrellian decay.

The charge consumed at the last step at $+0.5\,\mathrm{V}$ *vs.* Zn/Zn^{2+} ($E4$), which is directly corresponding to the amount of zinc reoxidized, decrease in the following order: $E2 = -0.5 > -0.4 > -0.6 > -0.8 > -0.7\,\mathrm{V}$ *vs.* Zn/Zn^{2+}, indicating that the polarization of copper electrodes at very negative potentials ($E2 \leq -0.7\,\mathrm{V}$ *vs.* Zn/Zn^{2+}) is not so efficient for the formation of Z and its subsequent reduction to zinc.

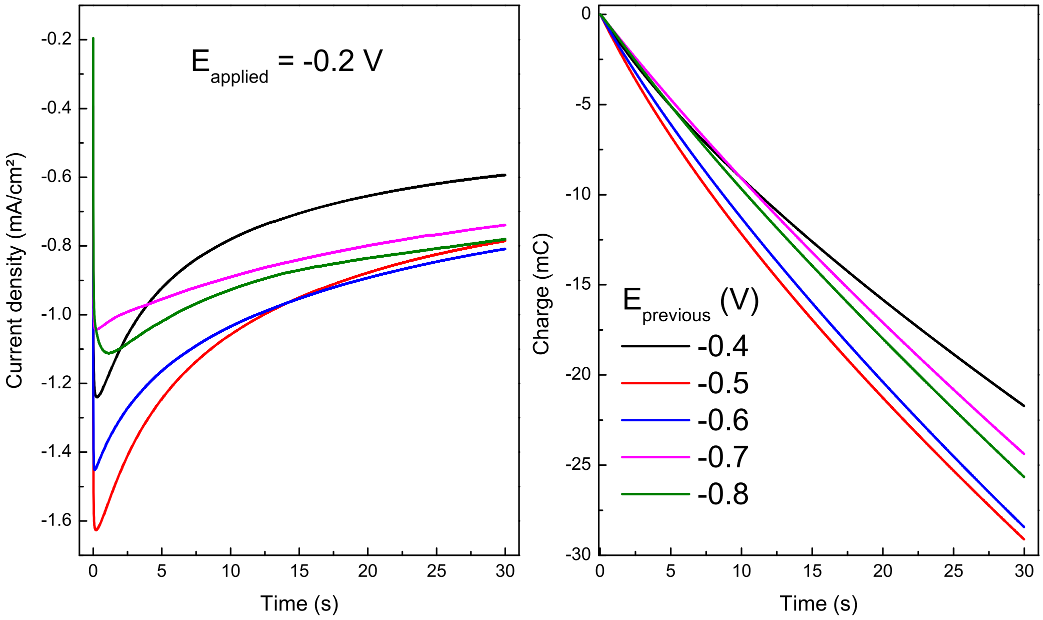

Figure 5.11. Current and charge *versus* time for $0.3\,\mathrm{mol{\cdot}L^{-1}}$ ZnCl$_2$ 12CE on Cu at the step $E3 = -0.2\,\mathrm{V}$ with the indicated applied potential.

Sample voltammograms constructed from the charge consumed at the step $E2$ for 30 s in the 12CE electrolyte with and without zinc chloride is presented in Figure 5.12. At potential steps ranging from -0.1 to $-0.3\,\mathrm{V}$ *vs.* Zn/Zn^{2+} the charge consumed is higher for the electrolyte containing ZnCl$_2$ because deposition of zinc occurs simultaneously with hydrogen evolution, increasing the charge. For $E < -0.3\,\mathrm{V}$ *vs.* Zn/Zn^{2+} the charge is larger for the electrolyte without zinc, because the overpotential for hydrogen evolution is higher on zinc than on copper electrodes.

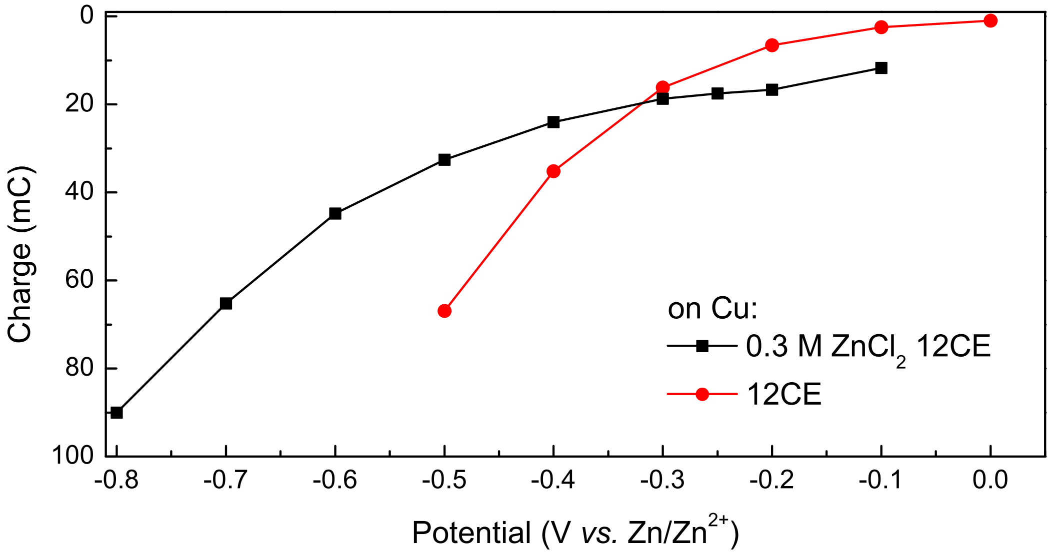

Figure 5.12. Sampled voltammogram contructed from cumulative charge *vs.* time transients from 12CE electrolytes with and without 0.3 mol·L^{-1} of ZnCl$_2$ on a copper disk electrode at 30 °C.

5.1.3 Morphology and composition characterization

Zinc was potentiostatically deposited on a copper disk (0.95 cm^2) at −0.25 V for 5340 s until a charge of 4.0 C had been consumed. This would lead to a 2 μm thick zinc layer for the normal bulk zinc density (7.4 g·cm^{-3}), based on Faraday's law and assuming 100 % coulombic efficiency.

The zinc layer deposited on the copper had a dark-pale optical appearance and was characterized by SEM and EDX (Figure 5.13). From the SEM images, it can be seen that the morphology of the zinc deposited on Cu is very similar to that observed for zinc on platinum electrodes (Subsection 4.1.3). However, the platelets on Cu are thicker. This kind of morphology for zinc deposits from 12CE electrolytes has been reported in the literature [45] and correlated to the assembly of the molecules in the electrochemical double layer of the deep eutectic. EDX of the surface revealed a composition of 96 % Zn and 4 % oxygen, the latter being due to the formation of zinc oxide. No Zn−Cu alloy could be detected at the surface of the disk.

A cross section of the deposit is shown in Figure 5.14. From the contrast in the FIB images of Figure 5.14 a and b, 3 different phases can be observed: the Cu substrate (at the bottom), Cu−Zn intermetallics (in the interface). The darker phase at the top is from a Pt protection coating.

X-ray fluorescence (XRF) of the coating revealed a zinc thickness of 1.4 μm, measured with an aperture of 2 mm from at least 5 different spots of the sample. As the consumed

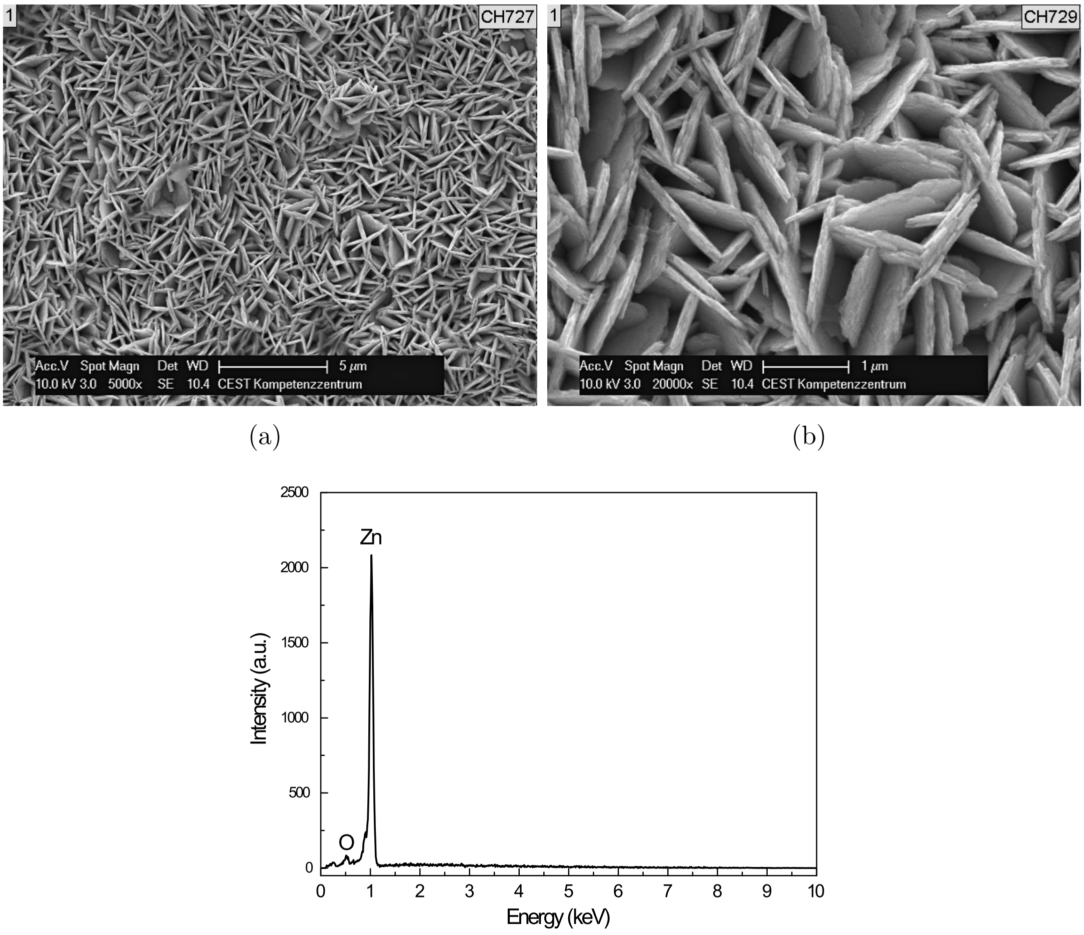

(a) (b)

(c)

Figure 5.13. a)–b) SEM micrographs of zinc deposits at copper disc substrates with different magnifications and c) EDX spectrum for surface composition analysis from image a). The deposits were produced in 0.3 mol·L^{-1} $ZnCl_2$ 12CE at 30 °C at −0.3 V *vs.* Zn/Zn^{2+}.

charge during the electrodeposition of zinc was enough for a 2 μm layer thickness, lower thickness indicates low coulombic efficiency due to parasitic reactions, e.g. hydrogen evolution. Cross-sectional FIB images reveal a thickness higher than 2 μm for the coating (Figure 5.14), nevertheless, the layer is porous and therefore not uniform.

A layer thicker than 2 μm, indicates interdiffusion between copper and zinc, resulting in a continuous growth of the alloy phase. Hence, the thickness of the intermetallic layer increases by diffusion of zinc into the copper substrate. Such interdiffusion happens in order to achieve an equilibrium through the elimination of the concentration gradient. This is also confirmed by the presence of voids in the interface (Figure 5.14 c). Vacancies in the interface of the electrodeposited metal and the substrate is usually a result of uneven interdiffusion or unequal mobilities between the metal couple, and they are commonly referred to as Kirkendall voids or Kirkendall porosity [55, 188]. These voids occur

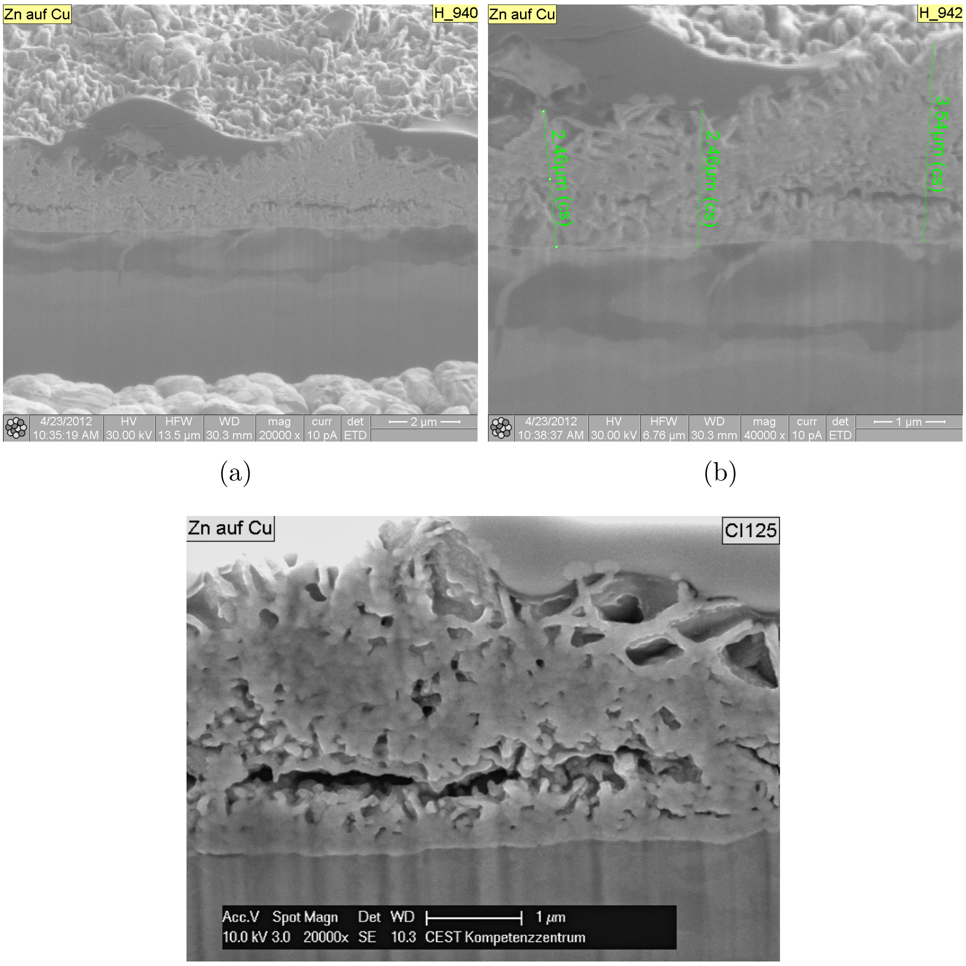

(a) (b)

(c)

Figure 5.14. a)–b) FIB and c) SEM micrographs of zinc deposits at copper disc substrates with different magnifications.

individually near the common interface. The Kirkendall effect is time and temperature dependent, nevertheless, it can also occur at room temperature, as it showed to be the case in the Cu−Zn system.

Lin et al. [189] characterized zinc deposited from Lewis acidic $ZnCl_2$-EMIMCl ionic liquids on copper discs at 120 °C. The authors observed that although the initial deposited Zn layer was 1 μm thick, cross-sectional SEM images showed that the Cu−Zn alloy layer had thickened to about 3 μm because of intediffusion of Zn and Cu atoms. This effect was more pronounced when the copper electrode was left in the ionic liquid at 120 °C for 12 h after zinc deposition. When the deposit was immediately taken off of the bath and left at room temperature, the interdiffusion of Zn and Cu was substantially retarded. Similar temperature-dependent interdiffusion and alloying has also been reported for Ag−Zn systems [166]. Nevertheless, it is important to note that the interdiffusion of Zn and Cu and the continuous alloying occurs at room temperature [190].

EDX composition analysis of the cross-section shows different concentrations of zinc and copper along the deposit (Figure 5.15). While the surface has a composition of 97 % Zn (Figure 5.15 b, sptY871), the intermediate layers (Figure 5.15 c) and d) have a composition of 30 % Cu / 70 % Zn and 65 % Cu / 35 % Zn, respectively, followed by e) 100 % Cu. The concentration gradient confirms interdiffusion of Zn into Cu and Cu into Zn. Such interdiffusion between zinc deposits on copper electrodes has also been observed in electrodeposition of zinc on copper from basic aqueous solutions [191].

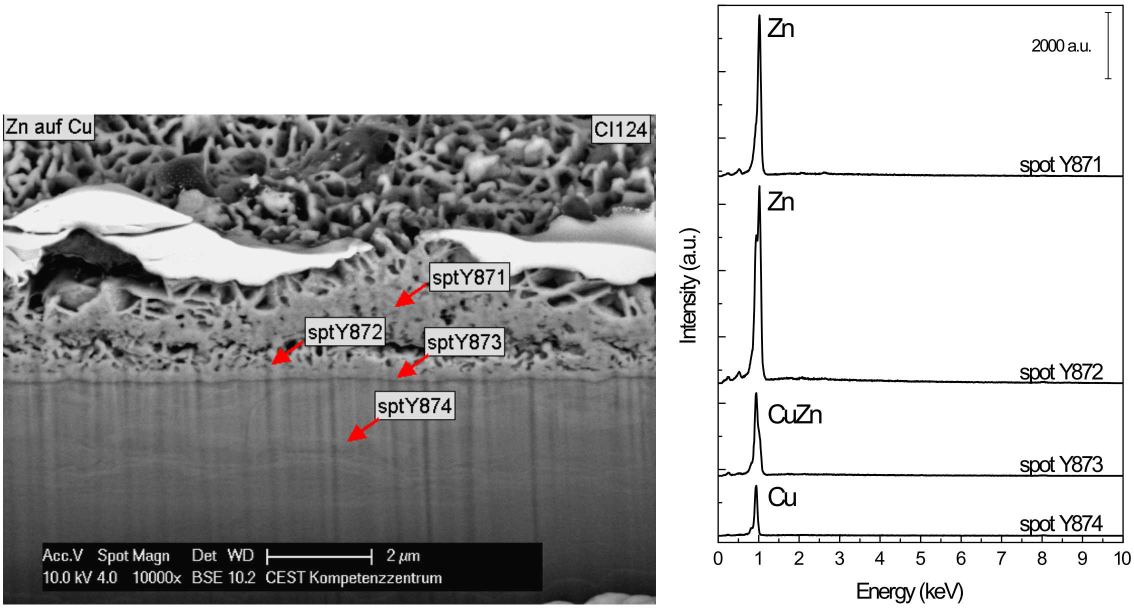

(a) cross section (b) EDX

Figure 5.15. a) SEM micrographs of a cross section from a zinc deposit onto a copper disc substrate. b) EDX spectra of composition analysis at the different spots indicated in a).

In order to characterize the phase of the coating, XRD data was collected from the zinc coating on a copper electrode (Figure 5.16). XRD analysis revealed the presence of three crystalline phases: 33 ± 1 wt % Cu (from the substrate), 56 ± 1 wt % Zn and 11 ± 1 wt % Cu_4Zn. Further quantitative analysis by Rietveld refinement revealed a crystallite size of 17 ± 1 nm Cu, 20 ± 1 nm Zn and 49 ± 5 nm Cu_4Zn.

Cu−Zn alloys are widely used for decorative purposes and engineering applications [192], as for promoting rubber adhesion into steel [193]. However, commercial Cu−Zn plating solutions are cyanide-based, what can lead to environmental and safety problems. Non-cyanide solutions usually suffer from a lack of stability, as it is noteworthy that the reversible standard potentials of Zn and Cu differ by more than 1 V [54]. Alternative

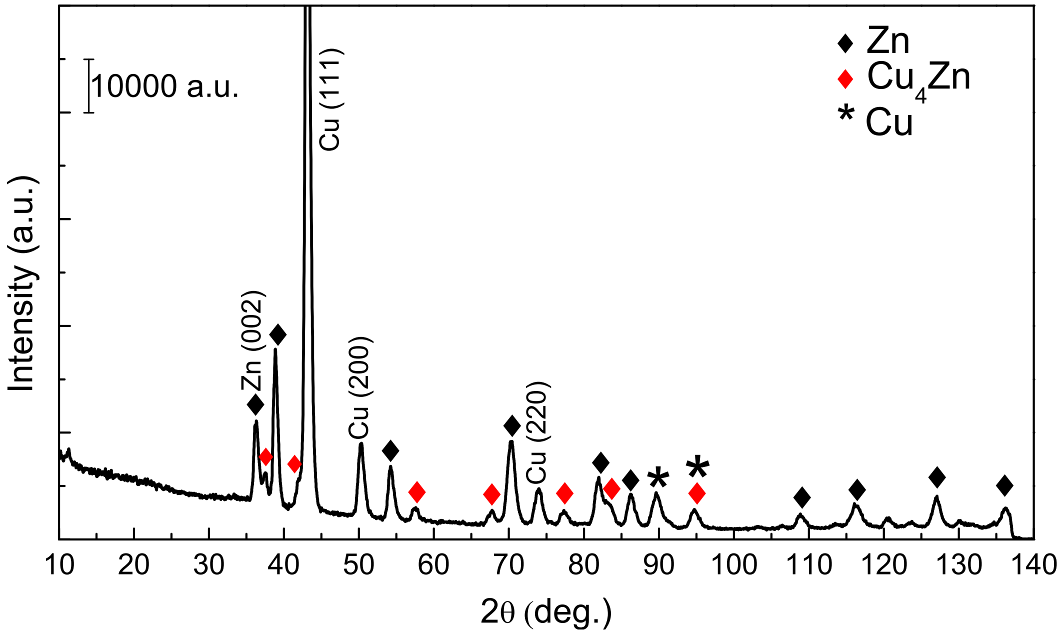

Figure 5.16. X-ray diffraction patterns of electrodeposited zinc at a copper disk from 0.3 mol·L^{-1} $ZnCl_2$ 12CE at 30 °C.

approaches involve depositing alternating layers of Zn and Cu with subsequent heating in order to promote alloying of the layers [55]. This procedure would obviate the undesired method of deposition via cyanide. Nonetheless, a single-step cyanide-free deposition method would be advantageous for such systems.

The electrodeposition of such materials from ionic liquids have been reported for Lewis acidic $ZnCl_2$-EMIMCl electrolytes by two routes: firstly co-deposition of zinc and copper [194] at Ni and W substrates at 80 °C; and secondly, by depositing zinc at copper electrodes at 120 °C [189], which is similar to our route but it requires a higher temperature.

Recently, electroless deposition of copper onto glass-fibre reinforced epoxy substrates followed by electro-deposition of Zn from [EMIM][Tf_2N] (1-ethyl-3-methylimidazolium [bis(trifluoromethyl)-sulfonyl]amide) at 150 °C was reported to lead to Cu−Zn alloy coatings [195].

Deep eutectic solvents comprising 1:2 choline chloride:urea have also been used as electrolyte for deposition of zinc and Ni−Zn alloys on copper electrodes at 70 °C [38].

The electrodeposition of zinc from a 12CE deep eutectic on Cu electrodes at 30 °C was studied. The voltammetric behavior of zinc deposition on copper is similar to that described for gold electrodes (Section 4.2). The morphology and phase of the deposit was characterized by SEM, EDX and XRD. XRD and EDX measurements suggested the formation of Cu−Zn alloys at room temperature.

5.2 Zinc deposition on steel

5.2.1 Voltammetric studies

Electrochemical investigations on a stainless steel disk electrode (1.4404) have been carried out. The cyclic voltammograms of the deep eutectic 12CE without and with 0.3 mol·L^{-1} of $ZnCl_2$ on a stainless steel disk at 30 °C are presented in Figure 5.17.

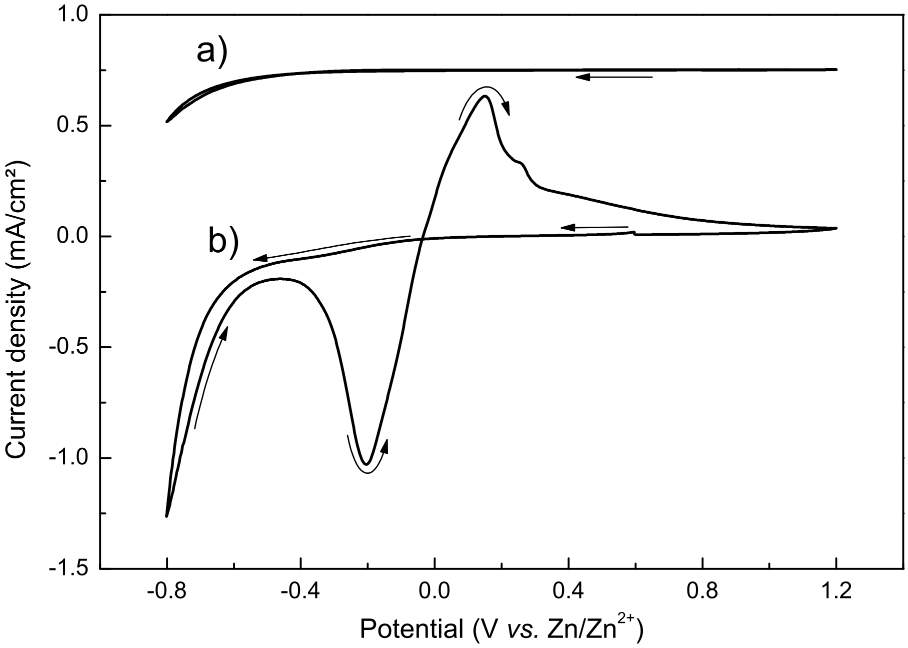

Figure 5.17. Cyclic voltammograms at a stationary steel electrode in: a) 12CE and b) 0.3 mol·L^{-1} $ZnCl_2$ 12CE at 10 mV·s^{-1} and 30 °C. The CV started at +0.5 V *vs.* Zn/Zn^{2+} with a negative sweep direction. Arrows indicate sweep direction.

Differently from platinum, gold and copper substrates, the electrochemical potential window of 12CE on stainless steel (SS) electrodes is much larger and the reduction of the electrolyte with formation of hydrogen becomes significant only at $E \leq -0.7$ V. Similarly to glassy carbon electrodes, electrodeposition of zinc only occurs during the reverse anodic sweep, at −0.24 V *vs.* Zn/Zn^{2+}. In the positive potential range, two anodic peaks were observed, at +0.15 and +0.26 V. The anodic charge (from 0 to +1.2 V *vs.* Zn/Zn^{2+}) was 49 % of that consumed in the cathodic potential range (from 0 to −0.8 V *vs.* Zn/Zn^{2+}), indicating that half of the charge was used for hydrogen evolution. However, the ratio of the total anodic charge over the charge consumed for the backward cathodic peak (integration range between 0 and −0.4 V) was 95 %, confirming that most of the zinc was deposited within this potential range, while at $E \leq -0.6$ V mainly reduction of ROH occurs. The cyclic voltammetric response of Zn:12CE on stainless steel electrodes is similar to that on glassy carbon (Chapter 3). Hence, the same mechanism already suggested for glassy carbon electrodes seems to apply to stainless steel surfaces, with formation of intermediate species Z and potential dependent blocking of the electrode surface by adsorbed species.

The effect of the cathodic potential limit on the zinc deposition was investigated by varying the switching potential while keeping the anodic limit and the scan rate constant (Figure 5.18). In the same way as for glassy carbon, the cathodic peak current on the reverse sweep varies with the cathodic potential limit, which is closely related to the formation of Z species at more negative potentials. The reduction of the electrolyte and the formation of Z, only occur at $E \leq -0.7\,\mathrm{V}$ *vs.* Zn/Zn^{2+}, which is more negative than for GC. This fact becomes evident from the peak current at $-0.24\,\mathrm{V}$, which decreases as the cathodic limit becomes more positive (from -0.8 to $-0.7\,\mathrm{V}$) and almost disappears for a potential limit of $\geq -0.6\,\mathrm{V}$. The ratio between the anodic charge from -0.1 to $+1.2\,\mathrm{V}$ and the cathodic charge from the respective cathodic limit until $-0.1\,\mathrm{V}$ for the cycles at $+0.4$, $+0.5$, $+0.6$, $+0.7$ and $+0.8\,\mathrm{V}$ *vs.* Zn/Zn^{2+} were 49, 39, 59, 67 and 87 %, respectively, indicating that the more negative the electrode is polarized, more parasitic reactions occur, hence decreasing the current efficiency.

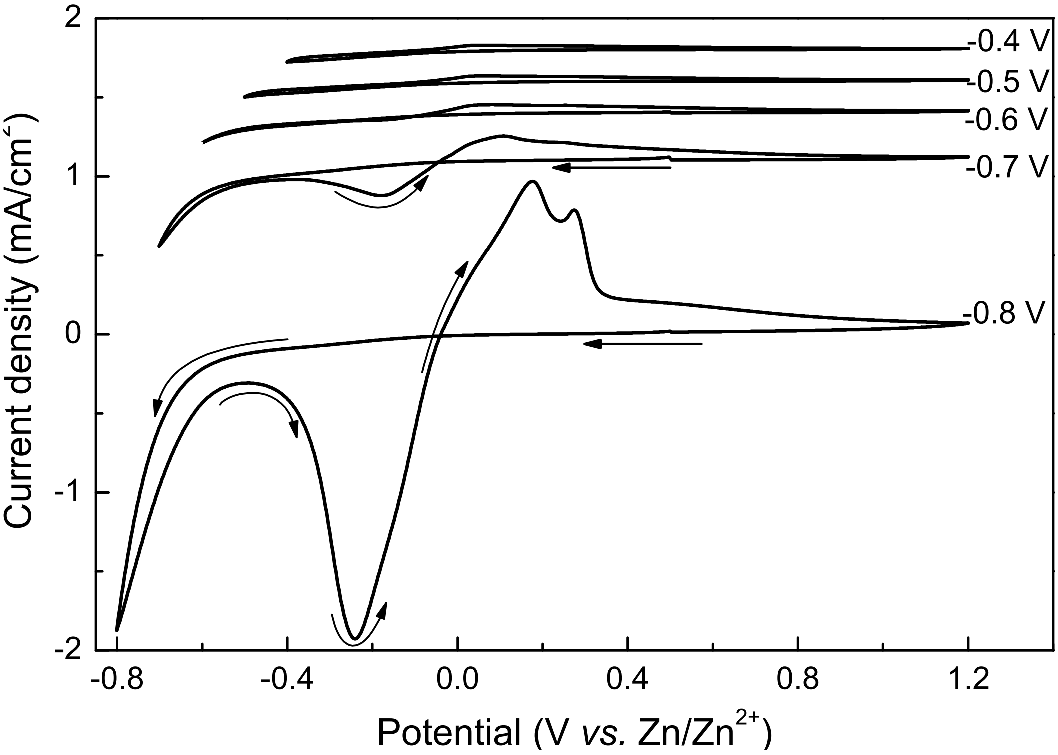

Figure 5.18. Cyclic voltammograms of $0.3\,\mathrm{mol{\cdot}L^{-1}}$ $ZnCl_2$ in 12CE electrolyte ($\nu = 10\,\mathrm{mV{\cdot}s^{-1}}$, $T = 30\,°\mathrm{C}$) at a stationary stainless steel disk electrode starting from $+0.5\,\mathrm{V}$ *vs.* Zn/Zn^{2+} with a negative sweep direction and the indicated cathodic limit. The CVs are offset on the current density scale for clarity. Arrows indicate sweep direction.

Further experiments have been performed varying the scan rate between 5 and 100 mV·s^{-1} while keeping the switching potentials fixed at −0.8 and +1.2 V *vs.* Zn/Zn^{2+} (Figure 5.19). The CVs clearly show that in the case of stainless steel, the kinetics of the zinc electrodeposition reaction during the reverse anodic scan is slow, therefore by increasing the scan rate the peak currents at −0.3 V decrease. Additionally, the second anodic peak at +0.29 V gets more pronounced at low scan rates. This second anodic peak was also observed on glassy carbon substrates, however not so prominent. This can be caused by the size of the two electrodes, which differs significantly. The stainless steel electrodes used have a surface area of 0.95 cm^2, while glassy carbon are 0.7 cm^2 big. The bigger dimension of the SS electrode may cause a stronger saturation of the diffusion layer with zinc ions. Hence, a second anodic peak is observed in the CVs with lower scan rates.

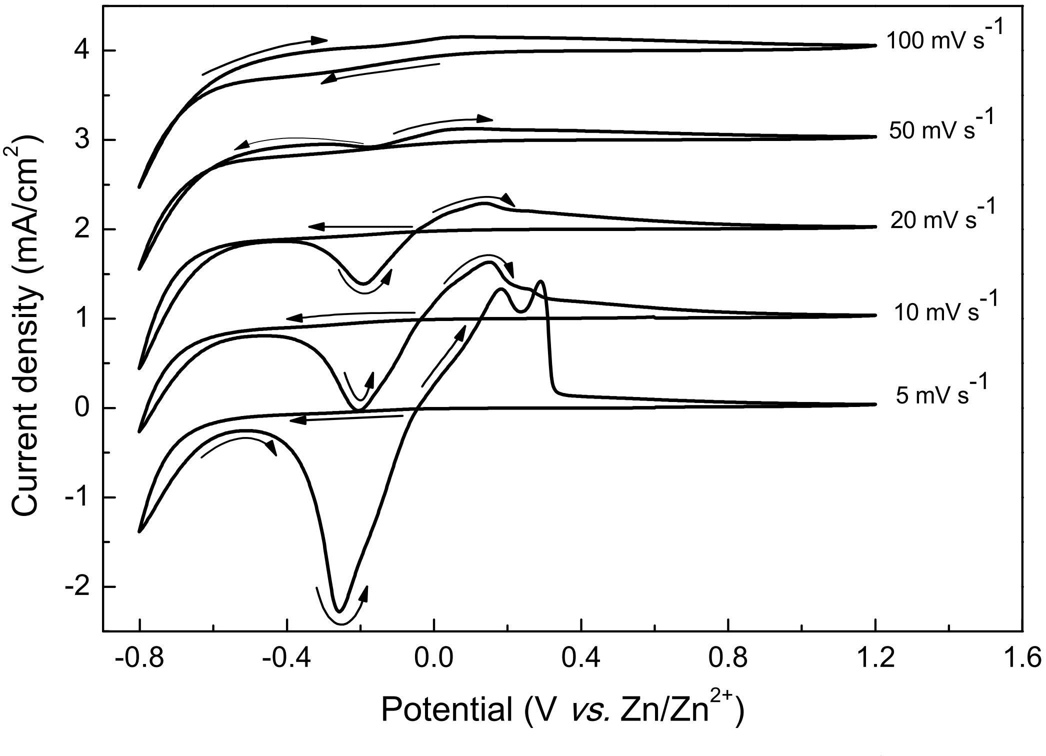

Figure 5.19. Cyclic voltammograms at different scan rates of 0.3 mol·L^{-1} of ZnCl$_2$ in 12CE electrolyte (T = 30 °C) at a stationary steel disk electrode starting from +0.6 V *vs.* Zn/Zn^{2+} with a negative sweep direction. The voltammograms at 10 to 100 mV·s^{-1} are offset by +1 mA·cm^{-2} on the current density axis for clarity.

Experiments using a rotating disk electrode (RDE) have been performed (Figure 5.20). Rotating the electrode caused the cathodic peak at −0.24 V and the anodic peak at +0.18 V *vs.* Zn/Zn^{2+} to decrease in magnitude, whereas the current at the switching potential of −0.8 V was more or less constant. The second anodic peak at +0.27 V practically disappeared with increasing rotation rate, confirming that this peak is due to the saturation of the diffusion layer with Zn^{2+} ions, because when the electrode is rotated the dissolved metal ions are transported into the bulk of the electrolyte, consequently no saturation of the diffusion layer occurs. The ratio of the total anodic over the total cathodic charge was 49, 35, 19, 19, 20 and 19 % for static and 100, 500, 1000, 2000 and 5000 rpm, respectively. Low peak current densities and coulombic efficiencies by applying hydrodynamic force indicate that much of the reducible species Z are transported into the bulk of the electrolyte.

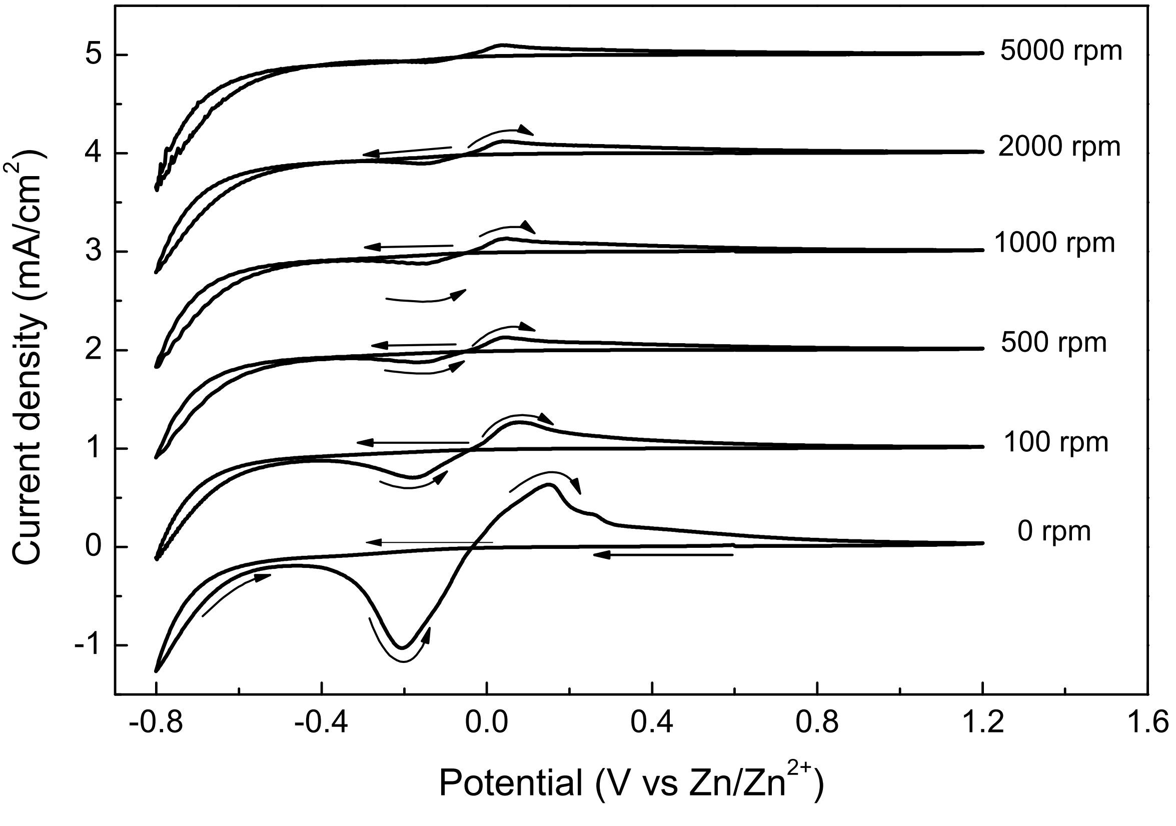

Figure 5.20. Cyclic voltammogams of a stainless steel electrode in 0.3 mol·L^{-1} of $ZnCl_2$ in 12CE at 10 mV·s^{-1} sweep rate, 30 °C and indicated rotation rate. Arrows indicate sweep direction. The voltammograms from 100 to 5000 rpm are offset on the current density axis for clarity.

The electrodeposition of zinc from 0.3 mol·L^{-1} of $ZnCl_2$ 12CE on steel electrodes has revealed to be analogous to that recorded on glassy carbon electrodes. On glassy carbon it was suggested that the active sites on the electrode surface are blocked by adsorbed species (hydrogen, ethylene glycol or choline) at low negative potentials, which gradually desorb at potentials > -0.5 V *vs.* Zn/Zn^{2+}. Zinc was then deposited from a dissolved species Z, formed during the reduction of the electrolyte, giving rise to a cathodic peak at -0.24 V *vs.* Zn/Zn^{2+} on sweeping the potential positive from -0.8 V *vs.* Zn/Zn^{2+} [42–44].

This unusual voltammetric behavior has also been reported for zinc electrodeposition fom 12CE at steel substrates (AISI 304) in a study of the effect of tartrate ions as additive [40]. A cathodic peak on the backward sweep was observed, besides multiple anodic peaks, indicating alloy formation such as Zn−Ni, Zn−Fe and/or Zn−Cr. The authors consider the mechanism of electrode blocking [42], although the formation of Z is not taken into account for the electrodeposition of zinc.

Investigations into the effect of polyethylene glycol 2000 (PEG) on the zinc electrodeposition at ASI 1018 steel substrates from highly concentrated chloride aqueous solutions [196], showed that PEG have a significant influence by producing a cathodic polarization effect associated with its partial adsorption onto the steel surface. Consequently, the mechanism of zinc electrodeposition (from $[ZnCl_4]^{2-}$ species) on steel is modified by the presence of PEG and its interaction with the electrode surface.

5.2.2 Chronoamperometric studies

Chronoamperometry was used to investigate the formation of Z species and the deposition of zinc at different potentials. Similarly to the chronoamperometric studies performed on glassy carbon electrodes (Section 3.2), four step chronoamperometry was carried out (Figure 5.21). In order to investigate the formation of Z, the potential was leapt from open circuit at $E1 = +0.8\,\mathrm{V}$ *vs.* $\mathrm{Zn/Zn^{2+}}$ to more negative potentials $E2$, ranging from -0.2 to $-0.8\,\mathrm{V}$. From $E2$ the electrode was stepped to $-0.2\,\mathrm{V}$ *vs.* $\mathrm{Zn/Zn^{2+}}$ ($E3$), where electrodeposition of zinc takes place according to the CV of the Zn:12CE system on steel (Figure 5.17). Finally, the deposits were reoxidised at $1.0\,\mathrm{V}$ *vs.* $\mathrm{Zn/Zn^{2+}}$ ($E4$). It is important to note that the surface of the steel electrode was renewed by mechanical polishing after each experiment.

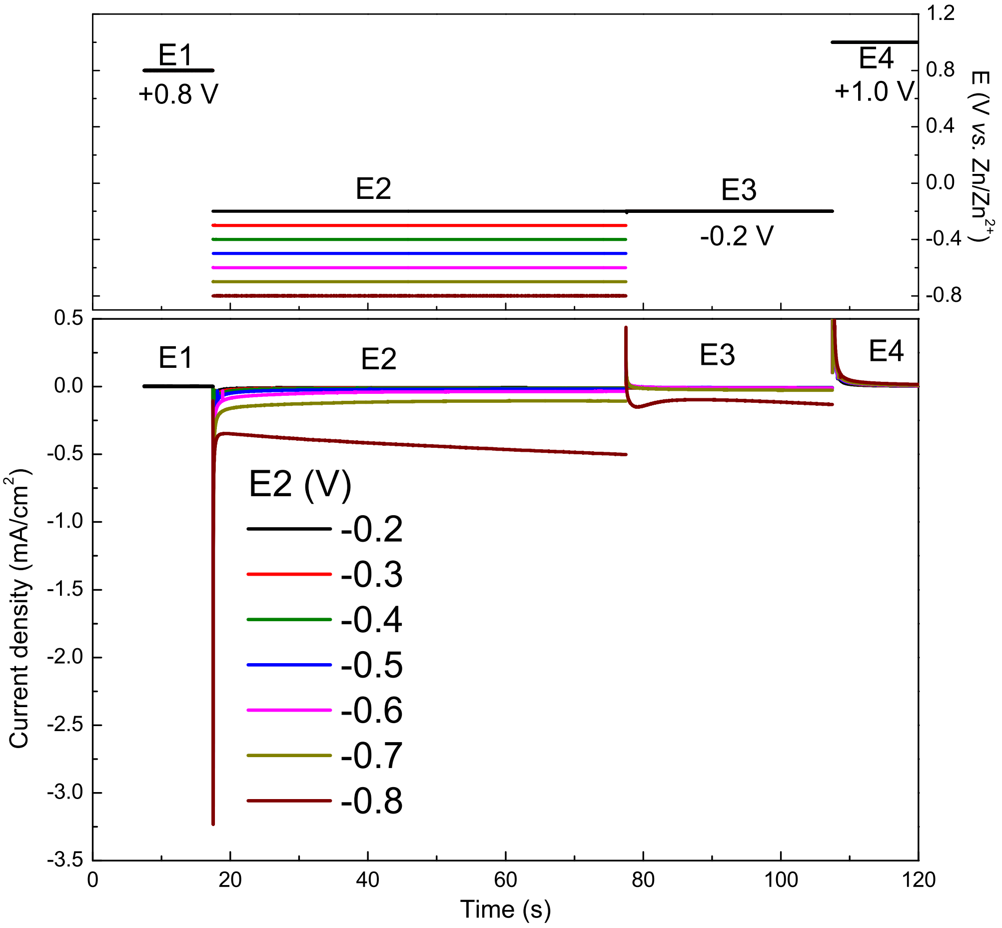

Figure 5.21. Current response for $0.3\,\mathrm{mol{\cdot}L^{-1}}$ $\mathrm{ZnCl_2}$ 12CE on stainless steel at different potentials steps. Applied potentials at $E2$ are indicated.

Figure 5.22 shows a family of transients $E2$ at different step potentials. At this potential, the formation of Z on the stainless steel electrode was investigated in the potential range between-0.2 and $-0.8\,\mathrm{V}$ *vs.* $\mathrm{Zn/Zn^{2+}}$. No nucleation peak is observed in the transients. Instead, the charge continuously increases within the time recorded (60 s). At potentials $\leq -0.7\,\mathrm{V}$ *vs.* Zn/Zn^{2+}, the current and charge was significantly higher than at more positive potentials. At $E2 = -0.8\,\mathrm{V}$ the charge consumed was 5 times larger than at $-0.7\,\mathrm{V}$, indicating that at this potential more electrolyte was reduced. As a result, a higher concentration of Z should be present at such negative potentials.

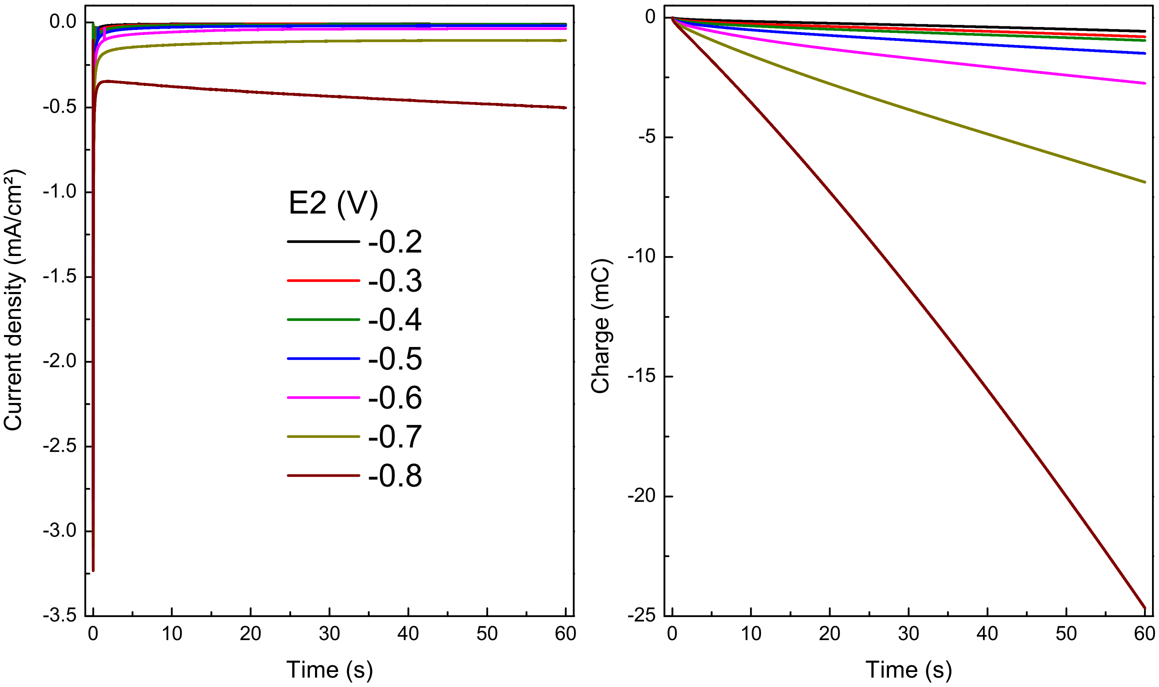

Figure 5.22. Current and charge *versus* time on stainless steel for the indicated potential E2 in $0.3\,\mathrm{mol{\cdot}L^{-1}}$ $ZnCl_2$ 12CE on steel at the step $E2$ at the indicated potential.

Figure 5.23 shows the current transients at the step $E3$ ($-0.2\,\mathrm{V}$ *vs.* Zn/Zn^{2+}), where electrodeposition of zinc from Z is expected to occur. The current density profile and the cumulative charge at this potential was directly dependent on the previous applied potential $E2$.

The presence of a nucleation peak was observed exclusively when the previous step potential was held at $-0.8\,\mathrm{V}$ *vs.* Zn/Zn^{2+}. This observation is consistent with the higher current observed previously at $E2$ for this potential step and also with cyclic voltammetric results, which show the formation of Z only at $E \leq -0.7\,\mathrm{V}$.

Analysing closely only this transient ($E2 = -0.8$ to $E3 = -0.2\,\mathrm{V}$ *vs.* Zn/Zn^{2+}), there is firstly a spike with positive current at very short times ($t < 0.5\,\mathrm{s}$), due to the double-layer charging. Subsequently, the current density increases exponentially up to a maximum $I_{\max}$ reached at a time $t_{\max}$, which is typical of crystal nucleation and growth processes. Finally, the current density declines, because the concentration of Z in the double layer diminishes. Nevertheless, the resulting decrease in current has a different nature

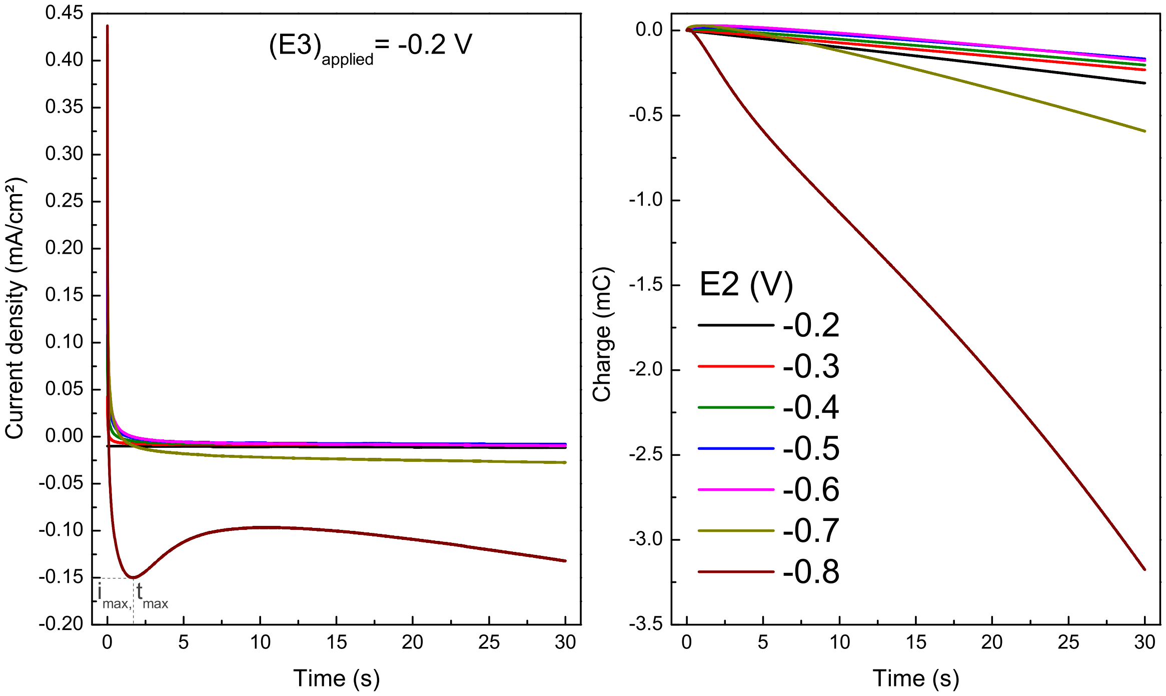

Figure 5.23. Current and charge *versus* time from 0.3 mol·L^{-1} $ZnCl_2$ 12CE on steel at the step $E3 = -0.2\,V$. The correspondent previous potential step $E2$ is indicated.

compared to that exhibited under diffusion limitations [50]. In the case of a Cottrell behavior, the diffusion limited current decays as a result of the increasing diffusion layer thickness (δ). In the present case, the current shows a minimum and then continuously increases again for the last 20 s of measurement, which is likely due to an increase of the electrode area. This behavior is similar to that reported by Smith et al. for the electrodeposition of zinc on Au-coated quartz crystals from 12CE electrolytes [197].

The nucleation and growth of metals on a foreign inert substrate, like stainless steel, can be predicted by several theoretical models [50, 167]. The early stages of an electrochemical reaction involving phase formation are usually associated with two-dimensional (2D) or three-dimensional (3D) nucleation processes [198–202]. The particular shape of the $I - t$ transient in Figure 5.23 [$E2(-0.8\,V) \rightarrow E3(-0.2\,V)$] shows that nucleation and growth processes are involved for Zn deposition. The transient is qualitatively consistent with the models for nucleation of 3D clusters and growth, with a maximum of current density $I_{max} = -0.15\,mA{\cdot}cm^{-2}$ at $t_{max} = 3\,s$.

Among the theoretical models describing the nucleation processes, that of Sharifker and Hills (SH) considers two limiting cases for a 3D nucleation: instantaneous (IN) or progressive (PN) nucleation [203–205]. The instantaneous model represents a situation in which all nucleation sites are activated at the beginning of the potential step experiment, whereas the progressive model refers to a situation in which the nucleation sites become activated gradually as the experiment proceeds.

To distinguish whether IN or PN apply to the electrodeposition of zinc in this case, the experimental data of the $I - t$ transient was normalized to a non-dimensional plot ($(I/I_{\max})^2$ *vs.* $(t/t_{\max})^2$) and analysed together with the theoretical transients given by Eq 5.1 for instantaneous and Equation 5.2 for progressive nucleation. The theoretical and experimental non-dimensional plots are presented in Figure 5.24.

$$\left(\frac{I}{I_{\max}}\right)^2_{IN} = 1.9542\left(\frac{t}{t_{\max}}\right)^{-1} \cdot \left[1 - \exp\left(-1.2564\,\frac{t}{t_{\max}}\right)\right]^2 \tag{5.1}$$

$$\left(\frac{I}{I_{\max}}\right)^2_{PN} = 1.2254\left(\frac{t}{t_{\max}}\right)^{-1} \cdot \left[1 - \exp\left(-2.3367\,\frac{t^2}{t^2_{\max}}\right)\right]^2 \tag{5.2}$$

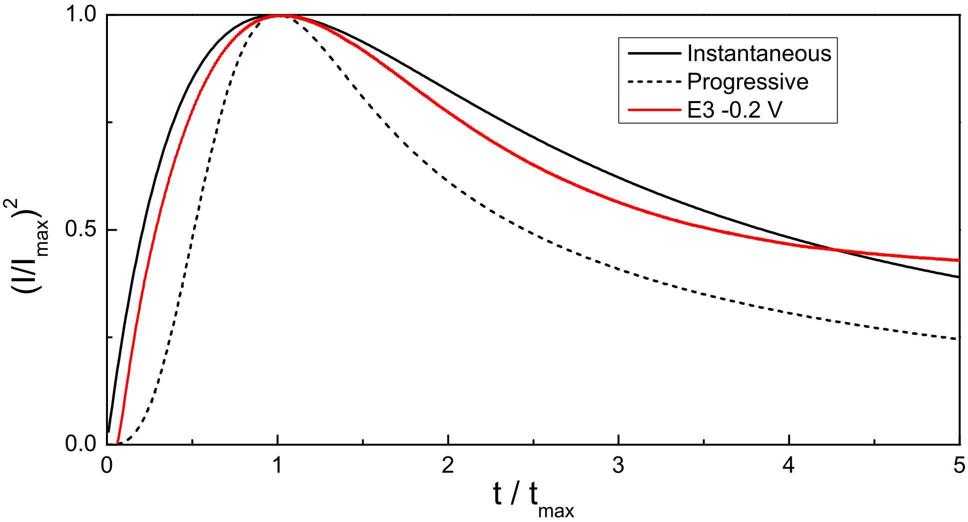

Figure 5.24. Comparison of the dimensionless experimental current-time transient derived on steel electrodes from the data in Figure 5.23 with the theoretical curves for the 3D instantaneous and progressive nucleation.

The result suggests that for $t/t_{\max} \leq 1$ the experimental data follows the 3D instantaneous process, i.e. the nuclei are formed immediately after the potential is set. At $t/t_{\max} \approx 1$ coalescence of the growing nuclei occur, followed by the hemispherical growth of the metal nuclei at $t/t_{\max} \geq 1$. Nevertheless, the experimental non-dimensional plot deviates from the limiting cases of instantaneous and progressive nucleation for $t/t_{\max} \geq 4$, as the theoretical plots follow the Cottrell behavior for diffusion controlled growth. This may indicate that the mechanism of nucleation is instantaneous with kinetic controlled growth, also reported for zinc [24] and silver [206] electrodeposition from imidazolium-based

Since the growth of a new phase occurs at the interface of the electrode and the solution, the nucleation mechanism should vary with the metal being deposited, the properties of the electrode, the electrolyte, the applied potential and the temperature [207]. Table 5.1 summarizes the nucleation mechanisms described in the literature for zinc electrodeposition from deep eutectic solvents, ionic liquids and aqueous solutions at several substrates.

The SH-theoretical comparison for the nucleation of zinc from 12CE at gold-coated quartz [197] and steel substrates [40] resembled the progressive model, whereas at platinum substrates [45] it did not fit to any of the theoretical models. Moreover, at gold substrates the chronoamperometric behavior revealed a very slow process for zinc deposition, also diverging from the diffusion-limited current for $t/t_{\mathrm{max}} \geq 3$. Time-resolved AFM analysis showed a gradual emergence and growth of separate crystallites, which the authors related to the progressive nucleation mechanism [197].

Electrocrystallization of zinc from the deep eutectic choline chloride:urea (12CU) follows the mechanism of instantaneous nucleation for Zn and Ni−Zn alloys [38, 45].

The electrodeposition of zinc from imidazolium-based ionic liquids reported in the literature present many different variables, which makes it difficult to generalize. Although these ionic liquids have the same cation, even comparing similar electrodes, the mechanism may not be the same [23, 24], which indicates that there might be other parameters, as the potential-dependent solvation layer for ionic liquids [6], which may affect the nucleation mechanism.

Electrodeposition of zinc from aqueous solution with a high concentration of chloride, i.e. for $[ZnCl_4]^{2-}$ species, leads to PN on GC electrodes [139, 140] and IN on steel [196], indicating that, as the GC is more inert than steel electrodes, it causes a change in the mechanism from PN to IN.

Table 5.1. Summary of nucleation mechanisms reported in the literature for zinc and zinc alloys deposition from DESs, ILs and aqueous solutions.

Deposit	Substrate	E (V)	Electrolyte	T (°C)	Mechanism	Ref.
Zn	Steel (1.4404)	stepping from −0.8 to −0.2, *vs.* Zn	12CE	30	IN	this
Zn	Steel (AISI304)	−1.5 *vs.* Calomel-ChCl	12CE	40	PN	[40]
Zn	Au	−1.1 *vs.* Ag	12CE	23	PN	[197]
Zn	Pt	−1.25 *vs.* Ag	12CE	40	none	[45]
Zn	Pt	−1.25 *vs.* Ag	12CU	40	IN	[45]
Ni−Zn	Cu	−0.75 *vs.* Ag	12CU	70	IN	[38]
Zn	GC	0.2 *vs.* Al	60-40 mol % $AlCl_3$-EMIMCl	40	PN	[22]
Zn	GC, Ni, W	−0.95 *vs.* Al	25-25-50 mol % $ZnCl_2$-$AlCl_3$-MEIC	30	PN	[23]
Zn	GC, Ni	−0.09 *vs.* Zn	50-50 mol % $ZnCl_2$-EMIMCl	50	IN	[24]
Cu−Zn	W, Ni	+0.08 to −0.02 *vs.* Zn	50-50 mol % $ZnCl_2$-EMIMCl	80	PN	[208]
Zn	Fe	+0.14 *vs.* Zn	40-60 mol % $ZnCl_2$-EMIMCl	90	2D-IN	[209]
Zn−Co	GC, W, Ni	−0.1 *vs.* Zn	40-60 mol % $ZnCl_2$-EMIMCl	80	IN	[194]
Ni−Zn	W	−0.026 *vs.* Zn	34-64 mol % $ZnCl_2$-EMIMCl	150	IN	[210]
Zn	GC	−1.3 *vs.* SCE	aq. 2.8 M KCl 0.01 M $ZnCl_2$	25	PN	[139]
Zn	GC	−1.3 *vs.* SCE	0.2 M $ZnCl_2$	25	IN/PN	[139]
Zn	GC	−1.3 *vs.* SCE	0.6 M $ZnCl_2$	25	IN	[139]
Zn	GC	−1.2 *vs.* SCE	aq. 10^{-2} M $ZnCl_2$, 1 M NH_4Cl	RT	PN	[140]
Zn	Steel (AISI1018)	−1.185 *vs.* SCE	aq. 0.1 M $ZnCl_2$, 2.8 M KCl, 0.32 M H_3BO_3	25	IN	[196]

The oxidation of the zinc deposited on stainless steel is presented in Figure 5.25. Because the oxidation charge is only related to the dissolution of the metal, i.e. there is no contribution of parasitic reactions at $E = +1.0\,\mathrm{V}$, one can correlate this charge to the amount of zinc deposited and consequently to the efficiency of the reaction. From the charge profile, it can be seen that the amount of deposited zinc decreases in the order $E2 = -0.8 > -0.7 > -0.6\,\mathrm{V}$, which is consistent with the mechanism of formation of Z at such potentials and subsequent reduction of Z to Zn at $E3 = -0.2\,\mathrm{V}$.

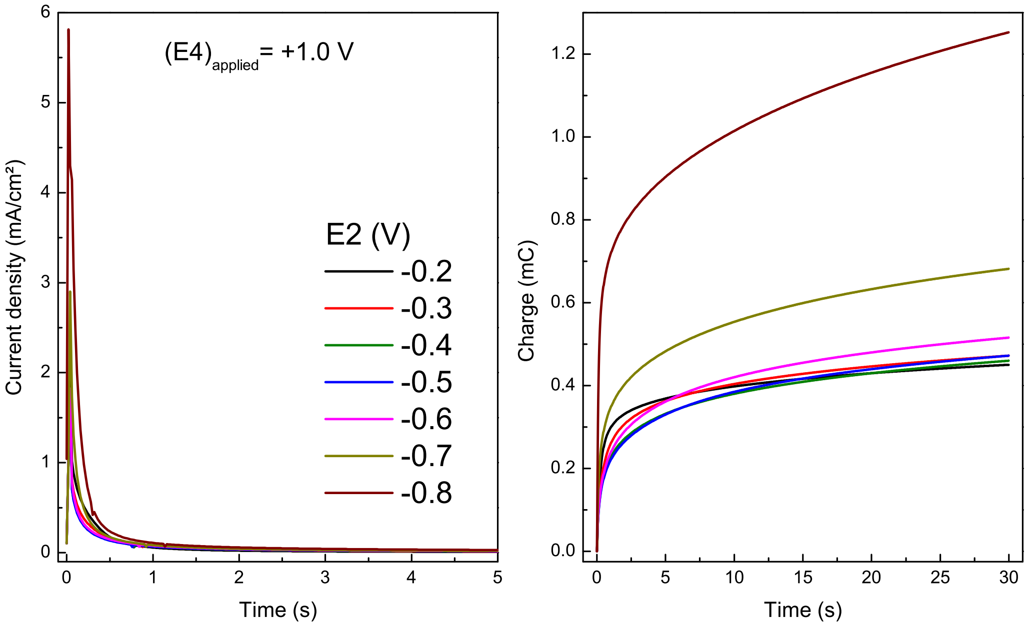

Figure 5.25. Current and charge *versus* time from $0.3\,\mathrm{mol{\cdot}L^{-1}}$ $\mathrm{ZnCl_2}$ 12CE on steel at the step $E4 = +1.0\,\mathrm{V}$.

The coulombic efficiency (CE) has been calculated from the ratio of the charge consumed in $E4$ over $E2$ or $E3$ or the sum of the charge for the two steps $E2 + E3$ (Figure 5.26). The efficiency calculated from $E4/E2$ or $E4/(E2+E3)$ resemble each other due to the higher contribution of the current from $E2$. The CEs decrease as the potential becomes more negative, due to parasitic reactions as hydrogen evolution, in particular at potentials more negative than $-0.6\,\mathrm{V}$. In contrast, the efficiency calculated from $E4$ over $E3$ (plot II in Figure 5.26), shows another trend. The CE is above $100\,\%$ for $E3 = -0.2\,\mathrm{V}$ and continuously increase from $E2 = -0.2$ to $-0.6\,\mathrm{V}$, indicating that most of the zinc was deposited during the previous step $E2$. However, for $E2 \leq -0.7\,\mathrm{V}$ *vs.* $\mathrm{Zn/Zn^{2+}}$, when there is a higher concentration of Z species, the CE decreases to $115\,\%$ for $E2 = -0.7\,\mathrm{V}$ and to $40\,\%$ for $E2 = -0.8\,\mathrm{V}$, indicating that most of the zinc was deposited during the third step. Alternatively, the low $E4/E3$ efficiency at $-0.8\,\mathrm{V}$, might also be due to poor solubility of zincate and insufficient time for oxidation of all zinc deposited (30 s).

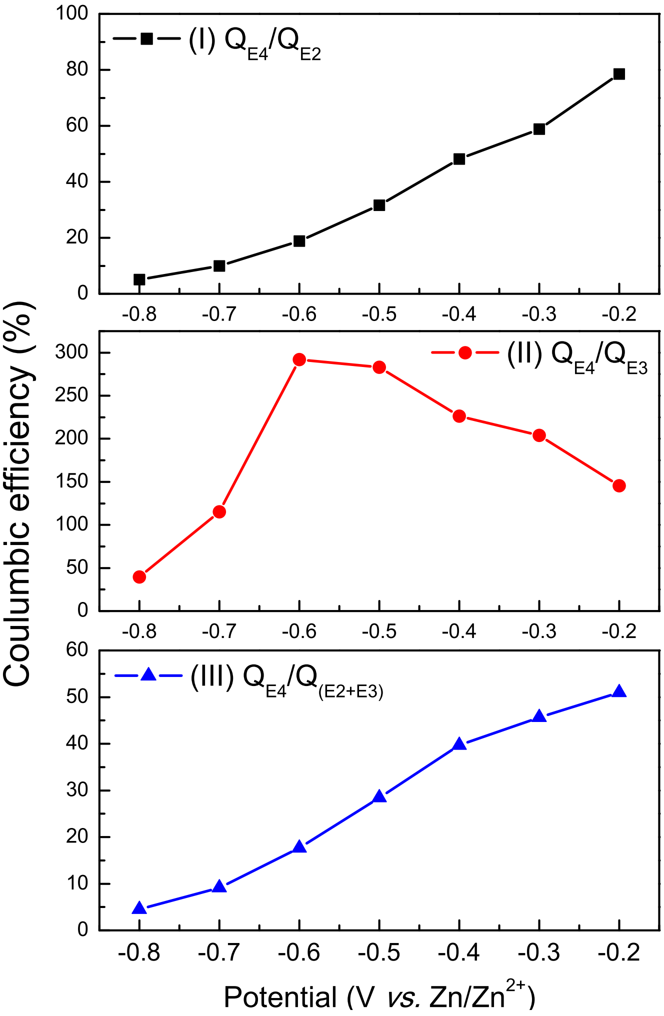

Figure 5.26. Coulombic efficiencies of 4-steps chronoamperometric experiments for 0.3 mol·L^{-1} $ZnCl_2$ 12CE on a steel working disk electrode at 30 °C.

Sampled voltammograms plotted from the charge consumed on steel electrodes in 12CE electrolyte with and without zinc are shown in Figure 5.27. The voltammograms were constructed from the charge consumed up to 30 s at the indicated step potential. Additionally, the charge corresponding to the step $E3 = -0.2$ V is shown. Differently from the other substrates (GC, Pt, Au and Cu), at stainless steel electrodes the charge consumed at more negative potentials is larger for the electrolyte containing zinc than without it, indicating that the overpotential for hydrogen evolution is lower on zinc than on stainless steel. Even compared to glassy carbon, SS is more inert. The charge consumed for the electrodeposition of zinc at $E3$ is also notably higher for $E2 = -0.8$ V compared to all other potentials, which is consistent with the CV presented in Figure 5.17 and all the chronoamperometric data presented.

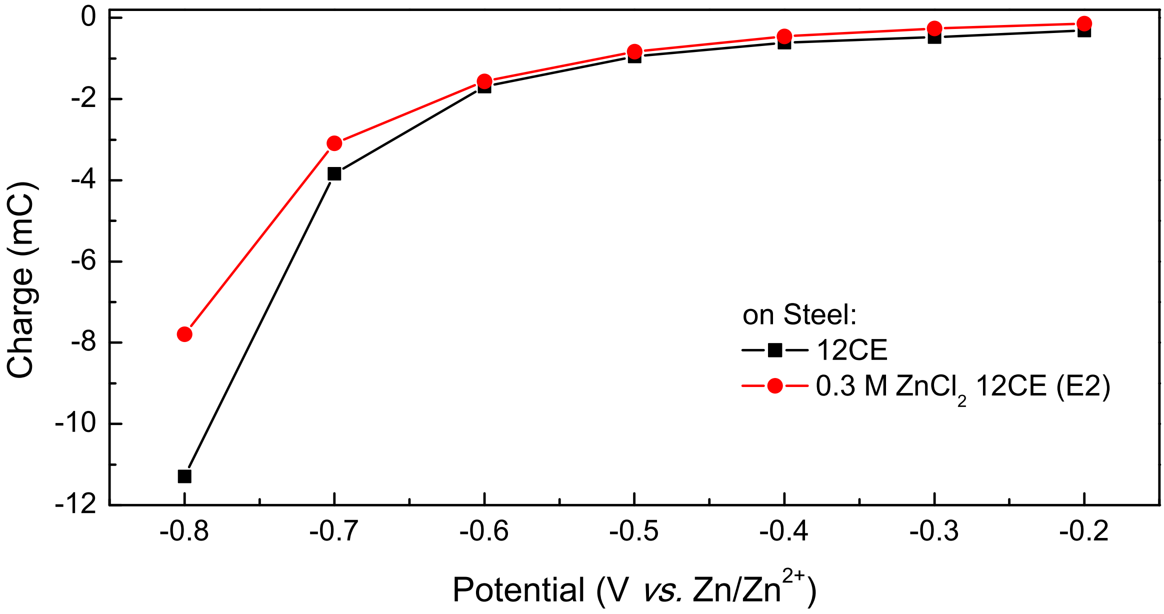

Figure 5.27. Sampled voltammogram constructed from cumulative charge *vs.* time transients from 12CE electrolyte with and without 0.3 mol·L^{-1} ZnCl$_2$. Sample charge collected at 30 s.

6 The substrate effect on zinc electrodeposition

6.1 General mechanism

Figure 6.1 shows the cyclic voltammograms of the 12CE electrolyte without zinc (background CVs) for all working electrodes used: GC, stainless steel, Pt, Au and Cu.

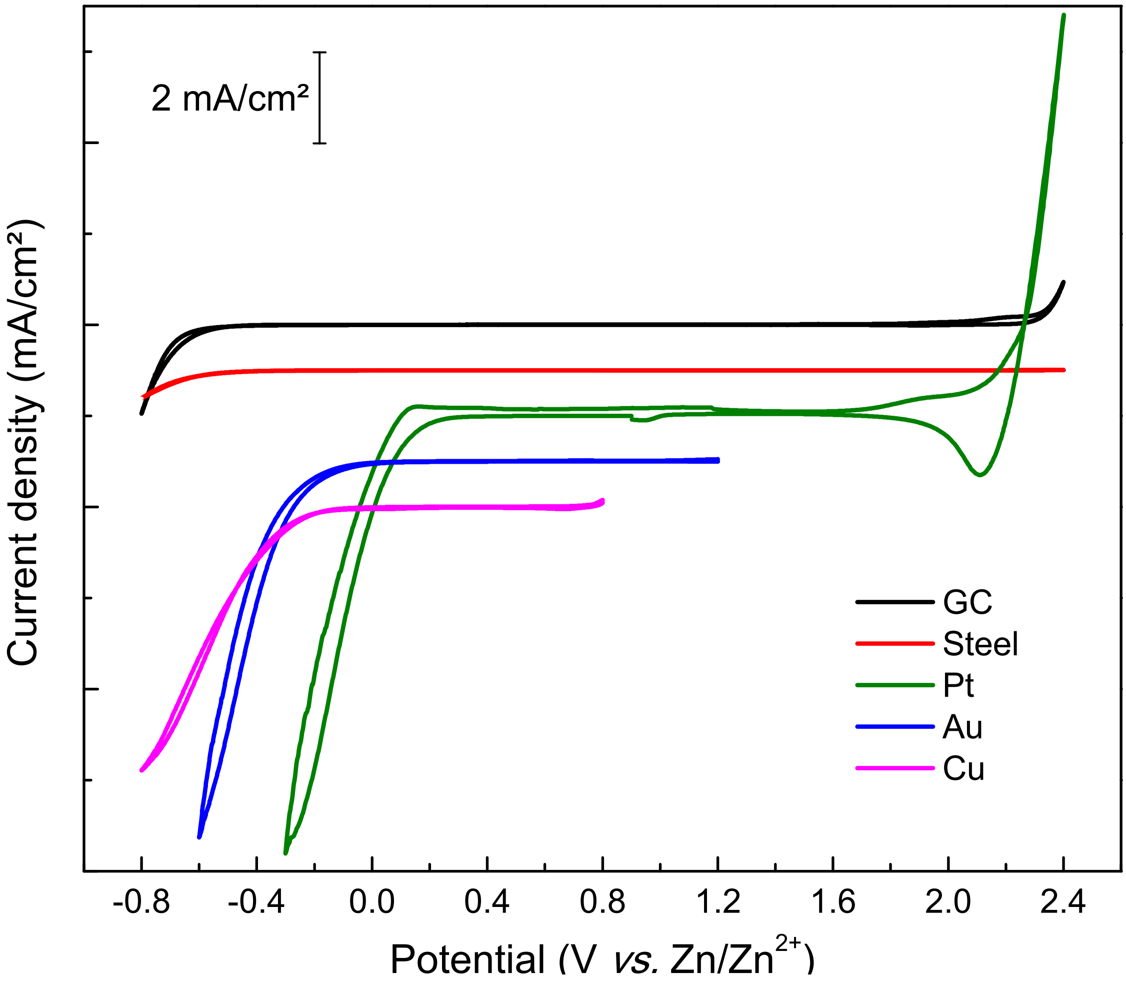

Figure 6.1. Cyclic voltammogram of 12CE electrolyte on GC, stainless steel, platinum, gold and copper disk electrodes at $\nu = 10\,\mathrm{mV{\cdot}s^{-1}}$, $T = 30\,°\mathrm{C}$.

As explained in Subsection 3.1.2, the mechanism of the zinc electrodeposition is closely related to the reduction of electrolyte components ROH to form RO^- ($RO^- \equiv OH^-$, $HOCH_2CH_2O^-$ or $(CH_3)_3N^+CH_2CH_2O^-$) and H_2. This reaction occurs at negative potentials, i.e. at the cathodic limit of the potential window, leading to the formation of Z and subsequently to the reduction of Z to Zn. The cathodic stability of the electrolyte depends strongly on the electrode material and its overpotential for hydrogen evolution. Therefore, the electrodeposition of zinc from this electrolyte depends on the electrode material. In Figure 6.1, it can be seen that the reduction of the electrolyte starts more readily for platinum (+0.1 V), followed by gold (−0.2 V), copper (−0.3 V), glassy carbon (−0.6 V) and steel (−0.7 V). Figure 6.2 shows the CVs of 0.3 mol·L^{-1} $ZnCl_2$ in 12CE at the different electrodes.

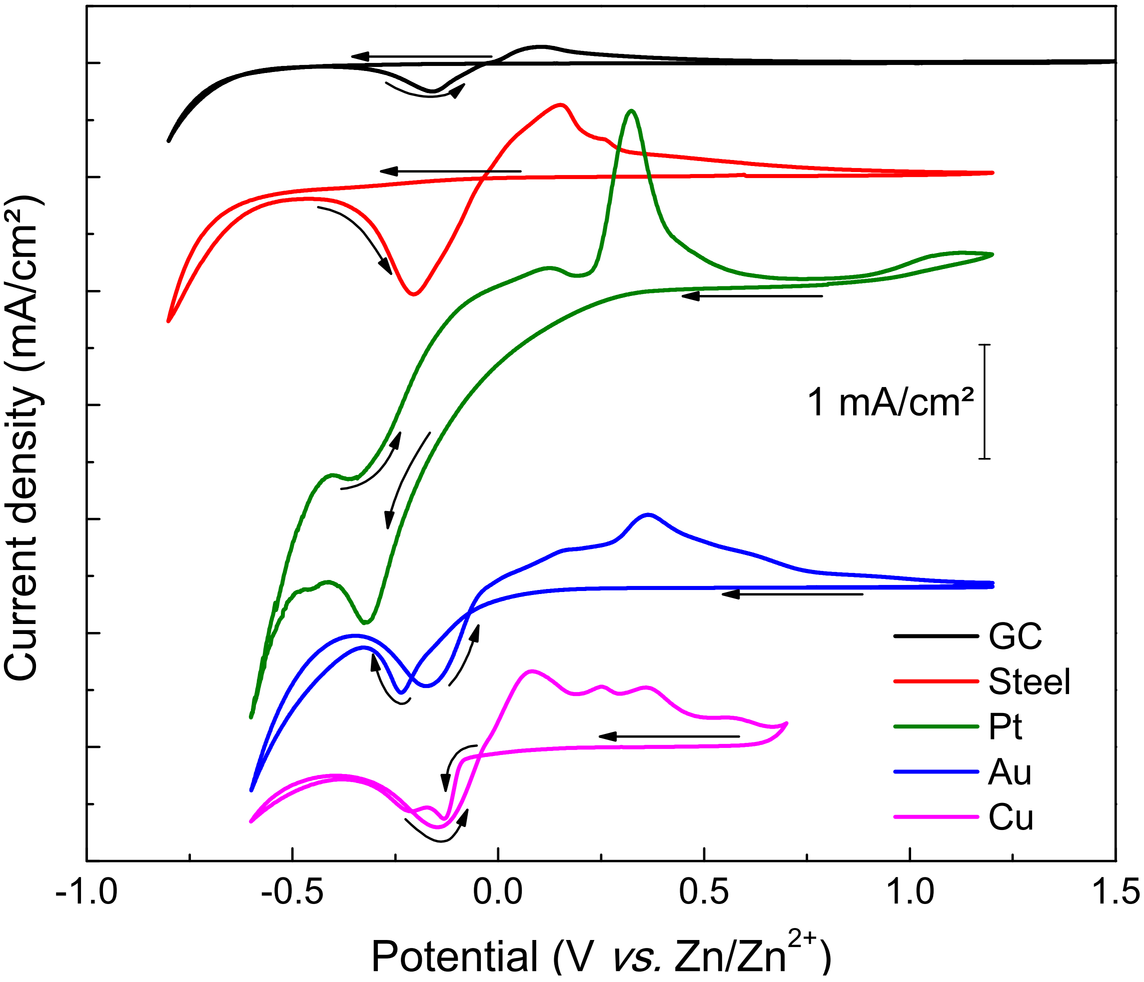

Figure 6.2. Cyclic voltammograms 0.3 mol·L^{-1} $ZnCl_2$ in 12CE at a GC, steel, platinum, gold and copper disk electrodes at $\nu = 10\,mV{\cdot}s^{-1}$, $T = 30\,°C$.

From Figure 6.2, it can be seen that deposition of zinc occurs more readily for platinum, followed by copper and gold. Therefore, in the presence of $ZnCl_2$, a peak related to reduction of Z to zinc is observed on the forward scan. Moreover, at these metal electrodes, a second cathodic peak is also observed on the backward scan. For glassy carbon and steel, which have a higher overpotential for hydrogen evolution, a cathodic peak is only observed on the backward scan.

Blocking effects — probably by Ch^+ species or adsorbed hydrogen — are observed at potentials $\leq -0.4\,\mathrm{V}$ for all substrates, resulting in a decrease of current density for all electrode materials. Desorption of the adsorbed layer on the reverse scan gives rise to a cathodic peak on the anodic return sweep. For Au and Cu, it can also be observed that, as the concentration of Z increases, the backward peak has a higher peak current.

At Pt electrodes, hydrogen evolution occurs to a significantly greater extent than on other electrodes. Therefore, the peaks have much higher current density compared to the CVs of the other electrodes. Moreover, on Pt, Au and Cu, the formation of Zn alloys along with zinc was evidenced by multiple anodic peaks. As GC and stainless steel are inert electrodes, no alloy formation was detected, but only zinc phase.

The results of zinc deposition onto different electrode materials was consistent with the mechanism proposed for GC with the formation of an intermediate species Z with formula $[\mathrm{ZnCl}_{(4\text{-}x)}(\mathrm{RO})_x]^{2-}$, the reduction of Z to Zn and potential-dependent blocking of the electrode surface [42–44]. More on this subject, specially investigations on the blocking effect by *in situ* spectroelectrochemistry is presented and discussed in Chapter 8.

6.2 Conclusions

The electrochemical behavior of the $ZnCl_2$/ChCl/EG electrolyte has been studied at a range of substrates comprising glassy carbon, platinum, gold, copper and stainless steel. The electrodeposition is somewhat complex and results support the hypothesis for the formation of an intermediate compound Z containing deprotonated solvent molecules in the inner coordination sphere of Zn^{2+}, with the formula $[ZnCl_{(4\text{-}x)}(RO)_x]^{2-}$. The zinc deposition mechanism is very sensitive to the nature of the substrate. Stainless steel electrodes are similar to glassy carbon, however, platinum, gold and copper, which have a relatively low overpotential for hydrogen evolution, exhibited distinctly different behavior. The mechanism of zinc deposition at all substrates is associated with the formation of Z, which is dependent on the reduction of the electrolyte to form RO^-. Since the reduction of ROH depends on the overpotential for hydrogen evolution of the electrode material, formation of Z happens at different potentials depending on the substrate. Therefore, electrodeposition of zinc also happens at different potentials.

Potential-dependent blocking of the electrode surface was observed for all substrates. This blocking effect resulted in a cathodic peak on the backward scan in all CVs.

Zinc deposits on platinum and copper have been characterized by electron microscopy, EDX and XRD. The morphology is similar for both substrates, with a nanostructured surface of nanoplatelets. Cross sectional characterization showed formation of alloys at the substrate/zinc interface in both samples. XRD analysis revealed the phases Pt_7Zn_{12} and Cu_4Zn for deposits of zinc on platinum and copper, respectively.

Analysis of the zinc nucleation mechanism on steel electrodes suggests that zinc deposits are formed by progressive three-dimensional nucleation and the growth of the nuclei deviates from the diffusion-controlled models. It is likely that kinetic effects are also influencing the mechanism of the zinc electrodeposition reaction.

Part III

PM-IRRAS of Dynamic Processes at the Glassy Carbon/Deep Eutectic Solvent Interface

7 Vibrational spectroscopic characterization of the DES

Zinc electrodeposition from the deep eutectic solvent comprising choline chloride and ethylene glycol has revealed a complex mechanism with formation of an intermediate reducible species Z containing deprotonated solvent molecules in the inner coordination sphere of the Zn^{2+} [41–44]. Experiments with $NaOC_2H_5$ added to the electrolyte support the hypothesis that Z contains RO^- anions. Moreover, blocking of the electrode surface by adsorbed species such as Ch^+, H_{ads} or EG is also suggested to explain the unusual cathodic behavior observed. In order to elucidate the mechanism of the reaction, chemical information on the involved species is required. Thus, spectroscopic investigations of the deep eutectic solvent 12CE will be presented in this chapter.

7.1 Introduction to PM-IRRAS

Polarization-modulation infrared reflection-absorption spectroscopy (PM-IRRAS) is a surface sensitive infrared method. This technique has been extensively used to investigate chemical processes on metal interfaces [60, 84, 86, 211–213], as unlike other spectroscopic methods, PM-IRRAS allows to distinguish between adsorbates on the electrode surface and species in the solution.

This external reflectance technique allows simultaneous detection of two mutually perpendicular polarized IR beams (p and s) by using a photoelastic modulator [86]. The s polarized radiation has its electric vector perpendicular to the surface of incidence, while the p-polarized is parallel [214, 215]. According to the surface selection rules, the incident p-polarized radiation can be absorbed by adsorbed and solution species whereas the s-polarized is only active for species in solution [85, 216]. Therefore, the s component can be used as a background leading to a surface spectrum by simply subtracting the s from p collected spectra. The resultant is normalized to the intensity of the total incident radiation ($s + p$) so that a surface signal $S(\nu)$ is obtained, according to the following equation:

$$S(\nu) = \frac{R_\mathrm{p}(\nu) - R_\mathrm{s}(\nu)}{R_\mathrm{p}(\nu) + R_\mathrm{s}(\nu)} \tag{7.1}$$

where $R_\mathrm{p}(\nu)$ and $R_\mathrm{s}(\nu)$ are the reflectance in p and s, respectively.

By this mathematical treatment, Equation 7.1 yields an IR spectrum exclusively of adsorbed species [86].

This unique feature of PM-IRRAS was applied to study the interface of a glassy carbon electrode with ethylene glycol, 12CE and $[ZnCl_4]^{2-}$ in 12CE at equilibrium and under potential variation. Although Au or Pt are known for high IR reflectivity, glassy carbon has also shown a high reflectance for the IR beam [84]. Furthermore, GC has the advantage of a higher hydrogen overpotential compared to Au and Pt, besides a well investigated electrochemistry for the DES 12CE. The unconventional electrochemical behavior can be well reproduced in this system. Therefore, this substrate was found to be ideal for the investigation of adsorption effects.

In order to perform *in situ* PM-IRRAS measurements, a spectroelectrochemical cell was designed to perform simultaneous electrochemical and spectroscopic measurements with ionic liquids in a water-free atmosphere. In this chapter, the performance of the cell for electrochemical measurements will be explored, as well as the applications of the cell for *in situ* PM-IRRAS measurements and the spectroscopic investigation of the electrolytes.

7.2 Performance of a PM-IRRA spectro-electrochemical cell

A spectroelectrochemical cell was designed to study the electrode/ionic liquid interface by PM-IRRAS. The design and construction of the cell is presented in Section 2.3. In the current section, the performance of the cell for electrochemical measurements is explored.

The spectroelectrochemical cell (SEC cell) was first evaluated using a standard redox couple. Ferrocene methanol was used as it is soluble, stable and it shows a simple, well-defined one-electron electrochemically reversible redox process in the DES and IL [217–221]. Furthermore, it is commonly used as a redox probe in aqueous electrolyte [222]. The experiments were carried out using the SEC cell in a Faraday cage. A glassy carbon disk ($1.54\,\mathrm{cm}^2$) was used as working electrode at a distance of 5 mm from the optical window. The electrode was polished and rinsed with deionised water and acetone and dried in air prior to use. A platinum wire was used as counter electrode and a Ag wire as quasi-reference.

The cyclic voltammograms of a $1\,m\mathrm{mol{\cdot}L^{-1}}$ of ferrocene methanol (FcMeOH) and $0.1\,\mathrm{mol{\cdot}L^{-1}}$ $\mathrm{KNO_3}$ aqueous solution with different scan rates are shown in Figure 7.1. As the reduction and oxidation of FcMeOH is an electrochemically reversible process, the peak current can be analysed according to the Randles-Sevcik Equation (at 25 °C):

$$I_\mathrm{p} = \left(2.69 \cdot 10^5\right) n^{3/2} A C D^{1/2} \nu^{1/2} \tag{7.2}$$

where I_p is the (anodic or cathodic) peak current (A), n is the number of electrons transferred, A is the electrode area (cm^2), C is the concentration of the electroactive species ($\mathrm{mol{\cdot}cm^{-3}}$) and ν the potential scan rate ($\mathrm{V{\cdot}s^{-1}}$) [51, 131].

From the Randles-Sevcik plot (I_p *vs.* $\nu^{1/2}$) shown in the inset, it can be seen that I_p^ox correlates linearly with the square root of the sweep rate, with a correlation coefficient of 0.996. This confirms that the reaction is electrochemically reversible i.e. diffusion controlled, which allows determining the diffusion coefficient from the measured currents. The diffusion coefficient calculated from the Randles-Sevcik equation for all scan rates has a mean value of $5.5 \cdot 10^{-6}$ $\mathrm{cm^2s^{-1}}$.

The voltammetric behavior of $1\,m\mathrm{mol{\cdot}L^{-1}}$ FcMeOH and $0.1\,\mathrm{mol{\cdot}L^{-1}}$ $\mathrm{KNO_3}$ in ethylene glycol was also monitored for sweep rates from 10 to $1000\,\mathrm{mV{\cdot}s^{-1}}$. As shown in Figure 7.2 insets, the plot of anodic peak current *vs.* the square root of sweep rate yields a straight line. This suggests that the charge transport occurs under diffusion control with a diffusion coefficient of $2.87 \cdot 10^{-7}$ $\mathrm{cm^2\ s^{-1}}$, calculated from the measured peak currents I_p^ox. The diffusion coefficient and the correlation coefficient calculated from the linear regression of I_p *vs.* $\nu^{1/2}$ for FcMeOH in EG are much smaller in EG than in water. This is because EG is more viscous than water, which causes a decrease in the mass transport rate of the electroactive species. It could be shown that the SEC cell has a good response for electrochemical measurements.

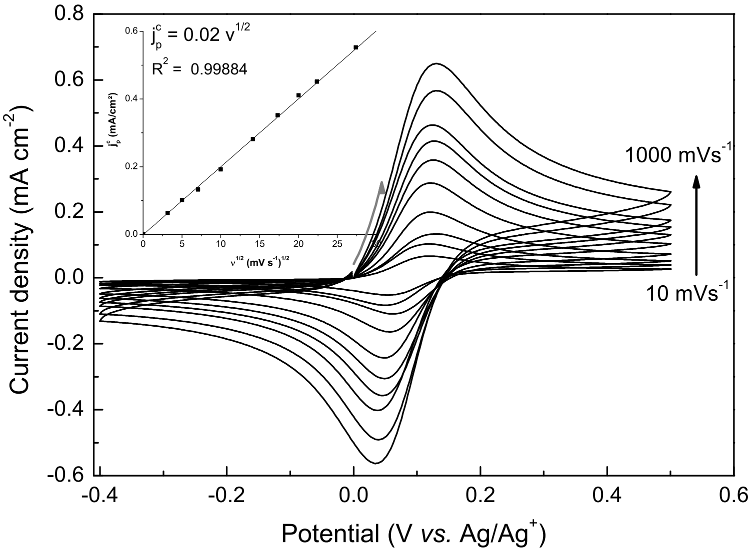

Figure 7.1. Cyclic voltammogram of 1 *m*mol·L^{-1} ferrocene methanol in 0.1 mol·L^{-1} KNO_3 aqueous solution starting from 0 V with a positive sweep direction. The scan rate of the CV was increased from 10 to 25, 50, 100, 200, 300, 400, 500, 750 and 1000 mV·s^{-1}. Arrows indicate sweep direction. The inset shows the plot of the cathodic peak current as a function of the square root of the voltammetric scan rate.

PM-IRRAS is suitable for the study of solid-liquid interfaces, however the thickness of the electrolyte film between the optical window and the electrode surface has to be sufficiently thin to allow transmission of the incident and reflected IR beam, specially because liquid electrolytes are usually good absorbers of infrared radiation [62]. Thus, the solution layer between the optical window and the metallic surface must be within 1 to 100 μm. However, it is well known that thin layer electrochemical measurements may lead to an increase in uncompensated resistance [52]. Therefore, the GC working electrode was aligned against the ZnSe window leaving a small volume of electrolyte in the optical path and the electrochemical response was investigated by cyclic voltammetry. Cyclic voltammetry of FcMeOH in EG as a function of the thickness of the electrolyte is shown in Figure 7.3. In these measurements the distance between the working electrode and the optical window was decreased stepwise by adjusting the micrometerscrew of the cell.

For an electrochemically reversible one-electron transfer, the separation between the anodic and the cathodic peak potential (ΔE_p) should be approximately 59 mV, according

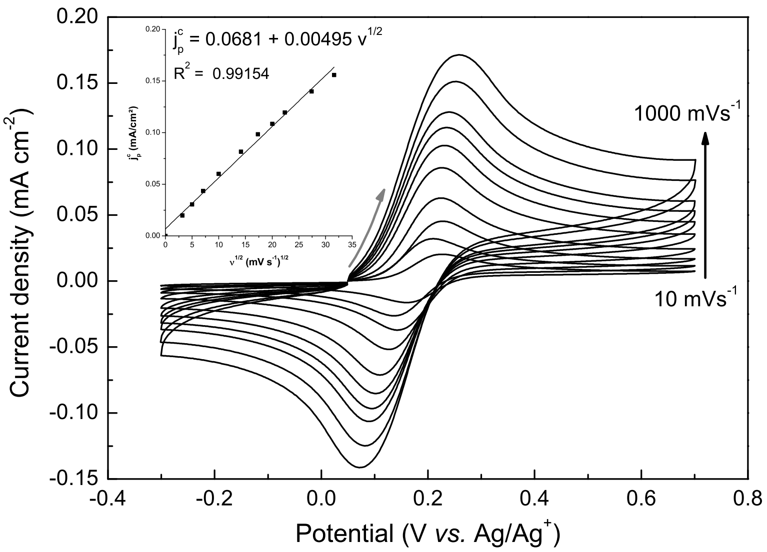

Figure 7.2. Cyclic voltammogram of 1 *m*mol·L^{-1} ferrocene methanol in 0.1 mol·L^{-1} KNO_3 in ethylene glycol starting from 0 V with a positive sweep direction. The scan rate of the CV was increased from 10 to 25, 50, 100, 200, 300, 400, 500, 750 and 1000 mV·s^{-1}. Arrows indicate sweep direction. The inset shows the plot of the cathodic peak current as a function of the square root of the voltammetric scan rate.

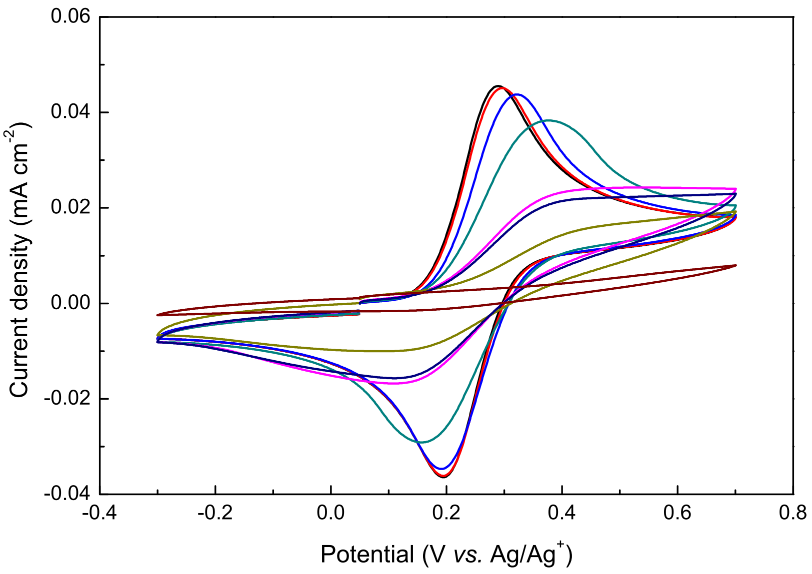

Figure 7.3. Cyclic voltammogram of 1 *m*mol·L^{-1} ferrocene methanol and 0.1 mol·L^{-1} KNO_3 in ethylene glycol starting from 0.05 V with a positive sweep direction with a scan rate of 50 mV·s^{-1}. The distance between the working electrode surface and the optical window was decreased from ▬ 4 mm to ▬ 3, ▬ 2, ▬ 0.9, ▬ 0.2, ▬ 0.13, ▬ 0.08 mm and ▬ 0 (in contact with the window).

to Equation 7.3 [52, 131]. From Figure 7.3 it can be seen that the peak potential difference increases from an initial value of 94 mV for a 4 mm thick layer to 101, 122, 217, 293, 304 and 367 mV to a thickness of 3, 2, 0.9, 0.2, 0.13 and 0.08 mm, respectively.

When the electrode was in contact with the window, no peak was observed, indicating that the *iR* drop increases by decreasing the thickness of the electrolyte film.

$$\Delta E_\mathrm{p} = E_\mathrm{p}^\mathrm{ox} - E_\mathrm{p}^\mathrm{red} = \frac{0.059}{n} \tag{7.3}$$

For thin layer electrochemistry measurements, as long as the cell thickness l is smaller than the diffusion layer thickness for a given experimental time, that is, $l << (2Dt)^{1/2}$, mass transfer within the cell can be neglected. With the potential stepped from a value E_1, where no current flows, to E_2, where a reaction takes place, the concentration of reactant at the electrode surface is essentially zero, and a typical voltammogram in a thin-layer cell would have a symmetrical shape [52]. However, a difficulty in these methods arises, especially when nonaqueous solutions are employed, due to the high resistance of the thin layer of solution. Since the reference and auxiliary electrodes are placed outside the thin layer of electrolyte, one can have seriously non-uniform current distribution and high uncompensated *iR* drop, and therefore the ΔE_p increases for this setup.

The same voltammetric behavior was observed for the eutectic mixture 12CE. Figure 7.4a shows cyclic voltammograms with an electrolyte layer of 5 mm thickness, while in the CVs in Figure 7.4b the thickness was increased from zero (touching the window) up to 0.14 mm. For the first measurement, with a 5 mm thick electrolyte layer, ΔE_p is 66 mV. Thin layer measurements cause this value to increase from 174 mV for a 140 μm thick electrolyte layer up to 337 mV for a 20 μm thick layer.

These measurements indicate that the electrochemical performance of the SEC cell is compromised by the uncompensated resistance (*iR* drop) that has to be minimized in order to control the electrode potential during *in situ* experiments. Although the *iR* drop cannot be avoided, it can be minimized by using a supporting electrolyte, reducing the size of the working electrode or reducing the distance between the working and the reference electrode [223–225]. Since none of these options are possible in our thin layer cell, the alternative strategy is to use the electronic feedback circuit for *iR* compensation available in the Autolab potentiostat, which automatically compensates the indicated resistance. Also, in the electrolyte containing zinc, a CV was recorded and the respective potentials of interest in this CV were used for potential steps measurements.

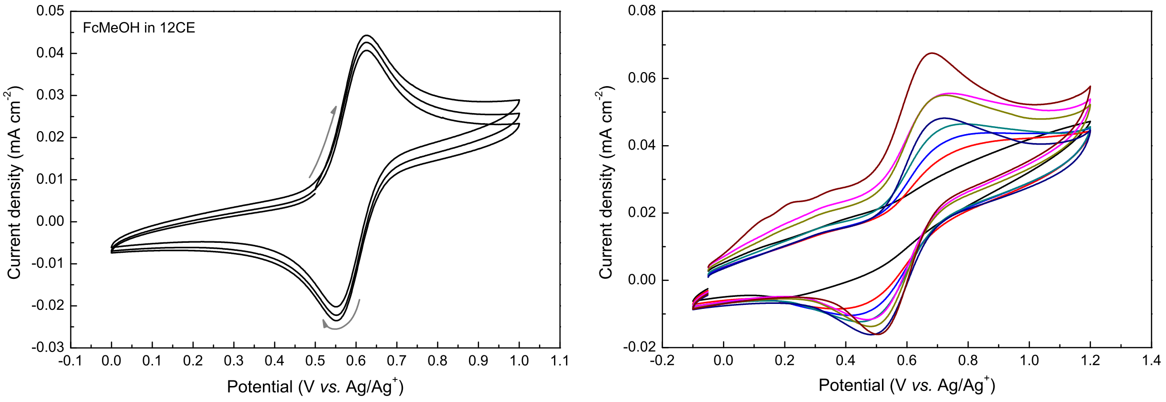

(a) (b)

Figure 7.4. CVs of 1 *m*mol·L^{-1} ferrocene methanol in 12CE at room temperature and with a scan rate of 50 mV·s^{-1} in the SEC cell: a) starting from −0.03 V with a positive sweep direction in a 5 mm thick electrolyte layer. b) starting from 0.05 V with a positive sweep direction and an electrolyte thickness of: — 0 (touching the window), — 0.02, — 0.04, — 0.06, — 0.08, — 0.10, — 0.12 mm and — 0.14 mm.

7.3 FTIR characterization of the bulk electrolyte

Fourier transform infrared spectroscopy (FTIR) is used to analyse and identify structures as well as to study interactions between different groups [57]. The vibrational spectra of the compounds of interest were first investigated and characterized using a spectrometer with attenuated total reflection (ATR) configuration. The spectrum of the bulk electrolyte is important for comparison with the PM-IRRAS surface spectra. Particularly, because interactions of the electrolyte with an electrode surface may result in frequency shifts, different band widths and absorbance values of the same bond [62]. Thereby, hints on the main functional groups interacting with the metal surface could be obtained. In this section ATR-FTIR spectra of ethylene glycol (EG), choline chloride (ChCl), 12CE and $0.3\,\mathrm{mol\cdot L^{-1}}$ $ZnCl_2$ in 12CE (Zn-12CE) are presented and analysed.

The ATR-FTIR spectra of ethylene glycol, choline chloride and the deep eutectic mixture of these two compounds (12CE) are shown in Figure 7.5.

The vibrational spectrum of ethylene glycol [226, 227] as well as that of choline chloride [228, 229] are well described in the literature. However, there are only few investigations on the interaction of ethylene glycol with choline chloride [230, 231] and none on FTIR characterization of the eutectic mixture 12CE. It has been reported that significant band shifts are observed on the FTIR spectrum of choline-based deep eutectics compared with the bands of the neat components [230–237], specially for those bands related to hydrogen bonds. From the IR spectra of the EG and ChCl, it can be observed that there are several band shifts upon formation of a deep eutectic solution.

In the O−H region (from 3800 to $3000\,\mathrm{cm^{-1}}$) in Figure 7.5 it can be noted that the strong ν(O−H) band shifts significantly from $3286\,\mathrm{cm^{-1}}$ in pure EG and $3214\,\mathrm{cm^{-1}}$ in ChCl to $3300\,\mathrm{cm^{-1}}$ when mixing these two components in a 1:2 molar ratio. This shift to higher wavenumbers indicates that the O−H bond becomes weaker. Such a change in EG is presumably due to the presence of Cl^- ions and formation of $H \cdots Cl^-$ hydrogen bonds, which has also been observed in other deep eutectic systems based on 12CE with $MgCl_2$ [231, 232]. Additionally, in the case of ChCl, the relatively sharp O−H band becomes broader due a higher concentration of hydrogen bonds — which is consistent with the fact that EG is a hydrogen-bond donor (HBD) — and due to a decrease of the lattice energy of ChCl and formation of a liquid phase in the deep eutectic solvent [6, 11]. A similar broadening of the O−H band of ChCl has been reported after mixing ChCl in a proportion 1:2 molar with urea [237] and with lactic acid [238] as HBDs. The interaction between the components upon formation of the deep eutectic solvent is represented in Equation 7.4, where $R_4N^+Cl^-$ represents the quaternary ammonium salt and H−O−R, the HBD, which are respectively choline chloride and ethylene glycol in the present work.

$$R_4{-}N^+\cdots Cl^- \;+\; H{-}O{-}R' \;\rightarrow\; R_4{-}N^+\cdots Cl^-\cdots H\cdots O{-}R' \qquad (7.4)$$

The IR spectrum of the eutectic mixture 12CE contains several bands corresponding to choline chloride. Two absorptions originating from the N$-$CH$_3$ group of ChCl are observed at 3033 cm^{-1} and 1477 cm^{-1} [239]. The bands at 955 and 923 cm^{-1} (too small to be visible in Figure 7.5) are attributed to the asymmetric and symmetric stretching modes of C$-$N, respectively [56].

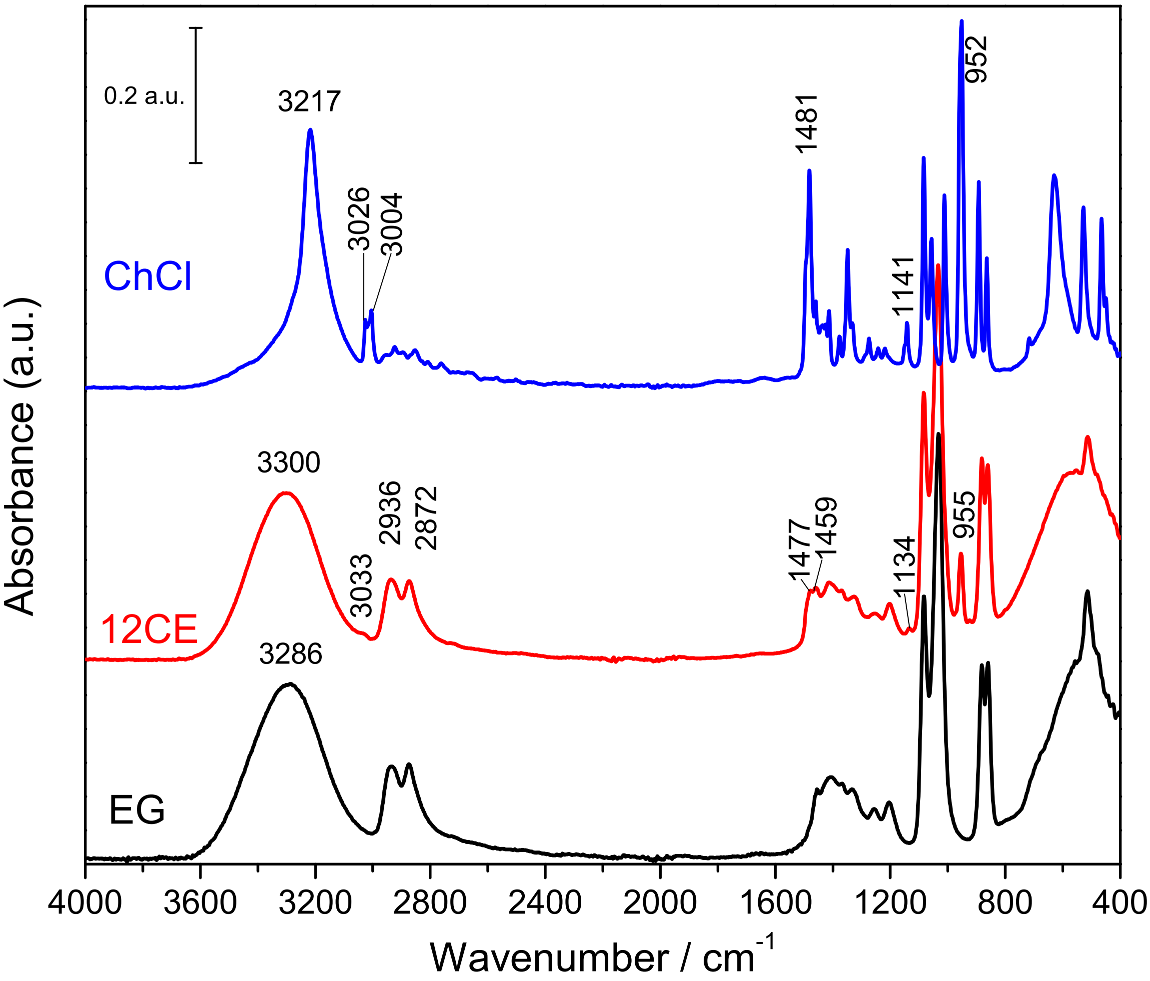

Figure 7.5. FTIR spectra of ethylene glycol (EG), choline chloride (ChCl) and of the eutectic mixture 12CE.

The FTIR spectra of the deep eutectic 12CE, plotted together with the 12CE containing 0.3 mol·L^{-1} of ZnCl$_2$, are shown in Figure 7.6. Since the vibrational bands of zinc halides have wavenumbers below 400 cm^{-1} [240], the modes of zinc chloride can not be characterized by mid-infrared spectroscopy and therefore it will not be addressed in this section. Alternatively, the vibration modes of $[ZnCl_4]^{2-}$ have been characterized by Raman spectroscopy [44], as shown in Chapter 3. From the comparison of these two IR spectra, it can be observed that they are quite similar and only very slight absorbance differences are observed in the fingerprint region (within 1500 and 500 cm^{-1}), however this region is quite difficult to analyse due to the superposition of bands. Moreover, it is noteworthy that the OH stretching mode shifts from 3292 cm^{-1} in 12CE to 3310 cm^{-1} when $ZnCl_2$ is added. The higher frequency of the OH mode in 12CE-Zn, indicates that due to the formation of $[ZnCl_4]^{2-}$, fewer Cl^- ions are available to form hydrogen bonds, therefore the O−H bonds become stronger (higher wavenumber). Furthermore, no bands that could be attributed to δH−O−H, usually at 1650 cm^{-1} [239], are observed, pointing out that both DES are quite dry. The detailed band assignments of ChCl, EG, 12CE and 0.3 mol·L^{-1} $ZnCl_2$ 12CE are shown in Table 7.1.

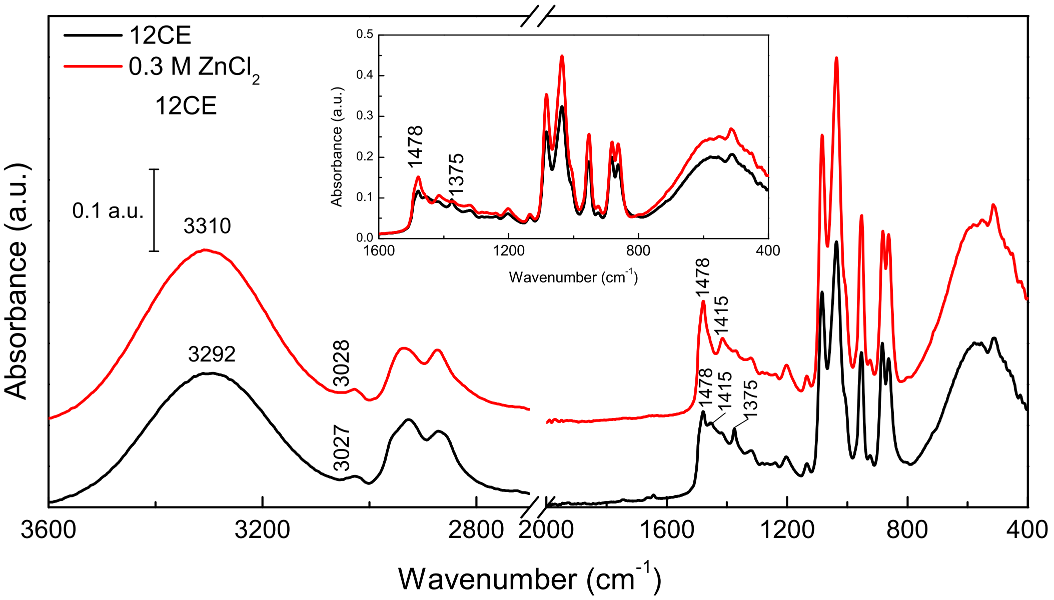

Figure 7.6. FTIR spectra of the eutectic mixture 12CE (black) and 12CE containing 0.3 mol·L^{-1} of $ZnCl_2$ (red).

Table 7.1. Band assignments for FTIR spectra of ChCl, EG, 12CE and 0.3 mol·L^{-1} ZnCl$_2$ 12CE.

ChCl[1]	**EG**[1]	**12CE**[1]	**0.3 mol·L^{-1} ZnCl$_2$ 12CE**[1]	**Assignment**[2]
3217	3286	3300	3312	ν(OH)
3025		3032	3035	$N-CH_3$
3014	2935	2936	2940	$\nu_{as}(C-H)$
3004	2874	2872	2877	$\nu_s(C-H)$
1728				$\nu[CH_2CH_2OH]$
1639				$\delta(H-O-H)$
1480		1477	1477	$\delta_{as}[N^+-(CH_3)_3]$
1459	1454	1459	1459	$\delta(CH_2)$
1413	1408	1413	1416	$\delta(C-O-H)$
1376	1368	1369	1372	$\gamma(CH_2)$
1348	1334	1325	1337	$\gamma(CH_2)$
1274			1280	$\nu C-N$
1242	1256	1253	1267	$\tau(CH_2)$
1219			1238	
	1204	1202	1204	$\tau(CH_2)$
1141		1134	1133	CN
1083	1083	1083	1083	$\nu(C-C-O)$
1056	1032	1032	1036	$\nu_{as}(C-O)$
951		955	953	$\nu_{as}C-N$
		925	923	$\nu_s C-N$
892	881	881	882	$\rho(CH_2)$
864	859	861	862	$\nu(C-C)$
630				$\gamma(C-O-H)$
528	512	512	514	$\delta(C-CO)$
450				$\delta(CO-H)$

---

[1] Frequencies in cm^{-1}

[2] ν = stretching, δ = bending; γ = wagging; τ = twisting; ρ = rocking, *as* = asymmetric; *s* = symmetric.

7.4 PM-IRRAS spectra of the electrolyte on glassy carbon

PM-IRRAS measurements of a glassy carbon surface immersed into electrolyte were carried out at open circuit potential.

The main feature of this technique is the possibility to measure an IR spectrum of the species adsorbed on an electrode surface by modulating the beam polarization between two orthogonal directions, namely perpendicular (s) and parallel (p) to the plane of incidence [86]. The electric field of the s-polarized light interacts destructively with the metal yielding no surface information, but only from the species in solution. On the other hand, the p-polarized light interacts constructively, resulting in an enhanced electric field, which can be used to obtain the spectrum of surface species, whereas the s-spectrum can be used as background [60].

For each measurement a p- and s-polarized spectrum have been obtained. The sum reflectivity itself can be considered as a single-beam spectrum of the liquid phase, due to the dominant light absorption by the liquid phase on the two spectra. The ratio of the difference over the sum of the two spectra, calculated according to Equation 7.1, results in the PM-IRRAS spectrum, which yields information about the species on the surface [86, 214, 215].

The surface spectra of ethylene glycol and 12CE on glassy carbon are shown in Figure 7.7.

From the spectrum of ethylene glycol, it can be observed that the O−H stretching mode of at 3600–3200 cm^{-1} seems to be of two different bands overlapping. In the FTIR of the bulk electrolyte (Figure 7.5), only one band is observed, at 3286 cm^{-1}, whereas in the PM-IRRAS spectrum, the same band has two maxima at 3430 and 3260 cm^{-1}. In this kind of measurement, the absorption by species with the dipole perpendicular to the surface is intensified and thus the presence of two bands may be due to the vibrational modes of two different OH groups, one adsorbed on the glassy carbon surface and a second at the end of the EG chain. Furthermore, the bending mode of C−O−H shifts from 1408 cm^{-1} in the IR spectrum of the bulk liquid to 1421 cm^{-1} on the GC surface.

Similar changes in the vibrational spectrum of ethylene glycol caused by adsorption at a metal surface have been reported for EG on platinum [241], palladium [242], rhodium [243] and silver [244, 245] surfaces using high resolution electron energy loss spectroscopy (HREELS). It was alleged that ethylene glycol interacts with Pt, Pd and Rh through both oxygen atoms (Figure 7.8 b) and decomposes through O−H activation forming ethylenedioxy ($-OCH_2CH_2O-$) surface intermediate species, which were further oxidized to form glyoxal (O=CH−HC=O) by increasing the temperature [241–243]. Monodentate $-OCH_2CH_2OH$ species have been observed by *in situ* IRRAS studies of EG on Mo(110) [246] and Rh(100) [247] surfaces. Monodentate species would allow adjacent O−H groups to interact with each other giving rise to a second νO−H band at lower frequency [246]. According to the literature, our results indicate that EG presumably has its C−C bond axis tilted to the glassy carbon surface instead of parallel, as shown in Figure 7.8a.

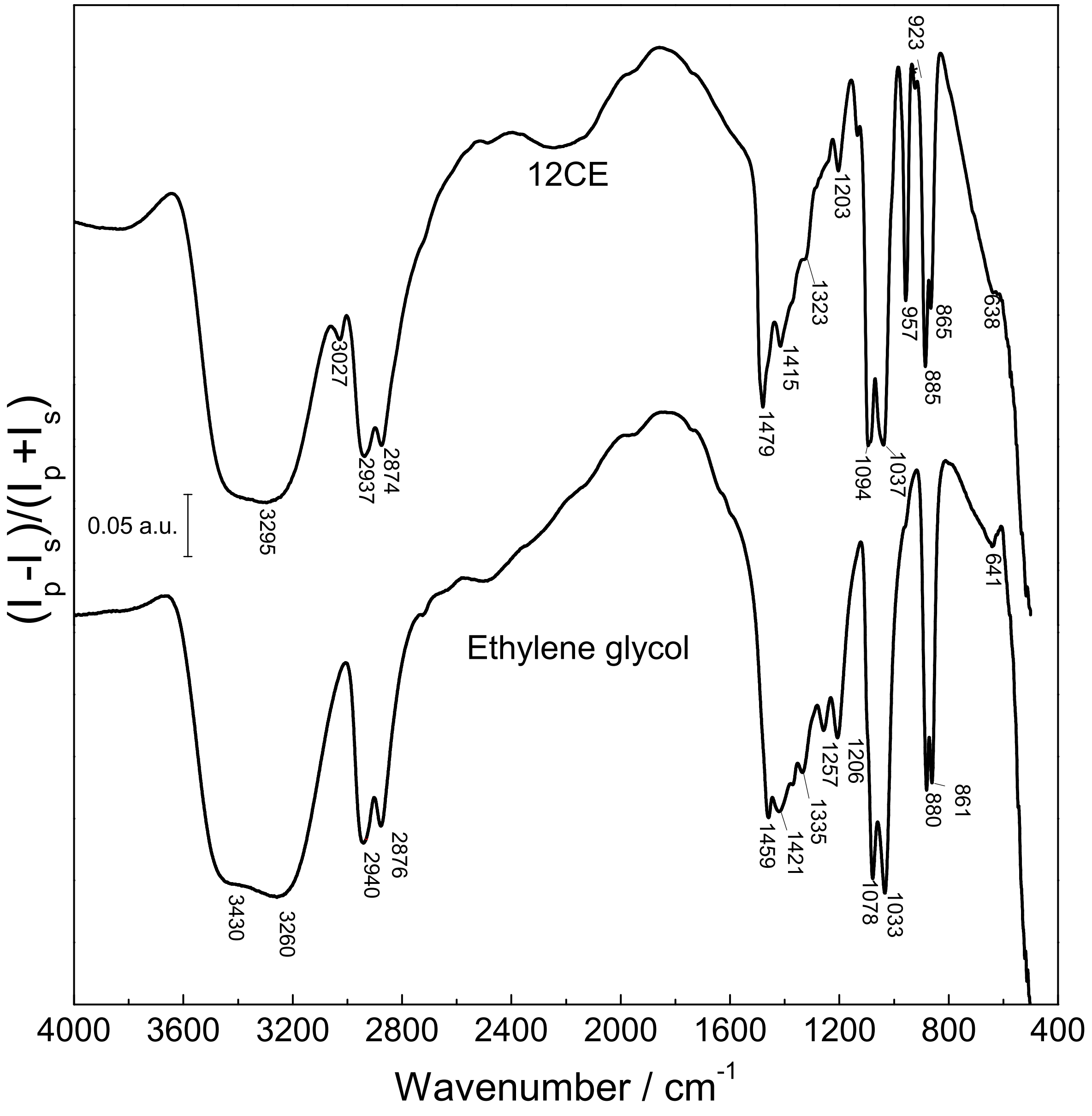

Figure 7.7. PM-IRRAS surface spectrum of the deep eutectic 12CE and ethylene glycol on glassy carbon.

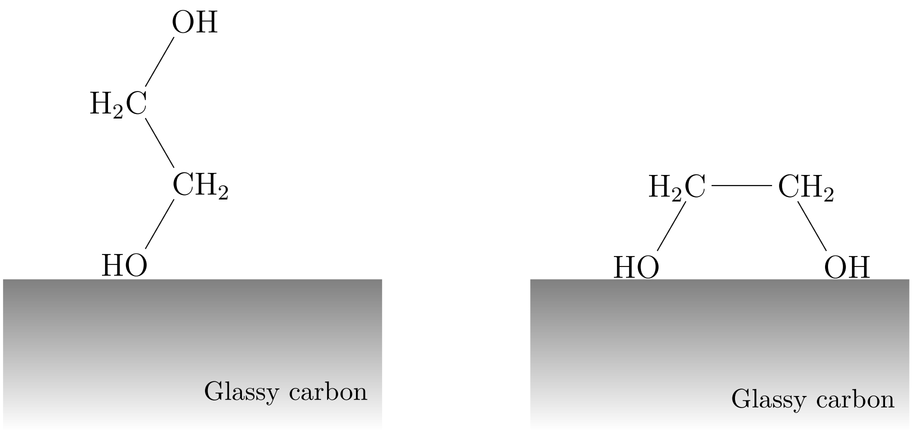

(a) (b)

Figure 7.8. Possible conformations for ethylene glycol on glassy carbon: a) monodentate and b) bidentate conformation.

The spectrum of 12CE shows a very intense absorption for OH at 3295 cm^{-1}. It also seems to be composed of two overlapping bands, similarly to the spectrum of pure EG. The vibrational modes associated with the amine function become stronger and sharper compared to the spectrum of the bulk 12CE. For instance, the asymmetrical bending of $(CH_3)_3N^+$ at 1479 cm^{-1}, which shows a significantly stronger absorption on GC and overlaps with the δCH_2 band at 1459 cm^{-1}. Moreover, the twisting mode of C−O at 638 cm^{-1} shifts by 4 cm^{-1} and is not so well resolved compared to that of pure EG. In none of these electrolytes the band associated with water at around 1650 cm^{-1} was observed, which confirms the water content to be very low.

A comparison of the vibrational modes in the bulk electrolyte and on a GC surface is shown in Table 7.2. It can be noted that most of the C−O vibrations as well as the C−N modes of ChCl show a significant shift or/and increase in intensity when measured on the GC substrate. These data indicate that ethylene glycol is adsorbed at the glassy carbon surface by one O−H functional group. The addition of choline chloride, upon formation of the DES, results in competition for active sites and the choline group $[(CH_3)_3N^+]$ is also preferentially in contact with the surface, which is evident by the increase of the absorption bands related to this group.

Table 7.2. Vibrational modes of EG and 12CE in the bulk liquid phase and on a glassy carbon (GC) surface.

EG[1]	**EG on GC**[1]	**12CE**[1]	**12CE on GC**[1]	**Assignment**[2]
3286	3430	3290	3295	ν(OH)
	3260			
		3032	3027	$\nu[N-(CH_3)_3]$
2935	2940	2936	2937	$\nu_{as}(C-H)$
2874	2876	2872	2874	$\nu_s(C-H)$
	2725		1647	$\delta(H-O-H)$
		1477	1479	$\delta_{as}[N^+-(CH_3)_3]$
1454	1459	1459	—	$\delta(CH_2)$
1408	1421	1413	1415	$\delta(C-O-H)$
1368	1370	1369	1367	$\gamma(CH_2)$
1334	1334	1325	1323	$\gamma(CH_2)$
1256	1257	1253	—	$\tau(CH_2)$
1204	1206	1202	1203	$\tau(CH_2)$
		1134	1133	C−N
1083	1078	1083	1083	$\nu_s(C-O)$
1032	1033	1032	1036	$\nu_{as}(C-O)$
		955	953	$\nu_{as}N^+-(CH_3)_3$
		925	923	$\nu O-CCN$
881	880	881	882	$\rho(CH_2)$
859	861	861	862	$\nu(C-C)$
	641		638	$\tau(C-CO)$
512		512	514	$\gamma(C-CO)$

---

[1] Frequencies in cm^{-1}

[2] ν = stretching, δ = bending; γ = wagging; τ = twisting; ρ = rocking, *as* = asymmetric; *s* = symmetric.

PM-IRRAS measurements of 12CE solutions with different concentrations of zinc chloride are illustrated in Figure 7.9. The addition of zinc chloride to the deep eutectic does not change significantly the IR spectrum of the 12CE solution, because the vibrational modes of $[ZnCl_4]^{2-}$ have wavenumbers lower than 400 cm^{-1}. Moreover, the complexes and intermediates that may be formed with zinc are only present upon applying a sufficiently negative electrode potential, therefore different species are unlikely to be detected at open circuit potential. Nevertheless, it can be noted that the $\nu(O-H)$ band slightly shifts to higher wavenumbers, indicating that the hydrogen bonds become stronger by increasing the concentration of $ZnCl_2$. This is likely so, because much of the Cl^- ions are complexed with zinc to form $[ZnCl_4]^{2-}$, strengthening the O−H bonds in the $R-O-H\cdots Cl^-$ network. Yet, this shift in the O−H band is difficult to evaluate because there is no band maximum.

A slight shift is also observed for the bending mode of the C−O−H at 1415 cm^{-1} and twisting of the C−CO chain at 638 cm^{-1}. These shifts indicate changes of the local environment of the C−O−H bonds by addition of $ZnCl_2$.

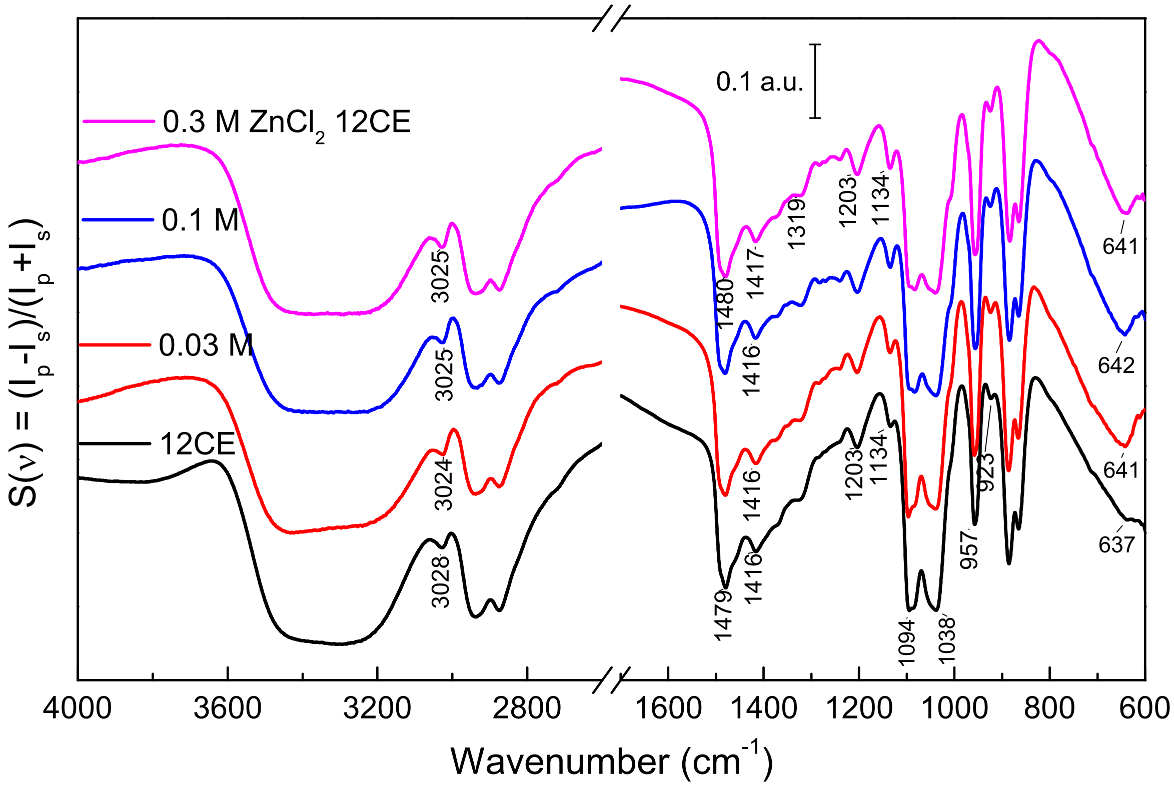

Figure 7.9. PM-IRRAS surface spectra of 12CE on glassy carbon with different concentrations of $ZnCl_2$.

8 Kinetic PM-IRRAS studies of the glassy carbon/deep eutectic electrolyte interface

8.1 PM-IRRAS at open circuit potential

Ethylene glycol and 12CE showed to adsorb strongly on glassy carbon, yielding well-resolved surface spectra. During our measurements it was observed that the absolute IR signal of EG and 12CE increased significantly when the spectrum of the electrolyte was recorded firstly on a clean glassy carbon surface and after some resting time. The open circuit potential (electrochemical equilibrium) can be significantly different from the potential of zero charge (PZC). Therefore, electrostatic interaction of the electrode with the ionic liquid cannot be disregarded. Hence, it is likely that the molecules of the ionic liquid assemble themselves in order to decrease the interface energy between the liquid phase and the glassy carbon surface at open circuit potential [248]. This self-assembly of the molecules of the deep eutectic solvent presumably alter the transition dipole of the molecules in the vicinity of the surface, causing an increasing PM-IRRAS signal — if the resulting conformation has a transition dipole perpendicular to the metal surface [61, 249]. Therefore, the change in PM-IRRAS absorbance spectrum may be associated with an increase in population and molecular orientation on the electrode.

In this section we present an investigation on the adsorption and self-assembly of ethylene glycol, 12CE and $0.03\,\mathrm{mol{\cdot}L^{-1}}$ $ZnCl_2$ 12CE on a glassy carbon surface at open circuit potential as a function of time.

8.1.1 Ethylene glycol

The experiments of time-dependent adsorption of ethylene glycol were carried out starting from a cleaned and dry glassy carbon surface. The electrolyte was added to the cell under nitrogen flow. Since the absorption of surface species changes with time, the spectra are presented as a ratio of spectral intensity at a sample time (t_x) over that at the starting time (t_1), which is the first spectrum measured ($\Delta S(\nu)_t$). The initial time that the adsorption process starts would be time zero (t_0), which is the first contact of the electrolyte with the electrode. This is about 5 min before the first measurement t_1. Figure 8.1 shows surface spectra of ethylene glycol as a function of time. The evolution of the bands of ethylene glycol on a GC surface was monitored from $t_1 = 5$ min up to 1440 min (24 h) at open circuit potential.

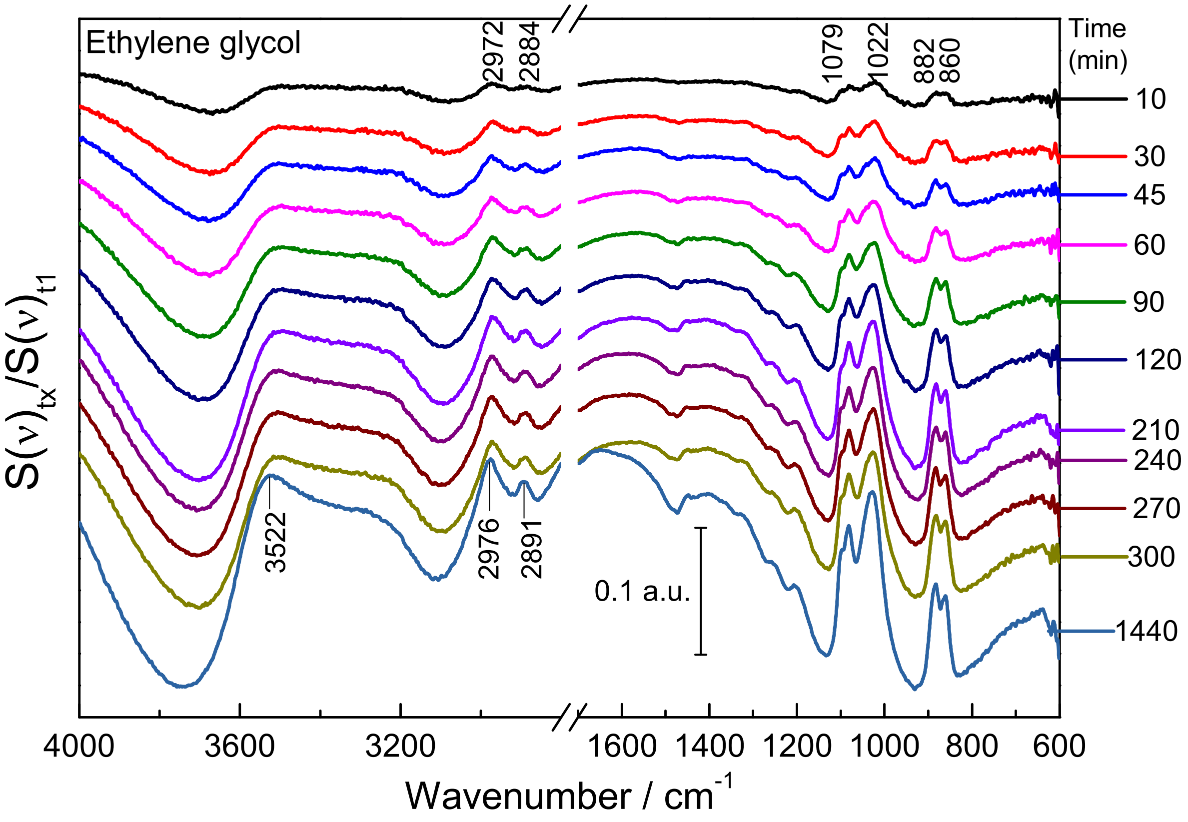

Figure 8.1. PM-IRRAS surface spectra of ethylene glycol on glassy carbon recorded at various time intervals after introduction of the solvent. The reference spectrum was recorded immediately after the glassy carbon had been immersed in the electrolyte (approximately 5 min). All measurements were made at open circuit potential.

The absorption bands, specially those related to O−H and C−O groups increase considerably within 24 h. In the R−H stretching region, the ν(O−H) at 3700–3100 cm^{-1} and ν(C−H) at 3100–2850 cm^{-1} increase substantially. In the fingerprint region (1600–800 cm^{-1}) there is a considerable increase in the absorption of the bands for ν(C−O) vibrations at 1130–950 cm^{-1} as well as for ρ(CH_2) and ν(C−C) skeleton vibrations of ethylene glycol at 930–820 cm^{-1}. At lower wavenumbers, the out-of-plane bending of the O−H group at 650 cm^{-1} also increases with time, which is consistent with the increase of the O−H stretching absorbance [56, 58, 174, 239]. The temporal evolution of the band areas are shown in Figure 8.2 together with the corresponding bands after baseline correction.

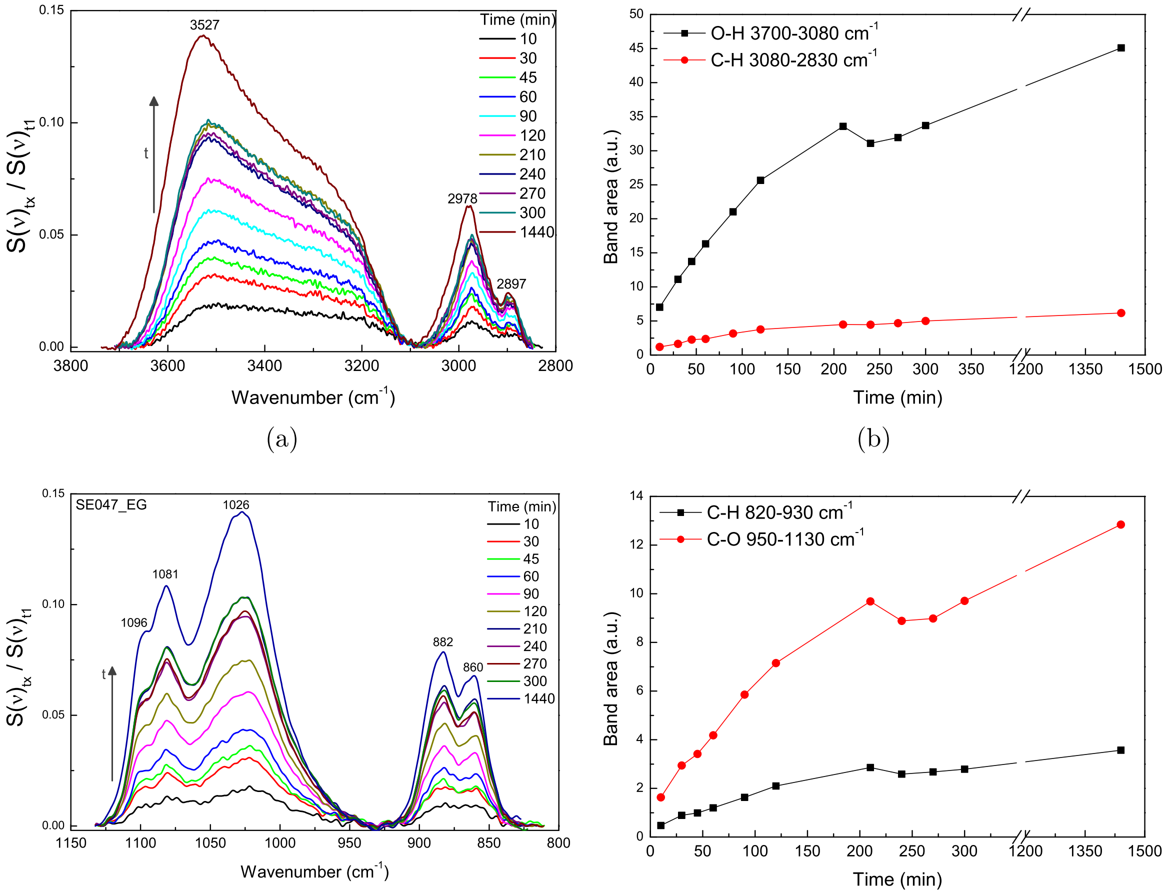

(a) (b)

(c) (d)

Figure 8.2. Temporal evolution of some bands of ethylene glycol on glassy carbon and its respective band area *versus* time (for clarity, b) and d) graphics have a gap between 400 and 1200 min).

The integration of the bands shows that the area corresponding to O–H, C–O and C–H modes increase with time. While the ν(C–O) and ν(O–H) increase constantly over 24 h, the C–H bands show more of a saturation profile. Additionally, the O–H stretching at 3528 cm^{-1} turns much more intense related to that at 3260 cm^{-1}. It is likely that these two peaks are related to two different modes of the O–H bond. Presumably, one group is adsorbed at the surface of GC, and therefore the O–H bond becomes weaker (with a lower wavenumber) and a second group, with lower intensity, would correspond to the functional group at the end of the molecule. The two possible conformations for the ethylene glycol on a glassy carbon surface are represented in Figure 8.3a.

As discussed in the previous subsection, the two possible conformations of EG would influence the wavenumber and intensity of the O–H stretching in the PM-IRRAS surface

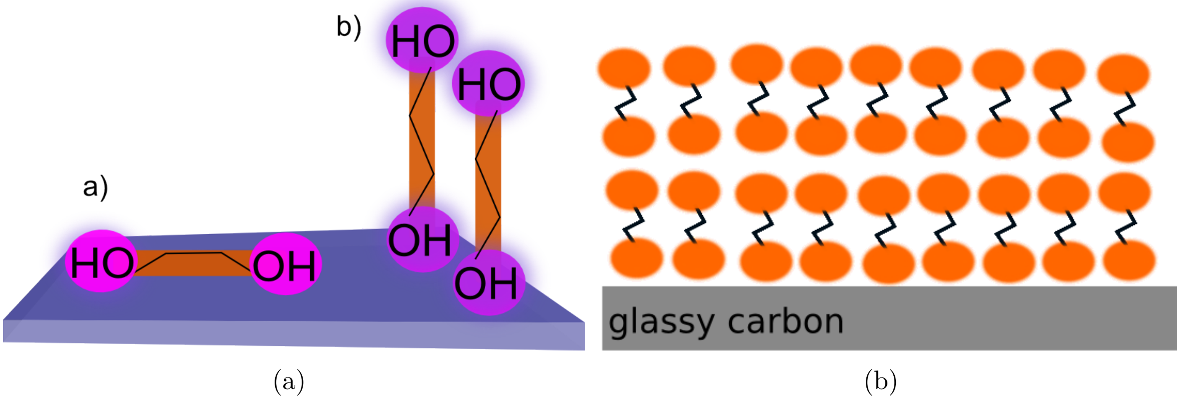

(a) (b)

Figure 8.3. Possible conformations for EG on GC with representation of multi-layers of EG after some equilibration time.

spectrum in different ways. The conformation A (C−C axis of the EG molecule parallel to the surface) would have an equal contribution from each OH group, whereas the conformation B (molecule axis perpendicular to the surface, or inclined with a resulting component with a perpendicular dipole moment) would generate two different bands, one for the OH adsorbed on the surface (which gets weaker, consequently it shifts to lower wavenumbers) and another band for the OH that is not in contact with the surface and interacts through hydrogen bonds with neighbours molecules. Indeed, two overlapping bands are observed for the ν(O−H) mode of EG in the PM-IRRAS spectrum, which indicates that the molecules are arranged in conformation B on the surface.

Although there might be condensation of water on the detector, because it is cooled with liquid nitrogen, the O−H absorption from these molecules are annulled through the subtraction of s- from p- polarized spectrum, since the absorption will be the same in both polarized components. Thus, the fact that the ν(O−H) band continuously increases with time in the PM-IRRAS spectra may be a consequence of the organization of ethylene glycol on the surface in a mono- or multilayer structure as sketched in Figure 8.3 b. This auto-assembly of the molecules at open circuit potential proceeds very slowly, as the band area does not reach a *plateau* even for measurement times as long as 24 h. Moreover, it is important to mention that PM-IRRAS is sensitive not only to surface species but also to the molecules that are in the proximity of the electrode surface (ca. 1 μm, or 1/4 of the wavelength of the incident radiation) [60], hence the increase in absorption may be correlated to the intensification of the transition dipole of the molecules caused by an increase in population and molecular orientation in the vicinity of the electrode surface.

8.1.2 12CE

After the time-dependent experiments with ethylene glycol, the liquid was removed from the cell and 12CE was added under nitrogen flow without additional cleaning. The PM-IRRAS spectra of 12CE on a glassy carbon surface as function of time are shown in Figure 8.4.

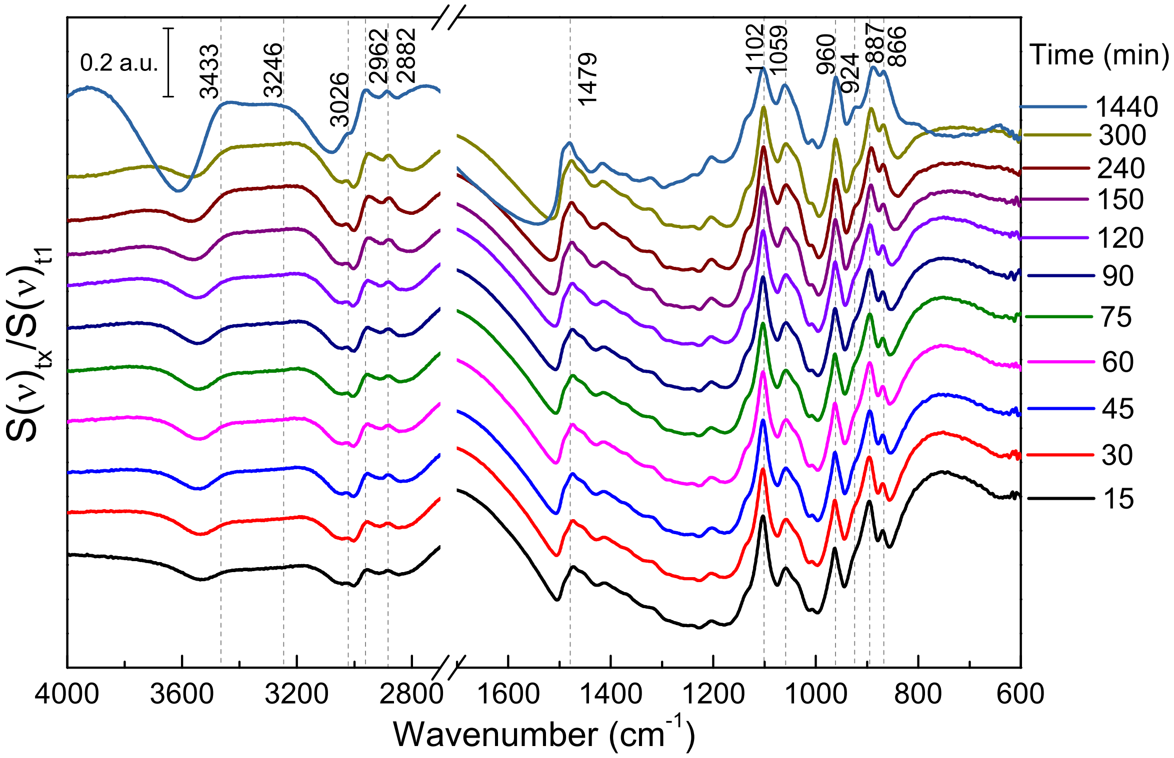

Figure 8.4. PM-IRRAS surface spectra of 12CE on glassy carbon recorded at various intervals of time after introduction of the electrolyte. All spectra are normalized to the spectrum recorded immediately after immersion of the electrolyte 12CE.

A significant increase in absorbance is observed after 15 min. However, differently from EG, the bands of the spectra do not show a significant increase of absorption with time. Obviously, this can be due to the glassy carbon surface already bearing an adsorbed layer of ethylene glycol prior to filling in the 12CE.

The baseline-corrected peaks and the areas of some bands on temporal scale are shown in Figure 8.5. Most of the analysed bands showed a rather constant intensity. The band areas showed a considerable increase after 15 min, thereafter it remained almost constant up to 24 h (1440 min). An increase in band area with time is noteworthy for the OH stretching at 3295 cm^{-1}. Moreover, the enhancement of the asymmetric bending mode of $(CH_3)_3N^+$ at 1479 cm^{-1} points out that the choline group might be competing with the OH for active sites on the electrode surface, although a similar increase is not observed for the asymmetric stretching of $(CH_3)_3N^+$ at $961\,cm^{-1}$ or the νC$-$N at $1133\,cm^{-1}$.

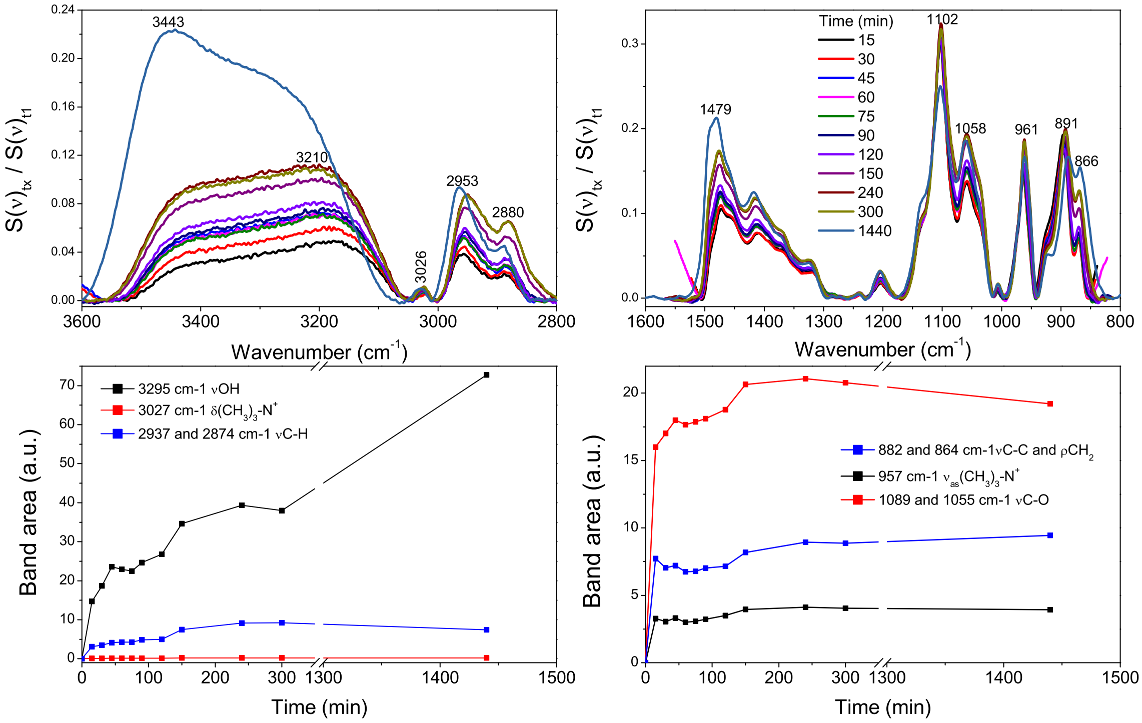

Figure 8.5. Temporal evolution of bands of 12CE on GC with their respective band area *versus* time.

8.1.3 0.03 mol·L^{-1} ZnCl$_2$ in 12CE

0.03 mol·L^{-1} of ZnCl$_2$ 12CE was added to a clean glassy carbon surface and PM-IRRAS spectra were frequently measured during a period of 24 h at open circuit potential. All sample spectra (t_x) were normalized to the first measurement (t_1), so that only the relative increase in absorption can be observed. The surface spectra of the electrolyte recorded at various time intervals are shown in Figure 8.6.

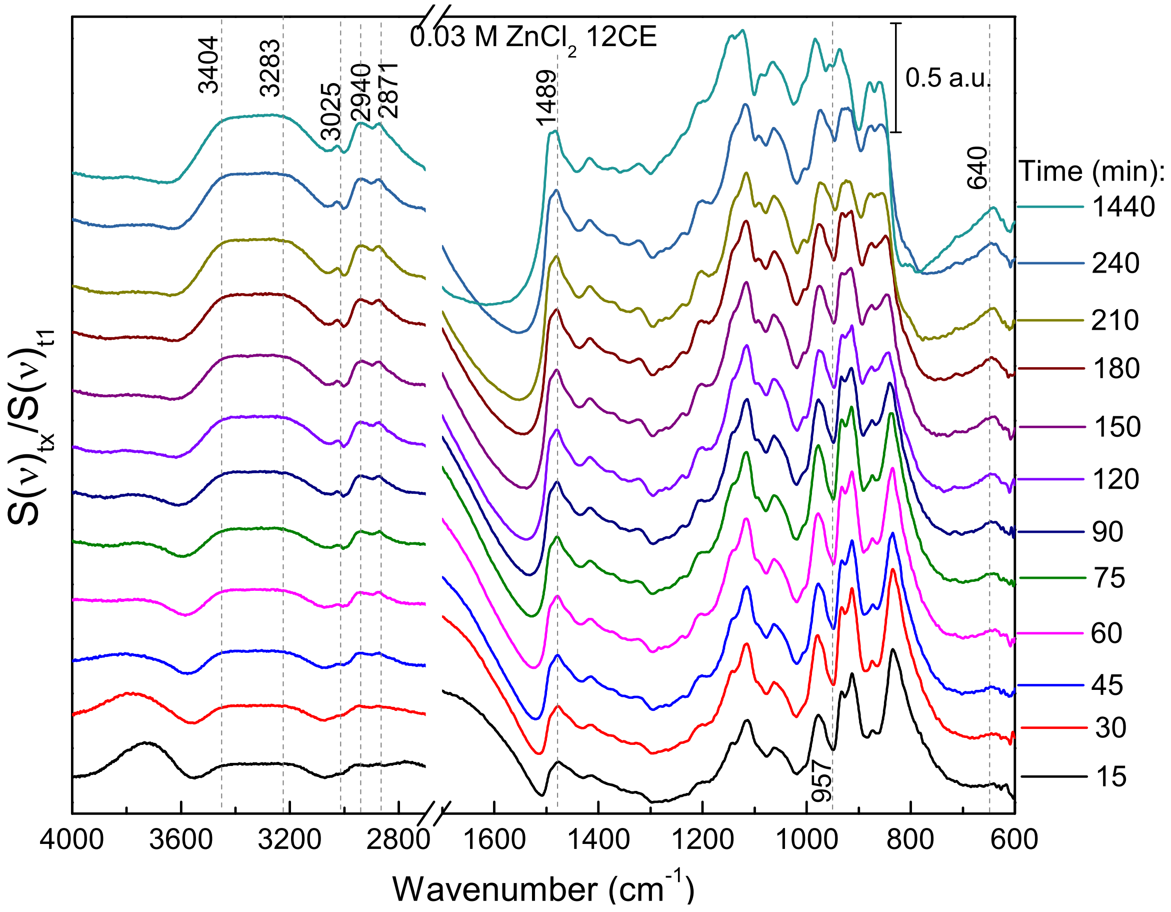

Figure 8.6. PM-IRRAS surface spectra of 0.03 mol·L^{-1} ZnCl$_2$ 12CE on glassy carbon recorded at various time intervals after introduction of the electrolyte. All spectra are normalized to a reference spectrum measured at the start of the experiment. The spectra presented in this Figure have not been smoothed or baseline corrected.

In this experiment, the adsorption of 0.3 mol·L^{-1} ZnCl$_2$ in 12CE on glassy carbon was different from the previous one in 12CE. As it starts from a clean surface, many of the bands show an increase in intensity and shift in wavenumber with time. The absorption bands and their respective temporal changes will be discussed consecutively, according to the IR spectral region.

Figure 8.7 shows the O−H and C−H stretching region (3600–2800 cm^{-1}) after baseline correction (with spline interpolation, according to the procedure described by Zamlynny et al. [60]) and the respective integrated band intensities.

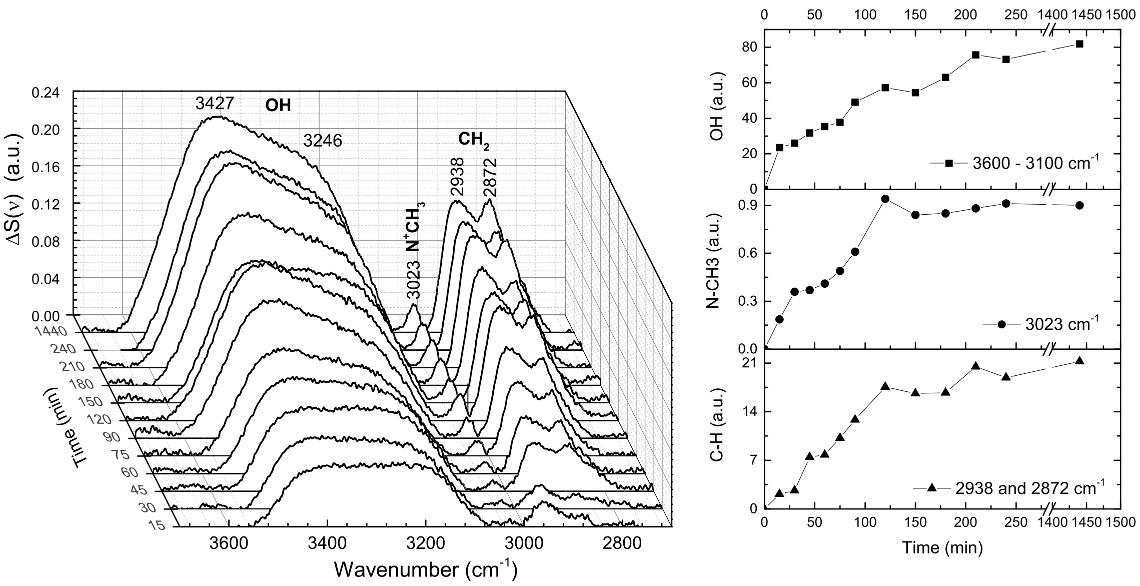

(a) (b)

Figure 8.7. Temporal evolution of a) PM-IRRAS spectra with a corrected baseline of the O−H and C−H stretching region of $0.03\,\mathrm{mol{\cdot}L^{-1}}$ $ZnCl_2$ in 12CE onto GC at room temperature and open circuit potential. b) The respective integrated band intensities *versus* time.

It can be noticed that the intensity of all bands in the R−H region increase considerably with time. The O−H band becomes broader and asymmetric, indicating that one of the overlapping bands contributes more to the overall absorption. The contribution from the O−H band at $3427\,\mathrm{cm^{-1}}$ becomes higher with time compared to that at $3246\,\mathrm{cm^{-1}}$. It is likely that the first band at at $3427\,\mathrm{cm^{-1}}$ originates from the O−H bond which is not in contact with the GC surface, i.e. at the end of the chain of EG and ChCl — supposing these two molecules assemble with the C−C axis inclined to the surface and also that ChCl adsorbs through the amine group. Because both ChCl and EG molecules bear O−H functional groups, the contribution of this band becomes higher as the surface coverage and molecular ordering, i.e. dipole alignment, increase.

The ν(C−H) band located at $3027\,\mathrm{cm^{-1}}$ corresponds to the terminal methyl CH_3 stretching mode of the $(CH_3)_3N^+$ group [250]. The intensity of this band starts from a very weak absorption at 15 min to a significantly high IR absorption after 120 min, which is consistent with the supposition that the Ch^+ group of ChCl is preferentially in contact with the surface and the surface population of this species increases with time.

The bands centered at 2938 and $2872\,\mathrm{cm^{-1}}$ are attributed respectively to the ν_{as}(C−H) and ν_s(C−H) of the methylene groups from ChCl and EG. The C−H stretching modes are usually conformation sensitive and may respond to changes of the trans/gauche ratio in the alkyl chains [239]. The increase in intensity of these stretching bands may be indicative of orientational changes of the sample relative to the substrate normal [251–253].

The relative intensity of the ν_{as}(C−H) at 2955 cm^{-1} is initially higher than that of ν_s(C−H) at 2881 cm^{-1}. This may be caused by absorption contributions from the CH_3 bending modes and Fermi resonance overtone from the methylene scissoring vibrations, which may overlap the ν_{as}(C−H) band [60, 96, 253]. On the other hand, the ν_s(C−H) arises purely from the symmetric stretching vibration of methylene groups [90]. After some resting time, the absorption intensity of the two stretching modes seem to equalize. The band intensity *vs.* time plot shows a saturation *plateau* after 120 min (Figure 8.7 b) for the ν_{as} and ν_s of CH_2, indicating that the degree of ordering of the adsorbed DES molecules increases until the system reaches a saturation point.

The formation of such packed-adlayer of the ionic liquid on the GC surface is also consistent with the wavenumber shift observed for the C−H stretching, from 2955 and 2881 cm^{-1} initially, to 2941 and 2871 cm^{-1} after 240 min and 2938 and 2872 cm^{-1} after 24 h. Changes in band positions and bandwidths of the CH_2 stretching bands have been used to investigate forms conversion in phosphocholine lipids, namely gel to liquid-crystalline phase-transitions [90, 251, 252]. It was alleged that the shift to lower wavenumbers of the (C−H) stretching modes are related to a higher degree of ordering of the acyl chains in lipid molecules [99, 253]. Similarly, the red-shift of the methylene stretching modes in DES may indicate a higher degree of ordering of the molecules on the GC surface.

Figure 8.8 shows the 1550-1300 cm^{-1} spectral region, which provides information about the C−H bending modes. The two overlapping bands at 1489 and 1479 cm^{-1} are attributed to the C−H bending of the $[N^+(CH_3)_3]$ group of choline chloride [239, 254] with a small contribution of the $\delta(CH_2)$ at 1450 cm^{-1} [255]. They overlap in the 12CE surface spectra due to the higher intensity of the $\delta_{as}[N^+(CH_3)_3]$ band on glassy carbon. The band at 1417 cm^{-1} is attributed to the δ(C−O−H) and the two other bands of lower frequency are ascribed to the methylene wagging.

The intensity of the $\delta_{as}[N^+(CH_3)_3]$ band increases substantially with time. The plot of integrated intensity of the bands *vs.* time shown in Figure 8.8b correlates quite well with the plot of the $\nu_{as}[N^+(CH_3)_3]$ band intensity (Figure 8.7b). The band area increased by almost three-fold during 120 min, approaching a *plateau* at 120 min. This *plateau* indicates saturation after 240 min. The increase in intensity with time is most likely caused by an increasing adsorbate coverage of the glassy carbon surface, resulting in a higher degree of orientational ordering of the molecular dipoles, thereby enhancing the p-polarized signal correlated to these vibrations.

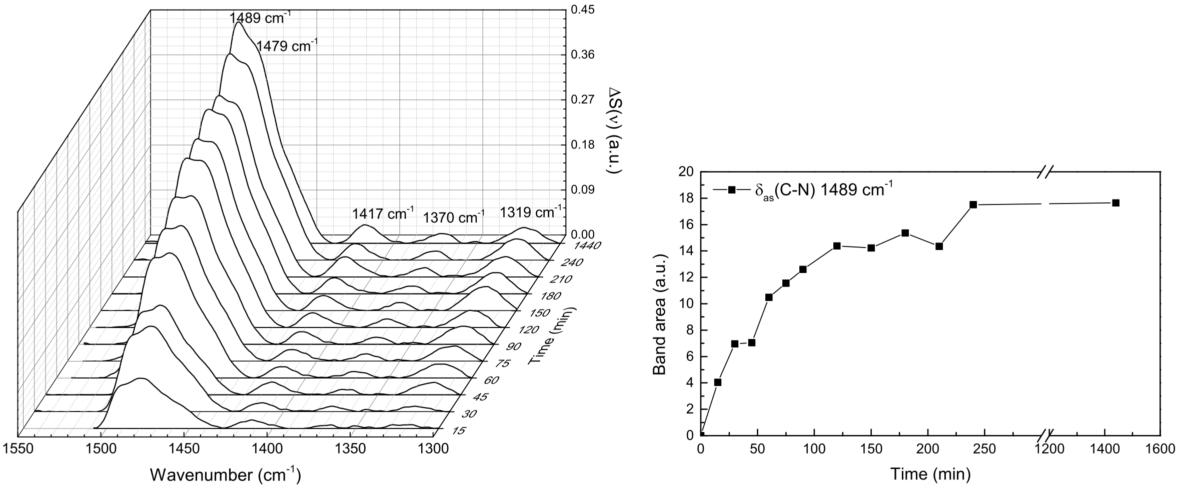

(a) (b)

Figure 8.8. a) PM-IRRAS spectra showing the temporal evolution of the C−H bending region of 0.03 mol·L^{-1} $ZnCl_2$ in 12CE on GC at room temperature and open circuit potential. b) Integrated band intensity of $\delta_{as}N^+(CH_3)_3$ as a function of time.

Figure 8.9 shows the 1300–1000 cm^{-1} region of the DES, which consists of bands from C−O and C−N stretching in combination with CH_2 wagging and twisting. These spectra are not normalized to the spectrum at t_1, but shown as the $S(\nu)$. As can be seen, there is a gradual decrease of the symmetrical and asymmetrical νC−O modes at 1096 and 1054 cm^{-1}. Moreover, the shape of the ν_sC−O changes considerably with time, indicating a change on the orientation of the adsorbed molecules.

The 1000–600 cm^{-1} region, where the C−N stretching bands of the choline can be found (1000–900 cm^{-1}), shows an inversion of the direction of the ν_{as}C−N band at 957 cm^{-1}, which may be facing up or down, as presented in Figure 8.10. This inversion of direction is more likely to be due to a change in reflectivity of the electrode upon formation of such multilayer assembly. Such inversions of bands have also been observed in PM-IRRAS studies of celullose films on Si/SiO_2 substrates [214] and were attributed to effects caused by the polarization of the beam and the angle of incidence on the film.

The increase in the bands corresponding to the choline function ($\nu_{as}N^+(CH_3)_3$ and $\delta_{as}N^+(CH_3)_3$) indicate that this group is preferentially in contact with the glassy carbon surface. This observation is consistent with the PM-IRRAS structural analysis of

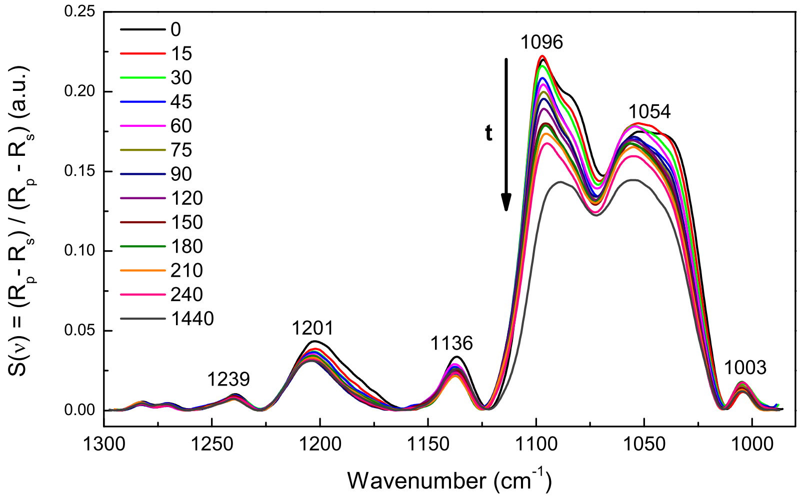

Figure 8.9. PM-IRRAS spectra showing the temporal evolution of the C−O stretching region of 0.03 mol·L^{-1} $ZnCl_2$ in 12CE on GC at room temperature and open circuit potential.

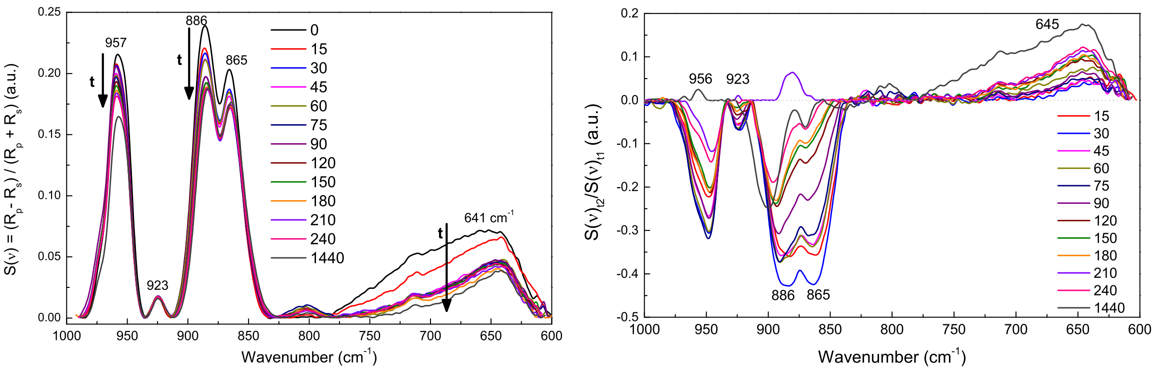

(a) (b)

Figure 8.10. Temporal evolution of the νC−N bands (957 cm^{-1}) of 0.03 mol·L^{-1} $ZnCl_2$ in 12CE on GC.

biomembranes with a choline head group [93, 94, 96, 98, 253, 256]. These studies have shown that bilayers of dimyristoryl-phosphatidyl-choline (DMPC) on SiO_2/Au [253, 256] and Au(111) substrates [93, 94, 96, 98] are directly adsorbed on the metal surface by the choline moiety [60, 90]. Therefore, the most likely structure of the DES on the glassy carbon surface at OCP might be as represented in Figure 8.11.

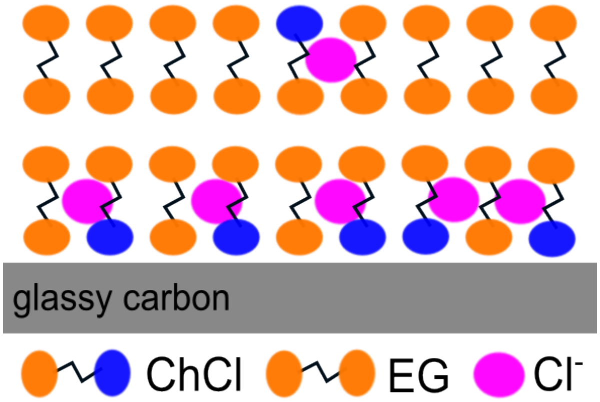

Figure 8.11. Possible conformations for 12CE on glassy carbon with representation of multi-layers of 12CE after some equilibration time.

8.2 Potential-dependent PM-IRRAS

Potential-dependent measurements were carried out by *in situ* controlling the electrode potential and simultaneously recording PM-IRRAS spectra. Each spectrum took 7 min to record, therefore 7 min potential-steps were programmed using the NOVA software. Most of the spectra are shown already normalized to a reference spectrum, which is calculated by: $\Delta S = S(\nu)_{E2}/S(\nu)_{E1}$, where $S(\nu)$ is given by Equation 7.1 and $E1$ is the indicated reference potential.

8.2.1 12CE

The electrolyte 12CE (3 mL) was added to the cell with a clean glassy carbon electrode under nitrogen flow. The potential of the glassy carbon working electrode was controlled *versus* a zinc wire as reference electrode. The uncompensated resistance (*iR* drop) was found to be about 190 Ω by using the *i*-interrupt and positive feedback tools of the NOVA software of the potentiostat. Thereby, the potential measurements were made with an automatic compensation of the *iR* drop.

The open circuit potential (OCP) of the cell filled with 12CE was +0.25 V *vs.* Zn/Zn^{2+}. Although it was seen from last sections that even at OCP self-assembly of the molecules occur, we assume that the kinetics of these changes should be much slower than the kinetics of potential-induced changes. Moreover, the system will be affected significantly as soon as faradaic reactions are initiated. Because no faradaic reactions should happen at OCP, the PM-IRRAS spectrum recorded at +0.25 V *vs.* Zn/Zn^{2+} (E_{ocp}) was chosen as reference for normalization of the PM-IRRAS surface spectra at different applied potentials (E_{n}).

From OCP at +0.25 V *vs.* Zn/Zn^{2+}, the potential was stepped in the negative direction until −0.8 V in intervals of −0.2 V and then back positively till +0.6 V. The sequence of potential steps together with the current responses are presented in Figure 8.12.

The electrochemical data reveal that at −0.4 V, there is an increase of the cathodic current, which is likely to be due to adsorption of the cations (Ch^+). At −0.6 V the cathodic current increases significantly, which might be due to the reduction of the electrolyte (ChCl, EG, or traces of water) and adsorption of hydrogen on the GC surface, as it was seen in the previous section that the reduction of 12CE takes place already at −0.6 V in the electrolyte without zinc. At −0.8 V, the cathodic current increases to $-0.3\,\mathrm{mA{\cdot}cm^{-2}}$, due to the reduction of the electrolyte over the whole GC surface. Up to 0 V some cathodic current is still observed, due to the capacitive charging of the electrochemical double layer (EDL). Stepping positively results in an anodic current, which is remarkably high at +0.6 V (+0.22 mA·cm^{-2}). The anodic charge consumed in these last steps presumably originates from the desorption of the Ch+ with replacement of these interfacial species by Cl$^-$ or RO$^-$. The reduction of Cl$^-$ ions to form Cl$_3^-$ would take place at much more positive potentials ($E \geq 2$ V *vs.* Zn/Zn^{2+}) [13, 44] and is not expected at +0.6 V *vs.* Zn/Zn^{2+} though. Thus, it is likely that the anodic charge is due to the reoxidation of RO$^-$ species to ROH. The electrochemical behavior of the DES could be monitored chronoamperometrically during the spectroscopic measurements and therefore the PM-IRRAS spectra corresponding to each potential step can be interpreted accordingly.

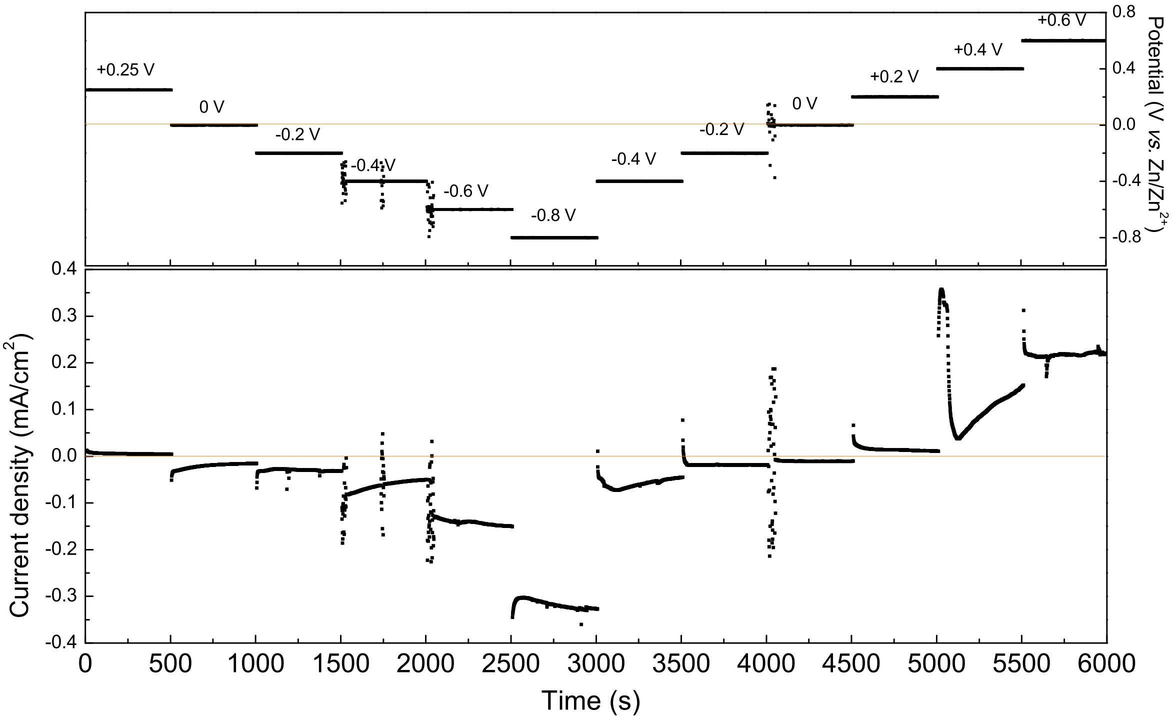

Figure 8.12. Working electrode potential and current density *versus* time of 12CE in the spectroelectrochemical cell during *in situ* PM-IRRAS experiments. The potential and corresponding current spikes are caused by external disturbance of the cell and are therefore artefacts.

The surface PM-IRRAS spectra corresponding to the different applied potentials are shown in Figure 8.13. It is important to mention that these spectra are not baseline corrected, but presented as measured: $\Delta S = S(\nu)_{E_\mathrm{n}}/S(\nu)_{E_\mathrm{ocp}}$. From this normalization, bands pointing up indicate an increase in absorption, whereas those pointing down have a lower IR absorption compared to the reference spectrum at OCP.

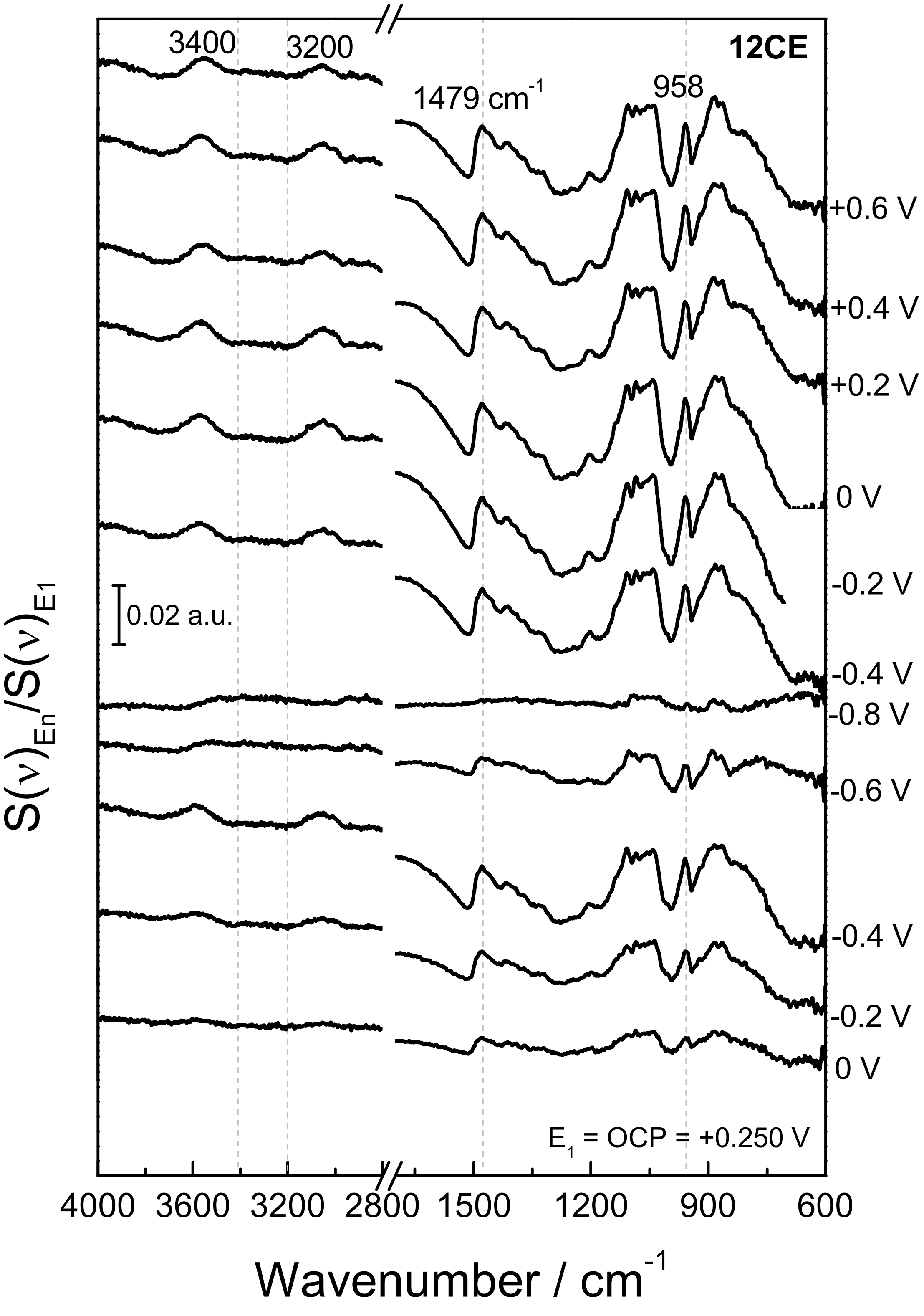

Figure 8.13. PM-IRRAS surface spectra of 12CE recorded at the indicated potential. All spectra are normalized to the PM-IRRAS spectrum at open circuit potential $E_{\mathrm{ocp}} = +0.25\,\mathrm{V}$.

It is likely that during the first measurement, at OCP (about 10 min after filling the SEC cell with 12CE), the molecules do not have a high degree of order on the GC surface. This implies that initially there might be amine as well as hydroxyl groups in contact with the electrode surface. Hence, by switching the potential from +0.25 to 0 V *vs.* Zn/Zn^{2+}, some preferential orientation might already take place at the interface, which is evident by an increase in the intensity of the bands at the fingerprint region (1500–800 cm^{-1}), specially those related to the vibrations of the quaternary amine at 1479 and 959 cm^{-1}. This increase in absorption intensity is accentuated as the potential is stepped more negative to −0.2 and −0.4 V *vs.* Zn/Zn^{2+}. A corresponding increase in the cathodic current can be followed in the electrochemical output of the measurement in Figure 8.12.

Stepping the potential to −0.6 and −0.8 V causes a decrease of the IR signal, compared to that at −0.4 V. From the electrochemical data shown in Figure 8.12, a significant increase in current density at −0.6 and −0.8 V is also noted, indicating reduction of the Ch^+ and/or EG to form hydrogen at these potentials. At −0.6 V reduction of the electrolyte might already occur only on some active sites. Subsequently, at −0.8 V, adsorption of hydrogen with gas evolution takes place on the whole surface of the electrode. Consequently, the adsorbed layer is desorbed and a decrease of the band intensities is observed in the whole PM-IRRAS spectrum. Massive gas formation is not expected though. In this case, the IR absorbance would be much lower than at the initial state of the experiment and the differential spectra ($E_\mathrm{n}/E_\mathrm{ocp}$) would have all bands pointing down. Instead, it turns more similar to the initial state, where the molecules are randomly oriented and distributed. Presumably, the surface is covered by adsorbed hydrogen, which does not absorb in the IR. The second layer after the adsorbed hydrogen is likely to be composed of Ch^+ and EG molecules, similarly to the initial state, therefore a decrease in signal in the differential spectrum at −0.8 V. Moreover, the formation of gas also contributes to the lower degree of order of this system.

The evolution of the bands with the applied potential can be better visualized in the spectra with a corrected baseline, as presented in Figure 8.14. The baseline was corrected using the spline interpolation as described by Zamlynny et al. [60]. The spectra were divided in three regions: the $\nu(\mathrm{O{-}H})$ region from 3600 to 2700 cm^{-1}, the $\delta[\mathrm{N^+(CH_3)_3}]$ region from 1500 to 1300 cm^{-1} and the $\nu(\mathrm{C{-}N})$ region from 1000 to 800 cm^{-1}.

In the $\nu(\mathrm{O{-}H})$ region (3600-3000 cm^{-1}), the O−H stretching bands increase in the negative direction upon decreasing the potential from 0 to −0.4 V. This indicates that the O−H groups of Ch^+ and EG gradually desorb, compared to the OCP. At −0.6 and −0.8 V a further decrease in absorbance is observed for these bands. However, stepping

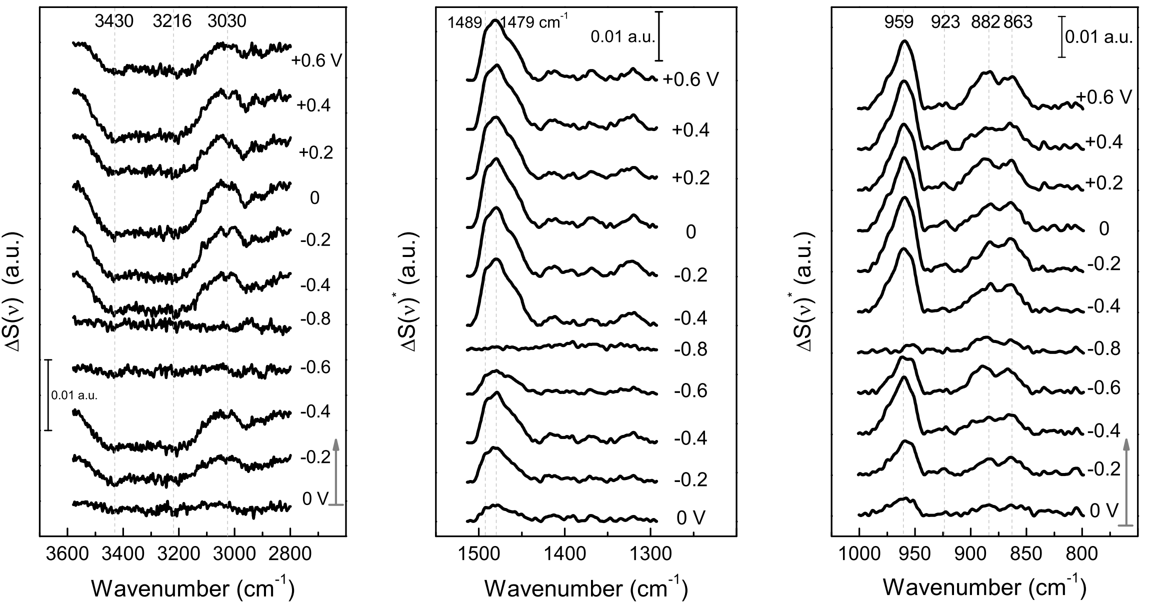

(a) (b) (c)

Figure 8.14. Baseline corrected PM-IRRAS surface spectra [$\Delta S^*(\nu)$] of 12CE at different applied potentials. Arrows indicate the start of the experiment. All spectra are normalized to the PM-IRRAS spectrum at open circuit potential (+0.25 V).The spectral regions are corresponding to: a) O−H and C−H stretching, b) C−H bending and c) C−N stretching.

the potential positively does not invert the absorption intensity upwards.

The asymmetrical C−H bending modes of $[\mathrm{N}^+(\mathrm{CH}_3)_3]$ at 1489 and 1479 cm^{-1} increase upwards by decreasing the potential to −0.4 V, indicating adsorption of this group on the electrode surface. At −0.6 and −0.8 V the absorption decreases due to coverage of the surface with adsorbed hydrogen. Interestingly, stepping the potential to the positive direction causes the $\delta_{\mathrm{as}}[\mathrm{N}^+(\mathrm{CH}_3)_3]$ band intensity to increase. The same behavior of band intensity with potential can be observed for the asymmetric C−N stretching at 959 cm^{-1} (Figure 8.14 c).

The band intensities corresponding to the νO−H, $\delta_{\mathrm{as}}[\mathrm{N}^+(\mathrm{CH}_3)_3]$ and $\nu_{\mathrm{as}}[\mathrm{C{-}N}^+(\mathrm{CH}_3)_3]$ modes were integrated with respect to the local baseline and are presented in Figure 8.15.

For the OH band, the increase in absolute value of area indicate desorption. It can be observed that from 0 to −0.4 V the area increases, so the OH groups are detached (probably replaced by Ch^+). Decreasing the potential further to −0.6 and −0.8 V *vs.* $\mathrm{Zn/Zn}^{2+}$ decreased the area. This can be correlated with the approach and further reduction of the OH groups to generate adsorbed hydrogen. Stepping positively from −0.8 to 0 V caused an increase in area of the νO−H, thus an increase in desorption. It is likely that in this potential range, there are mostly $\mathrm{N}^+(\mathrm{CH}_3)_3$ groups in contact with

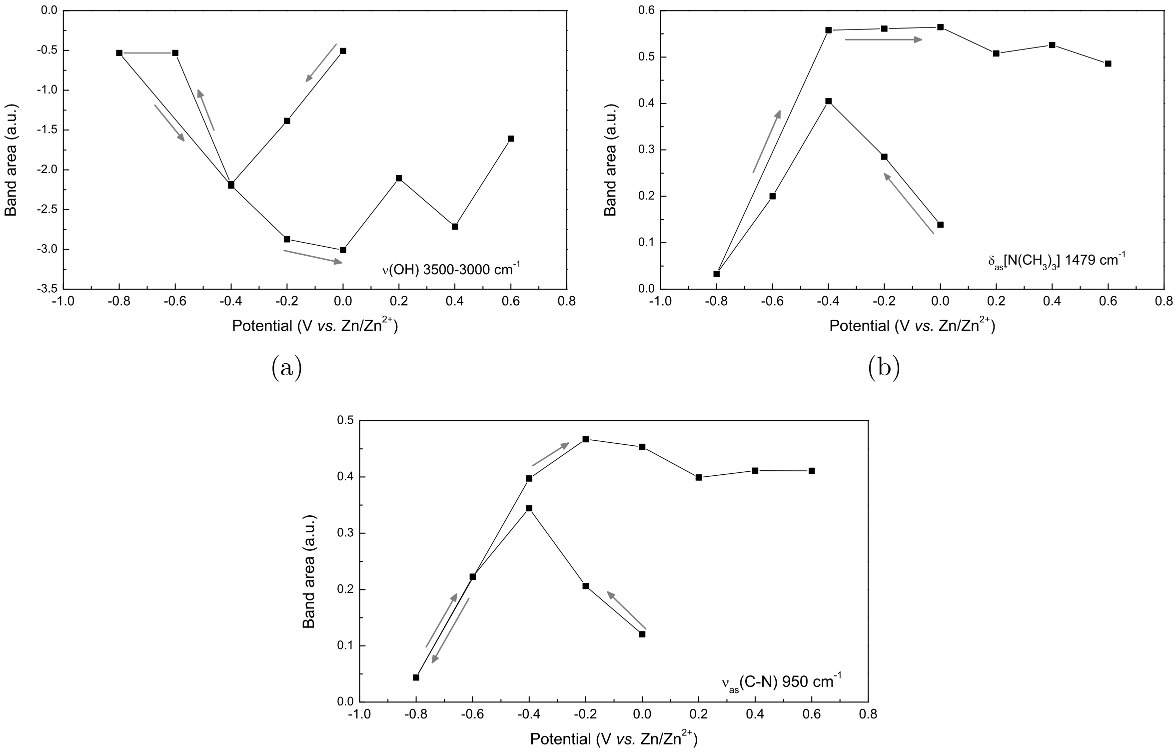

(a)

(b)

(c)

Figure 8.15. PM-IRRAS band intensities of a) ν(O−H), b) $\delta_{as}N^+(CH_3)_3$ and $\nu_{as}C{-}N^+(CH_3)_3$ of 12CE on GC as a function of electrode potential. The bands were integrated from the corrected baseline spectra in Figure 8.14 with respect to zero. Arrows indicate potential direction from the start of the experiment.

to electrode surface. From 0 to +0.6 V, the OH band area decreased slightly. Presumably, some EG molecules have replaced Ch^+ at positive potentials as it is unlikely that the surface is completely covered by Ch^+ molecules.

The effect of the applied potential on the band intensities from the $\delta N^+(CH_3)_3$ at 1479 cm^{-1} and $\nu_{as}N^+(CH_3)_3$ at 959 cm^{-1}, is shown in Figure 8.15 b and c. From 0 to −0.4 V, the increase in band intensity indicate adsorption of the choline groups on the GC electrode. From −0.6 to −0.8 V Ch^+ ions are replaced by adsorbed hydrogen. Stepping to −0.4 V causes readsorption of the Ch^+, which is evident by the strong increase of band intensities for these two vibrational modes. From −0.4 to 0 V the Ch^+ remains adsorbed on the surface.

Stepping positively from 0 V up to +0.6 V *vs.* Zn/Zn^{2+} caused the peak area of δ_{as} and ν_{as} $C{-}N^+(CH_3)_3$ to decrease slightly, however the band intensities are still considerably high. Re-adsorption of the ammonium group at a positively charged electrode would not be expected though. The anions in the deep eutectic would rather replace the cations at positive potentials. In the deep eutectic 12CE, these anions would be either Cl^- or

RO^- species, where the latter are generated through the reduction of the electrolyte (ChCl or EG) at $E \leq -0.6\,V$. In Figure 8.12, an anodic current of $0.22\,mA{\cdot}cm^{-2}$ is observed at $+0.6\,V$ and simultaneously, from Figure 8.13, there is a significant increase in absorption of the bands at the 1200–1000 cm^{-1} region, where the ν_{as} and ν_s of the C−O are situated. However, integration of these bands is difficult due to the influence of ν_sC−N at 1133 cm^{-1}, which overlaps with the νC−O modes.

Notwithstanding, the binding strength of the Ch^+ to the GC electrode can be evaluated by the position of the δ_{as} and ν_{as} $N^+(CH_3)_3$ band centers as a function of the applied potential, as presented in Figure 8.16. Variations on the vibration frequency of a band may indicate changes in adsorption geometry, surface coverage of the molecules or on the electrostatic properties at the electrode interface [257]. Band-shifts to lower wavenumber (red-shift) indicate that the bond became weaker, therefore it absorbs at a lower frequency. On the contrary, shifts to higher wavenumbers (blue-shifts) indicate a strengthening of the chemical bond. If the Ch^+ group is adsorbed to the electrode surface at negative potentials, it is expected that the induction of charge from the electrode will make the bond stronger, therefore a blue-shift is expected. Indeed, for the δ_{as} $N^+(CH_3)_3$, from 0 to $-0.2\,V$ a blue-shift of 6 cm^{-1} is observed, from 1478 cm^{-1} to 1484 cm^{-1}. At $-0.8\,V$, the frequency shifts to 1467 cm^{-1}, confirming the desorption of the Ch^+. Similar behavior is observed for the ν_{as} $N^+(CH_3)_3$, firstly a red-shift on from 958 cm^{-1} at 0 V to 962 cm^{-1} at $-0.6\,V$ due to direct adsorption of Ch^+ then a blue shift to 952 cm^{-1} at $-0.8\,V$ due to its desorption. Switching the potential to positive values caused the peak centers to return to 1479 cm^{-1} and 959 cm^{-1}, probably due to the induction of charge from Cl^-.

The PM-IRRAS spectroelectrochemical studies of the 12CE reveal some insights that can help to explain the blocking effects during zinc electrodeposition on GC from 12CE. It was previously suggested that at $E \leq -0.5\,V$ the GC surface could be blocked by strongly adsorbed Ch^+ species [42, 44]. However, the SEC-PM-IRRAS results show that the blocking layer is probably composed of adsorbed hydrogen, which in the electrolyte containing zincate would hinder zinc electrodeposition. However, it is still to explain why the peak intensities of the $N^+(CH_3)_3$ groups increase upon positive potential steps and whether these groups are still in contact with the surface.

Spectroscopic and theoretical investigations on ionic liquid interfaces with electrified electrodes suggest that the electrode surface acts as an electronic and structural template, where cations adsorb at $E \leq$ PZC and that at positive potentials the cations are replaced by anions [63, 65, 68, 70, 75, 78, 184, 258]. However this potential-dependent restructuring of cations and anions is not that simple and adsorption/desorption hysteresis [77, 83] and ultra-slow restructuring [185] have also been reported.

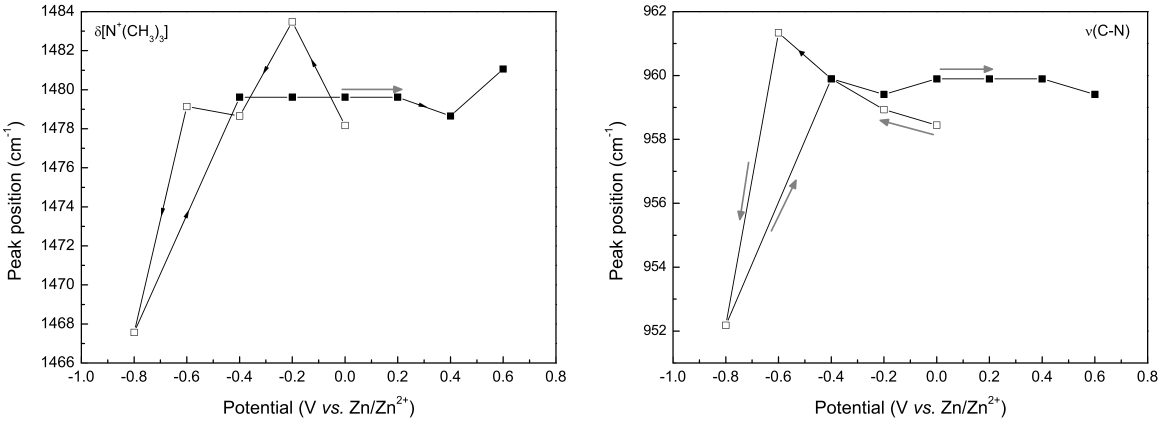

(a)

(b)

Figure 8.16. Frequency shift as a function of the electrode potential for the bands: a) δ_{as} $\mathrm{N^+(CH_3)_3}$ and ν_{as} $\mathrm{C{-}N^+(CH_3)_3}$. Empty squares indicate forward potential steps (from 0 to -0.8 V *vs.* $\mathrm{Zn/Zn^{2+}}$) while filled squares indicate the steps in a positive direction (from -0.4 to $+0.6$ V *vs.* $\mathrm{Zn/Zn^{2+}}$). Arrows point in the direction of the potential steps.

Motobayashi et al. [83] investigated the potential-dependent structure of 1-butyl-3-methylimidazolium bis(trifluoromethanesulfonyl)amide ([BMIM][TFSA]) by surface-enhanced infrared absorption spectroscopy (SEIRAS). Scanning the potential in the positive direction from -2.1 to $+0.9$ V *vs.* $\mathrm{Fc/Fc^+}$ caused the bands corresponding to the cations $\mathrm{BMIM^+}$, the $\nu(\mathrm{C{-}H})_{\mathrm{ring}}$, to increase in intensity. The authors suggested a potential-dependent reorientation of the imidazolium ring from a flat to a more vertical position, which would change the oscillating dipole of the molecule. A similar reorientation of the imidazolium ring at positive potentials, has also been observed using SFG (sum frequency generation) spectroscopy to study ionic liquids based on 1-butyl-3-methylimidazolium [$\mathrm{BMIM^+}$] cations with [$\mathrm{PF_6^-}$] (hexafluorophosphate) [259] and [$\mathrm{BF_4^-}$] (tetrafluoroborate) anions [78, 259].

Electrochemical, PM-IRRAS and neutron reflectivity studies of biological membranes based on DMPC (dimyristoylphosphatidylcholine) on gold surfaces by Lipkowski's group [91, 95, 97] have shown that by progressively decreasing the electrode potentials, the DMPC molecules adsorb on gold through the $\mathrm{Ch^+}$ moiety. By decreasing the potential further to $E \ll \mathrm{PZC}$, the DMPC is separated from the gold surface by a thin layer of $\mathrm{D_2O}$ (~ 1 nm). Furthermore, IRRAS experiments also showed that when the membrane is adsorbed directly at the metal surface all polar heads tend to interact with the metal, consequently the chains assume a more tilted orientation with respect to the surface normal, whereas at high negative charges, when the membrane is suspended on $\mathrm{D_2O}$, the tilt angle decrease, hence the molecules orient more perpendicular to the surface [94, 96].

From the electrochemical and PM-IRRAS results obtained for 12CE at a GC surface and by comparison with the literature for interfaces of biological membranes and ionic liquids with charged metal electrodes, we suggest the following potential effects on the interfacial structure of 12CE and GC, presented in Figure 8.17. It is important to mention that this Figure only shows qualitative sketches and does not represent the precise location, distribution and tilt angle of the molecules in the 12CE/GC system.

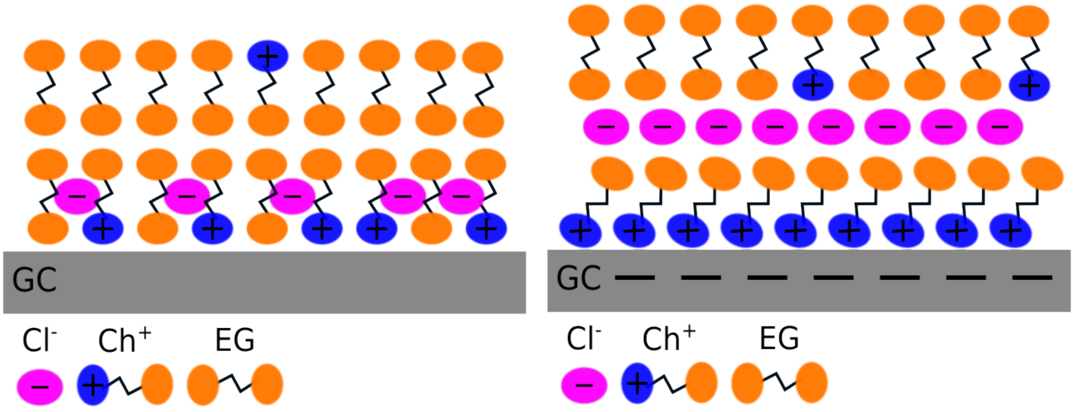

(a) OCP (b) $-0.4\,\mathrm{V}$

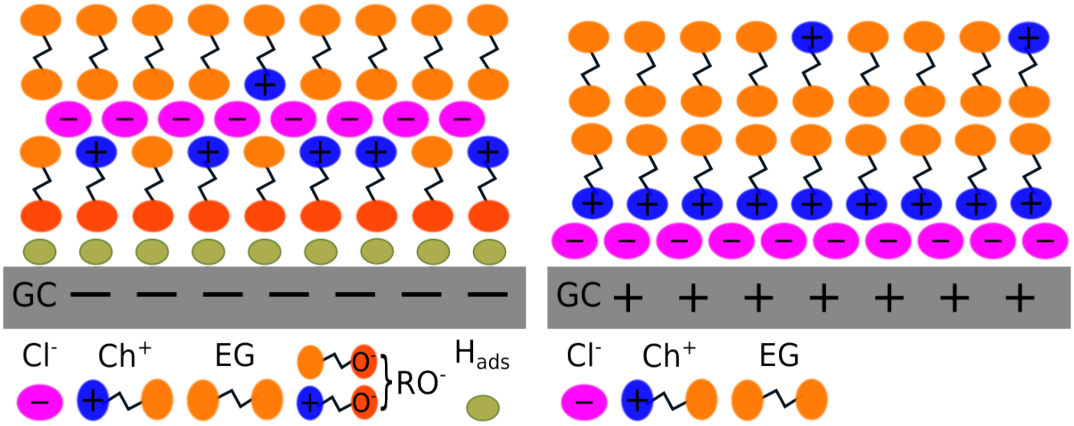

(c) $-0.8\,\mathrm{V}$ (d) $+0.6\,\mathrm{V}$

Figure 8.17. Schematic illustration of the potential-dependent changes in the structure of 12CE/GC a) at OCP, where ChCl and EG are at the surface; b) at $-0.4 \geq E \leq 0\,\mathrm{V}$, where the interface is dominated by the cations Ch^{+}; c) at $\leq -0.6\,\mathrm{V}$, where the surface is covered by adsorbed hydrogen and d) at sufficiently positive potentials, where the Ch^{+} layer is exchanged by Cl^{-}.

As suggested from *in situ* AFM [69, 70, 111] and X-ray scattering measurements [68], the ionic liquid/electrode interface has probably a multilayer architecture with alternating ions. At OCP, EG and ChCl molecules are in contact with the surface. At potentials more negative than OCP, the first layer consist mostly of Ch^{+} ions, which are strongly adsorbed in this potential range ($-0.6 \leq E \leq +0.25\,\mathrm{V}$, Figure 8.17 b). The second layer is likely to be Cl^{-} anions due to the interaction with the Ch^{+} cations in the first layer. Thereafter, the influence of the surface charge may decrease and the third layer is presumably composed of Ch^+ and EG.

At highly negative potentials ($E \leq -0.6$ V, Figure 8.17 c), the GC surface is covered by adsorbed hydrogen generated by reduction of EG and/or ChCl. This rearrangement of the interface causes the PM-IRRAS signal to become more similar to the initial state at OCP, when EG and ChCl were in contact with the surface, therefore a decrease in $\Delta S(\nu)$.

At potentials more positive than OCP, or positive enough to cause restructuring of the interface, it is likely that the surface is covered by Cl^- ions due to the electrostatic attraction of the anions by the electrode surface. Consequently, the second layer would be dominated by Ch^+ cations. However at such potentials the PM-IRRAS bands corresponding to the $N^+(CH_3)_3$ group increase in intensity. Comparing the restructuring of 12CE with those described for imidazolium-based ionic liquids at $E \geq$ OCP or PZTC (potential of zero total charge) [78, 83] and the detachement of DMPC membranes from Au surface by a 1 nm D_2O layer [91], one can assume that the increase in band intensity of $N^+(CH_3)_3$ is presumably due to a change in orientation of the Ch^+ molecules. When a negative potential is applied and the Ch^+ is directly adsorbed at the GC, the first layer of Ch^+ molecules might be forced to assume a more tilted orientation due to the coulombic interaction with the two terminal polar groups ($N^+(CH_3)_3$ and O−H). When the Ch^+ layer is separated from the surface by a Cl^- layer, the Ch^+ cations might be packed in a way to maximize the interaction with the anions, assuming a more vertical orientation with respect to the normal of the GC surface. From the surface selection rules [85, 86, 249] the vibrations that yield a resultant dipole moment perpendicular to the surface are selectively observable by PM-IRRAS. The reorientation of the Ch^+ from a tilted position at $E \leq$ OCP to a more vertical one at $E \geq$ OCP would explain the higher δ_{as} and ν_{as} $N^+(CH_3)_3$ band intensities at positive potentials. Furthermore, although ionic liquids may show a very slow response upon change in potential [134, 185, 260, 261], hysteretic desorption of the Ch^+ layer due to a slow restructuring of the interface is unlikely, because the measurement time for each spectrum is about 7 min. A considerable increase in anodic current is also observed at these potentials, indicating an anodic reaction with consumption of charge, possibly reoxidation of the glassy carbon surface and the molecular hydrogen adsorbed, as the oxidation of chloride would only be expected at $E \geq 2.0$ V *vs.* Zn/Zn^{2+} [44].

8.2.2 $0.3\,\mathrm{mol{\cdot}L^{-1}}$ $ZnCl_2$ in 12CE

It has been discussed in the previous chapters that zinc electrodeposition from the deep eutectic solvent 12CE involves several unusual features such as potential-dependent adsorption, resulting in potential-dependent blocking-unblocking of the electrode surface, in addition to the formation of intermediate reducible zinc species (Z). It is therefore of interest to investigate the interface of a glassy carbon electrode with the deep eutectic containing zinc. *In situ* spectroelectrochemical (SEC) PM-IRRAS experiments have been carried out in the DES containing $0.3\,\mathrm{mol{\cdot}L^{-1}}$ of $ZnCl_2$. A thin-layer cyclic voltammogram in the SEC cell of $0.3\,\mathrm{mol{\cdot}L^{-1}}$ $ZnCl_2$ in 12CE solution is shown in Figure 8.18.

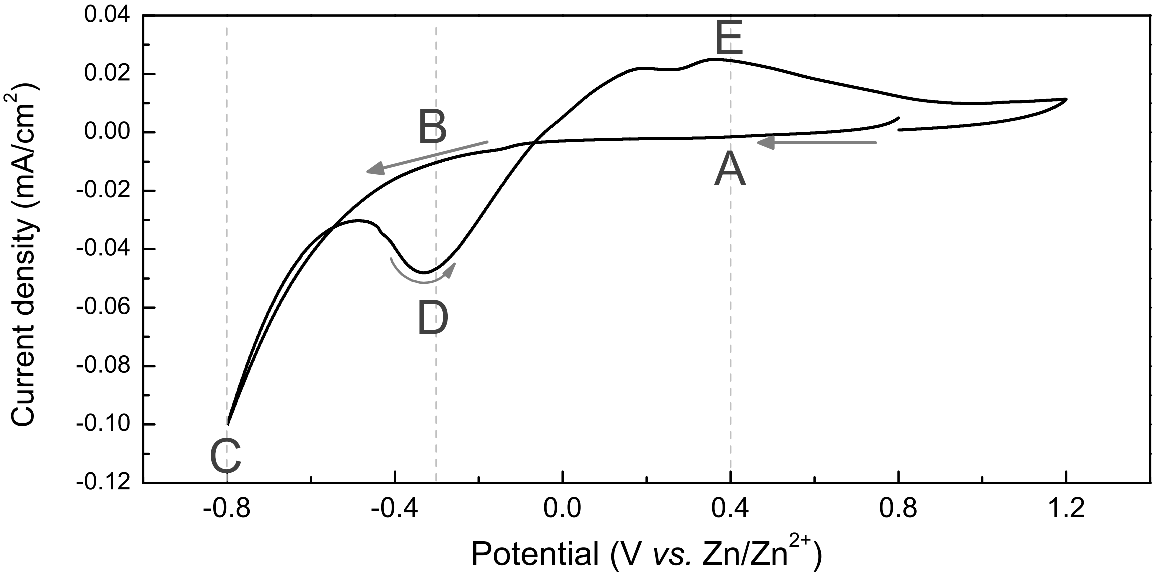

Figure 8.18. Thin-layer cyclic voltammogram of $0.3\,\mathrm{mol{\cdot}L^{-1}}$ $ZnCl_2$ in 12CE in the SEC cell at room temperature, $10\,\mathrm{mV{\cdot}s^{-1}}$ sweep rate, starting at +0.8 V with a negative direction, as indicated by the arrows. Glassy carbon ($1.54\,\mathrm{cm^2}$) was used as the working electrode and zinc wires (1 mm ϕ) as reference and counter electrodes. Letters A to E indicate the chosen potentials for *in-situ* PM-IRRAS measurements.

Based on this CV, PM-IRRAS spectra were measured at the indicated potentials (A to E). The potential steps and current transients are shown in Figure 8.19. The first step (A) was measured at +0.4 V, where no faradaic reaction should occur. Secondly, at −0.3 V (B), where no deposition should occur during the forward step because the reducible species have not yet formed. Although from the current profile at −0.3 V, it seems like some zinc was deposited from the Z species formed, as the current is of the same magnitude as for this reverse step at this potential. Subsequently, a PM-IRRAS spectrum at −0.8 V (C) was recorded. At this potential the Ch and EG molecules are reduced, the reducible Z species are formed and the GC surface is somehow blocked, hindering the deposition of zinc. The reduction of the electrolyte molecules is evident from the current profile at −0.8 V, which is noisy. In a thin layer cell configuration, the diffusion of the reactants and products are hindered, thus the hydrogen formed may be trapped in the thin-layer compartment (about 10 μm) and disturb the measurement.

By changing the potential in the positive direction from −0.8 V (C) back to−0.3 V (D), the surface is unblocked and zinc is deposited from Z. Stepping further positive to +0.4 V (E) causes the dissolution of zinc, which is also confirmed by the anodic current at this potential.

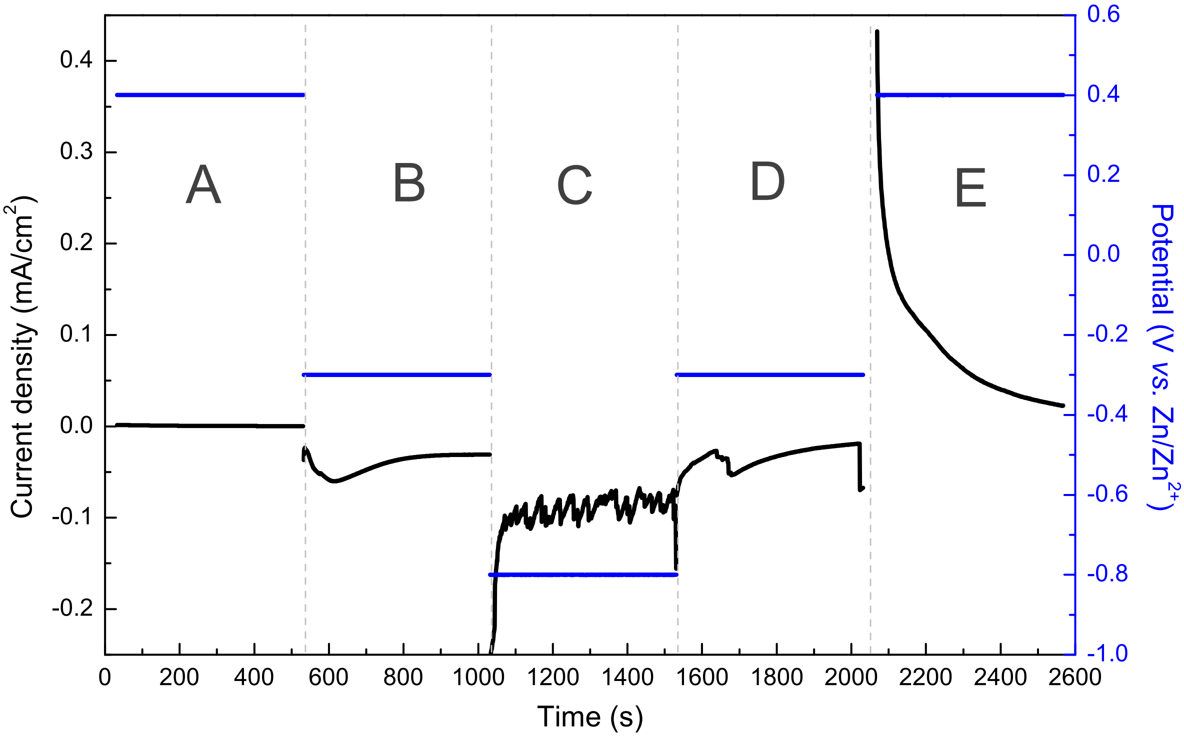

Figure 8.19. Working electrode potential (blue) and current response (black) *versus* time of 0.3 mol·L^{-1} $ZnCl_2$ 12CE in the spectroelectrochemical cell during *in situ* PM-IRRAS measurements.

The corresponding baseline corrected *in situ* PM-IRRAS spectra of 12CE-Zn in the fingerprint region are shown in Figure 8.20. The species in solution in the 0.3 mol·L^{-1} $ZnCl_2$ 12CE are: Ch^+, Cl^-, EG and $[ZnCl_4]^{2-}$. Nevertheless, it is important to remember that $[ZnCl_4]^{2-}$ does not absorb in the mid-infrared region, but only in the far-infared. Therefore the adsorption of these species on GC can not be directly observed by this method.

Decreasing the potential from +0.4 to −0.3 V causes a decrease in IR absorbance for the δ(C-H) and ν(C-N) bands from ($N^+(CH_3)_3$) at 1489 and 957 cm^{-1}. This decrease becomes more prominent at −0.8 V. However, it was expected that the PM-IRRAS vibrations attributed to the Ch^+ would increase at a negatively charged electrode, because the positively charged ammonium head group of the choline molecules would be more strongly attracted at negative potentials. However, there are some effects that could explain the unexpected result of this IR measurement in reflection configuration. The absorbance signal depends not only on the surface concentration and dipole moment of adsorbed molecules but also on the reflectivity of the surface [215, 262]. Hence, a change of the glassy carbon reflectivity due to deposition of zinc is likely at negative potentials. Yet, to which extent this change in reflectivity can affect the measurement of adsorbed species is still unclear. For the interpretation of the surface spectra shown in this section, only the population of adsorbate and dipole moment of the molecules at the interface will thus be taken into account.

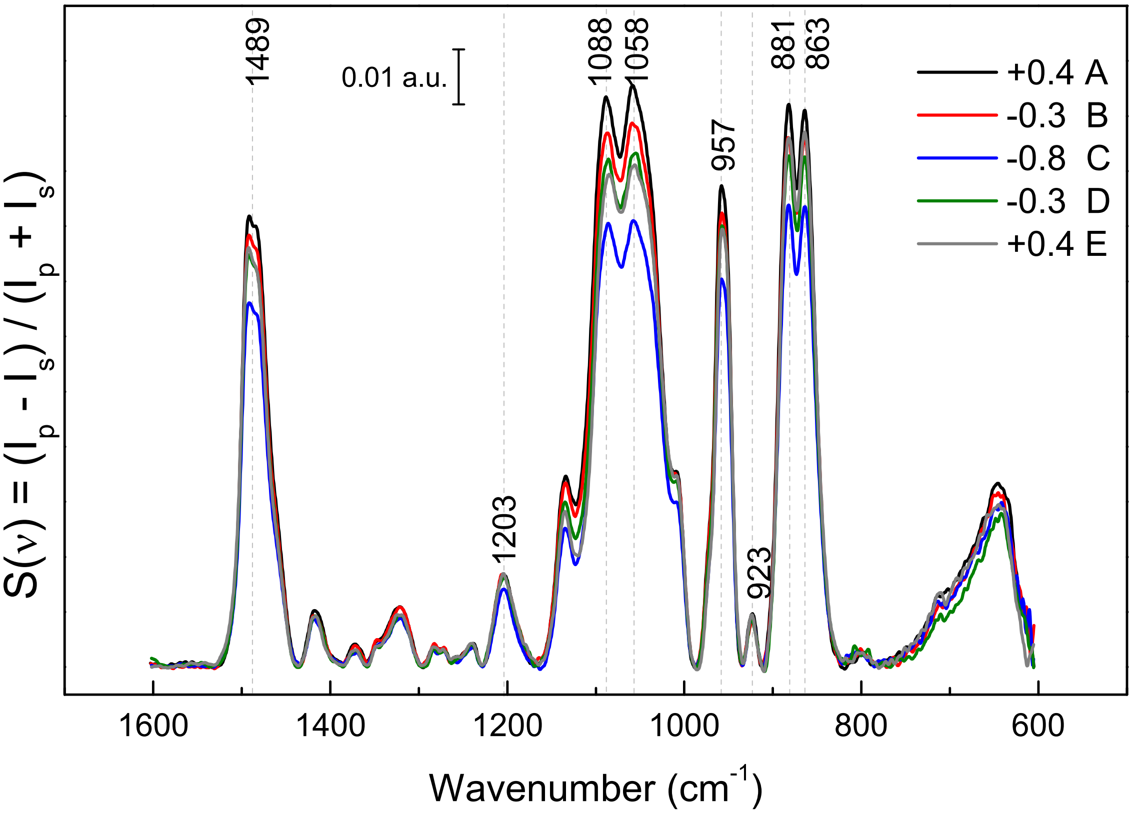

Figure 8.20. PM-IRRAS surface spectra of 0.3 mol·L^{-1} $ZnCl_2$ in 12CE recorded at the indicated potential steps. The first spectrum was collected at +0.4 V (spectrum in black) followed by spectra at the potentials shown in Figure 8.19.

The PM-IRRAS spectra show potential-dependent changes in the absorption intensity of the bands. Firstly, as mentioned above, a gradual decrease in intensity from +0.4 to −0.8 V, specially on the bending mode of the methylene groups of $N^+(CH_3)_3$ at 1489 cm^{-1}. The asymmetric stretching of (C−N) at 957 cm^{-1} also shows the same decrease in band intensity, whereas the symmetric mode at 923 $\mathrm{cm^{-1}}$ did not change with potential. The symmetric and asymmetric C−O stretching modes at 1088 and 1058 $\mathrm{cm^{-1}}$ as well as the CH_2 rocking and C−C stretching mode at 881 and 863 $\mathrm{cm^{-1}}$ also change with potential.

Figure 8.21 shows the potential-dependent variation in band intensity for the δ_{as} $(N^+(CH_3)_3$, $\nu_{as}(C{-}N^+(CH_3)_3$ and νC−O. It can be observed that switching the electrode potential in the positive direction from −0.8 V to −0.3 V causes the PM-IRRAS bands to increase in intensity. This is an important result, as it shows that the change in surface species absorption is caused by the applied potential and not only by a change in metal reflectivity or by time-dependent effects, as previously discussed in Section 8.1. Otherwise, in the case of change in reflectivity by electrodepositing zinc, it is likely that the IR signal would decrease continuously, whereas time-dependent adsorption would cause the IR signal to continuously increase. Switching the potential positively to +0.4 V caused the $\delta_{as}(N^+(CH_3)_3$ band intensity to slightly increase, whereas the $\nu_{as}(C{-}N^+(CH_3)_3$ and νC−O decrease.

To better visualise the changes on the surface caused by the applied potential, the spectra shown in Figure 8.20 were normalized with respect to a reference spectrum. The first spectrum measured at +0.4 V *vs.* Zn/Zn^{2+} was chosen as reference, because no faradaic current is observed at this potential (Figure 8.19). The normalized spectra was used for quantitative analysis of adsorption/desorption of the interfacial species. The normalized spectra are shown in Figure 8.22.

The ratios are always below 1, because the PM-IRRAS band intensities were highest in the reference spectrum. Thus, for the normalised spectra shown in Figure 8.22, the higher the band, the bigger is the difference compared to the spectrum A. For these normalized spectra, it can be observed that the ratio becomes bigger upon stepping from +0.4 to −0.8 V. Desorption of Ch^+ at −0.3 V is not expected. Moreover, stepping back in the positive direction causes the ratio to decrease, which would imply that the interface becomes more similar to the initial state at +0.4 V.

The corresponding *p*- and *s*- polarized IRRAS spectra of the deep eutectic solution are shown in Figure 8.23 for the fingerprint region (1500–600 $\mathrm{cm^{-1}}$). In these two data sets, one can observe the bands originating from the bulk electrolyte species (*s*-component) and those from the surface together with the bulk electrolyte species (*p*-spectra). In the *p*-spectra, there are some vibrational modes that are not present in *s*-spectra. Also some low intensity bands in the *s*-spectra, such as the $\delta_{as}N^+(CH_3)_3$ at 1479 and ν(C−N) at 950 $\mathrm{cm^{-1}}$, are much more intense in the *p*-spectra. Moreover, there is an evident difference in the *s*- and *p*- spectra for the ν_s(C−O) and ν_{as}(C−O) modes at 1100 and

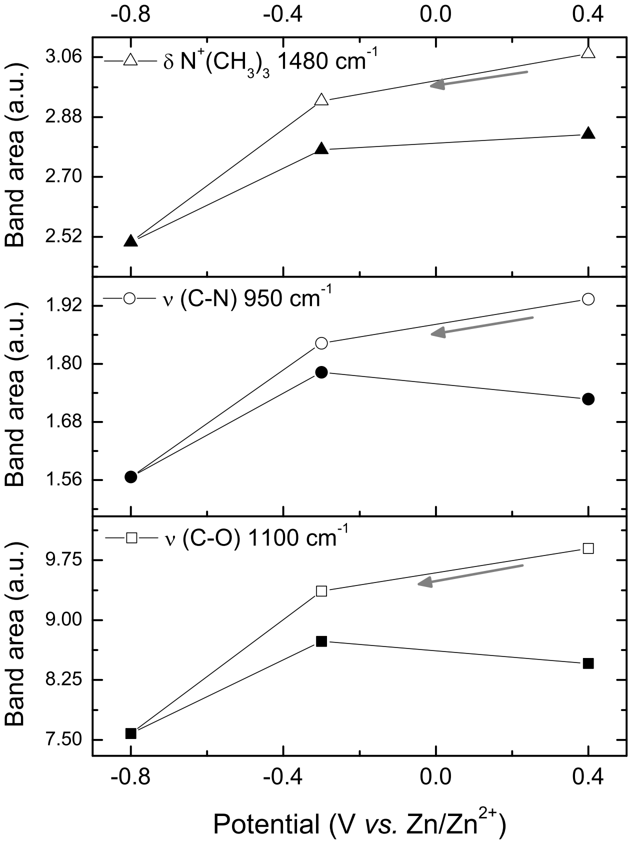

Figure 8.21. PM-IRRAS band intensities as function of electrode potential of 0.3 mol·L^{-1} $ZnCl_2$ in 12CE. Empty symbols indicate forward potential direction (from +0.4 to −0.3 V, A and B). Filled symbols indicate backward potential direction (−0.8 to +0.4 V, C, D and E). The band areas were obtained by the integration of the PM-IRRAS bands shown in Figure 8.20.

1060 cm^{-1}, respectively.

As it has been previously discussed for the PM-IRRAS measurements of 12CE without zinc, it is likely that at +0.4 V, the GC surface is covered by Cl^- ions. The second layer would consist of Ch^+, which would assume a more vertical orientation in order to maximize the electrostatic interaction of the ammonium group of the choline with the negative Cl^- layer. Charging the working electrode negatively would cause the $N^+(CH_3)_3$ group to adsorb directly at the electrode surface. Consequently, due to the electrostatic attraction on the two polar groups (ammonium and hydroxyl), the Ch^+ molecules would assume a more tilted orientation (with respect to the surface normal), causing a decrease in absorption intensity at −0.3 V.

The further decrease in the absorption ratio intensity upon stepping the potential from −0.3 to −0.8 V can be explained either by desorption of the molecules — yet without

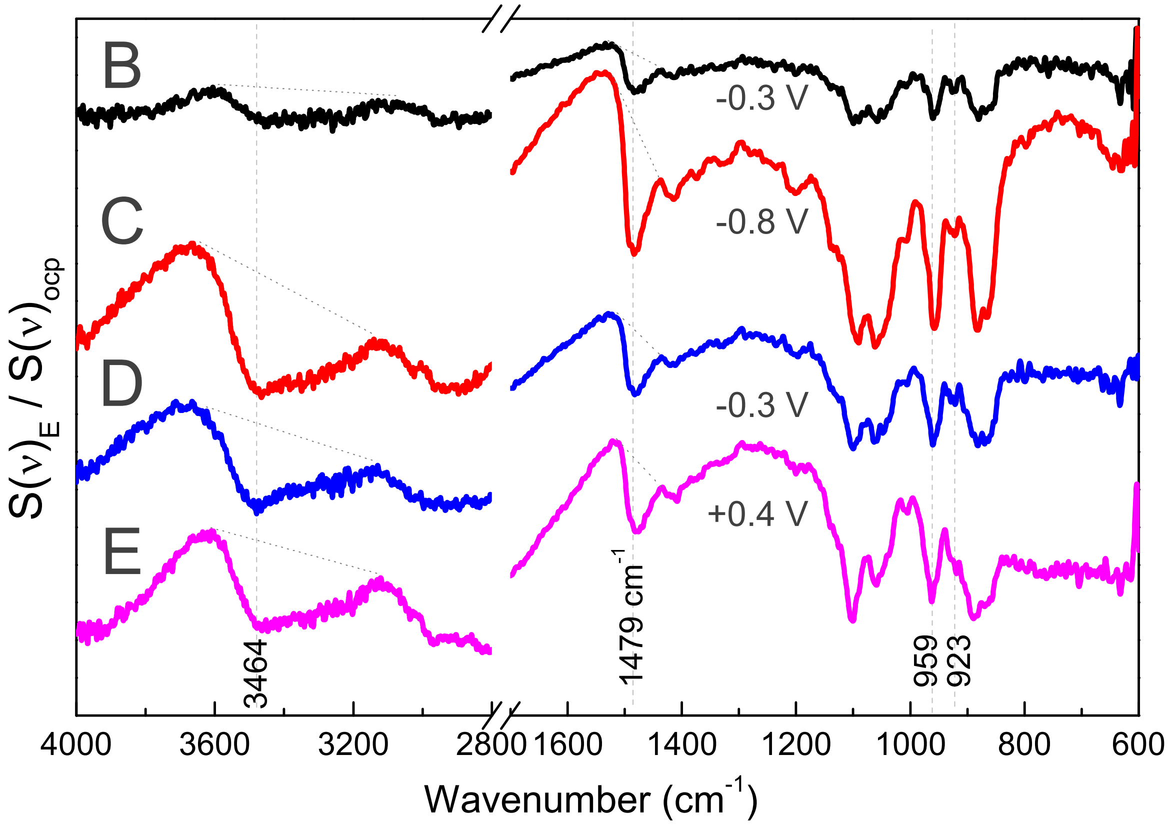

Figure 8.22. PM-IRRAS surface spectra for 0.3 mol·L^{-1} ZnCl$_2$ in 12CE recorded at the indicated potentials. The reference spectrum was measured at open circuit potential $E_{\mathrm{ocp}} = +0.25$ V.

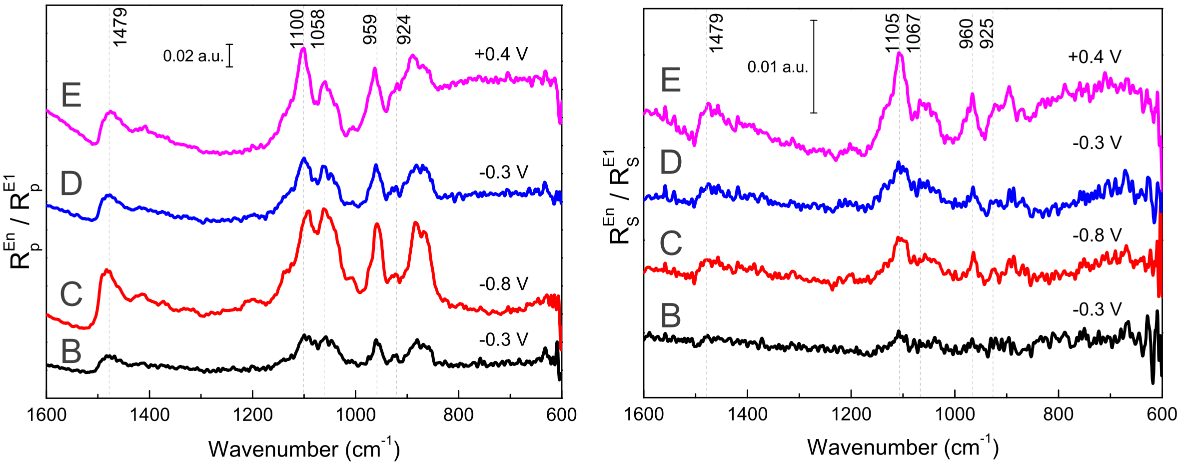

(a) p-polarized

(b) s-polarized

Figure 8.23. a) p- and b) s-polarized IR reflectance spectra for 0.3 mol·L^{-1} ZnCl$_2$ in 12CE on GC at different potentials. The reference spectrum was collected at +0.4 V.

replacement by other species, as no bands appear in the opposite direction — or by an additional decrease in the inclination angle of the molecules adsorbed with respect to the surface normal. The very negative potential of $-0.8\,\mathrm{V}$ would cause the adsorbed molecules to assume a more parallel orientation, consequently bringing the O−H group of the choline closer to the electrode surface, thereby facilitating its reduction with formation of hydrogen. On the basis of the surface selection rules of IRRAS [85], the resultant dipole will be cancelled by the 'reflecting mirror' created by the metal surface if it is oriented parallel to the surface. The adsorbed hydrogen and choline on the GC are likely to comprise the blocking layer that hinders the deposition of zinc.

A schematic representation of the GC/12CE-$[ZnCl_4]^{2-}$ interface is shown in Figure 8.24. From Figure a) to b), the replacement of Cl^- by Ch^+ cations for the potential step from $+0.4$ to $-0.3\,\mathrm{V}$ is represented. A more inclined orientation of the Ch^+ would explain the decrease in the δ and ν $N^+(CH_3)_3$ band. Step c) and d) represent the stronger inclination of Ch^+ with reduction of the O−H groups and blocking of the surface by adsorbed hydrogen at $-0.8\,\mathrm{V}$. The resulting alkoxy anions RO^- of EG and Ch form complexes with the zinc ions (Z species). At $-0.3\,\mathrm{V}$ (Figure 8.24 e) the hydrogen diffuses away and zinc deposition takes place. The re-adsorption of Ch^+ on the GC/Zn surface causes the PM-IRRAS bands for δ and ν $N^+(CH_3)_3$ to increase again. Finally, at $+0.4\,\mathrm{V}$ the surface is covered by chloride and dissolution of zinc occurs.

The band intensities and peak positions of the baseline-corrected ΔS^* spectra are presented in Figure 8.25. The potential causes significant changes of the intensity of the vibrational modes and slight shifts on the position of the bands centroid. The band areas of $\delta_{\mathrm{as}}(N^+(CH_3)_3$ and $\nu_{\mathrm{as}}(C{-}N^+(CH_3)_3$ decrease with potential by a factor of 3. This is probably caused by a closer approach of the molecule axis to the GC surface.

The frequency of the $\delta_{\mathrm{as}}(N^+(CH_3)_3$ and $\nu_{\mathrm{as}}(C{-}N^+(CH_3)_3$ bands shift in different directions. For the $\delta_{\mathrm{as}}(N^+(CH_3)_3$ mode, the change of electrode potential from -0.3 to $-0.8\,\mathrm{V}$ causes a blue-shift of $3\,\mathrm{cm}^{-1}$, indicating that the C−H bond become stronger at $-0.8\,\mathrm{V}$ *vs.* Zn/Zn^{2+}. This can be caused by the induction of charge from the electrode to the Ch^+ group, causing a strengthening of the methylene bonds. Stepping back to $+0.4\,\mathrm{V}$ causes a shift from 1481 to $1477\,\mathrm{cm}^{-1}$. On the other hand, the potential changes for the ν_{as}C−N causes the opposite frequency shift. Stepping to negative potentials, from -0.3 to $-0.8\,\mathrm{V}$, caused a $1\,\mathrm{cm}^{-1}$ shift (from $960.3\,\mathrm{cm}^{-1}$ at $-0.3\,\mathrm{V}$ to $959.7\,\mathrm{cm}^{-1}$ at $-0.8\,\mathrm{V}$ and back to $-0.3\,\mathrm{V}$ with a frequency of $961.3\,\mathrm{cm}^{-1}$). However, the spectral resolution of the IR spectrometer is only $2\,\mathrm{cm}^{-1}$ and such small frequency shifts ($\nu \ \leq 4\,\mathrm{cm}^{-1}$) do not leave room for interpretation. At $+0.4\,\mathrm{V}$, the ν_{as}C−N shifts to $964\,\mathrm{cm}^{-1}$, indicating that the C−N bond became stronger, which can be caused by a surface excess of Cl^-.

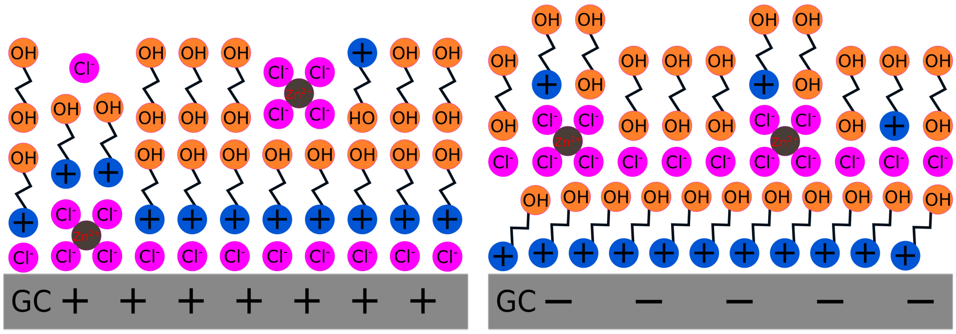

(a) +0.4 V A (b) −0.3 V B

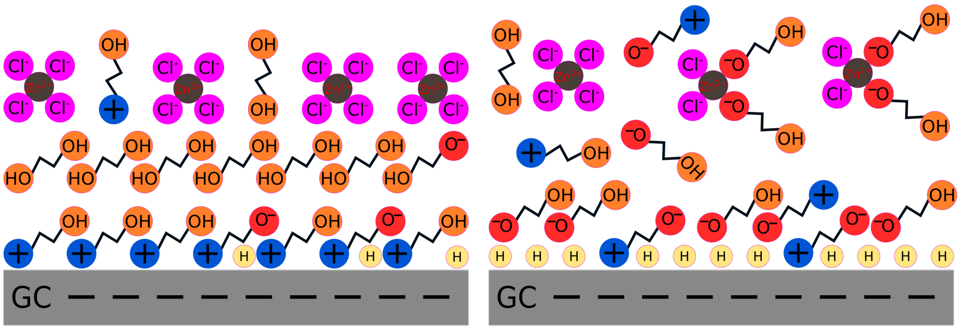

(c) −0.8 V C (d) −0.8 V C

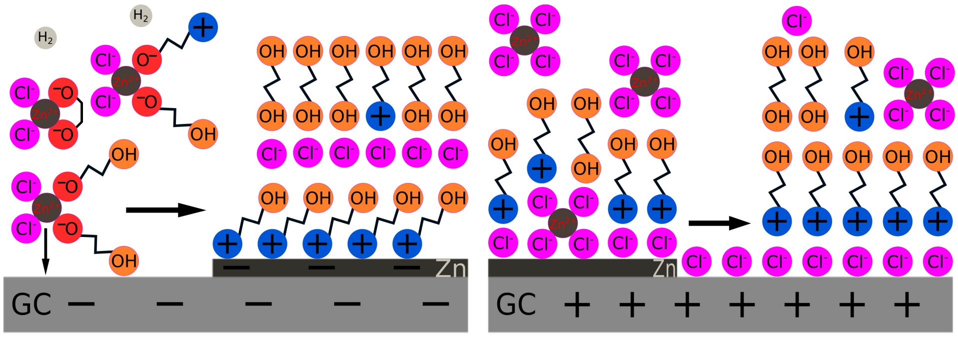

(e) −0.3 V D (f) +0.4 V E

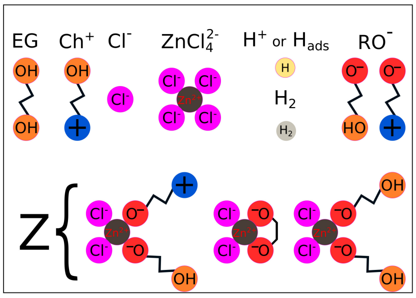

(g) legend

Figure 8.24. Schematic illustration of the potential-dependent changes in the structure of GC/12CE-$[ZnCl_4]^{2-}$: a) at the first step potential at +0.4 V; b) at −0.3 V, where the interface is dominated by the cations Ch^+; c) and d) at −0.8 V, where Ch and EG are reduced and the surface becomes covered by adsorbed hydrogen; e) at −0.3 V, where deposition of zinc from Z occurs; f) at +0.4 V, where the surface is covered by Cl^- ions and dissolution of zinc takes place; g) legend of the involved species.

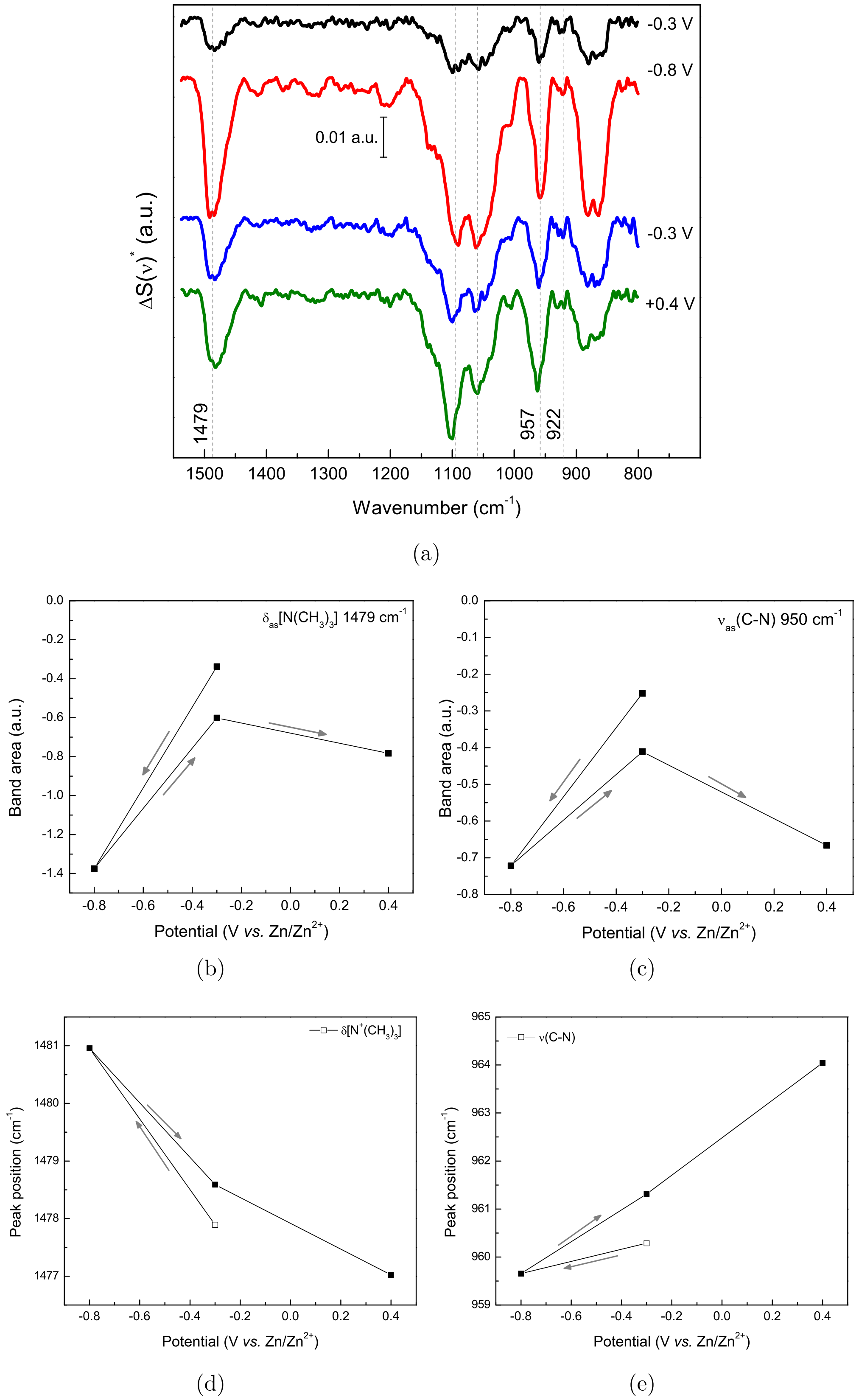

(a)

(b)

(c)

(d)

(e)

Figure 8.25. a) Baseline-corrected PM-IRRAS surface spectra for 0.3 mol·L^{-1} ZnCl$_2$ in 12CE on GC at different potentials. The reference spectrum was collected at +0.4 V. b) and c) band area; d) and e) peak position (centroid) of the bands corresponding to δ_{as}N$^+$(CH$_3$)$_3$ and νC−N$^+$(CH$_3$)$_3$, respectively.

The *in situ* PM-IRRAS results during multi-step-potential chronoamperomentric experiments for the deep eutectic 12CE with and without zinc chloride differ considerably. The overpotential for hydrogen evolution at zinc and glassy carbon differs significantly. Hydrogen evolution has a considerable influence on the zinc deposition, because the products of electrolyte reduction lead to the formation of the reducible zinc species Z.

Not much is known about the double layer in ionic liquids. In such room temperature molten salts, the structure of the double layer is quite different from those of traditional electrolytes and the Gouy-Chapman-Stern (GCS) model for diluted electrolyte solutions [52] does not apply. A proper understanding of the solvent solute interactions is not easy, because the IL is composed entirely of ions [66, 263, 264]. The structure of the electrical double-layer in ionic liquids and the ionic solvation of the solute may influence nucleation [65, 110], however the theory of the electrical double layer (EDL) for ionic liquids is still in its infancy.

AFM and STM *in situ* electrochemical measurements carried out in the groups of Endres and Atkins [70, 181, 258] have recently shown that the addition of small amounts of LiCl to a pyrrolidinium-based ionic liquid ([$Py_{1,4}$][FAP]) strongly alters the near surface structure of IL-gold interfaces. Also, the EDL of an [EMIM][FSI] (1-ethyl-3-methylimidazolium bis(fluorosulfonyl)imide) on graphite electrodes has been investigated for its charge-discharge behavior [265]. The authors described a change of the interfacial structure of the negatively charged electrode caused by the addition of Li[TFSI] (lithium bis(trifluoromethylsulfonyl)imide) to the IL.

PM-IRRAS measurements of the 12CE and 12CE/Zn^{2+} on GC provided some insight into the interfacial behavior of this system and reveal the nature of the blocking layer, which hinders zinc deposition. This technique is promising for the investigation of the electrical double layer of ionic liquids, because it allows the *in situ* study of the electrode/IL interface. Still, theoretical simulations including calculations of the molecular orientation on the electrode surface, which can be obtained from simulations, are needed to better understand such systems.

9 Conclusions

Cyclic voltammetry on glassy carbon electrodes of $ZnCl_2$ in a strongly Lewis-basic deep eutectic solvent comprising choline chloride and ethylene glycol at room temperature has revealed an unusual cathodic peak on sweeping the potential positive from $-0.8\,V$ *vs.* Zn/Zn^{2+}. The same voltammetric behavior is observed at elevated temperature.

Based on rotating disc electrode voltammetry under variation of the cathodic switching potential, the scan rate and the electrode rotation rate, a possible explanation for this feature has been given. It is suggested that active sites on the glassy carbon are blocked by adsorbed species such as choline, ethylene glycol or hydrogen at low potentials, which gradually desorb at potentials above $-0.4\,V$ *vs.* Zn/Zn^{2+}. Zinc is deposited from a reducible Zn species Z formed as intermediate during the cathodic sweep. Z is formed in the diffusion layer by replacement of one or more chloride ligands in the $[ZnCl_4]^{2-}$ ion, which Raman spectroscopy confirmed to be the dominating zinc species in the Lewis-basic DES. Furthermore, Z is transported into the bulk of the electrolyte by rotating the electrode. The formation of Z has slow chemical kinetics and increasing the potential scan rate decreases the zinc deposition rate. Hence, an ECE mechanism (E and C are electron transfer and chemical steps, respectively) was suggested to explain the zinc electrodeposition from 12CE.

The addition of sodium ethoxide to the DES increased the viscosity of the solution but facilitated the deposition of zinc. A cathodic peak for Zn deposition was observed at the same potential as without the ethoxide, in the cathodic, as well as in the anodic sweep. RDE experiments with the ethoxide containing electrolyte caused the current to increase with rotation rate, which supports the hypothesis that the intermediate Z contains RO^- anions as ligands and that in presence of an alkoxy base Z is already formed in the bulk of the electrolyte. This observation is consistent with the hypothesis that Z is a complex having the formula $[ZnCl_{4\text{-}x}(RO)_x]^{2-}$. Thus, hydrogen-free zinc electrodeposition could be achieved through addition of NaOEt to the deep eutectic solvent.

The zinc deposition mechanism is very sensitive to the nature of the substrate. Steel electrodes appeared similar to glassy carbon, however, gold, platinum and copper, which all can form extensive intermetallic phases with zinc exhibited distinctly different behavior. The overpotential for the hydrogen evolution on the different electrode materials was found to be very important for the formation of Z and consequently the electrodeposition of zinc. Platinum, gold and copper, which have a low hydrogen overpotential compared to GC, show reduction peaks on the forward cathodic as well as on the return anodic scan, whereas glassy carbon and stainless steel, which both have a high overpotential for hydrogen evolution, only show a reduction peak on the backward anodic voltammetric scan. This is again consistent with the mechanism proposed above.

Zinc deposits on platinum and copper electrodes have been characterized *ex situ*. SEM and FIB micrographs showed that the zinc layers for both substrates have a similar surface morphology with nanoplatelets. XRD of the deposit on platinum and copper revealed the typical pattern for the Pt_7Zn_{12} and Cu_4Zn phase, respectively, in addition to the reflexes of crystalline zinc.

The mechanism of zinc nucleation on stainless steel has been investigated. Comparison of the dimensionless experimental current-time transients with theoretical Sharifker and Hills curves indicated that the mechanism of zinc nucleation on stainless steel follows a 3D instantaneous nucleation process. The mechanism of zinc nucleation on SS from 12CE was compared to those reported in the literature from ionic liquids and aqueous electrolytes.

Spectroelectrochemical methods have been implemented for the system $ZnCl_2$ in 12CE in order to identify intermediate species and thus clarify the mechanism of zinc deposition. *In situ* polarization-modulation infrared reflection-absorption spectroscopy (PM-IRRAS) measurements have been carried out on a glassy carbon electrode. This technique allows to distinguish between chemical information from the solution and the species adsorbed on the electrode surface. However, due to the external reflection configuration, the electrochemical measurements have to be carried out in a thin electrolyte layer, which brings drawbacks of increasing the uncompensated resistance (*iR* drop) and also it prevents the diffusion of reactants and products from the electrode surface. In case gases are formed, like hydrogen, they are trapped in the thin-layer and may disturb both spectral and electrochemical measurements [61]. These disadvantages could be overcome by changing from the external to an internal reflection configuration. However, this configuration relays on the surface-enhanced infrared absorption (SEIRA) effect, which would require metal electrodes such as Au, Ag or Cu. Thus, in such configuration, it would not be possible to study the electrochemical mechanism on a glassy carbon electrode.

The three investigated electrolytes comprising ethylene glycol, 12CE as well as $ZnCl_2$

in 12CE, gave a very good response to PM-IRRAS in the spectroelectrochemical cell and most of the vibrations could be identified. This technique is a rather new approach for spectroelectrochemical investigations and consequently, not much has been found in the literature on PM-IRRAS for electrochemical *in situ* studies. To date PM-IRRAS spectroelectrochemistry has not been reported for ionic liquids.

The electrolyte molecules showed time dependent adsorption with ultra-slow kinetics (many hours) at open circuit potential.

The study of potential dependent adsorption for 12CE and $0.3\,\mathrm{mol{\cdot}L^{-1}}$ $ZnCl_2$ 12CE on glassy carbon electrodes showed that upon decreasing the potential from open circuit until $-0.6\,\mathrm{V}$, mostly Ch^+ ions are adsorbed on the surface. From 0 to $-0.6\,\mathrm{V}$ the adsorbed Ch^+ molecules become more tilted toward the electrode surface, consequently decreasing the resultant dipole moment and the PM-IRRAS signal. At $-0.8\,\mathrm{V}$, the EG and Ch^+ molecules are reduced and adsorbed hydrogen at the GC surface is accounted for hindering the electrodeposition of zinc at this potential. Stepping the potential positively caused the adsorbed hydrogen either to desorb as hydrogen gas or to be reoxidised. Hence, the surface is unblocked and zinc electrodeposition from Z species takes place.

From -0.6 to $+0.4\,\mathrm{V}$ *vs.* Zn/Zn^{2+} the Ch^+ molecules readsorb on the GC electrode, and an increase of IR absorbance is observed for the δ and ν vibrational modes of $N^+(CH_3)_3$. At $E \geq +0.4\,\mathrm{V}$ an overall change in the arrangement of the interfacial species takes place and Ch^+ ions are replaced by Cl^-. In this potential range, the bands attributed to the vibrational modes of Ch^+ increase due to a change in molecular orientation, which turns more vertical with respect to the surface in order to maximize the electrostatic interaction with the surface excess of Cl^-.

The unusual electrochemical behavior of zinc in choline-based deep eutectic electrolytes opens many questions not only on the mechanism of zinc reduction from ionic liquids but also on the structure of the electrode/electrolyte interface in such deep eutectic solvents and how this affects electrochemical reactions.

The current theories of electrochemical double layers (e.g. Helmholz and Gouy-Chapman-Stern models) only applies for diluted aqueous solutions, because it neglects the interactions between ions. Because ionic liquids consist of highly concentrated ionic solutions, the electrode/electrolyte interface presumably has a different configuration. It has been proposed that the IL/electrode interface consists of alternating layers of anions and cations [68] and our PM-IRRAS results are in agreement with such models for ionic liquids. Nevertheless, additional investigations on the electrode/electrolyte interface are required for a better understanding of these interactions. Therefore, other surface-sensitive methods, e.g. *in situ* surface X-ray scattering, of a DES on GC should be performed to corroborate the PM-IRRAS results. Through X-ray scattering measurements it is expected to obtain structural information about the IL/electrode interface, such as surface coverage and layer spacings. It is also expected to see a structural change in cations-anions ordering by charging the electrode more negative or positively than OCP.

References

[1] F. C. Porter, *Corrosion resistance of zinc and zinc alloys*, Marcel Dekker, New York, **1994**.

[2] H. Geduld, *Zinc Plating*, ASM International, Trowbridge, **1988**.

[3] X. G. Zhang, *Corrosion and Electrochemistry of Zinc*, Springer, **1996**.

[4] H. Ohno, *Electrochemical aspects of ionic liquids*, Wiley-Interscience, **2005**.

[5] M. Galinski, A. Lewandowski, I. Stepniak, *Electrochimica Acta* **2006**, *51*, 5567–5580.

[6] F. Endres, D. MacFarlane, A. Abbott (Eds.), *Electrodeposition from Ionic Liquids*, Wiley-VCH, Weinheim, **2008**.

[7] A. Kokorin, *Ionic Liquids: Applications and Perspectives*, Intech, **2011**.

[8] D. R. MacFarlane, N. Tachikawa, M. Forsyth, J. M. Pringle, P. C. Howlett, G. D. Elliott, J. H. Davis, M. Watanabe, P. Simon, C. A. Angell, *Energy and Environmental Science* **2014**, *7*, 232–250.

[9] P. Wasserscheid in *Green Industrial Applications of Ionic Liquids*, (Eds.: R. Rogers, K. R. Seddon, S. Volkov), NATO Science Series, Springer Netherlands, **2002**, pp. 29–47.

[10] A. P. Abbott, D. L. Davies, G. Capper, R. K. Rasheed, V. Tamyrajah, *pat.*, US 2004/0097755 A1, **2004**.

[11] A. P. Abbott, D. Boothby, G. Capper, D. L. Davies, R. K. Rasheed, *Journal of the American Chemical Society* **2004**, *126*, 9142–9147.

[12] C. A. Staples, J. B. Williams, G. R. Craig, K. M. Roberts, *Chemosphere* **2001**, *43*, 377–383.

[13] K. Haerens, E. Matthijs, K. Binnemans, B. Van der Bruggen, *Green Chemistry* **2009**, *11*, 1357–1365.

[14] K. Haerens, E. Matthijs, A. Chmielarz, B. Van der Bruggen, *J.Environ.Manage.* **2009**, *90*, 3245–3252.

[15] Q. Zhang, K. De Oliveira Vigier, S. Royer, F. Jerome, *Chemical Society Reviews* **2012**, *41*, 7108–7146.

[16] C. Russ, B. Koenig, *Green Chemistry* **2012**, *14*, 2969–2982.

[17] B. Tang, K. H. Row, *Monatshefte für Chemie* **2013**, 1427–1454.

[18] A. P. Abbott, G. Capper, D. L. Davies, R. K. Rasheed, V. Tambyrajah, *Chemical Communications* **2003**, 70–71.

[19] A. P. Abbott, G. Capper, D. L. Davies, K. J. McKenzie, Obi, S. U., *Journal of Chemical and Engineering Data* **2006**, *51*, 1280–1282.

[20] R. Rogers, J. Brennecke, K. Seddon, A. C. S. D. of Industrial, E. Chemistry, *Ionic Liquids IV: not just solvens anymore*, American Chemical Society, **2007**.

[21] N. V. Plechkova, K. R. Seddon, *Chemical Society Reviews* **2008**, *37*, 123–150.

[22] W. Pitner, C. L. Hussey, *Journal of the Electrochemical Society* **1997**, *144*, 3095–3103.

[23] Y.-F. Lin, I.-W. Sun, *Journal of The Electrochemical Society* **1999**, *146*, 1054–1059.

[24] Y.-F. Lin, I.-W. Sun, *Electrochimica Acta* **1999**, *44*, 2771–2777.

[25] J. Dogel, W. Freyland, *Physical Chemistry Chemical Physics* **2003**, *5*, 2484–2487.

[26] D. Borissov, A. Pareek, F. U. Renner, M. Rohwerder, *Physical Chemistry Chemical Physics* **2010**, *12*, 2059–2062.

[27] M.-J. Deng, P.-C. Lin, J.-K. Chang, J.-M. Chen, K.-T. Lu, *Electrochimica Acta* **2011**, *56*, 6071–6077.

[28] S. Ernst, M. Henstridge, R. Compton, *Journal of Solid State Electrochemistry* **2012**, *16*, 2329–2333.

[29] N. Doan, T. Vainikka, E.-L. Rautama, K. Kontturi, C. Johans, *International Journal of Electrochemical Science* **2012**, *7*, 12034–12044.

[30] T. Simons, A. Torriero, P. Howlett, D. MacFarlane, M. Forsyth, *Electrochemistry Communications* **2012**, *18*, 119–122.

[31] T. J. Simons, P. C. Howlett, A. A. J. Torriero, D. R. MacFarlane, M. Forsyth, *The Journal of Physical Chemistry C* **2013**, *117*, 2662–2669.

[32] M. Xu, D. G. Ivey, Z. Xie, W. Qu, *Electrochimica Acta* **2013**, *89*, 756–762.

[33] Z. Liu, S. Z. E. Abedin, F. Endres, *Electrochimica Acta* **2013**, *89*, 635–643.

[34] A. P. Abbott, G. Capper, K. J. McKenzie, K. S. Ryder, *Journal of Electroanalytical Chemistry* **2007**, *599*, 288–294.

[35] A. Bakkar, V. Neubert, *Electrochemistry Communications* **2007**, *9*, 2428–2435.

[36] A. P. Abbott, J. C. Barron, K. S. Ryder, *Transactions of the Institute of Metal Finishing* **2009**, *87*, 201–207.

[37] A. P. Abbott, J. C. Barron, G. Frisch, K. S. Ryder, A. F. Silva, *Electrochimica Acta* **2011**, *56*, 5272–5279.

[38] H. Y. Yang, X. W. Guo, X. B. Chen, S. H. Wang, G. H. Wu, W. J. Ding, N. Birbilis, *Electrochimica Acta* **2012**, *63*, 131–138.

[39] N. M. Pereira, S. Salomé, C. M. Pereira, F. A. Silva, English, *Journal of Applied Electrochemistry* **2012**, *42*, 561–571.

[40] N. M. Pereira, P. M. V. Fernandes, C. M. Pereira, F. A. Silva, *Journal of The Electrochemical Society* **2012**, *159*, D501–D506.

[41] M. Pölzler, A. H. Whitehead, B. Gollas, *ECS Transactions* **2010**, *25*, 43–55.

[42] A. H. Whitehead, M. Pölzler, B. Gollas, *Journal of The Electrochemical Society* **2010**, *157*, D328–D334.

[43] L. Vieira, A. Whitehead, B. Gollas, *ECS Transactions* **2013**, *50*, 83–94.

[44] L. Vieira, A. H. Whitehead, B. Gollas, *Journal of The Electrochemical Society* **2014**, *161*, D7–D13.

[45] A. P. Abbott, J. C. Barron, G. Frisch, S. Gurman, K. S. Ryder, A. Fernando Silva, *Physical Chemistry Chemical Physics* **2011**, *13*, 10224–10231.

[46] M. Kar, B. Winther-Jensen, M. Forsyth, D. R. MacFarlane, *Physical Chemistry Chemical Physics* **2013**, *15*, 7191–7197.

[47] S.-I. Hsiu, J.-F. Huang, I.-W. Sun, C.-H. Yuan, J. Shiea, *Electrochimica Acta* **2002**, *47*, 4367–4372.

[48] Y. Zou, H. Xu, G. Wu, Z. Jiang, S. Chen, Y. Huang, W. Huang, X. Wei, *The Journal of Physical Chemistry B* **2009**, *113*, 2066–2070.

[49] J. Estager, P. Nockemann, K. R. Seddon, M. Swadzba-Kwasny, S. Tyrrell, *Inorganic Chemistry* **2011**, *50*, 5258–5271.

[50] Southampton-Electrochemistry-Group, *Instrumental methods in electrochemistry*, E. Horwood series in physical chemistry, **1985**.

[51] P. Kissinger, W. Heineman, *Laboratory Techniques in Electroanalytical Chemistry, Second Edition, Revised and Expanded*, Taylor & Francis, **1996**.

[52] A. J. Bard, L. R. Faulkner, *Electrochemical methods: fundamentals and applications*, Wiley, New York, 2nd, **2001**.

[53] D. Pletcher, *A first course in electrode processes*, Electrochemical consultancy, Romsey, **1991**.

[54] M. Schlesinger, M. Paunovic, *Modern Electroplating*, Wiley, **2011**.

[55] M. Paunovic, M. Schlesinger, *Fundamentals of Electrochemical Deposition*, Wiley, **2006**.

[56] P. Larkin, *Infrared and Raman Spectroscopy; Principles and Spectral Interpretation*, Elsevier Science, **2011**.

[57] B. Mistry, *A Handbook of Spectroscopic Data Chemistry: (UV, IR, PMR, 13CNMR and Mass Spectroscopy)*, Oxford Book Company, **2009**.

[58] D. Pavia, *Introduction to Spectroscopy*, Brooks/Cole, Cengage Learning, **2009**.

[59] A. Wieckowski, C. Korzeniewski, B. Braunschweig, *Vibrational Spectroscopy at Electrified Interfaces*, Wiley, **2013**.

[60] V. Zamlynny, J. Lipkowski in *Advances in Electrochemical Science and Engineering*, (Eds.: R. C. Alkire, D. M. Kolb, J. Lipkowski, P. N. Ross), Wiley-VCH Verlag GmbH, **2008**, pp. 315–376.

[61] M. Osawa in *Advances in Electrochemical Science and Engineering, Vol. 9*, (Eds.: R. C. Alkire, D. M. Kolb, J. Lipkowski, P. N. Ross), Wiley-VCH Verlag GmbH, **2008**, pp. 269–314.

[62] J. Vickerman, I. Gilmore, *Surface Analysis: The Principal Techniques*, Wiley, **2009**.

[63] A. Kornyshev, *Journal of Physical Chemistry B* **2007**, *111*, 5545–5557.

[64] K. B. Oldham, *Journal of Electroanalytical Chemistry* **2008**, *613*, 131–138.

[65] Y.-Z. Su, Y.-C. Fu, Y.-M. Wei, J.-W. Yan, B.-W. Mao, *ChemPhysChem* **2010**, *11*, 2764–2778.

[66] M. Y. Lui, L. Crowhurst, J. P. Hallett, P. A. Hunt, H. Niedermeyer, T. Welton, *Chemical Science* **2011**, *2*, 1491–1496.

[67] P. Hapiot, C. Lagrost, *Chemical Reviews* **2008**, *108*, 2238–2264.

[68] M. Mezger, H. Schröder, H. Reichert, S. Schramm, J. S. Okasinski, S. Schöder, V. Honkimäki, M. Deutsch, B. M. Ocko, J. Ralston, M. Rohwerder, M. Stratmann, H. Dosch, *Science* **2008**, *322*, 424–428.

[69] R. Hayes, N. Borisenko, M. K. Tam, P. C. Howlett, F. Endres, R. Atkin, *The Journal of Physical Chemistry C* **2011**, *115*, 6855–6863.

[70] R. Atkin, N. Borisenko, M. Drüschler, F. Endres, R. Hayes, B. Huber, B. Roling, *Journal of Molecular Liquids* **2013**, in press.

[71] S. Maolin, Z. Fuchun, W. Guozhong, F. Haiping, W. Chunlei, C. Shimou, Z. Yi, H. Jun, *The Journal of Chemical Physics* **2008**, *128*, 134504.

[72] M. V. Fedorov, A. A. Kornyshev, *Journal of Physical Chemistry B* **2008**, *112*, 11868–11872.

[73] M. V. Fedorov, A. A. Kornyshev, *Electrochimica Acta* **2008**, *53*, 6835–6840.

[74] R. S. Payal, S. Balasubramanian, *ChemPhysChem* **2012**, *13*, 1764–1771.

[75] K. Kirchner, T. Kirchner, V. Ivanistsev, M. Fedorov, *Electrochimica Acta* **2013**, *110*, 762–771.

[76] B. Bozzini, A. Bund, B. Busson, C. Humbert, A. Ispas, C. Mele, A. Tadjeddine, *Electrochemistry Communications* **2010**, *12*, 56–60.

[77] W. Zhou, S. Inoue, T. Iwahashi, K. Kanai, K. Seki, T. Miyamae, D. Kim, Y. Katayama, Y. Ouchi, *Electrochemistry Communications* **2010**, *12*, 672–675.

[78] S. Baldelli, *Accounts of Chemical Research* **2008**, *41*, 421–431.

[79] S. Baldelli, *The Journal of Physical Chemistry Letters* **2013**, *4*, 244–252.

[80] V. O. Santos, M. B. Alves, M. S. Carvalho, P. A. Z. Suarez, J. C. Rubim, *The Journal of Physical Chemistry B* **2006**, *110*, 20379–20385.

[81] Y.-X. Yuan, T.-C. Niu, M.-M. Xu, J.-L. Yao, R.-A. Gu, *Journal of Raman Spectroscopy* **2010**, *41*, 516–523.

[82] Y.-Y. Yang, L.-N. Zhang, M. Osawa, W.-B. Cai, *The Journal of Physical Chemistry Letters* **2013**, *4*, 1582–1586.

[83] K. Motobayashi, K. Minami, N. Nishi, T. Sakka, M. Osawa, *The Journal of Physical Chemistry Letters* **2013**, *4*, 3110–3114.

[84] S. Best, A. L. Crumbliss, L. Dunsch, M. Haga, F. Hartl, C. P. Kubiak, R Winter, L. J. Yellowlees, C. Salsman, P. Murray, S. Dhungana, *Spectroelectrochemistry*, (Eds.: W. Kaim, A. Klein), The Royal Society of Chemistry, **2008**.

[85] R. G. Greenler, *The Journal of Chemical Physics* **1966**, *44*, 310–315.

[86] R. Schennach, C. Hirschmugl, E. Gilli, W. T. Tysoe, *Applied Spectroscopy* **2009**, *63*, 369–372.

[87] O. Hoefft, S. Bahr, V. Kempter, *Analytical Sciences* **2008**, *24*, 1273–1277.

[88] O. Hoefft, S. Bahr, V. Kempter, *Langmuir* **2008**, *24*, 11562–11566.

[89] N. Nanbu, Y. Sasaki, F. Kitamura, *Electrochemistry Communications* **2003**, *5*, 383–387.

[90] A. H. Kycia, Z. Su, C. L. Brosseau, J. Lipkowski in *Vibrational Spectroscopy at Electrified Interfaces*, John Wiley & Sons, Inc., **2013**, pp. 345–417.

[91] J. Lipkowski, *Physical Chemistry Chemical Physics* **2010**, *12*, 13874–13887.

[92] C. L. Brosseau, J. Leitch, X. Bin, M. Chen, S. G. Roscoe, J. Lipkowski, *Langmuir* **2008**, *24*, 13058–13067.

[93] I. Zawisza, X. Bin, J. Lipkowski, *Langmuir* **2007**, *23*, 5180–5194.

[94] X. Bin, J. Lipkowski, *Journal of Physical Chemistry B* **2006**, *110*, 26430–26441.

[95] I. Burgess, M. Li, S. Horswell, G. Szymanski, J. Lipkowski, S. Satija, J. Majewski, *Colloids and Surfaces B: Biointerfaces* **2005**, *40*, 117–122.

[96] X. Bin, S. L. Horswell, J. Lipkowski, *Biophysical Journal* **2005**, *89*, 592–604.

[97] I. Burgess, M. Li, S. Horswell, G. Szymanski, J. Lipkowski, J. Majewski, S. Satija, *Biophysical Journal* **2004**, *86*, 1763–1776.

[98] I. Zawisza, A. Lachenwitzer, V. Zamlynny, S. L. Horswell, J. D. Goddard, J. Lipkowski, *Biophysical Journal* **2003**, *85*, 4055–4075.

[99] S. L. Horswell, V. Zamlynny, H.-Q. Li, A. R. Merrill, J. Lipkowski, *Faraday Discussions* **2002**, *121*, 405–422.

[100] M. B. Alves, V. O. Santos jr., V. C. D. Soares, P. A. Z. Suarez, J. C. Rubim, *Journal of Raman Spectroscopy* **2008**, *39*, 1388–1395.

[101] J. Yoshimura, H. Waki, S. Tashiro, *Bulletin of the Chemical Society of Japan* **1962**, *35*, 412–415.

[102] E. A. Pavlatou, P. A. Madden, M. Wilson, *The Journal of Chemical Physics* **1997**, *107*, 10446–10457.

[103] O. Babushkina, S. Volkov, *Journal of Molecular Liquids* **1999**, *83*, 131–140.

[104] C. O. Quicksall, T. G. Spiro, *Inorganic Chemistry* **1966**, *5*, 2232–2233.

[105] O. G. Parchment, M. A. Vincent, I. H. Hillier, *The Journal of Physical Chemistry* **1996**, *100*, 9689–9693.

[106] J.-J. Lee, I. T. Bae, D. A. Scherson, B. Miller, K. A. Wheeler, *Journal of The Electrochemical Society* **2000**, *147*, 562–566.

[107] S. Schaltin, M. Ganapathi, K. Binnemans, J. Fransaer, *Journal of The Electrochemical Society* **2011**, *158*, D634–D639.

[108] M.-J. Deng, P.-Y. Chen, T.-I. Leong, I.-W. Sun, J.-K. Chang, W.-T. Tsai, *Electrochemistry Communications* **2008**, *10*, 213–216.

[109] S.-J. Pan, W.-T. Tsai, J.-K. Chang, I.-W. Sun, *Electrochimica Acta* **2010**, *55*, 2158–2162.

[110] F. Endres, O. Hofft, N. Borisenko, L. H. Gasparotto, A. Prowald, R. Al-Salman, T. Carstens, R. Atkin, A. Bund, S. Zein El Abedin, *Physical Chemistry Chemical Physics* **2010**, *12*, 1724–1732.

[111] R. Hayes, G. G. Warr, R. Atkin, *Physical Chemistry Chemical Physics* **2010**, *12*, 1709–1723.

[112] N. Borisenko, S. Zein El Abedin, F. Endres, *The Journal of Physical Chemistry B* **2006**, *110*, 6250–6256.

[113] A. P. Abbott, D. C. Loveday, A. R. Hillman, *Journal of the Chemical Society Faraday Transactions* **1994**, *90*, 1533–1535.

[114] A. P. Abbott, J. C. Harper, *Journal of the Chemical Society Faraday Transactions* **1997**, *93*, 3981–3984.

[115] A. P. Abbott, J. C. Harper, G. Stimsom, *Journal of Electroanalytical Chemistry* **2002**, *520*, 6–12.

[116] M.-H. Yang, I.-W. Sun, English, *Journal of Applied Electrochemistry* **2003**, *33*, 1077–1084.

[117] A. P. Abbott, J. Barron, K. Ryder, D. Wilson, *Chemistry A European Journal* **2007**, *13*, 6495–6501.

[118] A. P. Abbott, R. C. Harris, K. S. Ryder, C. D'Agostino, L. F. Gladden, M. D. Mantle, *Green Chemistry* **2011**, *13*, 82–90.

[119] C. D'Agostino, R. C. Harris, A. P. Abbott, L. F. Gladden, M. D. Mantle, *Physical Chemistry Chemical Physics* **2011**, *13*, 21383–21391.

[120] R. Evans, O. Klymenko, P. Price, *ChemPhysChem* **2005**, *6*, 526–533.

[121] O. Ciocirlan, O. Iulian, O. Croitoru, *Revista de Chimie* **2010**, *61*, 721–723.

[122] D. Lloyd, T. Vainikka, L. MurtomÃ¤ki, K. Kontturi, E. Ahlberg, *Electrochimica Acta* **2011**, *56*, 4942–4948.

[123] D. Lloyd, T. Vainikka, S. Schmachtel, L. Murtomaeki, K. Kontturi, *Electrochimica Acta* **2012**, *69*, 139–145.

[124] C. A. Angell, W. Xu, M. Yoshizawa, A. Hayashi, J.-P. Belieres, P. Lucas, M. Videa in *Electrochemical Aspects of Ionic Liquids*, John Wiley & Sons, Inc., **2005**, pp. 5–23.

[125] J. A. Smith, G. B. Webber, G. G. Warr, R. Atkin, *The Journal of Physical Chemistry B* **2013**, *117*, 13930–13935.

[126] C. Schreiner, S. Zugmann, R. Hartl, H. J. Gores, *Journal of Chemical & Engineering Data* **2010**, *55*, 1784–1788.

[127] H. Niedermeyer, J. P. Hallett, I. J. Villar-Garcia, P. A. Hunt, T. Welton, *Chemical Society Review* **2012**, *41*, 7780–7802.

[128] A. P. Abbott, *ChemPhysChem* **2005**, *6*, 2502–2505.

[129] A. P. Abbott, G. Capper, S. Gray, *ChemPhysChem* **2006**, *7*, 803–806.

[130] A. P. Abbott, R. C. Harris, K. S. Ryder, *The Journal of Physical Chemistry B* **2007**, *111*, 4910–4913.

[131] J. Wang, *Analytical Electrochemistry*, Wiley, 3rd, **2006**, p. 209.

[132] R. Atkin, N. Borisenko, M. Druschler, S. Z. El Abedin, F. Endres, R. Hayes, B. Huber, B. Roling, *Physical Chemistry Chemical Physics* **2011**, *13*, 6849–6857.

[133] T. Carstens, R. Hayes, S. Z. E. Abedin, B. Corr, G. B. Webber, N. Borisenko, R. Atkin, F. Endres, *Electrochimica Acta* **2012**, *82*, 48–59.

[134] L. Xiong, L. Aldous, M. C. Henstridge, R. G. Compton, *Analytical Methods* **2012**, *4*, 371–376.

[135] J. Zhang, A. Bond, *Analyst* **2005**, *130*, 1132–1147.

[136] L. Barrosse-Antle, A. Bond, R. Compton, A. O'Mahony, E. Rogers, D. Silvester, *Chemistry – An Asian Journal* **2010**, *5*, 202–230.

[137] D. Lide, *CRC Handbook of Chemistry and Physics, 85th Edition*, Taylor & Francis, **2004**.

[138] C. Zhao, G. Burrell, A. Torriero, F. Separovic, N. D. MacFarlane, D., A. Bond, *Journal of Physical Chemistry B* **2008**, *112*, 6923–6936.

[139] G. Trejo, R. O. B., Y. M. V., P. Ozil, E. Chainet, B. Nguyen, *Journal of the Electrochemical Society* **1998**, *145*, 4090–4097.

[140] M. Plata-Torres, S. L. Olvera-Vazquez, C. Ramirez-Rodriguez, H. J. Dorantes-Rosales, E. M. Arce-Estrada, *ECS Transactions* **2007**, *3*, 25–33.

[141] D. Knetsch, W. L. Groeneveld, *Inorganica Chimica Acta* **1973**, *7*, 81–87.

[142] H. Yamamoto, R. Iguchi, M. Morishita, *ECS Transactions* **2009**, *16*, 191–201.

[143] S. Pawar, A. Moholkar, P. Shinde, K. Rajpure, C. Bhosale, *Journal of Alloys and Compounds* **2008**, *459*, 515–520.

[144] T. Vorobyova, O. Vrublevskaya, *Surface and Coatings Technology* **2010**, *204*, 1314–1318.

[145] H. P. Nguyen, M. Wu, J. Su, R. J. Vullers, P. M. Vereecken, J. Fransaer, *Electrochimica Acta* **2012**, *68*, 9–17.

[146] H. Yamamoto, M. Morishita, Y. Mizuta, A. Masubuchi, *Surface and Coatings Technology* **2012**, *206*, 3415–3420.

[147] T. Iwagishi, Y. Nakatsuka, S. Harada, H. Yamamoto, K. Koyama, H. Shirai, *Electrochemistry* **2002**, *70*, 863–868.

[148] T. Iwagishi, H. Yamamoto, K. Koyama, H. Shirai, H. Kobayashi, *Electrochemistry* **2002**, *70*, 671–674.

[149] H. Yamamoto, S. Takeuchi, H. Shirai, K. Koyama, *Journal of The Surface Finishing Society of Japan* **2006**, *57*, 226–226.

[150] W. Schmickler, E. Santos, *Interfacial Electrochemistry*, Springer, **2010**, p. 163.

[151] Y. Meng, L. Aldous, S. R. Belding, R. G. Compton, *Chemical Communications* **2012**, *48*, 5572–5574.

[152] Y. Meng, L. Aldous, S. R. Belding, R. G. Compton, *Physical Chemistry Chemical Physics* **2012**, *14*, 5222–5228.

[153] Y. Meng, S. Norman, C. Hardacre, R. G. Compton, *Physical Chemistry Chemical Physics* **2013**, *15*, 2031–2036.

[154] Z. Moser, *Journal of Phase Equilibria* **1991**, *12*, 439–443.

[155] J.-F. Huang, I.-W. Sun, *Electrochimica Acta* **2004**, *49*, 3251–3258.

[156] J.-F. Huang, I. Sun, *Chemistry of Materials* **2004**, *16*, 1829–1831.

[157] J.-F. Huang, H.-Y. Chen, *Angewandte Chemie International Edition* **2012**, *51*, 1684–1688.

[158] Y. Okano, A. Katagiri, *Journal of The Electrochemical Society* **1997**, *144*, 1927–1932.

[159] M. A. Quaiyyum, A. Aramata, S. Moniwa, S. Taguchi, M. Enyo, *Journal of Electroanalytical Chemistry* **1994**, *373*, 61–66.

[160] K. Igarashi, A. Aramata, S. Taguchi, *Electrochimica Acta* **2001**, *46*, 1773–1781.

[161] Y. Yao, S. Xu, Y. Xia, Y. Yang, J. Liu, Z. Li, W. Huang, *International Journal of Electrochemical Science* **2012**, *7*, 3265–3273.

[162] A. R. Despic, M. G. Pavlovic, *Electrochimica Acta* **1982**, *27*, 1539–1549.

[163] E. Guerra, G. H. Kelsall, M. Bestetti, D. Dreisinger, K. Wong, K. A. R. Mitchell, D. Bizzotto, *Journal of The Electrochemical Society* **2004**, *151*, E1–E6.

[164] T. Boiadjieva, M. Monev, A. Tomandl, H. Kronberger, G. Fafilek, *Journal of Solid State Electrochemistry* **2009**, *13*, 671–677.

[165] J. F Huang, I. W Sun, *Advanced Functional Materials* **2005**, *15*, 989–994.

[166] F.-H. Yeh, C.-C. Tai, J.-F. Huang, I.-W. Sun, *Journal of Physical Chemistry B* **2006**, *110*, 5215–5222.

[167] Y. D. Gamburg, G. Zangari, *Theory and Practice of Metal Electrodeposition*, Springer Science & Business Media, LLC, New York, NY, **2011**.

[168] L. Giannuzzi, F. Stevie, *Introduction to Focused Ion Beams: Instrumentation, Theory, Techniques and Practice*, Springer, **2006**.

[169] L. Wei, Y.-J. Fan, N. Tian, Z.-Y. Zhou, X.-Q. Zhao, B.-W. Mao, S.-G. Sun, *The Journal of Physical Chemistry C* **2012**, *116*, 2040–2044.

[170] Y. Kang, J. B. Pyo, X. Ye, T. R. Gordon, C. B. Murray, *ACS Nano* **2012**, *6*, 5642–5647.

[171] N. S. Porter, H. Wu, Z. Quan, J. Fang, *Accounts of Chemical Research* **2013**, *46*, 1867–1877.

[172] Q. X. Liu, S. Z. E. Abedin, F. Endres, *Surface and Coatings Technology* **2006**, *201*, 1352–1356.

[173] C.-H. Chou, J.-C. Chen, C.-C. Tai, I.-W. Sun, J.-M. Zen, *Electroanalysis* **2008**, *20*, 771–775.

[174] D. Silvester, K. Ward, L. Aldous, C. Hardacre, R. Compton, *Journal of Electroanalytical Chemistry* **2008**, *618*, 53–60.

[175] R. P. Frankenthal, D. J. Siconolfi, *Journal of The Electrochemical Society* **1982**, *129*, 1192–1196.

[176] H. S. Liu, K. Ishida, Z. P. Jin, Y. Du, *Intermetallics* **2003**, *11*, 987–994.

[177] J. Dogel, R. Tsekov, W. Freyland, *The Journal of Chemical Physics* **2005**, *122*, 094703–094703.

[178] F. Jia, C. Yu, Z. Ai, L. Zhang, *Chemistry of Materials* **2007**, *19*, 3648–3653.

[179] M. G. Chu, J. McBreen, G. Adzic, *Journal of The Electrochemical Society* **1981**, *128*, 2281–2286.

[180] G. Pulletikurthi, A. Lahiri, T. Carstens, N. Borisenko, S. Zein El Abedin, F. Endres, English, *Journal of Solid State Electrochemistry* **2013**, *17*, 2823–2832.

[181] R. Hayes, N. Borisenko, B. Corr, G. B. Webber, F. Endres, R. Atkin, *Chemical Communications* **2012**, *48*, 10246–10248.

[182] M. Figueiredo, C. Gomes, R. Costa, A. Martins, C. M. Pereira, F. Silva, *Electrochimica Acta* **2009**, *54*, 2630–2634.

[183] R. Costa, M. Figueiredo, C. M. Pereira, F. Silva, *Electrochimica Acta* **2010**, *55*, 8916–8920.

[184] M. Z. Bazant, B. D. Storey, A. A. Kornyshev, *Physical Review Letters* **2011**, *106*, 046102/1–046102/4.

[185] N. Nishi, Y. Hirano, T. Motokawa, T. Kakiuchi, *Physical Chemistry Chemical Physics* **2013**, *15*, 11615–11619.

[186] H. Baker, *ASM handbook: Alloy phase diagrams*, ASM International, **1992**.

[187] C. Batchelor-McAuley, R. G. Compton, *Journal of Electroanalytical Chemistry* **2012**, *669*, 73–81.

[188] J. W. Dini, *Electrodeposition: The Materials Science of Coatings and Substrates*, Noyes Publications, **1993**.

[189] Y.-W. Lin, C.-C. Tai, I.-W. Sun, *Journal of the Electrochemical Society* **2007**, *154*, D316–D321.

[190] R. Juškenas, V Pakštas, A Sudavičius, V Kapočius, V Karpavičiene, *Applied Surface Science* **2004**, *229*, 402–408.

[191] I. T. Bae, *Journal of the Electrochemical Society* **2008**, *155*, D395–D399.

[192] R. Winand in *Modern Electroplating*, John Wiley & Sons, Inc., **2010**, pp. 285–307.

[193] W. J. van Ooij, *Rubber Chemistry and Technology* **July 1984**, *57*, 421–456.

[194] P. Chen, M. Lin, I. Sun, *Journal of The Electrochemical Society* **2000**, *147*, 3350–3355.

[195] A. Kitada, K. Yanase, T. Ichii, H. Sugimura, K. Murase, *Journal of The Electrochemical Society* **2013**, *160*, D417–D421.

[196] J. C. Ballesteros, P. Díaz-Arista, Y. Meas, R. Ortega, G. Trejo, *Electrochimica Acta* **2007**, *52*, 3686–3696.

[197] E. L. Smith, J. C. Barron, A. P. Abbott, K. S. Ryder, *Analytical Chemistry* **2009**, *81*, 8466–8471.

[198] M. E. Hyde, R. G. Compton, *Journal of Electroanalytical Chemistry* **2003**, *549*, 1–12.

[199] A. Milchev, L. Heerman, *Electrochimica Acta* **2003**, *48*, 2903–2913.

[200] E. Budevski, G. Staikov, W. Lorenz, *Electrochimica Acta* **2000**, *45*, 2559–2574.

[201] L. Heerman, A. Tarallo, *Journal of Electroanalytical Chemistry* **1999**, *470*, 70–76.

[202] M. Palomar-Pardavé, M. Miranda-Hernández, I. González, N. Batina, *Surface Science* **1998**, *399*, 80–95.

[203] G. Gunawardena, G. Hills, I. Montenegro, B. Scharifker, *Journal of Electroanalytical Chemistry and Interfacial Electrochemistry* **1982**, *138*, 225–239.

[204] B. Scharifker, G. Hills, *Electrochimica Acta* **1983**, *28*, 879–889.

[205] B. Scharifker, J. Mostany, *Journal of Electroanalytical Chemistry and Interfacial Electrochemistry* **1984**, *177*, 13–23.

[206] P. He, H. Liu, Z. Li, Y. Liu, X. Xu, J. Li, *Langmuir* **2004**, *20*, 10260–10267.

[207] A. Milchev, *Electrocrystallization: Fundamentals of Nucleation and Growth*, Springer, **2002**.

[208] P.-Y. Chen, I.-W. Sun, English, *Electrochimica Acta* **2001**, *46*, 1169–1177.

[209] J.-F. Huang, I.-W. Sun, *Journal of The Electrochemical Society* **2004**, *151*, C8–C14.

[210] S.-P. Gou, I. W. Sun, *Electrochimica Acta* **2008**, *53*, 2538–2544.

[211] V. Zamlynny, PhD thesis, University of Guelph, **2002**.

[212] D. M. Meier, PhD thesis, ETH Zürich, **2009**.

[213] F. Zaera, *Chemical Reviews* **2012**, *112*, 2920–2986.

[214] M. Djak, MA thesis, Graz University of Technology, Graz, Austria, **2011**.

[215] E. Gilli, PhD thesis, Graz University of Technology, Graz, Austria, **2011**.

[216] Y. Chabal, *Surface Science Reports* **1988**, *8*, 211–357.

[217] L. Nagy, G. Gyetvai, L. Kollar, G. Nagy, *Journal of Biochemical and Biophysical Methods* **2006**, *69*, 121–132.

[218] C. A. Nkuku, R. J. LeSuer, *The Journal of Physical Chemistry B* **2007**, *111*, 13271–13277.

[219] E. Rogers, D. Silvester, D. Poole, L. Aldous, C. H. Compton, R., *Journal of Physical Chemistry C* **2008**, *112*, 2729–2735.

[220] K. R. J. Lovelock, A. Ejigu, S. F. Loh, S. Men, P. Licence, D. A. Walsh, *Physical Chemistry Chemical Physics* **2011**, *13*, 10155–10164.

[221] P. De Vreese, K. Haerens, E. Matthijs, K. Binnemans, *Electrochimica Acta* **2012**, *76*, 242–248.

[222] W. Miao, Z. Ding, A. J. Bard, *The Journal of Physical Chemistry B* **2002**, *106*, 1392–1398.

[223] J. C. Myland, K. B. Oldham, *Analytical Chemistry* **2000**, *72*, 3972–3980.

[224] K. B. Oldham, N. P. C. Stevens, *Analytical Chemistry* **2000**, *72*, 3981–3988.

[225] W. Oelßner, F. Berthold, U. Guth, *Materials and Corrosion* **2006**, *57*, 455–466.

[226] K. Krishnan, R. Krishnan, English, *Proceedings of the Indian Academy of Sciences - Section A* **1966**, *64*, 111–122.

[227] W. Sawodny, K. Niedenzu, J. Dawson, *Spectrochimica Acta Part A: Molecular Spectroscopy* **1967**, *23*, 799–806.

[228] K. M. Harmon, S. L. Madeira, M. J. Jacks, G. F. Avci, A. C. Thiel, *Journal of Molecular Structure* **1985**, *128*, 305–14.

[229] K. M. Harmon, G. F. Avci, *Journal of Molecular Structure* **1986**, *140*, 261–268.

[230] Q. Abbas, PhD thesis, Graz University of Technology, **2011**.

[231] D. Yue, Y. Jing, J. Sun, X. Wang, Y. Jia, *Journal of Molecular Liquids* **2011**, *158*, 124–130.

[232] H. Wang, Y. Jing, X. Wang, Y. Yao, Y. Jia, *Journal of Molecular Liquids* **2012**, *170*, 20–24.

[233] L. Wang, H. Meng, P. K. Shen, C. Bianchini, F. Vizza, Z. Wei, *Physical Chemistry Chemical Physics* **2011**, *13*, 2667–2673.

[234] Y. Liu, G. Wu, M. Qi, *J.Cryst.Growth* **2005**, *281*, 616–622.

[235] D. Yue, Y. Jia, Y. Yao, J. Sun, Y. Jing, *Electrochimica Acta* **2012**, *65*, 30–36.

[236] L. Deng, Y. Jing, J. Sun, J. Ma, D. Yue, H. Wang, *Journal of Molecular Liquids* **2012**, *170*, 45–50.

[237] S. L. Perkins, P. Painter, C. M. Colina, *The Journal of Physical Chemistry B* **2013**, *117*, 10250–10260.

[238] M. Francisco, A. Bruinhorst, M. Kroon, *Angewandte Chemie International Edition* **2013**, *52*, 3074–3085.

[239] B. Stuart, *Infrared Spectroscopy: Fundamentals and Applications*, Wiley, **2004**.

[240] A. Büchler, W. Klemperer, A. G. Emslie, *The Journal of Chemical Physics* **1962**, *36*, 2499–2508.

[241] O. Skoplyak, M. Barteau, J. Chen, *Surface Science* **2008**, *602*, 3578–3587.

[242] M. B. Griffin, E. L. Jorgensen, J. W. Medlin, *Surface Science* **2010**, *604*, 1558–1564.

[243] N. F. Brown, M. A. Barteau, *The Journal of Physical Chemistry* **1994**, *98*, 12737–12745.

[244] A. J. Capote, R. J. Madix, *Journal of the American Chemical Society* **1989**, *111*, 3570–3577.

[245] A. Capote, R. Madix, *Surface Science* **1989**, *214*, 276–288.

[246] K. T. Queeney, C. R. Arumainayagam, M. K. Weldon, C. M. Friend, M. Q. Blumberg, *Journal of the American Chemical Society* **1996**, *118*, 3896–3904.

[247] M. Jansen, B. Nieuwenhuys, H. Niemantsverdriet, *ChemSusChem* **2009**, *2*, 883–886.

[248] J. Vos, R. Forster, T. Keyes, *Interfacial Supramolecular Assemblies*, Wiley, **2003**.

[249] W. Iwasita, F. Nart, *Progress in Surface Science* **1997**, *55*, 271–340.

[250] R. Silverstein, F. Webster, D. Kiemle, *Spectrometric identification of organic compounds*, John Wiley & Sons, **2005**.

[251] M. L. Mitchell, R. A. Dluhy, *Journal of the American Chemical Society* **1988**, *110*, 712–18.

[252] R. A. Dluhy, S. M. Stephens, S. Widayati, A. D. Williams, *Spectrochimica Acta Part A: Molecular and Biomolecular Spectroscopy* **1995**, *51*, 1413–1447.

[253] I. Zawisza, G. Wittstock, R. Boukherroub, S. Szunerits, *Langmuir* **2008**, *24*, 3922–3929.

[254] H. Binder, *Applied Spectroscopy Reviews* **2003**, *38*, 15–69.

[255] E. Pretsch, P. Bühlmann, *Structure Determination of Organic Compounds: Tables of Spectral Data*, Springer, **2009**.

[256] I. Zawisza, G. Wittstock, R. Boukherroub, S. Szunerits, *Langmuir* **2007**, *23*, 9303–9309.

[257] M. Röefzaad, D. Thanh Pham, K. Wandelt in *Vibrational Spectroscopy at Electrified Interfaces*, John Wiley & Sons, Inc., **2013**, pp. 307–326.

[258] F. Endres, N. Borisenko, S. Z. El Abedin, R. Hayes, R. Atkin, *Faraday Discussions* **2012**, *154*, 221–233.

[259] S. Rivera-Rubero, S. Baldelli, *Journal of Physical Chemistry B* **2004**, *108*, 15133–15140.

[260] T. R. Gore, T. Bond, W. Zhang, R. W. Scott, I. J. Burgess, *Electrochemistry Communications* **2010**, *12*, 1340–1343.

[261] S. Makino, Y. Kitazumi, N. Nishi, T. Kakiuchi, *Electrochemistry Communications* **2011**, *13*, 1365–1368.

[262] K. Yamamoto, H. Ishida, *Vibrational Spectroscopy* **1994**, *8*, 1–36.

[263] A. B. Pereiro, J. M. M. Araujo, F. S. Oliveira, C. E. S. Bernardes, J. M. S. S. Esperanca, J. N. Canongia Lopes, I. M. Marrucho, L. P. N. Rebelo, *Chemical Communications* **2012**, *48*, 3656–3658.

[264] A. Pereiro, J. Araújo, F. Oliveira, J. Esperan*c*a, J. C. Lopes, I. Marrucho, L. Rebelo, *The Journal of Chemical Thermodynamics* **2012**, *55*, 29–36.

[265] M. Yamagata, N. Nishigaki, S. Nishishita, Y. Matsui, T. Sugimoto, M. Kikuta, T. Higashizaki, M. Kono, M. Ishikawa, *Electrochimica Acta* **2013**, *110*, 181–190.

Curriculum vitae

Luciana Vieira

Curriculum Vitae

Personal

born June 28, 1983 in Teresina, Brazil

Education

2010–2013 **Doctor of Philosophy**, *Graz University of Technology*, Graz, Austria.
Mechanistic Studies of Zinc Electrodeposition from Deep Eutectic Solvents, under supervision of Prof. Dr. Bernhard Gollas

2006–2008 **Master of Science**, *State University of Campinas*, Campinas, Brazil.
Synthesis of tungsten and molybdenum sulfide nanostructured materials, under supervision of Prof. Dr. Oswaldo Alves

2002–2005 **Bachelor in Chemistry**, *State University of Campinas*, Campinas, Brazil.

Experience

2010–2013 **Junior Researcher**, *Austrian Competence Centre for Electro-chemical Surface Technology (CEST) and Graz University of Technology*, Graz, Austria.

- 2012–2013 Alumiol Project
- 2010–2011 ARIoL Project

Working on projects involving the electrodeposition of metals from ionic liquids. The Alumiol project involves aluminium deposition on mild and stainless steel from 1-ethyl-3-methylimidazolium chloride (EMIM Cl) and the characterization of deposits by Scanning Electron Microscopy (SEM), Focused Ion Beam (FIB) and X-Ray Diffraction (XRD). The ARIoL project involves the investigation of anodic reaction in ionic liquids. To study such reactions, classical electrochemical and spectroscopic methods were employed.

2008–2009 **Trainee**, *CEST and Graz University of Technology*, Graz, Austria.
Traineeship on the project: "Erosion-resistant layers on Carbon Fibre Reinforced Plastics (CFRP) for low-drag aircraft". Investigated the influence of different pre-treatments of CFRP samples on the quality of the metal coating.

2003–2008 **Traineeships**, *State University of Campinas*, Campinas, Brazil.

- 2004–2005 - The effect of residual catalyst on the thermal and photo-oxidative degradation of high density polyethylene, under supervision of Prof. Dr. Maria Isabel Felisberti
- 2003 - Alumina-catalyzed epoxidation of cyclooctene with hydrogen peroxide, under supervision of Prof. Dr. Ulf Schuchardt

Languages

Portuguese	**Native speaker**	
English	**Full professional proficiency**	*C2*
Spanish	**Professional working proficiency**	*C1*
German	**Professional working proficiency**	*B2*

Publications in Journals

Vieira, L.; Whitehead, A.; Gollas, B; Mechanistic Studies of Zinc Electrodeposition from Deep Eutectic Electrolytes, *Journal of The Electrochemical Society*,**161** (1) D7-D13 (2014).

Silveira, J. V, Vieira, L. L.; Mendes Filho, J; Sampaio, A. J. C.; Alves, O.A.; Souza Filho, A. G. Temperature-dependent Raman spectroscopy study in MoO_3 nanoribbons, *J. Raman Spectroscopy* **10**, 1407-1412 (2012)

Publications Congress Proceedings

Vieira, L.; Whitehead, A.; Gollas, B; Mechanistic Studies of Zinc Electrodeposition from Deep Eutectic Electrolytes, *ISE Transactions*, **50** (52) 83-94 (2013)

Oral Presentation in Conferences

Vieira, L.; Gollas, B.; Schennach, R.; Mechanistic Studies of Zinc Electrodeposition from Deep Eutectic Electrolytes. Oral Presentation in Chemietage, Graz-Austria, 07.09.2013

Gollas, B.; Vieira, L.; Schennach, R.; Mechanistic Studies of Zinc Electrodeposition from Deep Eutectic Electrolytes. Oral Presentation in Pacific Rim Meeting on Electrochemical and Solid-State Science, Honolulu-USA, 07.10.2012

Gollas, B.; Vieira, L.; Schennach, R.; Mechanistic Studies of Zinc Electrodepostion from Deep Eutectic Electrolytes. Oral Presentation in Electrochemistry 2012 from Gesellschaft Deutscher Chemiker, Munich-Germany, 17.09.2012.

Vieira, L.; Schennach, R.; Gollas, B.; Mechanistic Studies of Zinc Electrodepostion from Deep Eutectic Electrolytes. Oral presentation in Spectroelectrochemistry Meeting, Dresden-Germany, 26.08.2012

Vieira, L.; Gollas, B.; Schennach, R.; Mechanistic Studies of Zinc Electrodeposition from Deep Eutectic Electrolytes. Oral Presentation in the Chemietage, Linz-Austria, 07.09.2011

Gollas, B.; Whitehead, A.; Pölzler, M; Vieira, L.; Zinc electrodeposition from a deep eutectic system containing choline chloride and ethylene glycol. Oral Presentation in the Electrochemistry 2010, Bochum-Germany, 13.09.2010

Poster Presentation in Conferences

Kosmus, P.; Vieira, L.; Gollas, B. and Steiner, O.; Electroplating of aluminium from ionic liquids, Poster presentation in the 4th South-East Europe Symposium on Electrochemistry, Ljubljana-Slovenia, 26.05.2013.

Vieira, L. and Gollas, B.; Zinc electrodeposition from a choline chloride-based deep eutectic electrolyte, Poster presentation in The 63rd Annual Meeting of the International Society of Electrochemistry, Prague-Czech Republic, 19.08.2012.

Vieira, L.; Ferreira, O. P. and Alves, O. L.; Synthesis of WS_2 nanotubes from WO_3 *in situ* generated nanorods, Poster presentation in the E-MRS 2009 Spring Meeting, Strasbourg-France, 10.06.2009.

Vieira, L.; Dias Neto, J. M.; Ferreira, O. P. and Alves, O. L.; Synthesis of tungsten oxide nanorods from a WCl_6 precursor, Poster presentation in the 31st Annual meeting of the Brazilian Chemical Society, Aguas de Lindoia - Brazil, 26.05.2008.

Vieira, L.; Ferreira, O. P. and Alves, O. L.; Synthesis and characterization of molybdenum oxide nanorods, Poster presentation in the 31st Annual meeting of the Brazilian Chemical Society, Aguas de Lindoia - Brazil, 27.05.2008.

Vieira, L.; Ferreira, O. P. and Alves, O. L.; Synthesis and characterization of tungsten oxide nanorods, Poster presentation in the 30st Annual meeting of the Brazilian Chemical Society, Aguas de Lindoia - Brazil, 02.06.2007.

Vieira, L.; Paulino, I. S. and Felisberti, M. I.; The effect of the residual catalyst on the photo- and thermal-degradation of high density polyethylene, Poster presentation in the 8th Brazilian Conference on Polymers (CBPol), Aguas de Lindoia - Brazil, 02.06.2005.

Extra activities

2007–2012 **IAESTE**, *The International Association for the Exchange of Students for Technical Experience.*

IAESTE is an independent, non-profit and non-political student exchange organization. It provides students in technical degrees with paind, cours-related training abroad. With over 80 countries, IAESTE is the largest organization of this kind in the world.

- 2011–2012 IAESTE Graz Internal Exchange - Organized the arrival of international students in Graz.
- 2010–2011 IAESTE Graz Summer Reception - Organized the reception and several activities for international students in Austria.
- 2008–2009 IAESTE Trainee in Austria - Traineeship in CEST through IAESTE.
- 2007–2008 IAESTE Brazil - Took part in several activities with international students during their traineeship in Campinas-Brazil.

2010–current **Capoeira**, *Centro Cultural Senzala de Capoeira Graz.*

Artistic capoeira presentations and short plays in cultural events in Graz

List of Figures

List of Tables